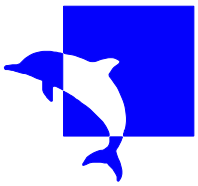

University of Southampton
Faculty of Engineering, Science and Mathematics
School of Electronics and Computer Science

Initial Synchronisation in the Multiple-Input Multiple-Output Aided Single- and Multi-Carrier DS-CDMA as well as DS-UWB Downlink

by

SeungHwan Won

BSc, MSc

A doctoral thesis submitted in partial fulfilment of the requirements for the award of Doctor of Philosophy at the University of Southampton

August 2008

SUPERVISOR: *Professor Lajos Hanzo*

M.Sc., Ph.D, FREng, DSc, FIEEE, FIET

Chair of Telecommunications

School of Electronics and Computer Science

University of Southampton

Southampton SO17 1BJ

United Kingdom

This thesis is dedicated to:

My parents
my beloved wife KangMi
my lovely little JiYou
with all my love and respect...

Abstract

UIVERSITY OF SOUTHAMPTON
FACULTY OF ENGINEERING, SCIENCE AND MATHEMATICS
SCHOOL OF ELECTRONICS AND COMPUTER SCIENCE

Doctor of Philosophy
Initial Synchronisation in the Multiple-Input Multiple-Output Aided Single- and Multi-Carrier DS-CDMA as well as DS-UWB Downlink
by SeungHwan Won

In this thesis, we propose and investigate code acquisition schemes employing both co-located and cooperative Multiple Input/Multiple Output (MIMO) aided Single-Carrier (SC) and Multi-Carrier (MC) Code Division Multiple Access (CDMA) DownLink (DL) schemes. We study their characteristics and performance in terms of both Non-Coherent (NC) and Differentially Coherent (DC) MIMO scenarios. Furthermore, we also propose iterative code acquisition schemes for the Direct Sequence-Ultra WideBand (DS-UWB) DL.

There is a paucity of code acquisition techniques designed for transmit diversity aided systems. Moreover, there are no in-depth studies representing the fundamental characteristics of code acquisition schemes employing both co-located and cooperative MIMOs. Hence we investigate both NC and DC code acquisition schemes in the co-located and cooperative MIMO aided SC and MC DS-CDMA DL, when communicating over spatially uncorrelated Rayleigh channels. The issues of NC initial and post-initial acquisition schemes as well as DC schemes are studied as a function of the number of co-located antennas by quantifying the attainable correct detection probability and mean acquisition time performances.

The research of DS-UWB systems has recently attracted a significant interest in both the academic and industrial community. In the DS-UWB DL, initial acquisition is required for both coarse timing as well as code phase alignment. Both of these constitute a challenging problem owing to the extremely short chip-duration of UWB systems. This leads to a huge acquisition search space size, which is represented as the product of the number of legitimate code phases in the uncertainty region of the PN code and the number of legitimate signalling pulse positions. Therefore the benefits of the iterative code acquisition schemes are analysed in terms of the achievable correct detection probability and mean

acquisition time performances. Hence we significantly reduce the search space size with the aid of a Tanner graph based Message Passing (MP) technique, which is combined with the employment of beneficially selected generator polynomials, multiple receive antennas and appropriately designed multiple-component decoders. Finally, we characterise a range of two-stage iterative acquisition schemes employing iterative MP designed for a multiple receive antenna assisted DS-UWB DL scenario.

Acknowledgement

I owe a debt of gratitude to many people who have helped me with my research in diverse ways. Without their generosity and assistance, the completion of this thesis would not have been possible. First of all, I wish to thank my supervisor, Professor Lajos Hanzo, for his continual encouragement, enthusiasm, excellent guidance, generous support and friendship. I am aware of how fortunate I am to have such an open-minded supervisor, who allowed me to choose my research topic without any restrictions.

I would like to thank the academic staffs of the communications research group, namely Professor Sheng Chen, Dr. Lie Liang Yang, Dr. Soon Xin Ng and Dr. Robert Maunder for their kindness and informative guidance in my research. My heartfelt thanks go to Dr. Byoung Jo Choi and Dr. Seung-Hoon Hwang for their support and assistance in the early days of my research. I also would like to express my gratitude to my former colleagues in the Communications research group, namely to Dr. Andreas Wolfgang, Dr. Jin Wang, Dr. Ming Jiang, Dr. Sohail Ahmad and Dr. Wei Liu for their friendship. My special thanks go to our current colleagues in the group, especially to Dr. Kung Chun Lee, Dr. Osamah Alamri, Dr. Yosef Akhtman, Anh Pham Quang, Chun-Yi Wei, Du Yang, Lei Xu, Li Wang, Mohammed El-Hajjar, Nan Wu, Nicholas Bonello, Noor Othman, Qasim Ahmed, Ronald Y Tee, Rong Zhang, Shuang Tan, Thanh Nguyen Dang, Wei Fang, Xiongfeng Shi and others. Finally I really would like to acknowledge my parents, my beloved wife KangMi Kim and little lovely daughter JiYou Won for their sincere love and support during these years.

List of Publications

Journal Papers, Letters and Magazines: (Total: 10)

1. SeungHwan Won and Lajos Hanzo, "Differentially Coherent Code Acquisition in the MIMO-Aided Multi-Carrier DS-CDMA Downlink", IET Communications, Vol. 1, Issue 4, 2007, pp 662-670.

2. SeungHwan Won and Lajos Hanzo, "Non-Coherent Code Acquisition in the Multiple Transmit/Multiple Receive Antenna Aided Single- and Multi-Carrier DS-CDMA Downlink", IEEE Transactions on Wireless Communications, Vol. 6, Issue 11, 2007, pp 3864–3869.

3. SeungHwan Won and Lajos Hanzo, "Iterative Code Acquisition for the DS-UWB Downlink Using Multiple-Component Decoders", Electronics Letters, Vol. 44, Issue 2, 2008, pp 162–163.

4. SeungHwan Won and Lajos Hanzo, "Analysis of Serial-Search-Based Code Acquisition in the Multiple Transmit/Multiple-Receive-Antenna-Aided DS-CDMA Downlink", IEEE Transactions on Vehicular Technology, Vol. 57, Issue 2, 2008, pp 1032-1039.

5. SeungHwan Won and Lajos Hanzo, "Non-coherent and Differentially Coherent Code Acquisition in MIMO Assisted DS-CDMA Multi-path Downlink Scenarios", IEEE Transactions on Wireless Communications, Vol. 7, Issue 5, Part 1, 2008, pp 1585-1593.

6. SeungHwan Won and Lajos Hanzo, "Initial and Post-Initial Code Acquisition in the Non-Coherent Multiple Input/Multiple Output Aided DS-CDMA Downlink", To appear in the IEEE Transactions on Vehicular Technology, 2008

7. SeungHwan Won, Kyungchun Lee and Lajos Hanzo, "Initial Code Acquisition in the Cooperative Non-coherent MIMO DS-CDMA Downlink", To appear in the IEEE Transactions on Vehicular Technology, 2008

8. SeungHwan Won and Lajos Hanzo, "Initial Acquisition Performance of the Multiple Receive Antenna Assisted DS-UWB Downlink Using Search Space Reduction and Iterative Code Phase Estimation", Revised for the IEEE Transactions on Wireless Communications, June 2008.

9. SeungHwan Won and Lajos Hanzo, "Synchronisation Issues in Non-coherent MIMO Systems", Submitted to the IEEE Communications Magazine, July 2008.

10. SeungHwan Won and Lajos Hanzo, "Synchronisation Issues in Cooperative MIMO Environments", Submitted to the IEEE Communications Magazine, July 2008.

Conference Papers: (Total: 8)

1. SeungHwan Won and Lajos Hanzo, "Analysis of Serial Search Based Code Acquisition in the Multiple Transmit Antenna Aided DS-CDMA Downlink", Proc. of IEEE VTC'05 Fall, vol. 1, 25-28 September 2005, Dallas, USA, pp 98–102

2. SeungHwan Won and Lajos Hanzo, "Differentially Coherent Code Acquisition in the Multiple Transmit/Receive Antenna Aided DS-CDMA Downlink", Proc. of WCNC2006, 3-6 April 2006, Las Vegas, USA, pp 1009–1014

3. SeungHwan Won and Lajos Hanzo, "Initial and Post-Initial Acquisition in the Serial Search Based Noncoherent Multiple Transmit/Receive Antenna Aided DS-CDMA Downlink", Proc. of IEEE VTC'06 Spring, vol. 5, 7-10 May 2006, Melbourne, Australia, pp 2246–2250

4. SeungHwan Won and Lajos Hanzo, "Serial Search Based Initial Code Acquisition in the Multiple Transmit/Receive Antenna Aided Multi-Carrier DS-CDMA Downlink", Proc. of ISSSTA 2006, 28-31 August 2006, Manaus, Brazil, pp 64–68

5. SeungHwan Won and Lajos Hanzo, "Differentially Coherent Code Acquisition in the Multiple Transmit/Receive Antenna Assisted Multi-Carrier DS-CDMA Downlink", Proc. of IEEE VTC'07 Spring, 23-25 April 2007, Dublin, Ireland, pp 1831-1835.

6. SeungHwan Won, Kyungchun Lee and Lajos Hanzo, "Serial Search Based Code Acquisition in the Cooperative MIMO Aided DS-CDMA Downlink", Proc. of ICC 2008, 19-23 May 2008, Beijing, China, pp5058 - 5062.

7. SeungHwan Won and Lajos Hanzo, "Two-Stage Code Acquisition Employing Search Space Reduction and Iterative Detection in the DS-UWB Downlink", Proc. of WCNC2008, 31 March-3 April 2008, Las Vegas, USA, pp 136-141.

8. SeungHwan Won and Lajos Hanzo, "Iterative Spreading-Sequence Acquisition in the Multiple Receive Antenna Aided DS-UWB Downlink", To appear in the Proc. of IEEE VTC'08 Fall.

List of Symbols

- A symbol having the subscript $(\cdot, ..., \cdot)$ which encompasses at least two parameters, represents 'per-path' element, for instance $\alpha_{(l,m,n,u)}$.

- A symbol having $(\cdot)$ which includes a single parameter, represents either a time instant or a chip sampling instant depending on the scenarios.

- Alphabetical order having upper characters, followed by lower characters is used.

- Then greek alphabetical order having upper characters, followed by lower characters.

- $\|\cdot\|^2$ stands for the Eucledian norm of the complex-valued argument.

- The superscript $(\cdot)^*$ is used to indicate complex conjugation.

- $Re[\cdot]$ represents the real operation of the complex value.

- Exact notations used in both MIMO Aided SC- and MC DS-CDMA as well as in the SIMO Aided DS-UWB systems are only provided once.

List of Symbols for MIMO Aided SC- and MC DS-CDMA

$b(\cdot)$:	Binary input data sequence assuming values of +1 or -1
$C(\cdot)$:	A common PN sequence having a cell-specific code-phase offset
$c(\cdot)$:	Unique user-specific PN sequence
D_0 :	A decision that hypothesis H_0 was only if the data point y lies in region R_0
D_1 :	A decision that hypothesis H_1 was only if the data point y lies in region R_1
$D(\Delta f_t)$:	Signal energy reduction expressed as a function of the frequency mismatch
d :	Code phase offset with respect to the phase of the local code
E_c :	Pilot signal energy per PN code chip
E_c/I_0:	Signal-to-Interference plus Noise Ratio per chip
$(E_c/I_0)^{'}$:	E_c/I_0 degraded by the effects of both timing errors and frequency mismatch
$E[T_{ACQ}]$:	Mean acquisition time
$E[Y_{tot}^{(I)}]$:	Mean values of the I-channel outputs
$E[Y_{tot}^{(Q)}]$:	Mean values of the Q-channel outputs
$\overline{E_c}$:	Average chip energy
f :	Carrier frequency
f_0 :	Carrier frequency
f_u :	u^{th} subcarrier frequency
$f^{'}$:	Carrier frequency distorted by the clock-drift-induced frequency mismatch and the Doppler shift
$f_u^{'}$:	Carrier frequency of the u^{th} subcarrier distorted by the clock-drift-induced frequency mismatch and the Doppler shift
H_0 :	Hypothesis test for the desired signal being absent
$H_0(z)$:	Probability of the desired user's signal at the output of the acquisition scheme being absent indicated by an insufficiently high correlator output or because the receiver is waiting for the penalty time to expire
H_1 :	Hypothesis test for the desired signal being present

$H_D(z)$:	Transfer function corresponding to the correct detection probability
$H_M(z)$:	Overall miss probability of a search run carried out across the entire uncertainty region
$H_x^{'}(z)$:	Derivative of $H_x(z)\|_{x=D,\, M\, or\, 0}$
$h(\cdot)$:	Impulse response of the pulse shaping filter
I_0 :	One-sided power spectral density of the AWGN
$\mathcal{I}_0(x)$:	The zeroth-order modified Bessel function
I_{OC} :	Other-cell interference imposed by the remaining sectors (56 sectors)
I_{SC1} :	Serving-cell interference imposed by the multi-path signals
I_{SC2} :	Serving-cell interference imposed by the other channels
$I_{SC(Total)}$:	Serving-cell interference on the DL
$I_{(Total)}$:	Total amount of channel-induced impairments on the DL
$I_{\zeta}^{(\dot{\imath})}$:	Imaginary part of I_ζ
$I_{(\zeta-N)}^{(\dot{\imath})}$:	Imaginary part of N-chip delayed I_ζ
$I_{\zeta}^{(r)}$:	Real part of I_ζ
$I_{(\zeta-N)}^{(r)}$:	Real part of N-chip delayed I_ζ
$I_{(\cdot,\ldots,\cdot)}(t)$:	Complex-valued AWGN having a double-sided power spectral density of I_0 at the per-path
$I_{\zeta(\cdot,\ldots,\cdot)}$:	Complex-valued AWGN having zero means and variances of σ^2=2 for both real and imaginary parts
$I_{\zeta(\cdot,\ldots,\cdot)}(t)$:	Complex-valued AWGN having a double-sided power spectral density of I_0 at the per-path
$I_{(\zeta-N)(\cdot,\ldots,\cdot)}$:	N-chip delayed $I_{\zeta(\cdot,\ldots,\cdot)}$
K :	False locking penalty factor
$K_a(\cdot)$:	Modified Bessel function of the second kind and of order a
L :	Number of multi-path components
L_1 :	Link loss
M^2 :	Square of the mean values of $Y^{(I)}$ and $Y^{(Q)}$
$\overline{M^2}$:	Square of the mean values of $Y^{(I)}$ and $Y^{(Q)}$ weighted the fading signal power

m :	The exponent of z in the verification mode
N :	A coherent integration interval of chip durations
N_0 :	Thermal noise spectral power density
N_i :	A coherent integration interval of chip durations for i^{th} dwell
$n(\cdot)$:	Additive White Gaussian Noise
P :	Number of transmit antennas (Co-located scenario)
P :	Number of relay stations and base station (Cooperative scenario)
$P_{Dj}^{(1)}$:	Correct detection probability associated with the j^{th} testing of the first integration dwell interval
$P_{Dj}^{(2)}$:	Correct detection probability associated with the j^{th} testing of the second integration dwell interval
$P_F^{(1)}$:	False alarm probability of the first dwell
$P_F^{(2)}$:	False alarm probability of the second dwell
P_D :	Correct detection probability
P_{Dj}:	Probability of correct detection associated with testing the correlator's output for the j^{th} occasion
P_D^{dc} :	Probability of correct detection in DC scheme
P_F^{dc} :	False alarm probability in DC scheme
P_F :	Probability of false alarm
P_M :	Probability of missed detection
P_{Total} :	Total transmit power allocated at the BS
$p_0(y)$:	PDF of y conditioned on H_0
$p_0(Y^{(I)}, Y^{(Q)})$:	PDF of $Y^{(I)}$ and $Y^{(Q)}$ at each branch for the signal being absent
$p_0(Z)$:	PDF conditioned on the hypothesis of the desired signal being absent
$p_1(y)$:	PDF of y conditioned on H_1
$p_1(Y^{(I)}, Y^{(Q)}\|\phi)$:	PDF of $Y^{(I)}$ and $Y^{(Q)}$ at each branch for the signal being present

$p_1(Y^{(I)}, Y^{(Q)})$:	Unconditional PDF in the presence of the desired signal by averaging $p_1(Y^{(I)}, Y^{(Q)}\|\phi)$ over ϕ
$p_1(Z)$:	PDF conditioned on the hypothesis of the desired signal being present
$p_1(Z, \beta)$:	PDF corresponding to the SINR β conditioned on the hypothesis of the desired signal being transmitted over an AWGN channel
$p(\beta)$:	Probability of occurrence of encountering the SINR
$p_{Z_{\zeta(\cdot,...,\cdot)}}(z\|H_x, \beta)$:	PDF corresponding to a specific SINR β conditioned on the hypothesis of the desired signal being transmitted over an AWGN channel having this specific SINR at the per-path
$p_{Z_\zeta}(z\|H_x)$:	PDF of a desired user's signal at the output of the acquisition scheme conditioned on the presence of the desired signal in $p_{Z_\zeta}(z\|H_x)$ derived for transmission over a spatially uncorrelated Rayleigh channel
$p_{Z_\zeta(\cdot,...,\cdot)}(z\|H_x)$:	PDF of $Z_{\zeta(\cdot,...,\cdot)}$ conditioned on the presence of the desired signal at the per-path
$p_{X_\zeta}(\cdot, ..., \cdot)(z\|H_x)$:	PDF of a desired user's signal at the output of the acquisition scheme conditioned on the presence of the desired signal in $p_{X_\zeta}(z\|H_x)$ derived for transmission over a spatially uncorrelated Rayleigh channel at the per-path
$p_{Y_\zeta}(\cdot, ..., \cdot)(z\|H_x)$:	PDF of a desired user's signal at the output of the acquisition scheme conditioned on the presence of the desired signal in $p_{Y_\zeta}(z\|H_x)$ derived for transmission over a spatially uncorrelated Rayleigh channel at the per-path
$p_{Z_\zeta^{dc}}(z\|H_x)$:	PDF of Z_ζ^{dc} conditioned on the desired signal being present or absent
$p_{Z_\zeta(\cdot,...,\cdot)}(z\|H_x)$:	PDF of $Z_{\zeta(\cdot,...,\cdot)}$ conditioned on the presence of the desired signal at the per-path
R :	Number of receive antennas
R_0 :	Acceptance region where H_0 is accepted
R_1 :	Critical region, in which case H_0 is rejected and H_1 is considered to be true
$R(N_i)$:	Correlation value recorded for N

$R(\tau)$:	Autocorrelation function of the timing error
$\tilde{R}$:	Radius of a circle which connects the six vertices of the hexagon
$r_{tot}(\cdot)$:	Signal at receiver that is a composite of L multi-path signals having a time delay of τ_l
r_{ζ}^{MF} :	Output of the MF assigned to each path
$r_{(\zeta-N)}^{MF}$:	N-chip delayed r_{ζ}^{MF}
$r(\cdot)$:	Received signal of the user
S :	Number of LFSR stages uniquely and unambiguously describing the m-sequence
$S(\cdot)$:	Signal transmitted of the user
S_{Load} :	The smallest span of chips required for the sake of evaluating a specific parity-check sum
SF :	Spreading factor of the subcarrier signals in the MC-DS-CDMA system
SF_1 :	Spreading factor of a corresponding identical-bandwidth SC-DS-CDMA system
$S_{tot}(\cdot)$:	Signal transmitted of the desired user at the BS of a multiple transmit antenna aided system
$S_{\zeta(\cdot,\ldots,\cdot)}$:	A deterministic value, which depends on whether a signal is present or absent
$S_{\zeta(\cdot,\ldots,\cdot)}$:	A deterministic value, which depends on whether a signal is present or absent
$S_{(\zeta-N)(\cdot,\ldots,\cdot)}$:	N-chip delayed $S_{\zeta(\cdot,\ldots,\cdot)}$
T :	Number of PDI stages
T_b :	Bit duration of the data sequence before Serial-to-Parallel (SP) conversion
T_c :	Chip duration
T_{c1} :	Chip duration of the corresponding SC-DS-CDMA signal
T_{H_1} :	Minimum time interval between two consecutive H_1 hypothesis tests
T_M :	Delay spread corresponding to an environment having the highest possible delay spread, as in an urban area

T_m :	Delay spread corresponding to an environment having the shortest delay spread considered (experienced, e.g., in an indoor environment)
T_s :	Symbol duration
T_{sym} :	Number of symbols over which integration is carried out
t :	Time instant of the user at the Base Station
U :	Number of subcarriers
$U(z)$:	Total transfer function averaged over all the $(\nu - 2l)$ starting node
$U_i(z)$:	Transfer function from an initial mode that is i branches counterclockwise from the top to the final correct destination mode
$V/2$:	Variances of $Y^{(I)}$ and $Y^{(Q)}$
V_F :	Summation of the variance and $\overline{M^2}$
W :	Bandwidth allocated
$W_{1,\zeta}$:	$\frac{1}{2}(I_{\zeta}^{(r)} + I_{(\zeta-N)}^{(r)})$
$W_{2,\zeta}$:	$\frac{1}{2}(I_{\zeta}^{(r)} - I_{(\zeta-N)}^{(r)})$
$W_{3,\zeta}$:	$\frac{1}{2}(I_{\zeta}^{(\dot{\imath})} + I_{(\zeta-N)}^{(\dot{\imath})})$
$W_{4,\zeta}$:	$\frac{1}{2}(I_{\zeta}^{(\dot{\imath})} - I_{(\zeta-N)}^{(\dot{\imath})})$
$w_m(\cdot)$:	Specific Walsh code assigned to the m^{th} transmit antenna
$Y^{(I)}$:	Energy accumulated in the integral dwell time of τ_D for I-phase outputs
$Y^{(Q)}$:	Energy accumulated in the integral dwell time of τ_D for Q-phase outputs
y :	(Maybe multi-dimensional) data point
$y^{(I)}$:	Vectors for I-phase outputs assigned to each path
$y^{(Q)}$:	Vectors for Q-phase outputs assigned to each path
Z_1 :	Decision variable of the search mode
Z_2 :	Decision variable of the verification mode
Z_{tot} :	Final output variable generated by the outputs of correlators combined
$Z_{(\cdot,\ldots,\cdot)}$:	Output variable assigned to per-path
Z_{ζ} :	Decision variable at chip sampling instant
z :	Unit-delay operator

α :	Number of correct timing hypotheses tested
α_1 :	Orthogonality factor (0.4 – 1)
α_l :	Envelope at the l^{th} path signal obeying the Rayleigh distribution of the user
$\alpha_{(\cdot,\ldots,\cdot)}$:	Envelope of the per-path signal obeying the Rayleigh distribution
β :	A chi-square distribution having two degrees of freedom
β_1 :	Fraction of the first received path's power
Δ :	Sampling inaccuracy caused by having a finite search step size
Δf_d :	Frequency mismatch caused by the Doppler shift
Δf_m :	Clock-drift-induced frequency mismatch between the BS's transmitter and the MS's receiver
Δf_t :	Total frequency mismatch on the received signal
Φ :	Reduced length chip sequence defined by Ξ/Ψ
ϕ :	Carrier phase of the user's modulator
ϕ_l :	Carrier phase at the l^{th} path signal of the user
ϕ_u :	u^{th} subcarrier phase of the modulator
$\phi_{(\cdot,\ldots,\cdot)}$:	Signal phase of the per-path having a uniform distribution over $(0, 2\pi)$
$\Gamma(\cdot)$:	Gamma function
λ_x :	Z_ζ's noncentrality parameter
$\overline{\lambda_x}$:	Noncentrality parameter corresponding to $(E_c/I_0)'$
μ_x :	A new biased noncentrality parameter
ν :	Total uncertainty region, namely the number of phases to be tested
θ :	Decision threshold
θ_1 :	Threshold of the search mode
θ_2 :	Threshold of the verification mode
θ_i :	Decision threshold for i^{th} dwell
σ^2 :	Variance of the constituent Gaussian distribution
ς_p :	Fraction of the transmitted pilot power with respect to the total allocated transmit power

τ :	Timing errors on the received signal
τ_D	Integral dwell time
τ_{D1} :	The first integer dwell time
τ_{D2} :	The second integer dwell time
τ_l :	A time delay having a tap spacing of one chip-duration T_c
τ_p :	Relative time difference of the signal received from a RS with respect to the signal received from the BS
τ_R :	Memory of the fading channel's multi-path components
τ_S :	Memory of the fading channel's shadowing components
Ξ :	Chip duration of an m-sequence
$\pm\xi$:	Reduced uncertainty region for the post-initial acquisition procedure
Ψ :	Number of non-coherent Inphase (I)- Quadrature phase (Q) MFs
ψ :	Probability of false alarm being kept at the given value
ζ :	Chip sampling instant of the user at the Base Station

List of Symbols for SIMO Aided DS-UWB

$CN(i)$:	Set of VNs connected to the i^{th} CN
d :	Unknown time shift jointly imposed by the oscillator's frequency drift as well as the receiver's mobility
D :	Delay unit
$g(D)$:	Generator Polynomial
$h(t)$:	CIR of the S-V model
$H_i(z)$:	Transfer function derived for exiting the i^{th} H_1 cell
H_x :	Hypothesis of the desired signal
I_1 :	Number of the maximum iterations assigned
I_A :	Average number of iterations
I_M :	Maximum allowable number of iterations
$I_r(t)$:	AWGN having a variance of $\frac{I_0}{2}$ in the r^{th} path
KK :	Number of bins to be searched
$max\,[\cdot]$:	An operator, which selects the largest value between two arguments
N :	Number of chips over which the correlator output is accumulated
N_1 :	Number of P-C connections in the PCM when considering $N_I = 1024$
N_2 :	Number of P-C connections in the PCM when considering $N_I = 512$
N_I :	Truncated PN sequence-length
$\lfloor N_I/S \rfloor$:	Number of non-overlapping segments of S consecutive chips in the N_I-chip truncated PN sequence
N_s :	Number of chips over which the correlator output is accumulated in the TA stage
N_v :	Number of chips in the verification mode
N_V :	Number of chips used for the verification mode
$N[\mu_\eta, \sigma_\eta]$:	Normal distribution
$p_0(r_n)$:	Likelihood functions of each sample when the signal is absent
$p_1(r_n)$:	Likelihood functions of each sample when the signal is present
$p_0(Y)$:	Likelihood functions conditioned on the hypothesis of the desired signal being absent

$p_1(Y)$:	Likelihood functions conditioned on the hypothesis of the desired signal being present
P :	MLSR sequence of period
$P_{Dl}(\theta)$:	Probability of correct detection at l^{th} path
$P_{Dl_{tot}}$:	Probability of correct detection for the CD method
$P_F(\theta)$:	Probability of false alarm
$P_{F_{tot}}$:	Probability of false alarm for the CD method
$P_L(d)$:	Path-loss at a distance d
$\overline{P_L}(d_o)$:	Average path-loss at the so-called reference point just outside the antenna's near-field
P_M :	Missed detection probability
$P(v\ \cdot)$:	Probability of encountering v additional clusters at time instant T
$P(\beta_{u,v})$:	PDF of the Nakagami-m distribution
$P(\tau_{u,v}\|\tau_{u-1,v})$:	Inter-arrival time of two adjacent rays
$Q(x)$:	Q function
$r(j)$:	Soft signal received from the channel
r_n :	Each sample
S :	Number of stages in LFSR
$sgn[\cdot]$:	'signum' function assuming values of either 1 or -1
T :	Time instant
T_c :	Chip-duration
T_{CPA} :	Another threshold assigned to the verification mode of the CPA stage
T_D :	Processing time of a correct detection event
T_f :	Frame duration, which is defined as the pulse repetition period
T_F :	Processing time for a false alarm event, which is also equivalent to the false locking penalty time
T_m :	Maximum delay-spread of the communication channel
T_M :	Processing time of a missed detection event
T_p :	A signalling impulse
T_{TA} :	A threshold value assigned to the TA stage

T_v :	Arrival time of the vth cluster (Chapter 5.2)
T_v :	A threshold value assigned to the verification mode (Chapter 5.4)
u_γ :	A factor accounting for the increase of the decay rate as a function of the delay
U :	Number of resolvable multi-path components in a cluster
$U(Z)$:	Transfer function of the CPA stage
v :	Additional clusters
V :	Number of clusters
$VN(j)$:	Set of CNs linked to the j^{th} VN
W :	Signal bandwidth
x_n :	Chip pattern of the PN sequence at the n^{th} position
$X(j)$:	LLR of the soft value received from the AWGN channel
$X(j,i)$:	Message passed from the j^{th} VN to the i^{th} CN
$X(j,i)^{'}$:	Message passed from the j^{th} VN to the i^{th} CN during the offset-based MSA of CN processing
X_σ :	Shadow fading term
X_σ :	A Gaussian distributed Random Variable (RV) having a standard deviation of σ (in dB)
Y :	Likelihood functions based on the absolute value of the sum
$Y(i,j)$:	Message passed from the i^{th} CN to the j^{th} VN

α :	Probability of the lower-arrival-rate clusters
β :	A nonnegative number selected by optimising a threshold of the offset-based MSA
$\beta_{u,v}$:	Amplitude of the uth multi-path component within the vth cluster
$\overline{\beta_{1,1}^2}$:	Expected power of the first resolvable path of the received UWB signal
$\overline{\beta_{u,v}^2}$:	Average power of a multi-path component at a given delay $T_v + \tau_{u,v}$
η :	Path-loss exponent
η_1 :	A Gaussian RV having a mean of zero and a unit variance
η_2 :	Zero mean RV
η_3 :	Zero mean RV
γ :	Ray-decay factor within a cluster
Γ :	Cluster-decay factor
$\Gamma(m)$:	Gamma function
λ :	Ray-arrival rate within a cluster
λ_1 :	Ray-arrival rate of the first Poisson process
λ_2 :	Ray-arrival rate of the second Poisson process
λ_v :	Mean multi-path arrival rate within the vth cluster
$\lambda^{'}$:	Resultant logical value after a hard decision was performed
Λ :	Cluster-arrival rate
$\Lambda^{'}$:	*a posteriori* LLR of each VN
ν :	Number of chips in the entire uncertainty region to be searched
θ :	A normalised threshold value associated with Th being T_{TA}
σ :	Standard deviation
σ_σ :	A unit-variance normal RV
τ :	Integral dwell time over which the received samples are accumulated during the correlation operation
$\tau_{u,v}$:	Arrival time of the uth multi-path component within the vth cluster
$\omega_r(t)$:	A chip waveform having a duration of T_p
$\Omega_{u,v}$:	Second moment of the amplitude of the uth multi-path component in the vth cluster

Glossary

- **AF** Amplify-and-Forward
- **AFC** Automatic Frequency Control
- **AWGN** Additive White Gaussian Noise
- **BP** Belief Propagation
- **BS** Base Station
- **CD** Coincidence Detection
- **CDMA** Code Division Multiple Access
- **CFAR** Constant False-Alarm Rate
- **CIR** Channel Impulse Response
- **CN** Check Node
- **CPA** Code Phase Acquisition
- **CSI** Channel State Information
- **DC** Differentially Coherent
- **DC-MF** Differential Correlations based Matched Filter
- **DC-MUSIC** Differential Correlations based MUltiple SIgnal Classification
- **DDSS** Double Dwell Serial Search
- **DF** Decode-and-Forward
- **DL** DownLink

- **DRSSE** Differential Recursive Soft Sequential Estimation
- **DS-CDMA** Direct Sequence-Code Division Multiple Access
- **DSR** Decoder Shift Register
- **DS-UWB** Direct Sequence-Ultra WideBand
- **EGC** Equal Gain Combining
- **FPC** Full-Period Correlation
- **GP** Generator Polynomial
- **GPS** Global Positioning System
- **HF-UWB** High Frequency Ultra WideBand
- **HO** HandOvers
- **ISE** Improved Sequential Estimation
- **ISI** Inter Symbol Interference
- **LDPC** Low-Density Parity-Check
- **LFSR** Linear Feedback Shift Register
- **LF-UWB** Low Frequency Ultra WideBand
- **LLR** Log-Likelihood Ratio
- **LOS** Line-Of-Sight
- **MAT** Mean Acquisition Time
- **MC-DS-CDMA** Multi Carrier-Direct Sequence-Code Division Multiple Access
- **MF** Matched-Filter
- **MIMO** Multiple-Input Multiple-Output
- **MLD** Majority Logic Decoding
- **MLSR** Maximum Length (linear) Shift Register

- **MP** Message Passing
- **MRC** Maximum Ratio Combining
- **MS** Mobile Station
- **MSA** Min-Sum Algorithm
- **NC** Non-Coherent
- **NLOS** Non-Line-Of-Sight
- **OFDM** Orthogonal Frequency Division Multiplexing
- **P-C** Parity-Check
- **PCM** Parity Check Matrix
- **PDF** Probability Density Function
- **PDI** Post-Detection Integration
- **PN** Pseudo-Noise
- **PP** Primitive Polynomial
- **PPC** Partial-Period Correlation
- **P-SCH** Primary Synchronization Channel
- **RARASE** Recursion-Aided RASE
- **RASE** Rapid Acquisition by Sequential Estimation
- **RS** Relay Station
- **RSSE** Recursive Soft Sequential Estimation
- **RV** Random Variable
- **SC-DS-CDMA** Single Carrier-Direct Sequence-Code Division Multiple Access
- **SCDU** Soft-Chip Delay Unit
- **SDM** Spatial Division Multiplexing

- **SDMA** Spatial Division Multiplexing Access
- **SD-RA** Single Dwell Random Search
- **SDSS** Single Dwell Serial Search
- **SeC** Selection Combining
- **SF** Spreading Factor
- **SIMO** Single-Input Multiple-Output
- **SINR** Signal-to-Interference plus Noise Ratio
- **SISO** Single-Input Single-Output
- **SI/SO** Soft-In/Soft-Out
- **SP** Serial-to-Parallel
- **SPA** Sum-Product Algorithm
- **SS-IA** Single-Stage Iterative Acquisition
- **SS-SDSS** Single-Stage Single Dwell Serial Search
- **STBC** Space-Time Block Coding
- **STDL** Statistical Tapped-Delay-Line
- **STS** Space-Time Spreading
- **STTC** Space-Time Trellis Coding
- **S-V** Saleh-Valenzuela
- **TA** Timing Acquisition
- **TS-IA** Two-Stage Iterative Acquisition
- **TS-SDSS** Two-Stage Single Dwell Serial Search
- **TSTD** Time-Switched Transmit Diversity
- **UC** UnCorrelated

- **UL** UpLink
- **VL** Variable Node
- **WCDMA** Wideband Code Division Multiple Access
- **WIBRO** WIreless BROadband

Contents

Chapter 1

Introduction

1.1 Overview of Code Acquisition

Code Division Multiple Access (CDMA) [1] based mobile communication systems have been widely advocated by the standardisation bodies, leading to the IS-95 [1] and the Third-Generation (3G) [2] systems. In the inter-cell synchronous CDMA-2000 system, the Mobile Station's (MS) receiver must be capable of coarsely synchronously aligning a locally generated Pseudo-Noise (PN) code with the received composite multi-user signals containing the desired user's PN sequence [3, 4, 5, 6] before the transmission of the desired signal. This process is referred to as 'initial acquisition', followed by optimum post-initial acquisition [7, 8], where the term 'post-initial acquisition' [7] refers to identifying the timing instants of the affordable-complexity-dependent number of delayed received signal paths, which will be combined by Rake receiver.

In general, code synchronisation is achieved in two consecutive steps. Code acquisition is invoked first for coarse code alignment and code phase tracking for fine alignment [3, 5, 9]. We focus our attention on code acquisition in this thesis. Substantial research efforts have been devoted to the design of code acquisition techniques [4, 5, 6]. A variety of serial search [3, 4], parallel search [10, 11], as well as sequential estimation [12, 13] based code acquisition techniques have been proposed in the literature. In order to achieve a high performance, numerous detector structures such as multiple dwell based search schemes [3, 4, 5], Post-Detection Integration (PDI) [3, 14, 15] and Differentially Coherent (DC) [16, 17, 18] schemes have also been studied in the literature. The performance of code acquisition systems has been widely investigated when communicating over Additive White

Gaussian Noise (AWGN) channels [10, 19, 20] and frequency nonselective, as well as frequency selective Rayeligh or Rician fading channels [10, 19, 20, 21, 22]. Moreover, Yang and Hanzo investigated the performance of code acquisition systems for transmission over Nakagami-m fading channels [23], since this model is versatile and often fits the experimental data generated in a variety of fading environments encompassing urban as well as indoor radio propagation channels at a higher confidence level than the Rayleigh and Rice distribution [24]. Furthermore, the Nakagami-m distribution function models a continuous transition from a Rayleigh fading channels to a Gaussian channel by varying fading parameter, m from unity to infinity.

Employing multiple subcarriers in the DownLink (DL) of wireless systems exhibits significant benefits in terms of an increased flexibility, as argued in [6, 25, 26]. Furthermore, diverse combinations of Single-Carrier Direct Sequence (SC DS) -CDMA and Orthogonal Frequency Division Multiplexing (OFDM) [27] have attracted research efforts [6, 25, 26, 28, 29, 30, 31]. The code acquisition performance of Multi-Carrier (MC) DS-CDMA evaluated with the aid of serial and parallel search based schemes has been investigated in [6, 23] and [32], respectively. A variety of schemes employing multiple antennas in the DL of wireless systems constitute an attractive technique of reducing the detrimental effects of time-variant multipath fading environments [33, 34]. The substantial appeal of MIMOs is that their capacity increases linearly with the SINR, as opposed to the more modest logarithmic increase of the classic Shannon-Hartley law, which may be simply exemplified by assigning the increased transmit power to an additional antenna and hence linearly increasing the throughput [35]. However, most of code acquisition schemes have been designed for Single-Input Single-Output (SISO) systems [3, 15, 22] and hence there is a paucity of code acquisition techniques designed for transmit diversity aided systems [8]. Moreover, there are no in-depth studies in the open literature representing the fundamental characteristics of code acquisition schemes, regardless whether co-located or cooperative Multiple Input/Multiple Output (MIMO) scenarios considered. On the other hand, there have been numerous contributions on code acquisition techniques designed for receive diversity aided systems [36, 37, 38]. Again, since there are no in-depth studies representing the fundamental characteristics of code acquisition schemes assisted by either co-located or cooperative MIMOs, even though there are thousands of papers on showing the performance improvements of diverse MIMOs in perfect initial synchronisation scenarios, this is the first objective of the thesis.

Furthermore, the research of Ultra WideBand (UWB) systems has recently attracted a

significant interest in both the academic and industrial research community [39, 40, 41]. The emerging UWB systems are capable of supporting both wireless personal computers and home entertainment equipment, both requiring high data rates. Similarly, UWB systems may also be used in a variety of sensor networks operating at low data rates and at a low power consumption. Direct Sequence-Ultra WideBand (DS-UWB) techniques are characterised by low-duty-cycle pulse trains having a very short impulse duration [42, 43]. In the DS-UWB DL, initial acquisition is required for both coarse timing as well as for code phase alignment and both of these constitute a challenging problem owing to the extremely short signalling chip-duration [42, 43]. This leads to a huge timing- and code-phase search space size, which is represented as the product of the number of legitimate code phases in the uncertainty region of the PN code and the number of legitimate signalling pulse positions. For the sake of significantly reducing the search space size, we will investigate two-stage code acquisition schemes employing an iterative Message Passing (MP) algorithm designed for a multiple receive antenna assisted DS-UWB DL scenario, which constitutes the second objective of the thesis. Figure 1.1 highlights the various design factors affecting the performance of code acquisition schemes, most of which have to be carefully balanced against each other for the sake of finding attractive design trade-offs.

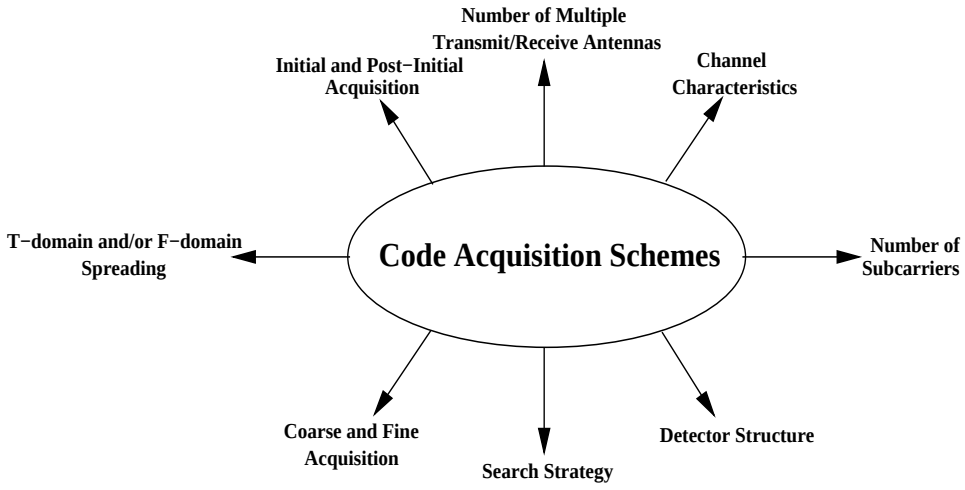

Figure 1.1: Design factors affecting the performance of code acquisition schemes.

Before proceeding further, the generic structure of the synchronisation module and of the Rake receiver at the MS is highlighted in Figure 1.2. Explicitly, the synchronisation module at the top of Figure 1.2 is constituted by the combined operations of initial acquisition, fine timing tracking and post-initial acquisition, which is also associated with the Automatic Frequency Control (AFC). On the other hand, the Rake receiver module at the bottom of

Figure 1.2 incorporates the Rake finger manager, each Rake finger's correlator, the Rake combiner and the channel estimator. In the inter-cell synchronous CDMA-2000 system, the

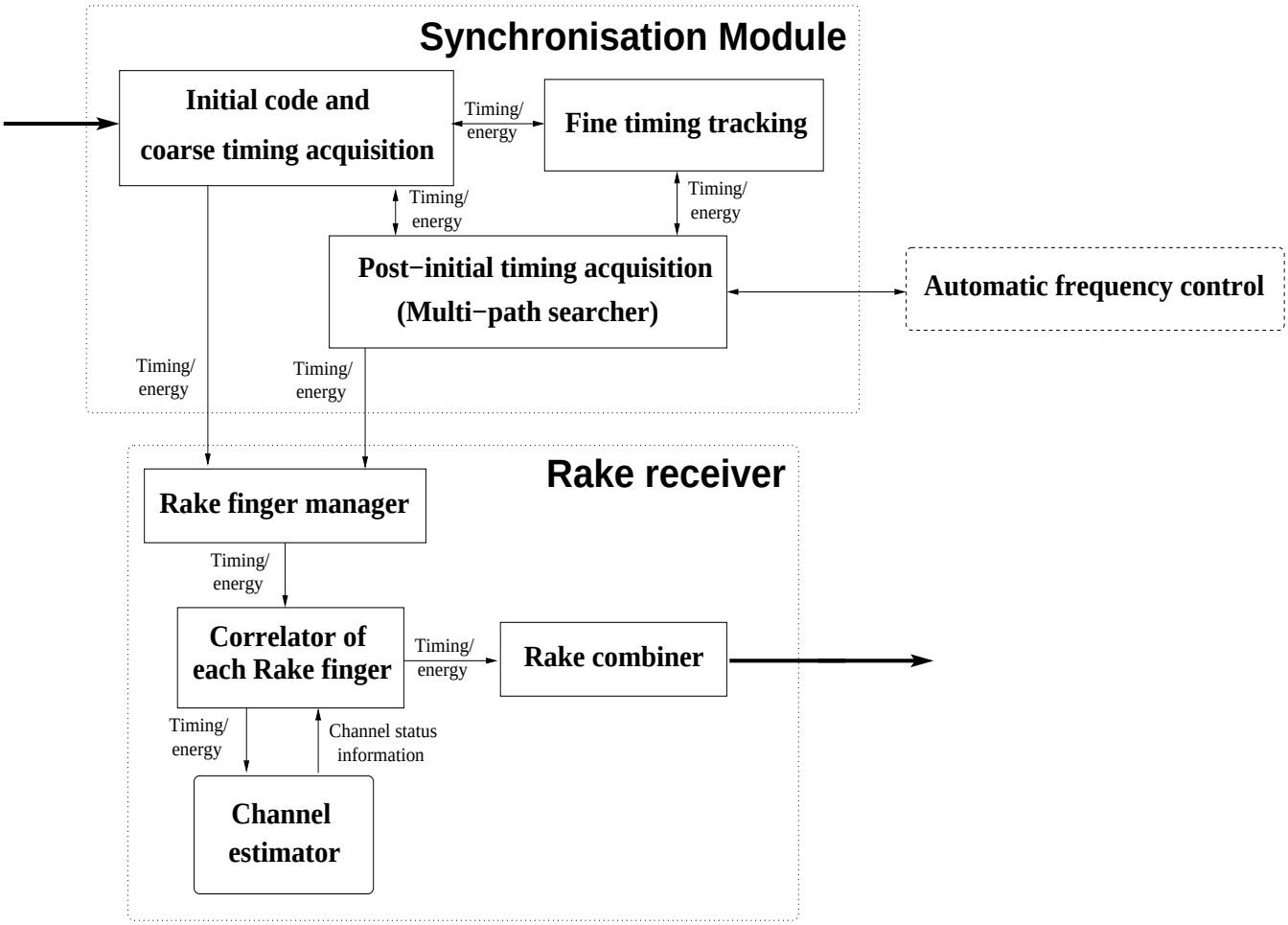

Figure 1.2: Generic structure of the synchronisation module and Rake receiver of the mobile station.

MS's receiver must be capable of coarsely aligning a locally generated PN code with the received composite multi-user signals containing the desired user's PN sequence [3, 4, 5, 6] before the transmission of the desired signal. This process is referred to as 'initial acquisition'. After code acquisition, which ensures the above-mentioned coarse code alignment, timing tracking invoked for fine code alignment commences [3, 5, 9]. Following the successful initial acquisition the AFC operation has to be activated for the sake of mitigating the total frequency mismatch, which represents the sum of the clock-drift-induced frequency mismatch between the Base Station's (BS) transmitter as well as the MS's receiver, and of the effect of the Doppler shift. Finally, the post-initial acquisition procedure follows [7], in order to identify the timing instants of the affordable-complexity-dependent number of

delayed received signal paths, which will be combined by the Rake receiver. The 'Rake finger manager' is capable of controlling the allocation and deallocation of Rake fingers based on both the timing and energy of the resolvable paths provided by the post-initial acquisition stage. Based on the decisions of the Rake finger manager, all the Rake receiver's resolvable paths are coherently combined in order to achieve the best possible performance. The operational procedure of the DS-UWB system is also similar to that of the inter-cell synchronous CDMA-2000 system, except for the AFC operation, because the transmitted signal of the DS-UWB is constituted by an impulse train, which is not affected by the frequency mismatch.

1.2 Code Acquisition Procedures in the Downlink and Uplink

The initial processing stage of CDMA systems is the acquisition of the correct timing of the incoming signals received both in the DownLink (DL) and UpLink (UL). The code acquisition in the DL is the first operation that has to be carried out, as soon as the MS is switched on. The operation is carried out by processing an unmodulated pilot signal, which is spread according to the the chip rate and is broadcast over the entire cell. There is no power control during this stage. In the DL, the uncertainty region (or search window width) corresponds to the entire duration of the PN sequence, which tends to be quite wide, for example $(2^{15} - 1)$ chip intervals in the DL of the inter-cell synchronous CDMA-2000 system [3, 15, 44] [1]. Hence the Mean Acquisition Time (MAT) is minimised in the context of serial search techniques by achieving the best possible correct detection probability, while maintaining as low a value of the false alarm probability and false locking penalty as possible. The effect of the above-mentioned high uncertainty region of the DL could be potentially mitigated by testing the correct spreading code alignment hypotheses using parallel search techniques [2]. However, given the wide uncertainty region of the DL, the implementation of the parallel search based hardware often becomes impractical due to its high complexity.

[1] After the Base Station (BS) transmitted the pilot to the MS, the MS responds with a preamble and hence the BS becomes aware of the system's turn-around delay, which determines the MS's distance from the BS. This technique allows the MS to advance its transmission instant by the estimated amount of the propagation delay, which in turn allows the BS to shorten its search window duration. This also allows the BS to detect immediately after the elapse of code phase verification, if a false alarm locking event was encountered.

[2] In [21] the classic parallel acquisition arrangement was referred to as the Maximum Likelihood (ML) technique.

On the other hand, in the UL code acquisition scenario, the MS transmits a short preamble in response to the Base Station (BS)'s pilot signal. Again, this preamble is short in order to avoid consuming a high amount of energy. The MS's preamble is then aligned in time - using classic correlation techniques - with the pilot signal transmitted by the BS after the previously mentioned code acquisition in the DL. The MS is capable of invoking an open-loop power control procedure by estimating the received pilot signal power in the DL and then adjusting its transmitted power. In this case no acknowledgment is received from the BS and hence, repeated transmission attempts are made by the MS using an increased transmitted power at random time instants [44]. Based upon the above-mentioned procedure, the BS instructs the MS to advance its transmission instant in order to precompensate the effect of the propagation delay imposed on the spreading code phase. The duration of the uncertainty region within which the code phase of the received preamble has to be located depends on the maximum distance between the BS and MS. Accordingly, the uncertainty region in the UL corresponds to a fraction of the entire duration of the $(2^{15}-1)$-chip PN sequence. For example, it is less than 200 PN chip intervals in the UL of the inter-cell synchronous CDMA-2000 system [21]. The BS has to recognise the correct timing of the MS's transmitted signal within the given search window duration and collect all the multi-path components available in order to achieve the highest possible Rake combining gain. Finally, it is worth emphasising that in the context of the UL the MAT is more critically dominated by achieving the best possible correct detection probability than by attaining the lowest possible false locking probability, since the detrimental effect of a false locking event is deweighted by the short duration of the UL uncertainty region [21]. Hence the correct detection probability is typically increased with the aid of a sufficiently low detection threshold at the cost of an increased false alarm probability.

1.3 Search Strategy

1.3.1 Serial Search Based Code Acquisition

One of the widely used initial acquisition techniques is constituted by the serial search based scheme [3, 4, 5, 45]. The classic serial search technique has been employed in scenarios, where the uncertainty region (also referred to as the search window width) is quite wide and hence in the context of serial search the MAT is the vital performance criterion, as argued for the DL of the inter-cell synchronous CDMA-2000 system in [3, 15]. In this scheme, all

the potential initial code phase-related time-offsets are serially searched until the correct phase is found. The correct code phase is deemed to be found, when a sufficiently high energy correlator output exceeding a threshold value optimised in terms of the achievable MAT performance is found. If the estimated code phase is deemed correct, direct-sequence despreading will be carried out. Figure 1.3 depicts the schematic diagram of the Non-Coherent (NC) Matched-Filter (MF) based receiver designed for serial search based code acquisition.

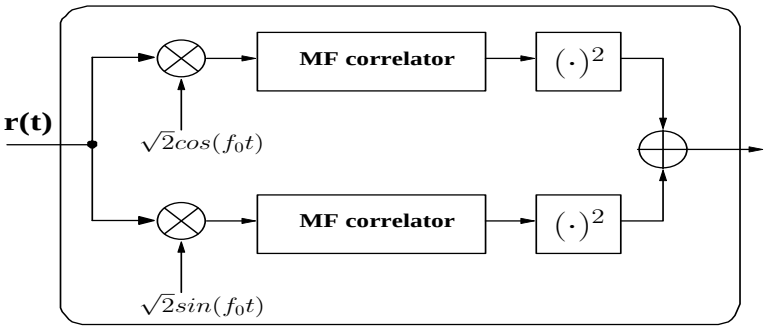

Figure 1.3: Schematic diagram of the serial search based receiver.

1.3.2 Parallel Search Based Maximum-Likelihood Code Acquisition

One of the natural acquisition scheme extensions invoked for the sake of accomplishing an improved correct phase acquisition is to utilise a bank of Ψ parallel non-coherent Inphase (I)- Quadrature phase (Q) MFs [6, 10, 11], which are capable of searching Ψ code phase positions simultaneously. As a result of employing the Ψ parallel branches, the achievable MAT may be expected to decrease by a factor of Ψ at the cost of a higher hardware complexity. Figure 1.4 portrays the schematic diagram of the resultant parallel search based receiver employing Ψ parallel NC I-Q MFs [10]. Each of the Ψ parallel NC I-Q MFs obeys the structure of Figure 1.3 [10].

The Ξ-chip duration of an m-sequence is divided into Ψ shorter sequences, each having a length of $\Phi = \Xi/\Psi$ chips and then each NC I-Q MF branch is configured to acquire one of the Ψ shorter sequences. The best code-phase is found for each of the Ξ number of Φ-chip shorter sequences and the best code-phase of the original Ξ-chip sequence is decided on the basis of the most reliable, i.e. highest-output Φ-chip correlator of Figure 1.4. To elaborate a little further, the code phase associated with the highest energy correlator output among all the Ψ outputs is compared to an optimised threshold value. Then, if the largest correlator

output exceeds the optimised threshold value, the acquisition system declares that the code-phase of the corresponding Φ-chip reduced-length sequence is indeed the correct code phase of the original Ξ-chip sequence. If the threshold value is not exceeded, the above-mentioned process will be repeated, until a reliable Φ-chip code-phase is found. It is worth noting that the shorter the reduced-length Φ-chip sequences are, the higher the number of parallel branches becomes. This potentially increases the attainable acquisition speed, but reduces the reliability of detecting the correct phase of the original full-length Ξ-chip sequence. Accordingly, there is a trade-off between the increased speed and decreased reliability of code acquisition.

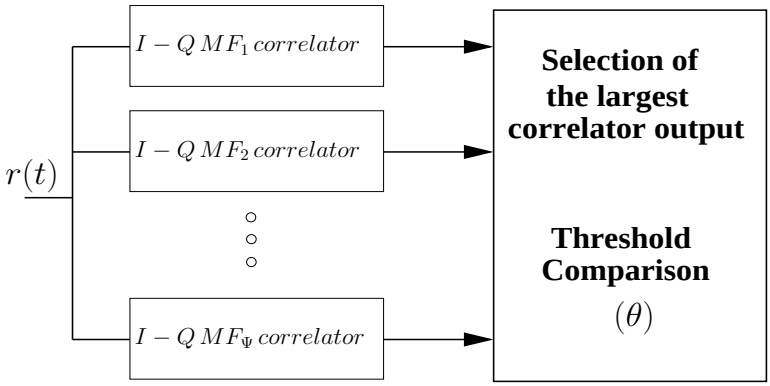

Figure 1.4: Schematic diagram of the parallel search based receiver.

1.3.3 Sequential Estimation Based Code Acquisition

The philosophy of sequential code-phase estimation based code acquisition is similar to that of the Rapid Acquisition using Sequential Estimation (RASE) scheme of [12] which is quite attractive in terms of its achievable performance right across Signal-to-Interference plus Noise Ratio (SINR) range. Moreover, as opposed to the classic serial [3, 4] or parallel search [10, 11] based schemes, this scheme is quite vulnerable to the effect of AWGN and to interferening signals, since sequential code-phase estimation does not have an innate interference rejection capability, This is because the phase acquisition process is accomplished on the basis of a chip-by chip correlation operation, rather than by exploiting the inherent structure of PN codes. By contrast, both Recursion-Aided RASE (RARASE) [46] and Majority Logic Decoding (MLD) based RASE [47] constitute well known enhanced versions of the original RASE scheme [12], although they still exhibit certain performance limitations. For the sake of overcoming these limitations, Recursive Soft Sequential Estimation (RSSE) based acquisition schemes exploiting the inherent properties of m-sequences and

based upon the widely known turbo principle [48, 49, 50, 51] were proposed in [13, 52, 53]. Further details on these topics will be provided in the following subsections.

1.3.3.1 Rapid Acquisition Using Sequential Estimation

The concept of sequential estimation based code acquisition was originally proposed by Ward [12], where a sequential estimation of the Linear Feedback Shift Register (LFSR) states of the PN code sequence generator is employed. The schematic diagram of the RASE is provided in Figure 1.5. In this figure, the PN code chip detector estimates the first S received PN code chips of the $(2^S - 1)$-chip m-sequence, where S is the number of LFSR stages uniquely and unambiguously describing the m-sequence. Then these chips are loaded into the LFSR based upon modulo-2 operations for the sake of generating the entire m-sequence having the correct code-phase. The lock-detector determines, whether the related decision is deemed correct or not by using the various test statistics of [12] based upon the correlation between the received signal and the locally generated one. Finally, the decision concerning the activation of the reloading command or whether to activate the code tracking loop is controlled by the load/track logic module of Figure 1.5. Both the estimation and loading processes are performed periodically, until the correct initial LFSR state is successfully identified.

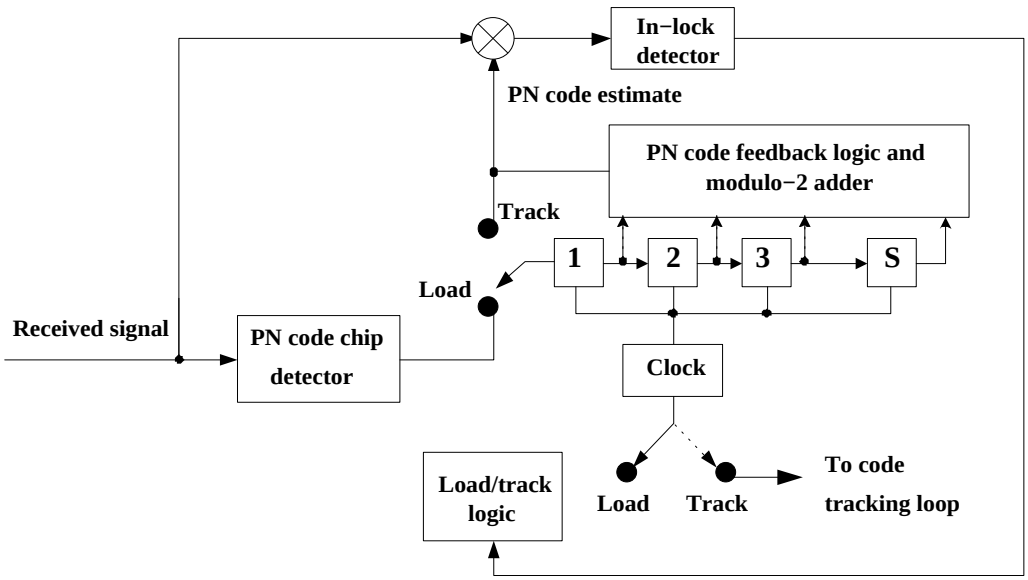

Figure 1.5: Schematic diagram of the rapid acquisition using sequential estimation [12].

1.3.3.2 Recursion-Aided Rapid Acquisition using Sequential Estimation

The enhanced versions [46] of the original RASE schemes rapidly discard the majority of the incorrect code-phase estimation results and hence accelerate the search as well as increase the reliability of detecting the correct code-phase. Accordingly, this concept is similar to that of the multiple dwell based search [4, 46]. A modified version of the original RASE scheme [12], which is known as Recursion-Aided RASE (RARASE) was proposed by Ward and Yiu [46]. This scheme exploits the fact that knowing S consecutive chips of the PN sequence to be acquired uniquely and unambiguously describes all the $2^S - 1$ chips of the m-sequence, because once the S chips entered the shift-register seen in Figure 1.5, they determine all the $(2^S - 1)$-chips. Hence based on the initial S chips the receiver is capable of deciding whether the initial estimate of the entire $(2^S - 1)$-chip received signal is correct or not. By invoking the procedure, a considerable proportion of low-likelihood initial estimate may be discarded using a relatively simple device, which consists of several adders and an AND gate.

1.3.3.3 Majority Logic Decoding Based Rapid Acquisition Using Sequential Estimation

For the sake of generating the resultant $(2^S - 1)$ chips, this scheme makes use of a majority voting method [54], which collects multiple independent estimates of the consecutive S chips for the sake of obtaining the considerably higher number of up to $(2^{S-1} - 1)$ parity-check sums and then employs a majority logic voting device for the sake of determining the initial 'S' chips to be loaded into the Linear Feedback Shift Register (LFSR) [47]. The number of multiple estimates is chosen based upon the achievable target performance, which typically varies from unity to $(2^{S-1} - 1)$ [47, 54, 55]. Accordingly, the performance of this scheme is highly dependent upon the number of estimates used in the majority logic voting device. Compared to the RASE system of Figure 1.5, the correct detection probability of the scheme is considerably increased at the expense of an increased hardware complexity.

The detailed procedure of the MLD based rapid code acquisition procedure exploiting sequential estimation is as follows [47]. The incoming chip is shifted into the majority logic decoder. When all the S_{Load} number of chips are fully loaded in the Decoder Shift Register (DSR), where the parameter S_{Load} indicates the smallest span of chips required for the sake of evaluating a specific parity-check sum, a majority vote of the multiple estimates is taken

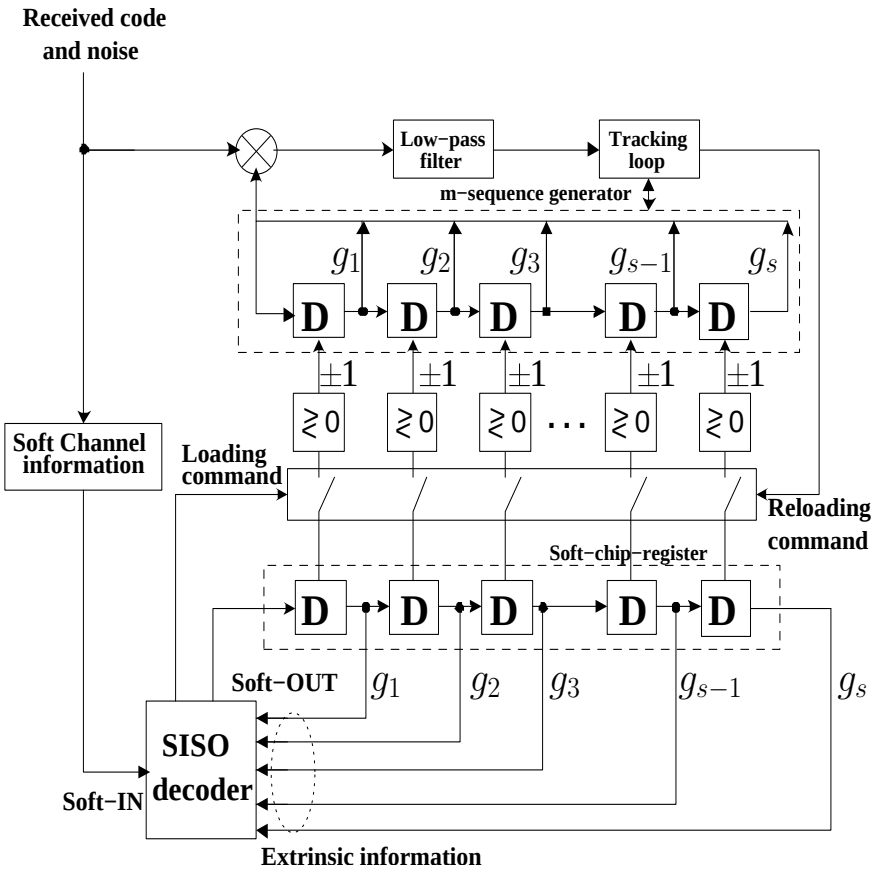

Figure 1.6: Schematic diagram of the recursive soft sequential estimator [13].

and then the result is loaded into the local PN code generator as the estimate of the first initial load value. For the sake of obtaining all the estimates of the remaining chips, the above-mentioned process is repeated, until S consecutive chips have been identified. Then the local PN code generator's outputs are correlated with the received codes over a specific examination period. During this time new chips are loaded into the majority logic decoder. If successful acquisition is not achieved at the end of the examination period, the next S chips have to be determined by the decoder, where the S chips are shifted into the local code generator, and then the same procedures are repeated again. The entire process is performed periodically, until the correct initial LFSR state is successfully identified.

1.3.3.4 Recursive Soft Sequential Estimation

The most imperative requirement for the sake of achieving successful acquisition of PN sequences based upon sequential estimation such as RASE [12] is that S successive chips of the received noise contaminated PN sequence must be correctly estimated. Hence the

iterative Soft-In/Soft-Out (SI/SO) decoding principle, may be invoked [56], which was inspired by turbo channel decoding [48, 49, 50, 51, 57, 58] in order to enhance the reliabilities associated with deciding on the S consecutive chips. This Recursive Soft Sequential Estimation (RSSE) acquisition scheme determining the $(2^s - 1)$-chip m-sequence of Figure 1.6 exploits again the inherent properties of m-sequences uniquely and unambiguously determined by S successive chips output by a recursive SI/SO decoder [13, 43, 52, 53, 59]. The recursive SI/SO decoder receives both soft information from the channel's output related to the current chip as well as soft extrinsic information [48, 49, 50, 51, 58] from the soft channel outputs related to the previous chips, which convey information dispersed by the channel encoder, but related to the current chip. The SI/SO decoder then exploits both the soft channel-output information and the extrinsic information provided by the previous estimates of the SI/SO decoder in order to calculate a reliable soft output for the sake of updating the contents of the soft-chip register. The soft output of the recursive SI/SO decoder is then shifted into the so-called soft-chip register of Figure 1.6, which provides extrinsic information for supporting the forthcoming decoding steps. A cardinal characteristic of the RSSE acquisition scheme is that it makes use of the real-time knowledge of the reliabilities associated with the S consecutive chips. The real-time knowledge of the chip reliabilities can be exploited for the sake of determining the probability of successful acquisition of an m-sequence of length $(2^S - 1)$.

Again, the schematic diagram of the RSSE acquisition scheme is shown in Figure 1.6 [6, 13], which encompasses four constituent building blocks, namely, an m-sequence generator, a soft-chip register, a SI/SO decoder and a code phase-tracking loop. The soft-chip register has S number of delay units, which are referred to as soft-chip delay units (SCDUs) of the m-sequence generator. The SCDUs store the instantaneous log-likelihood ratio (LLR) values of S consecutive chips. With the aid of these S LLR values, S consecutive chips can be determined and loaded into the corresponding delay units of the m-sequence generator of Figure 1.6. The SI/SO decoder estimates the corresponding LLR soft outputs after obtaining a soft channel output sample related to a given chip of the m-sequence. In addition to the so-called intrinsic information of this chip, which was received from the channel, the so-called a priori (extrinsic) information related to the chip, based upon the previous decoded LLR values stored in the SCDUs of Figure 1.6 is also exploited. The soft output of the SI/SO decoder is then shifted to the left-most position of the SCDUs in the soft-chip register, whilst the soft value in the right-most SCDUs is shifted out and dumped. More explicitly, the soft-chip register always stores the most recent S number

of soft outputs of the SI/SO decoder, which corresponds to S consecutive chips of the transmitted m-sequence.

Whenever the amplitude of the most recent S soft outputs of the SI/SO decoder becomes sufficiently high for the sake of guaranteeing a sufficiently low erroneous loading probability, a "loading command" is activated. Then S consecutive chips are decided, employing hard decisions based upon the most recent S LLR values stored in the soft-chip register of Figure 1.6. Then, the S successive chips are loaded into the corresponding delay units of the local m-sequence generator. Once the m-sequence generator is loaded with the initial chip values, the received spread-spectrum signal can be despread, employing the locally generated m-sequence replica, provided that the initial chip values of the m-sequence generator have been correctly loaded. The despread signal is then low-pass filtered and sent to the code tracking loop. If the code tracking loop is capable of tracking the phase, the entire code acquisition process is completed. By contrast, unless the tracking loop is capable of tracking the phase, the code tracking loop activates a "reloading command" in an effort to load another group of S successive chips into the delay units of the m-sequence generator. The above process will be repeated, until code acquisition is successfully accomplished. Finally, the total mean acquisition time of the RSSE scheme can be approximately determined by the duration of time required for the RSSE to accomplish recursive SI/SO decoding, so as to achieve a sufficiently low erroneous loading probability. Table 1.1 shows the history of a variety of sequential estimation based code acquisition schemes and the evolution of sequential estimation in spread-spectrum communication systems.

1.3.4 Random Search Based Code Acquisition

When considering a realistic UWB channel, the numerical analysis of serial search based schemes becomes intractable for the channel impulse response constituted by sparse clumps of multi-path components [62]. However, recently a random search aided scheme was proposed as a realistic alternative for the analysis of the UWB channel model [63], because the random search stipulates no particular assumption regarding the channel model and hence can be applied to arbitrary models. Furthermore, based on the results of Fig.6 in [63], the performance of the serial search based scheme approaches that of the random search. The schematic of the random search aided receiver is exactly the same as that of the serial search based one seen in Figure 1.3, except that the search algorithm shifts the code phase of the

Table 1.1: Contributions on Sequential Estimation Based Code Acquisition

Year	Authors	Contribution
1965	R. Ward [12]	This scheme employs sequential estimation of the Linear Feedback Shift Register (LFSR) states of the PN code sequence generator.
1973	C. Kilgus [47]	This arrangement makes use of a majority voting aided method, which collects multiple independent estimation results for each of 'S' chips and then employs a majority logic voting device for the sake of determining the most reliable initial 'S' chips to be loaded into the LFSR.
1977	R. Ward and Y. Kai [46]	This scheme rapidly discards the majority of the incorrect estimation results, therefore accelerates the search and also increases the reliability of achieving correct acquisition.
1988	L.S. Lee and J.H. Chiu [60]	This sequential estimation based PN code acquisition scheme employs a so-called extended characteristic polynomial.
1994	R.T. Barghouthi and G.L. Stüber [61]	A sequence acquisition scheme based on both sequential estimation and soft-decision combining methods was invoked for DS-CDMA systems, which exploits the algebraic properties of Kasami sequences and hence becomes capable of providing a very reliable estimate of the correct phase of the local LFSR.
2002	L.L. Yang and L. Hanzo [52]	The proposed Recursive Soft Sequential Estimation (RSSE) acquisition scheme exploits the inherent properties of m-sequences namely that they are uniquely described by 'S' successive chips based upon a recursive SI/SO decoder.
2004	J.H. Lee, I.H. Song, S.R. Park and J.M. Lee [55]	This scheme is a majority logic decoding method based one using a decision logic for the sake of improving the performance of the majority logic decoding based RASE of [47].
2004	L.L. Yang and L. Hanzo [13]	The proposed RSSE acquisition scheme exploits the inherent properties of m-sequences namely that they are uniquely described by 'S' successive chips based upon a recursive SI/SO decoder.
2005	L.L. Yang and L. Hanzo [53]	This Differential Recursive Soft Sequential Estimation (DRSSE) acquisition scheme exploits the inherent properties of m-sequences namely that they are uniquely described by 'S' successive chips based upon a recursive SI/SO decoder.
2005	K.M. Chugg and M. Zhu [43]	Iterative message passing algorithms are applied to PN code acquisition problems for the sake of approaching the achievable maximum-likelihood synchronisation performance.
2006	O. W. Yeung and K.M. Chugg [59]	A new iterative algorithm and its hardware architecture are proposed based on iterative message passing algorithms which are applied in the context of an ultra-wideband system.

local sequence by a random amount selected between 0 and $(\nu - 1)$, where ν represents the number of chips in the entire uncertainty region to be searched.

1.4 Detector Structure

1.4.1 Non-Coherent Code Acquisition

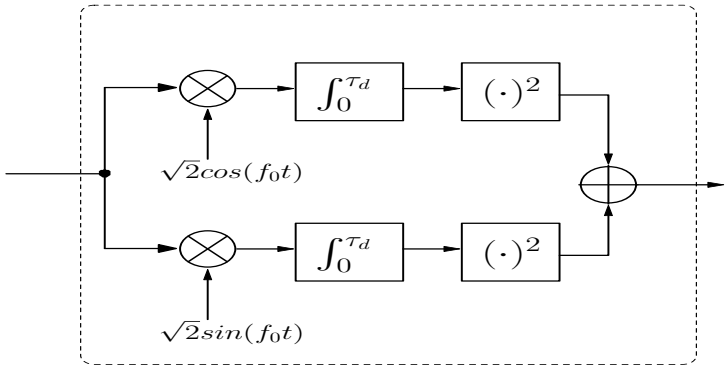

Figure 1.7: Schematic diagram of the non-coherent receiver.

Initial acquisition is incapable of employing any prior information concerning the transmitter's carrier phase. Therefore, during initial acquisition either Non-Coherent (NC) [3, 4, 5, 6] or Differentially Coherent (DC) [17, 18] schemes have to be used. The system seen in Figure 1.7 explicitly shows an example of the NC scheme's structure. Observe in Figure 1.7 that the chip energy accumulated during a predetermined integration dwell time is squared and then the accumulated energies of both the I and Q branches are summed in order to generate a final decision variable.

1.4.2 Differentially Coherent Code Acquisition

Similarly to the NC code acquisition scheme of Figure 1.7, DC code acquisition [17] does not require any prior information concerning the transmitter's carrier phase. An additional benefit of employing the DC code acquisition scheme of Figure 1.8 is that it is capable of providing a better performance than using a NC one [17, 18]. This is, because the DC scheme has a performance gain of just under 3 dB in comparison to the NC one in terms of a pair of the correct detection and false alarm probabilities. There are two types of DC code acquisition schemes in the literature [16, 17]. First of all, Chung [16] proposed the chip-based DC detection scheme of Figure 1.8 that employs a differential receiver having a one-chip

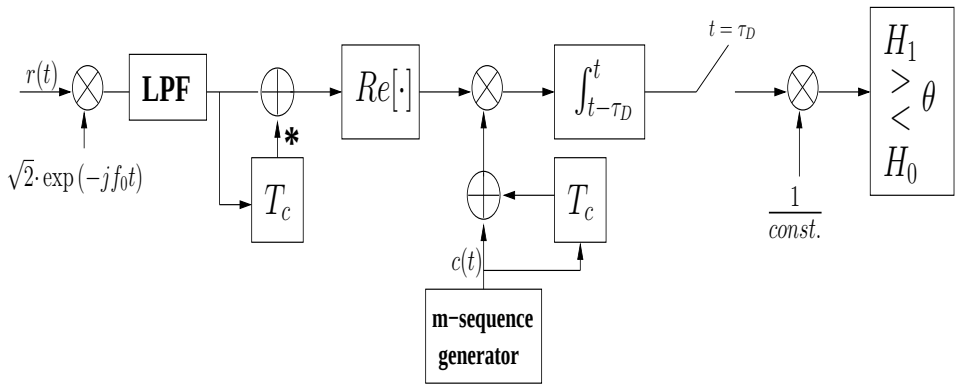

Figure 1.8: Schematic diagram of the chip based-differentially-coherent acquisition scheme [16].

time delay, which has the potential of mitigating the typical code acquisition performance degradation experienced in fast-fading mobile channels, where T_c is the chip duration, the integral dwell time represents τ_D, $c(t)$ denotes the unique user-specific PN sequence and f_0 is the carrier frequency. The chip based-DC receiver of Figure 1.8 first evaluates the modulo-2 function of the current and previous chip values for both the received m-sequence and the locally generated m-sequence. As mentioned before, at this stage no knowledge of the transmitter's carrier phase is available at the receiver, but it is reasonable to assume that the channel-induced magnitude and phase changes of two consecutive chips are similar. Hence, by exploiting this assumption, the differential detector of Figure 1.8 eliminates the effects of the channel-induced as well as carrier-drift-induced phase changes and despite the absence of a coherent detector, it has a good chance of correctly detecting the transmitted m-sequence. Then, as seen in Figure 1.8, the differentially encoded received as well as locally stored m-sequences are compared, i.e. correlated with each other and the correlator output is compared to the decision threshold of θ. As also shown in Figure 1.8, there are two hypotheses, namely H_1 and H_0, which correspond to the desired signal being either present or absent, respectively. For further details please refer to [16].

Secondly, instead of squaring the energy accumulated over N chips as suggested by the principle of the NC receiver of Figure 1.7, the channel's chip-based output samples are summed over either fraction of or over the entire duration of a full m-chip spreading code period, which are then multiplied by the conjugate of the N-chip-delayed samples [17],

[3] according to the philosophy of the Partial-Period-Correlation (PPC) [17] or the Full-Period Correlation [17] (FPC) based schemes, [4] respectively. The schematic diagram of the

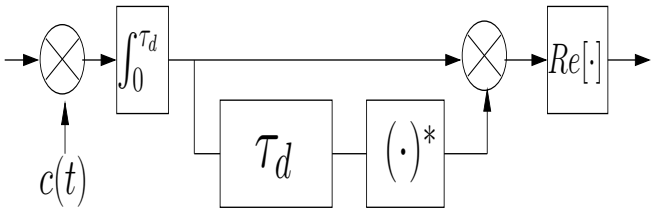

Figure 1.9: Schematic diagram of the differentially-coherent acquisition based receiver employing FPC.

DC acquisition based receiver employing FPC is shown in Figure 1.9. It is interesting to note in [17] that the achievable detection performance of the partial and full correlation based methods becomes similar in the context of NC acquisition schemes, as the length of the integration used by the correlation of Figure 1.7 is gradually increased, whilst their performances are rather different in the context of DC schemes [17]. The superiority of the DC schemes is a consequence of the statistical characteristics of the noise samples contaminating the successive channel output samples in the low SINR region. Namely, the DC scheme is more efficient in terms of reducing the effects of AWGN and interference than the NC one in the low SINR ranges. To elaborate on the above fact a little further, in the low SINR region, the false alarm probabilities of the DC and NC schemes differ by a factor of two. This result leads to the superiority of the DC scheme over the NC one [17]. DC schemes outperform the corresponding NC arrangements in terms of both their correct detection probability and false alarm probability, [5] and hence they also exhibit a considerably better achievable MAT performance. Table 1.2 outlines the history of DC acquisition schemes.

[3]Selection of the optimised N value is highly dependent upon the performance degradation of the carrier frequency mismatch between the base-station's transmitter and the mobile station's receiver.

[4]The main philosophical difference of the PPC and FPC techniques is that the correlation is performed over a predefined segment of the total PN code sequence in conjunction with PPC, whereas the correlation is carried out over a full m-chip spreading code period when exploiting FPC.

[5]The false alarm probability is defined as the probability of mistakenly deciding on which specific spreading sequence was used at the desired user's transmitter, which is a direct consequence of the channel-induced impairments imposed by fading, noise and inteference.

Table 1.2: Contributions on Differentially Coherent Code Acquisition

Year	Authors	Contribution
1994	H.S. Liaw and C.D. Chung [64]	A chip based differentially coherent (DC) detection scheme was proposed, which employs a differential receiver having one-chip time delay in an effort to mitigate the code acquisition performance degradation inflicted by fast fading mobile channels.
1995	C.D. Chung [16]	A chip based DC detection scheme was proposed, which employs a differential receiver having one-chip time delay in an effort to mitigate the code acquisition performance degradation inflicted by high-Doppler fading mobile channels. The proposed serial search based code acquisition scheme using chip based DC detection outperforms its parallel search based counterpart in terms of the achievable mean acquisition time.
1997	M.H. Zarrabizadeh, and E.S. Sousa [17]	In this scheme, the channel's output samples are summed over either a fraction or the entire duration of a full spreading code period and they are multiplied by the conjugate of the τ_D-chip-delayed samples for the sake of achieving a better performance over the noncoherent counterpart, as seen in Figure 1.9.
2001	T. Ristaniemi and J. Joutsensalo [65]	Coarse delay estimates are obtained by both a differential correlation based matched filter (DC-MF) and a differential correlation based multi-class signal classifier (DC-MUSIC) in order to efficiently mitigate the effects of both noise and interferers.
2002	Y.K. Jeong, O.S. Shin and K.B. Lee [66]	Slot synchronisation designed for fast and reliable cell search was proposed for inter-cell asynchronous DS-CDMA systems employing a DC combining scheme, using multiple observations over a number of slots in order to increase the reliability of code acquisition.
2002	J.C. Lin [18, 67]	DC PN code acquisition using full-period correlation (FPC) in both chip-synchronous and chip-asynchronous direct sequence/spread spectrum receivers was designed and analyzed.
2003	O.S. Shin and K.B. Lee [68]	The employment of DC combining was proposed for improving the performance of a double-dwell acquisition system by increasing the reliability of the code-phase verification stage.
2005	L.L. Yang and L. Hanzo [53]	The proposed Differential Recursive Soft Sequential Estimation (DRSSE) acquisition scheme exploits the inherent properties of m-sequence estimates, namely that they are uniquely and unambiguously described by 'S' successive chips based upon a recursive SI/SO decoder invoking differential pre-processing.

1.4.3 Single-Dwell and Multiple-Dwell Time

In single-dwell search based systems [3] the receiver examines all the possible chip-delayed code phases in either a serial or parallel fashion, until the correct code phase is identified. In this scenario, the achievable Mean Acquisition Time (MAT) is typically quite high due to the full hypothesis-testing of all possible code phase.

Accordingly, the achievable MAT performance of both serial search based and parallel search based code acquisition may be substantially improved by performing tests assuming multiple dwell times [3, 4, 5]. Since most of the so-called cells associated with specific chips correspond to incorrect code-phase alignments, their rapid elimination leads to a significant reduction of the MAT. The multiple-dwell based search may be viewed as a generalisation of the single-dwell based scheme. Figure 1.10 illustrates the flowchart of the multiple-dwell based search scheme, where the detector's dwell-intervals are ordered for the sake of improving the correct detection probability on the basis of how high the correlation $R(N_i)$ recorded for dwell-interval N_i was, yielding $R(N_1) \leq R(N_2) \leq \ldots R(N_n)$. The predetermined correlation threshold values $\theta_1 \ldots \theta_n$ constitute important system parameters, which have to be increased for the sake of decreasing the associated false alarm probability. It is worth noting that in practice the optimum MAT value is typically achieved in the false alarm probability range spanning from 10^{-3} to 10^{-4} in conjunction with the best possible correct detection probability, given a specific length of the coherent summation. In practice, double-dwell based search schemes are widely used [3, 15], since they constitute an attractive tradeoff between the achievable MAT performance and the affordable hardware complexity. Further details on these topics will be provided in Chapter 2.

1.4.4 Post-Detection Integration

The Post-Detection Integration (PDI) technique of Figure 1.11 [3, 14, 15] is widely used in initial acquisition and/or post-initial acquisition modules of the commercial CDMA based systems, such as the CDMA-2000 [1] and WCDMA systems [2]. [6] The underlying philosophy is that a decision variable is generated by accumulating T consecutive N-spaced signal samples observed over multiple N-spaced time intervals to improve the correct detection probability in the mobile channel imposing both fading and poor SINR conditions. In order

[6]The so-called post-initial acquisition procedure defined in [7, 8] extracts the accurate timing positions of the typically reduced-power delayed paths and identifies the appropriate paths earmarked for processing by the Maximum Ratio Combining (MRC) scheme of the Rake receiver. Accordingly, the post-initial acquisition performance has a major impact on the performance of the Rake receiver [8].

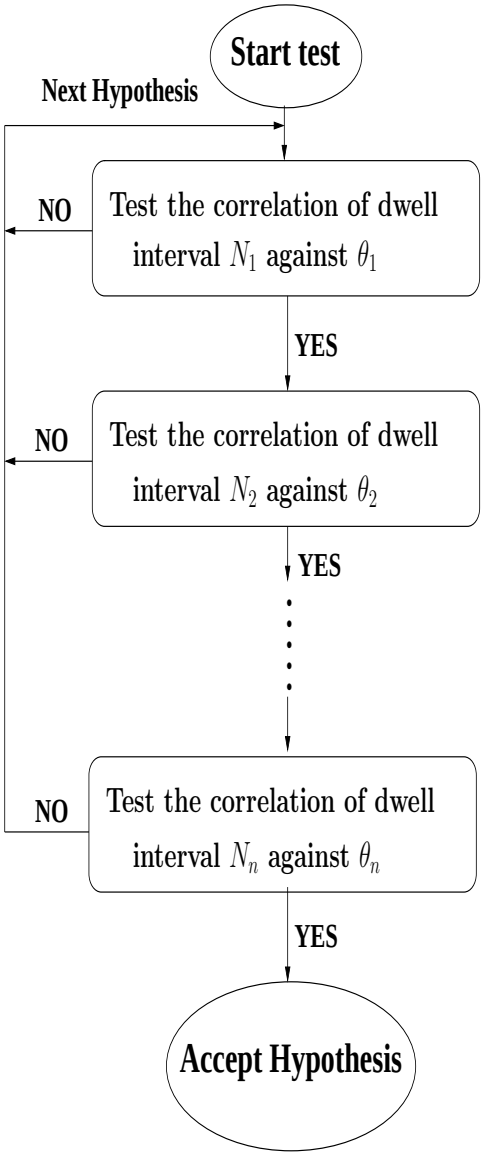

Figure 1.10: Schematic diagram of multiple dwell based search system.

to improve the correct detection probability at the cost of a minor hardware increase compared to the complexity of acquisition modules using no PDI, more explicitly, the number of PDI stages must be increased, requiring the summation of a specific number of consecutive N-chip-spaced integrator outputs for the sake of generating the final decision statistics. [7] The number of PDI stages should be determined depending on whether initial acquisition or post-initial acquisition is considered, as well as depending on the number of both transmit and receive antennas for the sake of achieving the minimum required acquisition performance. There is a tradeoff between the number of the PDI stages and the attainable MAT performance. Figure 1.11 depicts the schematic of a serial search based receiver employing the PDI technique of [3, 14, 15].

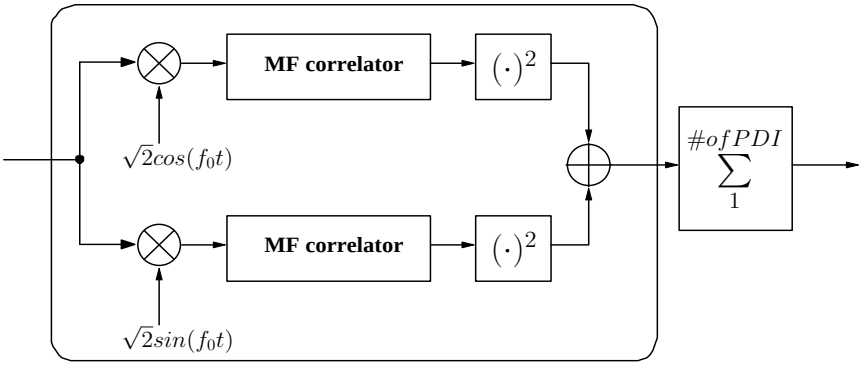

Figure 1.11: Schematic diagram of the serial search based receiver employing post-detection integration.

1.5 Code Acquisition in MC-DS-CDMA

During the early 1990s, MC-DS-CDMA transmission schemes have been proposed in [28], in order to achieve further advantages in terms of bandwidth efficiency, frequency diversity, reduced-complexity parallel signal processing and interference rejection capability in high data-rate transmissions [29, 30, 31]. The parallel code acquisition performance of a MC-DS-CDMA system has been analysed in [32], when communicating over AWGN or flat Rayleigh fading channels. In the MC-DS-CDMA system considered in [32], the authors characterised various code acuqisition scenarios in the context of a MC-DS-CDMA system based upon both Equal Gain Combining (EGC) and Selection Combining (SeC). The performance of both scenarios was examined in both AWGN and Rayleigh fading channels. To elaborate

[7] This specific number must be determined by satisfying a pair of targeted correct detection and false alarm probabilities in terms of minimised MAT.

a little further, it was stated in [32] that the performance of using EGC is better than that when exploiting SeC in the context of an MC-DS-CDMA or Single-Carrier system. These conclusions were applicable to the UL case, i.e. the MS to BS link of both MC- and SC-DS-CDMA systems. A parallel search based maximum-likelihood code acquisition scheme was adopted at the receiver. On the other hand, the code acquisition performance of MC-DS-CDMA attained with the aid of a serial search based scheme has been investigated in [6, 23].

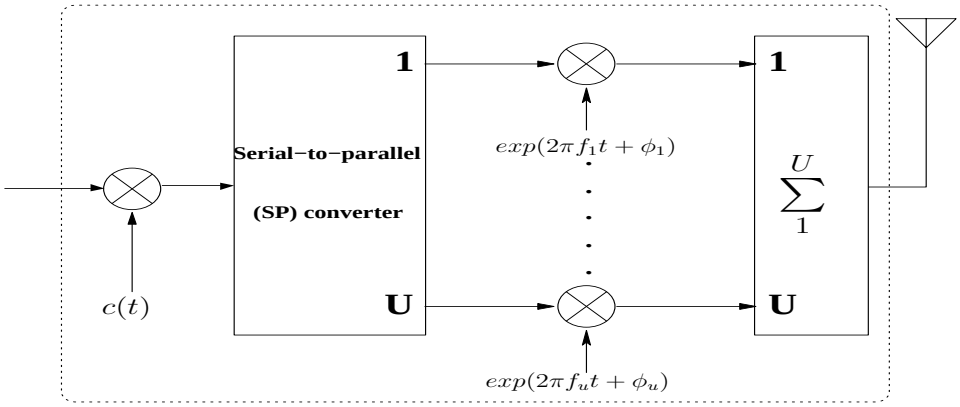

Figure 1.12: Transmitter schematic of the MC-DS-CDMA downlink having U subcarriers.

Figure 1.12 illustrates the schematic diagram of the transmitter used in the generalised MC-DS-CDMA system of [23], where $u = 1, ...U$ denotes the number of subcarriers, $c(t)$ is the unique user-specific PN sequence, f_u denotes the u^{th} subcarrier frequency and ϕ_u is the u^{th} subcarrier phase of the modulator. Furthermore, T_b indicates the bit duration of the data sequence before Serial-to-Parallel (SP) conversion, whilst T_s represents the symbol duration after SP conversion. In the MC-DS-CDMA system considered the input bit sequence is SP converted and each of the parallel sequences is then transmitted on a separate subcarrier. Consequently, we have $T_s = U \cdot T_b$. Furthermore, $SF = T_s/T_c$ denotes the spreading factor of the subcarrier signals in the MC-DS-CDMA system, whilst the spreading factor of a corresponding identical-bandwidth SC-DS-CDMA system is $SF_1 = T_b/T_{c1}$, where T_{c1} represents the chip duration of the corresponding SC-DS-CDMA signal. For simplicity, in our forthcoming discourse we assume that there is no overlap between the main spectral lobes of two adjacent subcarriers in the MC-DS-CDMA system considered [23]. Furthermore, we postulate that each subcarrier signal occupies an identical bandwidth and the total bandwidth is equally divided among the U number of subcarriers. Hence, the relationships of $T_c = U \cdot T_{c1}$ and $SF_1 = SF$ hold, since we have $T_s = U \cdot T_b$. Based upon the above assumptions, both the MC- and the corresponding SC-DS-CDMA systems maintain an identical

bandwidth of $2/T_{c1}$, as proposed in [23]. It is also worth noting that the PN sequence' chip duration T_{c1} of the SC-DS-CDMA system is U times lower than that of the MC-DS-CDMA arrangement. Hence we have $T_{c1} = T_c/U$. This is because given the same allocated bandwidth and the same total transmitted energy per chip, the bandwidth of the SC-DS-CDMA signal is U times higher than that of the subcarrier signals in the MC-DS-CDMA system using U subcarriers. Moreover, in an effort to maintain a constant integral dwell time of τ_D, the chip energy summed by the SC-DS-CDMA receiver during the period of τ_D is U times higher than that collected by the MC-DS-CDMA correlator of each subcarrier, since the number of chips within the period of τ_D is U times higher for the SC-DS-CDMA system than that of the MC-DS-CDMA system [23]. The receiver structure of a serial search based NC

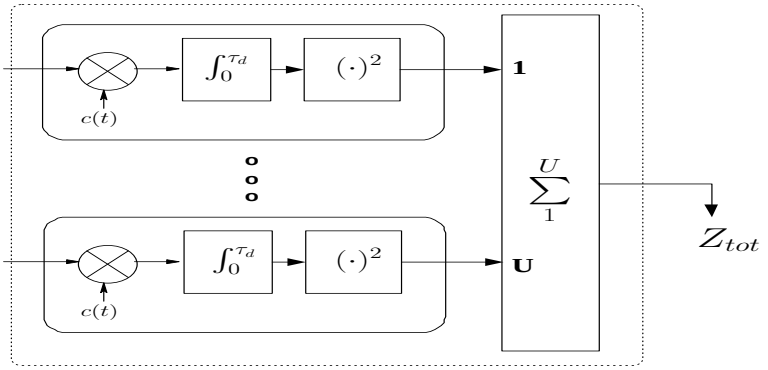

Figure 1.13: Receiver structure of a noncoherent code acquisition system employing U subcarriers.

code acquisition scheme employing U subcarriers is portrayed in Figure 1.13. The received signal is first down-converted to each subcarrier. For each subcarrier the corresponding correlator evaluates the correlation between the locally generated PN sequence and the received baseband signal, while integration takes place over the duration of the dwell time of τ_D seconds. Then the output of each correlator is squared and accumulated. Finally, the outputs of the U NC subcarrier correlators are combined, in order to generate the output variable, Z_{tot} seen in Figure 1.13. Observe in Figure 6 (a) of [23] that the code acquisition performance of a MC-DS-CDMA system using EGC significantly improves, as the number of subcarrier signals combined increases, over the Signal-to-Interference plus Noise Ratio (SINR) per chip (E_c/I_0) range considered. Moreover, the code acquisition performance of the MC-DS-CDMA system employing EGC was formed to be better in Figure 6 of [23] than that of the corresponding MC-DS-CDMA system employing SeC and also better than that of the identical bandwidth SC-DS-CDMA system. The major trend is that the characteristics of the serial search based code acquisition arrangements are similar to these of the

parallel search based one.

1.6 Code Acquisition in DS-UWB

The research of UWB systems has recently attracted a significant interest in both the academic and industrial community [39, 40, 41]. The emerging UWB systems are capable of supporting both wireless personal computers and home entertainment equipment, both requiring high data rates. Similarly, UWB systems may also be used in a variety of sensor networks operating at low data rates and at a low power consumption. DS-UWB techniques are characterised by low-duty-cycle pulse trains having a very short impulse duration [42, 43], because the high bandwidth results in a fine resolution of the timing uncertainty region. Depending on the logical value to be conveyed, a signalling impulse of T_p width having the required polarity is allocated at multiples of the frame duration T_f, where T_f is defined as the pulse repetition period, i.e. the time between two consecutive signalling pulses. In the DS-UWB DL, initial acquisition is required for both coarse timing as well as for code phase alignment and both of these constitute a challenging problem owing to the extremely short chip-duration [42, 43]. Again, this leads to a huge search space size, which is represented as the product of the number of legitimate code phases in the uncertainty region of the PN code and the number of legitimate signalling pulse positions. Both the Timing Acquisition (TA) and PN Code Phase Acquisition (CPA) must be achieved within the allowable time limits. Most acquisition schemes considered in the literature rely on either serial- or hybrid-search based acquisition schemes [42, 63, 69]. Relatively short PN codes have to be employed, in order to avoid having an excessive search space.

The code acquisition schemes typically used in the DS-UWB DL may be categorised into the following five classes:

1. Detection based approaches: [42]
   Some of the acquisition schemes proposed for the DS-UWB DL are reminiscent of those applied in conventional DS-CDMA systems.

2. Structured search strategies: [42, 63]
   A search strategy specifies the order in which the candidate phases in the timing uncertainty region are evaluated by the acquisition scheme. When there are more

than one acquisition phases in the uncertainty region, the serial search which simply searches through the uncertainty region in a consecutive manner is no longer the optimal search strategy. More efficient non-consecutive search strategies, such as for example the 'look-and-jump-by-KK-bins' search and the bit-reversal search were proposed in [42]. For the scenario, when the acquisition phases to be evaluated are KK consecutive phases in the uncertainty region, it has been claimed that the 'look-and-jump-by-KK-bins' search is the optimal serial search permutation when KK is known, while the 'bit-reversal' is the optimal search permutation, when KK is unknown. Moreover, the random search may also be considered to be an efficient search strategy, which relies on the specific characteristics of the UWB channel model [63].

3. Search space reduction techniques: [42, 69, 70, 71]
   Some of the acquisition techniques have been dedicated to the reduction of the search space by using two-stage acquisition schemes. More specifically, a two-stage acquisition scheme obeying a specific signalling format has been characterised in [42, 70] and as a result, the size of the search space has been reduced to a certain degree.

4. Estimation-based schemes: [42]
   Certain solutions designed for code acquisition in DS-UWB systems have employed estimation theoretic methods to attain the timing information of the received signal.

5. Iterative MP algorithm based schemes: [6, 13]
   A variety of sequential estimation based code acquisition schemes have been proposed in the literature [5, 45]. As another attractive design option, recursive soft sequence estimation aided acquisition based on the iterative soft-in soft-out decoding principle has also been proposed in [6, 13]. These iterative acquisition schemes have been designed for PN codes by exploiting the available *a priori* knowledge about how PN codes are generated with the aid of Linear-Feedback Shift Registers (LFSRs). Explicitly, a $(2^S - 1)$-chip PN code can be generated with the aid of a LFSR using a specific Primitive Polynomial (PP), once the associated S-stage LFSR was filled with S number of chip values [59, 72]. This beneficial property can also be exploited by the initial acquisition scheme at the receiver, because once we estimated S number

of channel-contaminated chip values, the acquisition scheme becomes capable of reconstructing the entire $(2^S - 1)$-chip code. Recently, in [43, 59] the authors proposed rapid code acquisition schemes based on the iterative MP algorithm, which adopted a philosophy similar to that used for Low Density Parity Check (LDPC) codes. When considering high-reliability military systems, where the employment of long PN codes is necessary for achieving robustness against malicious jamming and interception, the schemes of [43, 59] are beneficial in terms of reducing the size of the search space.

1.7 Chapter Summary and Conclusions

In this chapter, we have provided a brief overview of a range of code acquisition schemes. We commenced the chapter with a brief classification of the family of the code phase acquisition techniques and a generic structure of searcher and Rake receiver on the mobile station in Section 1.1. Then we illustrated procedures of code acquisition in the DL and UL in Section 1.2. This was followed by a discussion on various search strategies in Section 1.3. The underlying serial search based code acquisition was presented in Section 1.3.1, followed by the parallel search (maximum-likelihood) based code acquisition scheme in Section 1.3.2. Then the set of known sequential estimation based code acquisition schemes were classified into four categories in Section 1.3.3, which includes rapid acquisition using sequential estimation, recursion-aided RASE, majority logic decoding based RASE and recursive soft sequential estimation. Finally, in Section 1.3.4, the random search based code acquisition was presented.

We introduced a variety of widely used detector structures in Section 1.4. More specifically, NC code acquisition was highlighted in Section 1.4.1. Specifically, both a chip based-DC detection scheme and a Full-Period Correlation (FPC) based DC detection scheme were highlighted in Section 1.4.2. In Section 1.4.3, the concepts of both single-dwell and multiple-dwell based techniques were presented. The widely-used post-detection integration concept of practical code acquisition receivers was highlighted in Section 1.4.4. In Section 1.5, we have briefly summarised the characteristics of various code acquisition schemes designed for Multi-Carrier DS-CDMA systems. Then, code acquisition schemes designed for the DS-UWB DL have been briefly presented in Section 1.6. We summarised the historic evolution of sequential estimation based code acquisition as well as that of DC acquisition schemes in

Tables 1.1 and 1.2, respectively. Finally, Figure 1.14 also classifies the various schemes used in the following chapters. More explicitly, in the top trace of Figure 1.14 serial search based scenarios of the inter-cell synchronous CDMA-2000 system are classified into five categories, which will be characterised in Chapters 3 and 4. On the other hand, both random search and iterative MP algorithm based DS-UWB DL scenarios will be investigated in Chapter 6, which are featured at the bottom of Figure 1.14.

1.8 Outline of the Thesis

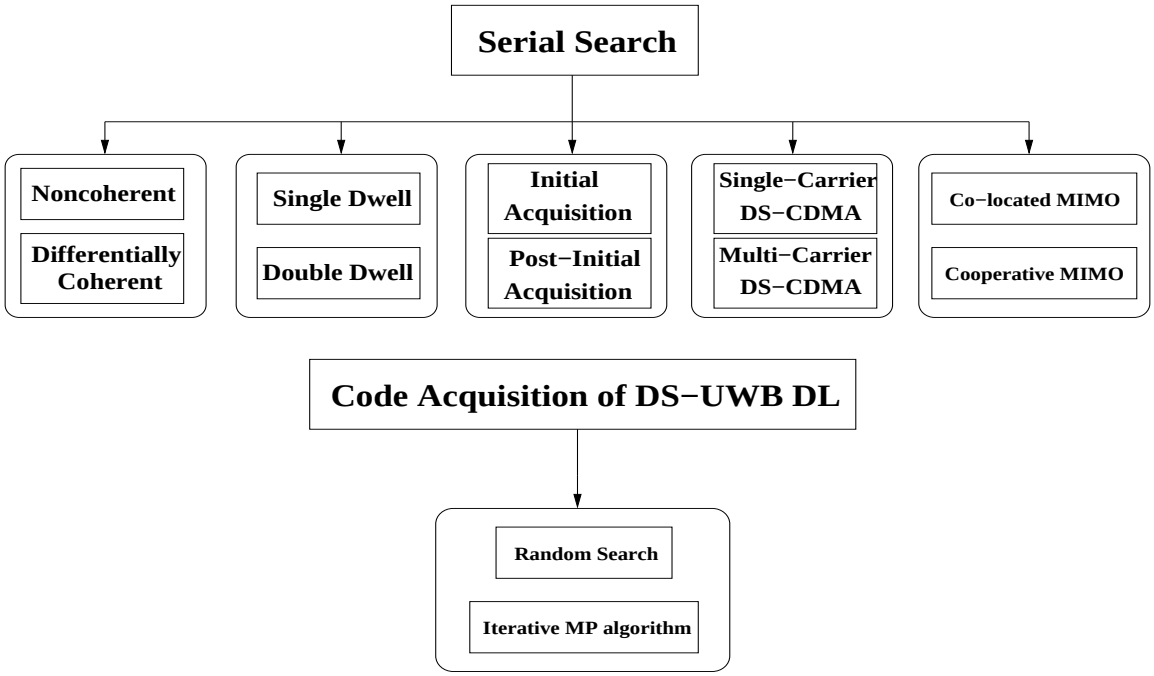

Figure 1.14: Outline of the various schemes used in the following chapters.

This thesis is organised as follows. **Chapter 2** provides the necessary preliminaries on co-located and cooperative MIMO aided code acquisition employing serial search techniques. More specifically, the channel model, the correct detection and false alarm probabilities of both NC and DC code acquisition schemes as well as the Mean Acquisition Time (MAT) of a range of code acquisition schemes are characterised in terms of both Single Dwell Serial Search (SDSS) and Double Dwell Serial Search (DDSS) arrangements. The definition of E_c/I_0 in the context of a DS-CDMA system is also provided.

Chapter 3 provides the detailed analysis of four associated topics in terms of minimising the achievable MAT of the NC serial search based acquisition scheme of both the SC- and

MC-DS-CDMA DL. An in-depth analysis of various cooperative MIMO scenarios is also provided. More specifically, the topics to be examined are as follows:

- The detection performance of NC serial search based code acquisition applied in the co-located MIMO aided DS-CDMA DL;
- The initial and post-initial acquisition in the NC serial search based co-located MIMO aided SC-DS-CDMA DL;
- NC code acquisition in the co-located MIMO aided SC- and MC-DS-CDMA DL;
- NC code acquisition in the cooperative MIMO assisted SC-DS-CDMA DL.

In **Chapter 4** the detailed analysis of two associated topics is provided, namely the minimisation of the achievable MAT of a DC serial search based scheme employed in both the co-located MIMO aided SC- and MC-DS-CDMA DL with an emphasis on DC code acquisition in comparison to NC code acquisition used as a benchmark.

In **Chapter 5** the necessary preliminaries on the topic of multiple receive antenna assisted code acquisition in DS-UWB DL are highlighted. More specifically, the channel model, the correct detection and false alarm probabilities of random search and iterative Message Passing (MP) based code acquisition schemes as well as the resultant MAT performance are analysed.

Chapter 6 provides the detailed analysis of iterative code acquisition designed for the DS-UWB DL using multiple-component decoders and characterises the initial acquisition performance of the multiple receive antenna assisted DS-UWB DL using both search space reduction as well as iterative code phase estimation.

Our conclusions and future research ideas are offered in **Chapter 7**.

1.9 Novel Contributions

Finally, the novel contributions of the thesis are summarised as follows:

- The fundamental characteristics of code acquisition schemes using co-located MIMO are investigated [73, 74];

- The performance of DL code acquisition schemes assisted by co-located MIMO is investigated in the context of both initial and post-initial acquisition schemes [75, 76];
- An in-depth analysis of the achievable diversity gain on serial search based spreading code acquisition schemes designed for the co-located MIMO aided MC-DS-CDMA DL is provided [77, 78];
- The characteristics of serial search based DC code acquisition schemes designed for co-located MIMO aided systems are analysed [79, 80];
- In-depth studies on the fundamental characteristics of code acquisition schemes designed for a co-located MIMO assisted MC-DS-CDMA system are provided in the context of DC code acquisition schemes [81, 82].
- A detailed analysis of DL code acquisition schemes employing cooperative MIMO is given [83, 84];
- In-depth studies on the fundamental characteristics of iterative code acquisition based schemes designed for a DS-UWB DL are provided [85, 86, 87, 88].

Chapter 2

Serial Search Based MIMO Aided Code Acquisition Preliminaries

2.1 Introduction

In this chapter, we will provide the necessary preliminaries of serial search based code acquisition schemes for both co-located and cooperative MIMO. We will commence the chapter with the portrayal of our channel model, when both single- and multi-path scenarios are considered, and diverse fading conditions as well as the effects of both spatial and inter-subcarrier fading correlation on the attainable performance are quantified in Section 2.2. Then the underlying formulas of both the correct detection and false alarm probabilities will be presented in Section 2.3. More specifically, the Neyman-Pearson criterion is highlighted in Section 2.3.1, followed by the derivation of the decision variable's PDFs for co-located MIMO aided NC code acquisition schemes in both the SC-DS-CDMA and MC-DS-CDMA DL in Sections 2.3.2 and 2.3.3 in terms of both a direct approach and a PDF-based one, when considering both the SC-DS-CDMA and MC-DS-CDMA DL. Then, the PDFs of cooperative MIMO aided NC code acquisition schemes invoked for the SC-DS-CDMA DL are derived in Section 2.3.4. Based on the above-mentioned facts, the MAT analysis is provided for both SDSS and DDSS aided code acquisition schemes in co-located MIMO aided scenarios, when considering both single- and multi-path propagation environments in Sections 2.4.1 and 2.4.2, respectively. Furthermore, the MAT analysis of DDSS aided code acquisition schemes operating in cooperative scenarios is also given for a multi-path propagation environments in Section 2.4.3. Finally, in Section 2.5 the effect of different

E_c/I_0 values on the achievable performance of DS-CDMA systems is studied.

2.2 Channel Model

2.2.1 Single-Path versus Multi-Path Scenario

For the sake of simplifying the performance analysis of the code acquisition schemes considered, numerous papers adopted a Rayleigh-faded single-path model in the literature [3, 4, 5, 6]. A range of more sophisticated studies considered a multi-path fading channel [7, 22, 89, 90, 91, 92]. The latter studies may be classified into two different categories. First of all, most authors simply considered the deleterious effects of multiple-paths, but in [22, 92], the authors proposed a new code acquisition scheme that goes far beyond this passive analysis and actively exploits the multiple-paths. More specifically, this scheme adopted both non-consecutive search and joint triple-cell detection, which takes advantage of the characteristics of the multi-path phenomenon in the frequency-selective Rayleigh fading channels encountered. On the other hand, in [7], Glisic and Katz defined the channel's multi-path profile characterised by a vector, which hostile delays of all the received paths. Both a deterministic model and a probabilistic model of the channel's multi-path profile are considered. All the transfer functions consisting of the formula for deriving the Mean Acquisition Time (MAT) were derived based upon the both models. Historically speaking, [22] adopted a tapped delay line model for describing the frequency-selective channel from [93]. Finally, a range of dispersive channel models, spanning from two-path to L-path channel models were adopted in [89, 90, 91]. The achievable MAT was derived by stipulating the assumption of encountering a multi-path scenario associated with either an equal- or unequal-power assigned to each path. Hence MAT studies in the open literature [7, 22, 89, 90, 91] except for [92] employed a similar multi-path channel model in their discourse. Amongst these models, a widely accepted model of the frequency-selective multi-path fading channel is the finite-length tapped delay line channel model [22, 93] shown in Figure 2.1. In the model $S(t)$ represents the transmitted signal of a user, T_c is the chip duration, ϕ_l is the carrier phase of the signal received for the l^{th} path of the user, α_l represents the envelope at the l^{th} path obeying the Rayleigh distribution, $n(t)$ represents the Additive White Gaussian Noise (AWGN) and $r(t)$ denotes the signal of the user received through the L-tap delay-line channel model. Furthermore the L tap weights α_l are assumed to be independent identically distributed (i.i.d.) Rayleigh-faded multi-path signals, each

arriving with a time delay τ_l having a tap spacing of one chip-duration T_c [22], where L is the number of multi-path components. In this thesis both the single- and multi-path models are in our performance analysis.

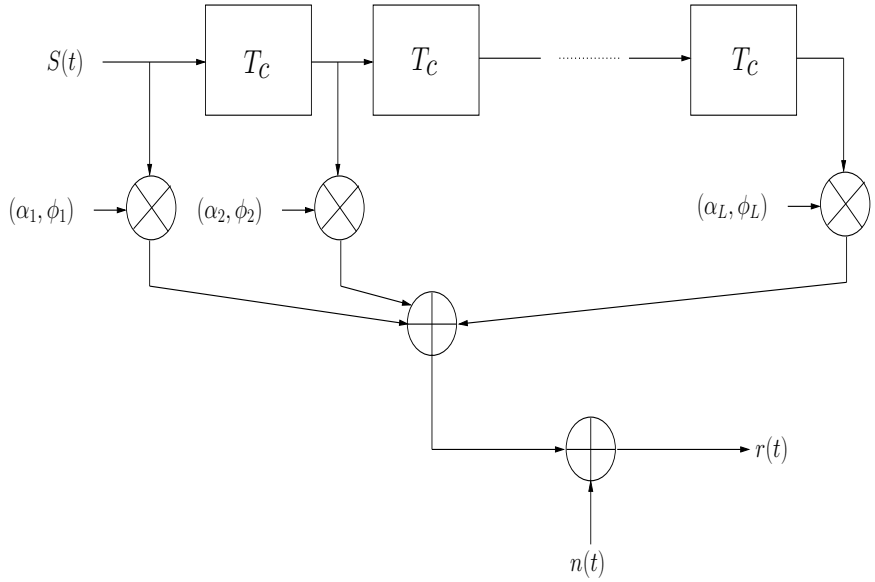

Figure 2.1: Tapped delay line model of the frequency-selective multi-path fading channel.

2.2.2 Fading Conditions for Our Performance Analysis

As in [44, 94], it is useful to characterise the fading channel's correlation on the basis of the memory τ_R and τ_S of its multi-path and shadowing components, where the memory is defined as the temporal span which has to be exceeded by the multi-path components, in order to ensure the statistical independence of the fading samples. Let T_{H_1} be the minimum time interval between two consecutive H_1 hypothesis tests [44], where the H_1 hypothesis test indicates a test of whether the currently hypothesised signal is present or not. We opt for the following basic assumptions for our analytical studies:

(1) Static shadowing is deemed to be encountered, whenever we have $\tau_S >> T_{H_1}$; the shadow-fading envelope is constant during the entire code acquisition process.

(2) Fast multi-path fading is assumed to be present, whenever we have $\tau_R < T_{H_1}$; the multi-path fading envelope is considered to be independent between the current H_1 hypothesis testing and the next one.

(3) As a subclass of the rapidly fading multi-path case, we consider the fading to be UnCorrelated (UC), whenever we have $N \cdot T_c < \tau_R$; In this scenario, the fading envelope is

considered to be independent in two consecutive integration intervals, but it is considered to be constant over N chip intervals.

Our analytical formulation will be based on the above-mentioned scenarios. Accordingly, we employ the flow-graph based approach of [3, 44, 94], assuming the above-mentioned fast multi-fading scenario associated with UC fading, namely that the fading is independent between the current H_1 hypothesis testing and the next. The analytical derivation of both the correct detection and false-alarm probabilities applies strictly to the UC case, for which a fully analytical approach is possible. Moreover, [94] confirmed that the scenario considered in [3] corresponds to the UC case.

For the sake of further emphasising the validity of our analytical formulation, the simulation results of [94] demonstrate that accurate results were obtained by using the approximation that σ^2 is a constant [3, 44, 94], where σ^2 is the variance of the constituent Gaussian distribution. Similarly to our assumptions in this thesis, the fast-fading envelope is modeled as a Rayleigh process in [3, 44, 94]. Furthermore, it may be inferred by the inspection of Figures 5 and 6 in [94], which show the impact of the fading envelope's correlation on the system's performance, that different fading characteristics lead to different levels of performance, although we will demonstrate that the difference in terms of the Signal-to-Interference plus Noise Ratio (SINR) per chip (E_c/I_0) required for maintaining a specific MAT is generally less than 1 dB. In conclusion, even though we only consider the specific scenario of an UC fading channel, the results generated by our analytical approach are valid for both the full correlation and partial correlation scenarios defined in [44]. Hence the impact of the fading channel's correlation on the systems attainable performance, depends on the system's characteristics, such as for example the number of dwell intervals, as well as on the (E_c/I_0) value encountered when a Constant False-Alarm Rate (CFAR) [1] based approach is adopted.

2.2.3 Effects of Spatial and Inter-Subcarrier Fading Correlation

In recent years various smart antenna designs have emerged, which have found application in diverse scenarios and the four most wide-spread MIMO types are briefly summarised in Table 2.1. These four MIMO schemes were designed for achieving various design goals. The family of Spatial Division Multiplexing (SDM) [27, 95] schemes aims for maximising the

[1] The definition of CFAR will be explained in depth in the next section

SDM Systems [95]	SDM systems employ multiple antennas, but in contrast to SDMA arrangements, not for the sake of supporting multiple users. Instead, they aim for increasing the throughput in the DL of wireless systems in terms of the number of bits per symbol that can be transmitted by a given user in a given bandwidth at a given integrity.
SDMA [27]	SDMA exploits the unique, user-specific "spatial signature", i.e. the CIRs of the individual users for differentiating amongst them. This allows the UL system to support multiple users within the same frequency band and/or time slot, provided that their CIRs are sufficiently different and are accurately measured.
Spatial Diversity (STBC [96, 97], STTC [97, 98]) and Space-Time Spreading (STS) [6]	In contrast to the $\lambda/2$-spaced phased array elements of beamforming, in spatial diversity schemes, such as space-time block or trellis codes [98] the multiple antennas are positioned as far apart as possible, so that the transmitted signals of the different antennas experience independent fading, resulting in the maximum achievable diversity gain.
Beamforming [99]	Typically $\lambda/2$-spaced antenna elements are used for the sake of creating a spatially selective transmitter/receiver beam. Smart antennas using beamforming have been employed for mitigating the effects of cochannel interfering signals and for providing beamforming gain.

Table 2.1: The four main applications of MIMOs in wireless communications.

attainable multiplexing gain, i.e. the throughput of a single user by exploiting the unique, antenna-specific Channel Impulse Responses (CIRs) of the array elements. By contrast, Space Division Multiplexing Access (SDMA) arrangements [27] are close relatives of SDM schemes, but they maximise the number of users supported, as opposed to maximising the throughput of a single user by sharing the total system throughput amongst the users supported. Alternatively, attaining the maximum possible diversity gain is the objective of the family of Space-Time Block Coding (STBC) [96] as well as Space-Time Trellis Coding (STTC) [97] schemes found in the literature [98]. Finally, beamforming mitigates the effects of interfering users roaming in the vicinity of the desired user [99], provided that their received signals are angularly separable. In this treatise code acquisition schemes designed for both SDM [27, 95] and Space-Time Coding [96, 97] schemes will be considered in detail. However beamforming based schemes will not be considered in this treatise.

When considering the effects of spatial fading correlation among either the multiple transmit antennas or the multiple receive antennas, based on the results of [100], we would like

to underline the following facts:
When the spatial correlation is sufficiently low, the performance attained in the case of moderately correlated antenna signals is similar to that obtained in the case of entirely uncorrelated antennas. In [100], the effects of spatial correlation recorded as a function of the antenna spacing and azimuth were considered. The results of both Figures 6 and 7 in [100], demonstrate that partially correlated antennas provide a similar performance to that of entirely uncorrelated antennas. This fact is directly related to our scenarios, when deriving the correct detection probability formula. In typical mobile communication scenarios the BS antennas are situated on a rooftop and the MS is surrounded by numerous obstacles. The spacing of the multiple transmit antennas of the BS and the multiple receive antennas of the MS are assumed to be 10 λ (at least 4 λ) and 0.5 λ, respectively, which may be considered as practical at a center frequency of $2GHz$, where the wavelength is 15 cm. Hence our results are unlikely to be highly affected by the spatial correlation. Accordingly, this fact is the rationale for using the phrase 'transmission over a spatially uncorrelated Rayleigh channel' in the thesis.

Our system may be deemed reminiscent of the CDMA-2000 3x arrangement, which has three 1.25 MHz-bandwidth subcarriers, while our MC-DS-CDMA system has four 0.625 MHz-bandwidth subcarriers. Similar to SC-DS-CDMA, the DS-spread subcarrier signals of our MC-DS-CDMA arrangement experience frequency selective fading. The delay spreads are assumed to be limited to the range of $[T_m,T_M]$, where T_m corresponds to the environment having the shortest delay spread considered (as experienced, for example in an indoor environment). By contrast, T_M is associated with an environment having the highest possible delay spread, as in an urban area. Propagation measurements conducted in typical wireless environments, including various indoor, open rural, suburban and urban areas show that the delay spread is typically distributed over the range of $[0.1\mu s,3\mu s]$ [25, 101]. Accordingly, when communicating over various fading channels having delay spreads in the range of $[0.1\mu s,3\mu s]$, flat fading is experienced by each subcarrier signal, if the chip duration T_c is higher than the highest delay spread T_M (i.e., when $T_c > T_M$). Mobile communication studies often implicitly assume encountering urban, suburban or rural areas, unless indoor environments are explicitly stipulated. Furthermore, it is usually assumed that the BS antennas are positioned on a rooftop. When considering both indoor environments and teletraffic hot spots in an urban area, due to the reflections and refractions imposed by the propagation channel between the MS and BS, the delay spreads imposed on the transmitted signals are typically longer than the chip duration encountered by our MC-DS-CDMA

systems, where the chip duration is T_c=1/0.6144μs = 1.6276μs. Hence, typically frequency selective fading would be encountered. Furthermore, a bandwidth of 0.625 MHz per subcarrier is allocated, which is significantly wider than those of typical MC-DS-CDMA systems, where the latter assume frequency non-selective flat fading channels, when a significantly higher number of the subcarriers was assigned. As a result of our assumptions, the fading coefficient of the adjacent subcarriers may be considered to be uncorrelated.

2.3 Detection and False Alarm Probabilities

2.3.1 Neyman-Pearson Criterion

There are a number of ways to describe the best decision strategy in terms of the correct detection and false alarm probabilities [102]. One of the most useful strategies is constituted by the Neyman-Pearson criterion [102], which is likely to be the most important criterion in both radar and sonar detection problems. The hypothesis testing adopted in our system is based on the Neyman-Pearson criterion, which seeks to minimise the probability of choosing '0' when '1' is true (a 'miss'), while maintaining an acceptable probability of choosing a '1' when a '0' is true (a 'false alarm') [3, 102]. More explicitly, this strategy chooses the decision rule by ensuring that the false alarm probability P_F is no higher than some specified upper bound and within this constraint, maximises the probability of the correct detection. Furthermore, an important benefit of this criterion is that it yields a Constant False-Alarm Rate (CFAR) [44, 102].

Let us now assume that an 'experiment' is carried out in order to determine, which of two events generated the data considered. More explicitly, we have two of hypotheses H_i, $i = 0, 1$, and one of them represents the outcome of the experiments at the time instant, when the data were generated. Given that only two hypotheses are legitimate, which are denoted by H_0, H_1, we have a binary hypothesis-testing problem. Traditionally the hypothesis H_0 is referred to as the null hypothesis and H_1 is the alternative hypothesis [102]. The space is divided into the regions R_0 and R_1, where R_0 represents the acceptance region, when H_0 is accepted, while in the so-called critical region R_1, H_0 is rejected and H_1 is considered to be true [102]. To elaborate a little further, the acquisition scheme makes the decision D_0 that hypothesis H_0 is true if and only if the data point y lies in the decision region R_0 and opts for decision D_1 otherwise. In the binary hypothesis testing scenario

these two regions must encompass every legitimate point of the y-space. Hence the regions R_0 and R_1 dichotomise the data space.

Let us now continue our discourse by defining a number of mathematical terms, which will be used in our forthcoming discussions. Let us now define the null hypothesis H_0 as the one that the desired user's spreading code is absent, while H_1 represents the hypothesis that is present. Naturally, we would always like to arrive at the correct decision D_0 when H_0 is tested and D_1, when H_i is being tested. However, we also have to consider the two erroneous decisions, namely when H_0 is being tested and we arrive at the decision D_1 in vice versa. More explicitly, the probability of the erroneous decision D_1 encountered, when we are testing the hypothesis H_0 that the desired user's signal is absent is referred to as a false alarm event, because the channel impairments resulted in a high correlator output - despite the absence of the desired user. Similarly, when the hypothesis H_1 is being tested - namely that of the desired user's spreading sequence being present - but we arrive at the decision D_0 owing to experiencing a low correlator output due to severe channel impairment, we refer to this event as a 'miss'. The corresponding erroneous decisions are termed as the 'false alarm' and 'miss' probabilities, which are denoted by $P_F = P(D_1|H_0)$ and $P_M = P(D_0|H_1)$, respectively. Finally the correct decision probability is given by $P_D = P(D_1|H_1) = 1 - P(D_0|H_1)$.

Again, the Neyman-Pearson criterion is used, in order to maximise the probability of correct detection, whilst maintaining as low a false alarm probability, as possible, which is formulated as

$$max\, P(D_1|H_1) = max\left[\int_{R_1} p_1(y)dy\right] \; and \; P(D_1|H_0) = \left[\int_{R_1} p_0(y)dy\right] \leq P_F, \quad (2.1)$$

where y indicates the data available for example at the correlator's output, while R_1 symbolises the particular region of the correlator output space, where the decision D_1 is inferred. The variables $p_0(y)$ and $p_1(y)$ represent the PDF of y conditioned on H_0 and H_1, respectively. Since the entire correlator output space has to be separated into the critical region R_1 and the acceptance region R_0, the first stage is to find the optimum partitioning. Those points y in R_1 are determined by employing a log likelihood ratio test [3, 102]. This test is expressed as $ln[p_1(y)/p_0(y)]$ $(> \; or \; <)$ θ, where a predetermined threshold, namely θ is obtained from the Neyman-Pearson constraint associated with a specific probability of false alarm, which is kept constant at the given value of ψ. More specifically, ψ is calculated by $\psi = Pr(z > \theta|H_0) = \int_\theta^\infty p_0(y)dy$. Now an experiment based upon the Neyman-Pearson criterion may be analysed in terms of both the probabilities of the correct detection and

false alarm. Finally, the criterion guarantees that any forms of both $p_1(y)$ and $p_0(y)$ are available and specifying the a priori probabilities of the two hypotheses is not necessary. In the following subsections we will employ the aforementioned criterion in an effort to derive both the probabilities of the correct detection and false alarm in the MIMO Aided SC- and MC- CDMA DownLink (DL).

According to references [3, 44, 94], code acquisition can be considered to be a classical binary hypothesis testing problem, namely that of testing, whether the desired signal is deemed to be present (an H_1 hypothesis), whilst eliminating all incorrect hypotheses denoted by H_0 and at the same time trying to avoid any missed detection and false alarm events. In our system a correlator output threshold-based decision criterion has been chosen. The correlator's decision threshold value has been optimised in the literature based upon a whole host of criteria [3, 45, 102]. The above-mentioned Neyman-Pearson criterion [3, 102] has often found favour in mobile environments [3, 44, 94], since it constitutes a CFAR based approach. According to the CFAR technique [44], the decision variables are appropriately normalised by the estimate of the background noise plus interference variance. Hence, in case of using a CFAR technique, the various probabilities associated with the code acquisition process, including those associated with H_0 hypothesis testing do not depend on the distribution of the fading. The adoption of the CFAR based approach is particularly desirable in the specific family of code acquisition arrangements, which have to be robust against fading. In fact, it was shown in [3, 44, 94] that in hypothesis testing based upon the CFAR technique, the effects of fading channels on the code acquisition process are restricted to the testing related to the H_1 hypothesis. Furthermore, in the presence of fading, it is important to adopt the CFAR based approach for the sake of decision threshold optimisation, in order to achieve the best possible acquisition performance. As a benefit of the above-mentioned normalisation associated with the CFAR-based approach [44], the fading channel does not affect the testing of the H_0 hypotheses. The resultant scenario and the related test becomes reminiscent of an AWGN scenario. As a consequence, the fading envelope only affects the correct detection probability. The exploitation of the statistical independence of the decision variables, which is a consequence of using sufficient statistics under the assumption of employing a CFAR technique allow us to generate the analytical expressions of both the correct detection and false-alarm probabilities.

2.3.2 PDF of Co-located MIMO Aided Non-Coherent Code Acquisition

2.3.2.1 Direct Analysis of SC-DS-CDMA

Here we derive the Probability Density Function (PDF) of a Non-Coherent (NC) scheme communicating over a spatially uncorrelated Rayleigh-faded channel in the MIMO Aided SC-DS-CDMA DL by exploiting the expression of its output PDF formulated in the context of an AWGN channel, in order to further interpret the Neyman-Pearson criterion based hypothesis testing [3, 102].

The signal transmitted at the ζ^{th} chip sampling instant of the desired user at the Base Station (BS) of a multiple transmit antenna aided system can be expressed as

$$S_{tot}(\zeta) = \sum_{m=1}^{P} [\sqrt{\frac{E_c}{P}} b(\zeta) C(\zeta) w_m(\zeta) h(t - \zeta T_c) \sqrt{2} \cos(2\pi f t + \phi)], \tag{2.2}$$

where P is the number of transmit antennas, $b(\zeta)$ represents the binary input data sequence assuming values of +1 or -1, $C(\zeta)$ denotes a common PN sequence having a cell-specific code-phase offset, $w_m(\zeta)$ identifies the specific Walsh code assigned to the m^{th} transmit antenna, E_c denotes the pilot signal energy per PN code chip, $h(t)$ is the impulse response of the pulse shaping filter, T_c is the chip duration, f is the carrier frequency and ϕ is the carrier phase of the user's modulator. The total allocated power is equally shared by the P transmit antennas. The spacing of the multiple transmit antennas at the BS and the multiple receive antennas at the MS are assumed to be 10 λ and 0.5 λ, respectively. It is also assumed that the BS antennas have a high elevation. The tapped-delay line channel model generates L multi-path signals arriving with a time delay of τ_l [15, 22] in Section 2.2.1, where L is the number of multi-path signals received. Therefore, the signal $r_{tot}(\zeta)$ at the receiver is a composite of L multi-path signals having a time delay of τ_l, which is expressed in the form of

$$r_{tot}(\zeta) = \sum_{l=1}^{L} \sum_{m=1}^{P} \sum_{n=1}^{R} [\alpha_{(l,m,n)} \sqrt{\frac{E_c}{P}} b(\zeta) c(\zeta) w_m(\zeta) h(t - \zeta T_c - \tau_l) \sqrt{2} \cos(2\pi f^{'} t + \phi_{(l,m,n)})], \tag{2.3}$$

where R is the number of receive antennas, and $\alpha_{(l,m,n)}$ represents the envelope of the $(l, m, n)^{th}$ path signal obeying the Rayleigh distribution, while $f^{'}$ is the carrier frequency distorted by the clock-drift-induced frequency mismatch and the Doppler shift. Furthermore, $\phi_{(l,m,n)}$ denotes the signal phase of the $(l, m, n)^{th}$ path having a uniform distribution over (0, 2π).

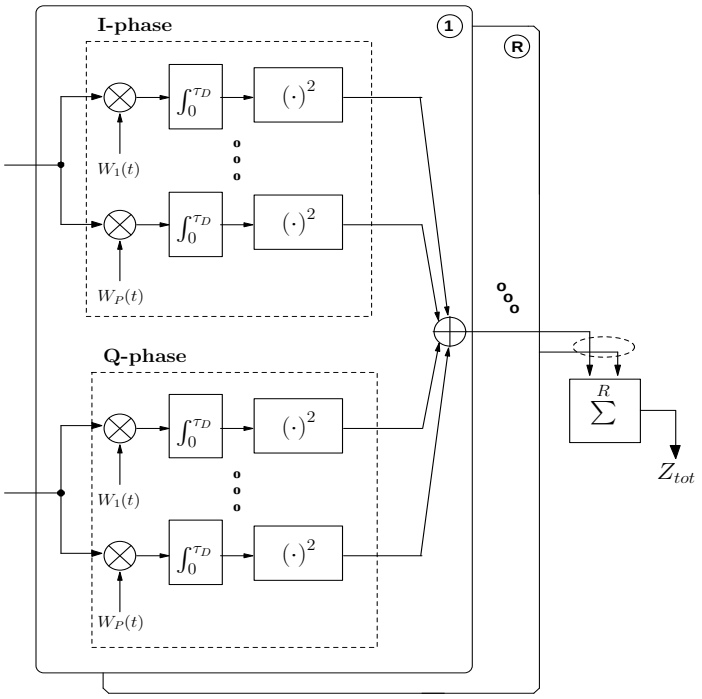

Figure 2.2: Receiver structure of NC scheme in the MIMO aided SC-DS-CDMA DL.

Figure 2.2 depicts the block diagram of the NC receiver designed for our code acquisition scheme using MIMO, where the timing hypothesis test is carried out for binary spreading. As seen in Figure 2.2, we generate a decision variable by accumulating $P \cdot R$ independently faded signals observed over a time interval to improve the correct detection probability in the mobile channel, which imposes both fading and poor SINR conditions, where the integral dwell time represents $\tau_D = N \cdot T_c$ and N is defined as τ_D/T_c. In order to derive the output PDF of the NC scheme considered for a Rayleigh-faded channel in this section we assume encountering a single-path model. The effects of a multi-path channel on the achievable Mean Acquisition Time will be considered in Section 2.4. Before deriving the PDF of the decision variable, let us now consider the effects of both the timing errors, τ and of the total frequency mismatch, Δf_t on the received signal. The timing errors are imposed by both the different delays of the signal received via a mobile channel and the sampling inaccuracy caused by having a finite - rather than infinitesimally low - search step size of $\Delta = 1/2T_c$. The total frequency mismatch is the sum of the clock-drift-induced frequency mismatch Δf_m between the BS's transmitter and the Mobile Station (MS)'s receiver as well as the contribution imposed by the Doppler shift, Δf_d.

Following the procedures outlined in [3], the mean values of the I- and Q- channel outputs

in Figure 2.2, are given by

$$E[Y_{tot}^{(I)}] \approx \sum_{m=1}^{P}\sum_{n=1}^{R}\alpha_{(m,n)}\sqrt{\frac{E_c}{P}}\,R(\tau)\left\{\sum_{\zeta=1}^{N}\cos[2\pi\zeta(\Delta f_m+\Delta f_d)T_c\,+\,\phi_{(m,n)}]\right\} \quad (2.4)$$
$$= \sum_{m=1}^{P}\sum_{n=1}^{R}\alpha_{(m,n)}\sqrt{\frac{E_c}{P}}\,R(\tau)\left\{A\cdot\cos(\phi_{(m,n)})\;-\;B\cdot\sin(\phi_{(m,n)})\right\},$$

$$E[Y_{tot}^{(Q)}] \approx \sum_{m=1}^{P}\sum_{n=1}^{R}\alpha_{(m,n)}\sqrt{\frac{E_c}{P}}\,R(\tau)\left\{\sum_{\zeta=1}^{N}\sin[2\pi\zeta(\Delta f_m+\Delta f_d)T_c\,+\,\phi_{(m,n)}]\right\} \quad (2.5)$$
$$= \sum_{m=1}^{P}\sum_{n=1}^{R}\alpha_{(m,n)}\sqrt{\frac{E_c}{P}}\,R(\tau)\left\{B\cdot\cos(\phi_{(m,n)})\;+\;A\cdot\sin(\phi_{(m,n)})\right\},$$

where we have $A = \sum_{\zeta=1}^{N}\cos[2\pi\zeta(\Delta f_t)T_c]$, $B = \sum_{\zeta=1}^{N}\sin[2\pi\zeta(\Delta f_t)T_c]$, while the autocorrelation function of the timing error is given by $R(\tau) = \int_{-\infty}^{\infty}|H(f)^2|\cos(2\pi f\tau)df$ and Δf_t is defined as $\Delta f_m + \Delta f_d$. If we take into account a strictly band-limited filter [3], $R(\tau)$ is expressed as [2]

$$R(\tau) = \frac{\sin(\pi\tau/T_c)}{(\pi\tau/T_c)} \equiv sinc(\tau/T_c). \quad (2.6)$$

Then, the output variable $Z_{(m,n)}$ assigned to each path is expressed as

$$Z_{(m,n)} = (E[Y_{(m,n)}^{(I)}])^2 + (E[Y_{(m,n)}^{(Q)}])^2 \quad (2.7)$$
$$= N^2(\frac{E_c}{P})sinc^2(\frac{\tau}{T_c})sinc^2(N\Delta f_t T_c).$$

Hence, taking Equation. 2.7 into account, the square of the mean values of $Y^{(I)}$ and $Y^{(Q)}$ formulated in Equation. 2.7 is given by

$$M^2 = N^2(\frac{E_c}{P})sinc^2(\frac{\tau}{T_c})sinc^2(N\Delta f_t T_c). \quad (2.8)$$

Thus, the signal energy reduction expressed as a function of the frequency mismatch becomes:

$$D(\Delta f_t) \approx sinc^2(N\Delta f_t T_c). \quad (2.9)$$

[2]The timing error effects imposed are highly dependent on the type of the linear waveform-shaping filter transfer function used, rather than on the type of the spreading codes considered, since without shaping they all exhibit rectangular chips. In our scenario we opted for a strictly bandlimited Frequency-Domain (FD) chip-shaping filter transfer function expressed as $H(f) = \frac{1}{\sqrt{W}}\left[u(f+\frac{W}{2}) - u(f-\frac{W}{2})\right]$, where $u(\cdot)$ denotes the unit step function, f is the frequency in $H(f)$ and W represents the total DS-spread bandwidth [3]. The resultant impulse response, $h(t)$ is given by $h(t) = \int_{-W/2}^{W/2}H(f)exp(2\pi ift)df = \sqrt{W}sin(\pi Wt)/(\pi Wt)$, where $W \equiv 1/T_c$. Therefore without loss of generality, when using the squaring operation seen in Figure 2.2, we have $X_n = +1$, where $n = 1, 2, ..., N$ and X_n represents a squared chip value at the n^{th} chip position, which effectively eliminates the influence of the polarity on the chip-waveform. When we define the ACF $R(\tau)$ as $\int_{-\infty}^{\infty}|H(f)|^2\cos 2\pi f\tau df$, based upon our assumption of the FD chip-shaping filter, we have Equation 2.6.

As a result of the above formulation, the effects of both timing errors and those of the frequency mismatch are encapsulated by the definition of the mean square, M^2 formulated in Equation. 2.8. This means that the effects of both of these detrimental factors are directly involved in the measured energy value. The other parameters remain the same as in the case of considering either timing or frequency errors in isolation.

In order to derive the PDF conditioned on both the hypotheses of the desired signal being present H_1 and absent H_0, let us assume that the amplitude is fixed, but that the phase is taken to be a uniformly distributed random variable. For simplicity, we omitted the subscripts of all the symbols used, which denoted each path. The vectors hosting the I- and Q- phase outputs assigned to each path may be expressed as

$$y^{(I)} = (y_1^{(I)}, y_2^{(I)}, ...y_N^{(I)}) \, and \, y^{(Q)} = (y_1^{(Q)}, y_2^{(Q)}, ...y_N^{(Q)}) \, . \tag{2.10}$$

Then we obtain the PDFs of both outputs conditioned on ϕ. The PDFs of the signals being absent and present are expressed as

$$p_0(y^{(I)}, y^{(Q)}) = \prod_{\zeta=1}^{N} \exp[-(y_\zeta^{(I)})^2/I_0] \cdot \exp[-(y_\zeta^{(Q)})^2/I_0]/\pi I_0 \, , \tag{2.11}$$

$$\begin{aligned} p_1(y^{(I)}, y^{(Q)}|\phi) &= \prod_{\zeta=1}^{N} \exp[-(y_\zeta^{(I)} - \sqrt{\frac{E_c}{P}} R(\tau) \{\cos\phi\})^2/I_0] \\ &\cdot \quad \exp[-(y_\zeta^{(Q)} - \sqrt{\frac{E_c}{P}} R(\tau) \{\sin\phi\})^2/I_0]/\pi I_0, \end{aligned} \tag{2.12}$$

respectively, where I_0 denotes the one-sided power spectral density of the AWGN. By introducing the following notation, the expressions of both $Y^{(I)}$and $Y^{(Q)}$ are defined by $Y^{(I)} = \sum_{\zeta=1}^{N} y_\zeta^{(I)}$ and $Y^{(Q)} = \sum_{\zeta=1}^{N} y_\zeta^{(Q)}$, respectively, which are physically proportional to the energy accumulated in the integral dwell time of τ_D. The variances of $Y^{(I)}$ and $Y^{(Q)}$ are defined as $V/2$, where we have $V \equiv NI_0$, whilst their means are given by $N\sqrt{\frac{E_c}{P}} R(\tau)\cos\phi$ and $N\sqrt{\frac{E_c}{P}} R(\tau)\sin\phi$, respectively. Accordingly, we formulate the PDF of $Y^{(I)}$and $Y^{(Q)}$ at each branch, which may be expressed in the context of an AWGN channel [3] as

$$p_0(Y^{(I)}, Y^{(Q)}) = \exp[-((Y^{(I)})^2 + (Y^{(Q)})^2)/V]/\pi V, \tag{2.13}$$

$$\begin{aligned} p_1(Y^{(I)}, Y^{(Q)}|\phi) &= \exp[-(Y^{(I)} - \sqrt{\frac{E_c}{P}} R(\tau) \{A\cos\phi - B\sin\phi\})^2/V] \\ &\cdot \quad \exp[-(Y^{(Q)} - \sqrt{\frac{E_c}{P}} R(\tau) \{B\cos\phi + A\sin\phi\})^2/V]/\pi V, \end{aligned} \tag{2.14}$$

where we have $A = \sum_{\zeta=1}^{N} \cos[2\pi\zeta(\Delta f_t)T_c]$ and $B = \sum_{\zeta=1}^{N} \sin[2\pi\zeta(\Delta f_t)T_c]$. Since the carrier

phase is modelled by a uniform random variable, we represent the unconditional PDF in the presence of the desired signal by averaging Equation. 2.14 over ϕ, yielding

$$
\begin{aligned}
p_1(Y^{(I)}, Y^{(Q)}) &= \frac{1}{2\pi}\int_0^{2\pi} p_1(Y^{(I)}, Y^{(Q)}|\phi)\, d\phi && (2.15)\\
&= \frac{1}{2\pi}\int_0^{2\pi} \exp\{-[(Y^{(I)})^2 + (Y^{(Q)})^2 + \frac{N^2E_c}{P}R^2(\tau)sinc^2(N\Delta f_t T_c)]/V\} && (2.16)\\
&\cdot\ \exp\{2\sqrt{\frac{E_c}{P}}R(\tau)[Y^{(I)}\{A\cos\phi - B\sin\phi\} + Y^{(Q)}\{B\cos\phi + A\sin\phi\}]/V\}\frac{1}{\pi V}d\phi\\
&= \frac{1}{\pi V}\exp\left(\frac{-[(Y^{(I)})^2 + (Y^{(Q)})^2]}{V}\right)\cdot\exp\left(-\frac{N^2E_c}{P}R^2(\tau)sinc^2(N\Delta f_t T_c)/V\right)\\
&\cdot\ \mathcal{I}_0\left(\frac{2\sqrt{\frac{N^2E_c}{P}R^2(\tau)sinc^2(N\Delta f_t T_c)[(Y^{(I)})^2 + (Y^{(Q)})^2]}}{V}\right), && (2.17)
\end{aligned}
$$

where $\mathcal{I}_0(x) \equiv \int_0^{2\pi}\exp(x\cdot\cos\phi)d\phi/2\pi$ is the zeroth-order modified Bessel function.

By using the Jacobian transformation [103], we arrive at the PDFs conditioned on both the hypothesis $p_0(Z)$ and $p_1(Z)$ of the desired signal being absent and present, respectively, in the context of an AWGN channel:

$$
\begin{aligned}
p_0(Z) &= \exp[-Z/V]/V,\ Z>0, && (2.18)\\
p_1(Z) &= \frac{\exp[-(Z+M^2)/V]}{V}I_0\left(\frac{2\sqrt{M^2Z}}{V}\right). && (2.19)
\end{aligned}
$$

For the sake of expressing the PDF $p_1(Z)$ conditioned on the presence of the desired signal derived for transmission over an uncorrelated Rayleigh channel, first the PDF $p_1(Z,\beta)$ corresponding to the SINR β conditioned on the hypothesis of the desired signal being transmitted over an AWGN channel is weighted by the probability of occurrence $p(\beta)$ of encountering the SINR β, as quantified by the PDF and then averaged over its range of $-\infty\sim\infty$, yielding:

$$
\begin{aligned}
p_1(Z) &= \int_{-\infty}^{\infty} p(\beta)p_1(Z,\beta)d\beta && (2.20)\\
&= \int_0^{\infty}\left(\frac{e^{-\beta/\sigma^2}}{\sigma^2}\right)\cdot\frac{\exp[(-Z+\beta M^2)/V]}{V}\cdot I_0\left(\frac{2\sqrt{\beta M^2Z}}{V}\right)d\beta && (2.21)\\
&= \frac{\exp[-Z/(V+M^2\sigma^2)]}{(V+M^2\sigma^2)} && (2.22)\\
&\equiv \frac{\exp[-Z/(V+\overline{M^2})]}{\left(V+\overline{M^2}\right)}, && (2.23)
\end{aligned}
$$

where we have $\overline{M^2} \equiv M^2\sigma^2 = N^2\overline{E_c}$. Upon defining $V_F = V + \overline{M^2} = N(I_0 + N\overline{E_c})$, and $\overline{E_c} = \sigma^2(E_c/P)sinc^2(\tau/T_c)sinc^2(N\Delta f_t T_c)$, we arrive at

$$p_0(Z) = \frac{1}{V}e^{-Z/V}, \tag{2.24}$$

$$p_1(Z) = \frac{1}{V_F}e^{-Z/V_F}. \tag{2.25}$$

The total amount of channel-induced impairments in the DL is constituted by the superposition of the background noise, plus the serving-cell's own interference imposed by the multi-path signals as well as the other-cell interference. Further details on the calculation of the total interference may be found in [3, 15]. In this thesis we essentially limit ourselves to considering MIMO without Post-Detection Integration (PDI), noting that PDI is capable of improving the achievable performance upon generating the decision variable by accumulating T consecutive signals observed over multiple time intervals, which improves the correct detection probability in mobile channels imposing both fading and poor SINR conditions [3, 15, 8]. Nonetheless, we will briefly highlight the beneficial effects of additionally using MIMO in conjunction with PDI. Here we assume that the signals collected in multiple time intervals are independent in both the spatial and the time domain, which leads to a straightforward extension of the formulas to the more general scenarios of invoking MIMO. Since the final decision variable is constituted by the sum of $(P \cdot R \cdot T)$ number of independent variables according to $Z_{tot} = \sum_{m=1}^{P}\sum_{n=1}^{R}\sum_{k=1}^{T} Z_{m,n,k}$, each of which has a PDF given by Equation. 2.24 or Equation. 2.25, we can determine the Laplace transform of each, by raising them to the $(P \cdot R \cdot T)^{th}$ power and then carrying out the inverse transform for the sake of generating the desired PDF [3].

Assuming that the number of PDI stages is T, in the case of MIMO using PDI, we arrive at

$$p_0(Z) = \frac{Z^{(PRT-1)}e^{-Z/V}}{(PRT-1)!V^{PRT}}, \tag{2.26}$$

$$p_1(Z) = \frac{Z^{(PRT-1)}e^{-Z/V_F}}{(PRT-1)!V_F^{PRT}}. \tag{2.27}$$

Using the procedures outlined above, the probability of correct detection is obtained as follows:

$$P_D = \int_{\theta}^{\infty} p_1(Z)dZ = \exp(-\frac{\theta}{V_F}) \sum_{k=0}^{(PRT-1)} \frac{(\theta/V_F)^k}{k!}. \tag{2.28}$$

Similarly, the probability of false alarm is expressed as

$$P_F = \int_{\theta}^{\infty} p_0(Z)dZ = \exp(-\frac{\theta}{V}) \sum_{k=0}^{(PRT-1)} \frac{(\theta/V)^k}{k!}, \tag{2.29}$$

where θ is a threshold value.

2.3.2.2 Direct Analysis of MC-DS-CDMA

Here we derive the PDF of the NC scheme considered for transmission over Rayleigh-faded channels in the MIMO aided MC-DS-CDMA DL by exploiting the expression of its output PDF formulated in the context of an AWGN channel, in order to further interpret the Neyman-Pearson Criterion based hypothesis testing [3, 102]. In the following subsections a method of deriving the PDF of the NC MC-DS-CDMA DL based upon the chi-square distributed random variable [18, 93] is formulated.

The transmitted signal at the ζ^{th} chip sampling instant of the desired user at the BS of both the multiple transmit antenna and multiple subcarrier aided system can be expressed as

$$S_{tot}(\zeta) = \sum_{m=1}^{P}\sum_{u=1}^{U}[\sqrt{\frac{E_c}{P}}b(\zeta)C(\zeta)w_m(\zeta)h(t-\zeta T_c)\sqrt{2}\cos(2\pi f_u t+\phi_u)], \tag{2.30}$$

where P is the number of transmit antennas, U is the number of subcarriers, $b(\zeta)$ represents the binary input data sequence assuming values of +1 or -1, $C(\zeta)$ denotes a common PN sequence having a cell-specific code-phase offset, $w_m(\zeta)$ identifies the specific Walsh code assigned to the m^{th} transmit antenna, E_c denotes the pilot signal energy per PN code chip, $h(t)$ is the impulse response of the pulse shaping filter, T_c is the chip duration, f_u is the carrier frequency of the u^{th} subcarrier and ϕ_u is the u^{th} subcarrier phase of the user's modulator. Figure 2.3 depicts the schematic diagram of the transmitter used in the MC-

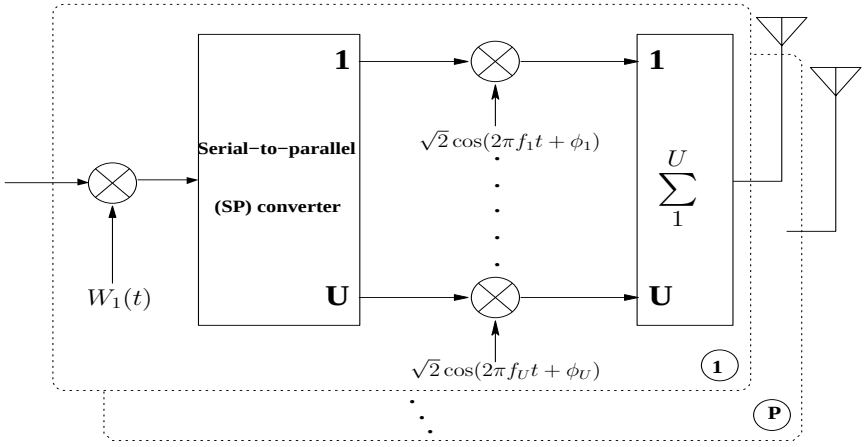

Figure 2.3: Transmitter schematic of the MC-DS-CDMA DL having both P antennas and U subcarriers.

DS-CDMA DL having both P antennas and U subcarriers, where the timing hypothesis

test is carried out for binary spreading. The total allocated power is equally shared by the P transmit antennas. The spacing of the multiple transmit antennas at the BS and the multiple receive antennas at the MS are assumed to be 10 λ and 0.5 λ, respectively. It is also assumed that the BS antennas have a high elevation. In the MC-DS-CDMA system considered the input bit sequence is Serial-to-Parallel (SP) converted and each of the parallel sequences is transmitted on a separate subcarrier. Furthermore, T_b represents the bit duration of the data sequence before SP conversion, while T_s indicates the symbol duration after SP conversion. Accordingly, we have $T_s = U{\cdot}T_b$. The spreading factor of the subcarrier signals in the MC-DS-CDMA system SF is T_s/T_c, while $SF_1 = T_b/T_{c1}$ denotes the spreading factor of T_{c1} chip duration and the corresponding SC-DS-CDMA system. For simplicity, we postulate in our forthcoming analysis that the main spectral lobes of two adjacent subcarriers do not overlap in the MC-DS-CDMA system considered [23]. Furthermore, we assume that each subcarrier signal occupies an identical bandwidth and the total bandwidth is equally divided among the U number of subcarriers. Therefore, the relationships of $T_c = U{\cdot}T_{c1}$ and $SF_1 = SF$ hold, since we have $T_s = U{\cdot}T_b$. According to the above assumption, both the MC- and the corresponding SC-DS-CDMA systems have the same bandwidth of $2/T_{c1}$, as suggested in [23], which allows their direct comparison in our forthcoming discourse. The tapped-delay line channel model generates L multi-path signals arriving with a time delay of τ_l [15, 22] in Section 2.2.1, where L is the number of multi-path signals received. Therefore, the signal $r_{tot}(\zeta)$ at receiver is a composite of L multi-path signals having a time delay of τ_l expressed in the form of

$$r_{tot}(\zeta) = \sum_{l=1}^{L}\sum_{m=1}^{P}\sum_{n=1}^{R}\sum_{u=1}^{U}[\alpha_{(l,m,n,u)}\sqrt{\frac{E_c}{P}}b(\zeta)C(\zeta)w_m(\zeta)h(t-\zeta T_c-\tau_l)\sqrt{2}\cos(2\pi f^{'}t+\phi_{(l,m,n,u)})], \tag{2.31}$$

where R is the number of receive antennas and $\alpha_{(l,m,n,u)}$ represents the envelope of the $(l,m,n,u)^{th}$ path signal obeying the Rayleigh distribution, while $f_u^{'}$ is the carrier frequency of the u^{th} subcarrier distorted by both the clock-drift-induced frequency mismatch and the Doppler shift. Furthermore, $\phi_{(l,m,n,u)}$ denotes the signal phase of the $(l,m,n,u)^{th}$ path having a uniform distribution over (0, 2π). Figure 2.4 depicts the receiver's schematic designed for our MC-DS-CDMA code acquisition scheme using MIMO. As seen in Figure2.4, we generate the decision variable by accumulating $(P{\cdot}R{\cdot}U)$ number of independently faded signals observed over a time interval to improve the correct detection probability in the mobile channel imposing both received signal fading and poor SINR conditions, where the integral dwell time represents $\tau_D = N{\cdot}T_c$ and N is defined as τ_D/T_c. Similarly, by using

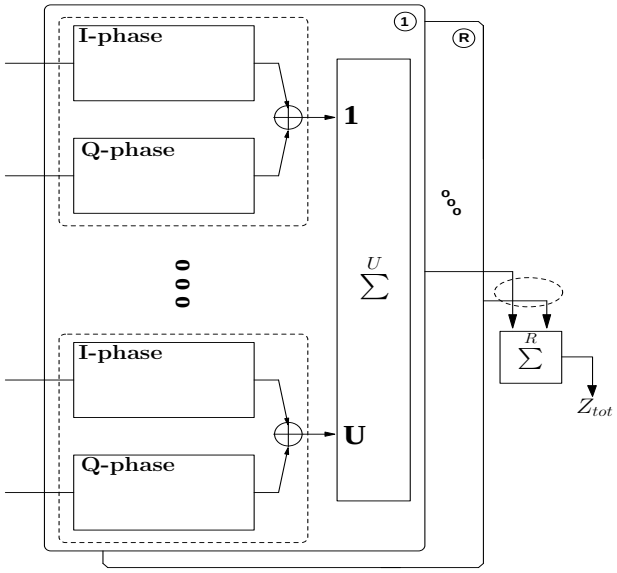

I−phase and Q−phase module:

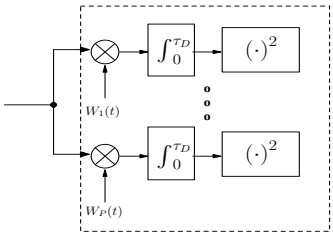

Figure 2.4: Receiver structure of NC scheme in the MIMO aided MC-DS-CDMA DL.

the procedures of the SC-DS-CDMA code acquisition scheme outlined in Section 2.3.2.1, in the case of MIMO using PDI, we arrive at

$$p_0(Z) = \frac{Z^{(PRUT-1)}e^{-Z/V}}{(PRUT-1)!V^{PRUT}}, \tag{2.32}$$

$$p_1(Z) = \frac{Z^{(PRUT-1)}e^{-Z/V_F}}{(PRUT-1)!V_F^{PRUT}}. \tag{2.33}$$

The probability of correct detection is obtained as follows:

$$P_D = \int_{\theta}^{\infty} p_1(Z)dZ = \exp(-\frac{\theta}{V_F}) \sum_{k=0}^{(PRUT-1)} \frac{(\theta/V_F)^k}{k!}. \tag{2.34}$$

Similarly, the probability of false alarm is expressed as

$$P_F = \int_{\theta}^{\infty} p_0(Z)dZ = \exp(-\frac{\theta}{V}) \sum_{k=0}^{(PRUT-1)} \frac{(\theta/V)^k}{k!}, \tag{2.35}$$

where θ is a threshold value.

It is worth noting that the PN sequence' chip duration T_{c1} for the SC-DS-CDMA system is U times lower than that of the MC-DS-CDMA arrangement, namely we have $T_{c1} = T_c/U$. This is because given the same allocated bandwidth and the same total transmitted energy per chip, the bandwidth of the SC-DS-CDMA signal is U times higher than that of the subcarrier signals in the MC-DS-CDMA system using U subcarriers. Moreover, for the sake of maintaining a constant integral dwell time of τ_D, the chip energy accumulated by the SC-DS-CDMA receiver during the period of τ_D is U times higher than that collected by the MC-DS-CDMA correlator of each subcarrier, since the number of chips within the period of τ_D is U times higher for the SC-DS-CDMA system than that of the MC-DS-CDMA system [23]. Finally, it is also worth mentioning that for SC-DS-CDMA, the coherent integration interval of N chip durations in the above formula should be substituted by $N_1 = NU$, since in this scenario $N_1 = \tau_D/T_{c1} = NU$ indicates the number of chips accumulated within the integral dwell time τ_D.

2.3.2.3 PDF Based Approach in SC-DS-CDMA

The signal transmitted by the BS having P transmit antennas can be expressed as

$$S_{tot}(t) = \sum_{m=1}^{P} [\sqrt{\frac{E_c}{PT_c}}\, b(t)\; C(t)\; w_m(t) \cdot \exp(2\pi ft + \phi)], \tag{2.36}$$

where we have P, which indicates the number of transmit antennas, $b(t)$ represents the pilot data sequence assuming a value of binary '1' [3], $C(t)$ denotes a common PN sequence having a cell-specific code-phase offset, $w_m(t)$ identifies the specific Walsh code assigned to the m^{th} transmit antenna, E_c denotes the pilot signal energy per PN code chip, T_c indicates the chip duration, f is the carrier frequency and ϕ is the carrier phase of a specific user's modulator. The signal of the MIMO-aided NC DS-CDMA DL received over the multi-path Rayleigh fading channel in Section 2.3.1 may be expressed as

$$r_{tot}(t) = \sum_{l=1}^{L}\sum_{m=1}^{P}\sum_{n=1}^{R}[\alpha_{(l,m,n)}\sqrt{\frac{E_c}{PT_c}}\, b(t+dT_c+\tau_l)\, C(t+dT_c+\tau_l)\; w_m(t+dT_c+\tau_l) \cdot \exp(2\pi f^{'} t+\phi_{(l,m,n)}) + I_{(l,m,n)}(t)], \quad (2.37)$$

where L is the number of multi-path signals received, R is the number of receive antennas, $\alpha_{(l,m,n)}$ represents the envelope of the $(l,m,n)^{th}$ path signal obeying the Rayleigh distribution, d is the code phase offset with respect to the phase of the local code, T_c is the chip duration and $f^{'}$ is the carrier frequency distorted by the clock-drift-induced frequency mismatch. Furthermore, $I_{(l,m,n)}(t)$ is the complex-valued AWGN having a double-sided power spectral density of I_0 at the $(l,m,n)^{th}$ path. Here the total allocated power is equally shared by the P transmit antennas. The spacing of the multiple transmit antennas at the BS and the multiple receive antennas at the MS are assumed to be 10 λ and 0.5 λ, respectively. It is also assumed that the BS antennas have a high elevation. The total amount of channel-induced impairments imposed on the DL is constituted by the superposition of the background noise, plus the serving-cell interference imposed by the multi-path signals and the other users as well as the other-cell interference. Further details on the calculation of the total interference may be found in [3, 15]. Figure 2.5 depicts the block diagram of the NC receiver designed for our code acquisition scheme using MIMO, which generates a decision variable by accumulating $(P \cdot R)$ number of independently faded signals observed over a time interval for the sake of improving the correct detection probability in the mobile channel imposing both received signal fading and poor SINR conditions, where the integral dwell time represents $\tau_D = N \cdot T_c$ and N is defined as τ_D/T_c and the timing hypothesis test is carried out for binary spreading.

By employing the procedures proposed in [18], the outputs of the Matched Filters (MF) are multiplied by a factor of $\frac{1}{\sqrt{2}} \cdot \sqrt{\frac{4E_c}{NI_0P}}$ in order to normalise the noise variance. In the context of the receiver structure of Figure 2.5, the final decision variable obeying the AWGN

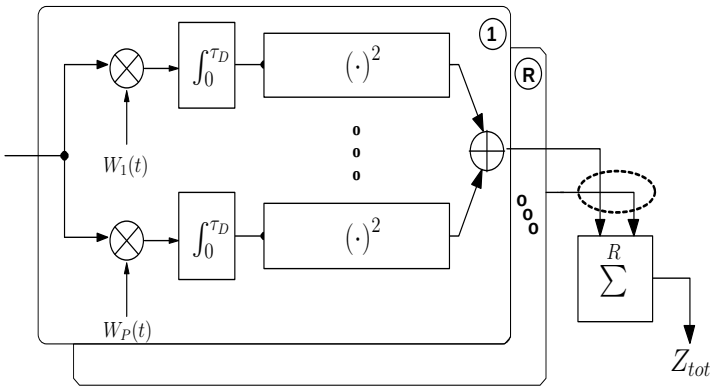

Figure 2.5: Receiver schematic of a SC-DS-CDMA code acquisition employing R receive antennas.

channel may be written as

$$Z_\zeta = \sum_{m=1}^{P}\sum_{n=1}^{R}\left\| \frac{1}{\sqrt{2}}\cdot\left(\sqrt{\frac{4E_c}{NI_0P}}\cdot S_{\zeta(m,n)} + I_{\zeta(m,n)}\right)\right\|^2, \tag{2.38}$$

where ζ denotes the ζ^{th} chip's sampling instant, $S_{\zeta(m,n)} = \frac{1}{T_c}\int_0^{NT_c} c(t)c(t+dT_c+kT_c)\cdot exp(j2\pi N\Delta f_t)dt$. If the PN codes have ideal ACFs, where the ACF has identical side-lobes to those of maximum length shift register sequences [3], $S_{\zeta(m,n)}$ can be expressed as $N\cdot exp(j2\pi N\Delta f_t)$ for the signal being present H_1 $(x=1)$. On the other hand, in case of the signal being absent H_0 $(x=0)$, it can be shown to be $-1\cdot exp(j2\pi N\Delta f_t)$. Therefore, $S_{\zeta(m,n)}$ becomes deterministic [18], while $I_{\zeta(m,n)}$ is the complex-valued AWGN having zero means and variances of σ^2=2 for both their real and imaginary parts, as shown in [18], while $\|\cdot\|^2$ represents the Eucledian norm of the complex-valued argument in Equation 2.38. The factor of $1/\sqrt{2}$ is employed in order to normalise according to the noise variance. It is worth noting that the outputs of the squaring operation invoked for both the in-phase and the quadrature branch of $Z_{\zeta(m,n)}$ in Figure 2.5 are modelled as the square of the Gaussian random variable, respectively. Accordingly, the decision variable $Z_{\zeta(m,n)}$ of each path obeys a non-central chi-square PDF with two degrees of freedom [22] and having a non-centrality parameter of λ_x, which is either $\frac{2N}{P}(\frac{E_c}{I_0})$ for the hypothesis of the desired signal being present H_1 $(x=1)$ or $\frac{2}{NP}(\frac{E_c}{I_0})$ for it being absent H_0 $(x=0)$ [18]. This PDF is given by [93]

$$p_{Z_{\zeta(m,n)}(z|H_x)} = \frac{1}{2}\cdot exp\left[-\frac{(z+\lambda_x)}{2}\right]\cdot\mathcal{I}_0\left(\sqrt{z\cdot\lambda_x}\right), \tag{2.39}$$

where we have $z \geq 0$, $x = 0\,\text{or}\,1$ while $\mathcal{I}_0(\cdot)$ is the $zero^{th}$-order modified Bessel function. Our aim is now that of expressing the PDF of a desired user's signal at the output of the acquisition scheme conditioned on the presence of the desired signal in $p_{Z_\zeta}(z|H_x)$ derived for

transmission over a spatially uncorrelated Rayleigh channel. In this scenario E_c is multiplied by the square of the Rayleigh-distributed fading amplitude, β, which exhibits a chi-square distribution having two degrees of freedom and it is hence expressed as $p(\beta) = \frac{e^{-\beta/\sigma^2}}{\sigma^2}$, where σ^2 is the variance of the constituent Gaussian distribution. Then, the average pilot signal energy $\overline{E_c}$ per PN code chip can be expressed as $\overline{E_c} = \overline{\beta}E_c = \sigma^2 E_c$ [3]. Hence, first the PDF $p_{Z_{\zeta(m,n)}}(z|H_x, \beta)$ corresponding to β conditioned on the hypothesis of the desired signal being transmitted over an AWGN channel having this specific SINR is weighted by the probability of occurrence $p(\beta)$ of encountering β, as quantified by the PDF. The resultant product is then averaged over its legitimate range of $-\infty \sim \infty$, yielding:

$$
\begin{aligned}
p_{Z_{\zeta(m,n)}}(z|H_x) &= \int_{-\infty}^{\infty} p(\beta) \cdot p_{Z_{\zeta(m,n)}}(z|H_x, \beta) d\beta && (2.40)\\
&= \int_{0}^{\infty} \left(\frac{e^{-\beta/\sigma^2}}{\sigma^2} \right) \cdot \frac{\exp[-(z + \beta\lambda_x)/2]}{2} \cdot \mathcal{I}_0 \left(\frac{2\sqrt{\beta\lambda_x z}}{2} \right) d\beta && (2.41)\\
&= \frac{\exp[-z/(2 + \lambda_x\sigma^2)]}{(2 + \lambda_x\sigma^2)} && (2.42)\\
&\equiv \frac{\exp[-z/(2 + \overline{\lambda_x})]}{(2 + \overline{\lambda_x})}, && (2.43)
\end{aligned}
$$

where $\overline{(E_c/I_0)'}$ is defined as $\overline{(E_c/I_0)'} = \overline{(E_c/I_0)} \cdot sinc^2(\frac{\tau}{T_c}) \cdot sinc^2(N\Delta f_t T_c)$, where the second multiplicative term of this definition represents the square of the autocorrelation function of the timing error, τ, while the third multiplicative term of the definition quantifies the signal energy reduction expressed as a function of the total frequency mismatch, Δf_t after the squaring operation seen in Figure 2.5. The corresponding non-centrality parameter, $\overline{\lambda_x} \equiv \lambda_x\sigma^2$ is either $\frac{2N}{P}(\overline{\frac{E_c}{I_0}})'$ when the desired signal is deemed to be present ($x = 1$) or $\frac{2}{NP}(\overline{\frac{E_c}{I_0}})'$ when it is deemed to be absent ($x = 0$). For notational convenience we also define $\mu_x = (2 + \overline{\lambda_x})$, which physically represents a new biased non-centrality parameter. Finally, we arrive at the PDF of $Z_{\zeta(m,n)}$ conditioned on the presence of the desired signal in the form of:

$$
p_{Z_{\zeta(m,n)}}(z|H_x) = \frac{1}{\mu_x} e^{-z/\mu_x}. \tag{2.44}
$$

Assuming that the number of PDI stages is T and taking into account that the decision variables Z_ζ are constituted by the sum of $(P \cdot R \cdot T)$ number of independent variables ($Z_\zeta = \sum_{m=1}^{P} \sum_{n=1}^{R} \sum_{k=1}^{T} Z_{\zeta(m,n,k)}$), which has a PDF given by Equation. 2.44, we can determine the Laplace transform[3] of each by raising them to the $(P \cdot R \cdot T)^{th}$ power and then carrying out

[3]Performing Laplace transform generates the characteristic function of each.

the inverse transform for the sake of generating the desired PDF [3], leading to:

$$p_{Z_\zeta}(z|H_x) = \frac{z^{(PRT-1)}e^{-z/\mu_x}}{\Gamma(PRT)\cdot{\mu_x}^{PRT}}, \tag{2.45}$$

where $\Gamma(\cdot)$ is the Gamma function. In the case of MIMO using PDI, finally, the probability of correct detection corresponding to $x = 1$ is obtained as

$$P_D = \int_\theta^\infty p_{Z_\zeta}(z|H_x)dz|_{x=1} \tag{2.46}$$

$$= \exp(-\frac{\theta}{\mu_x})\cdot\sum_{k=0}^{(PRT-1)}\frac{(\theta/\mu_x)^k}{k!}|_{x=1}, \tag{2.47}$$

where θ is a threshold value. Similarly, the probability of false alarm corresponding to $x = 0$ is expressed as

$$P_F = \int_\theta^\infty p_{Z_\zeta}(z|H_x)dz|_{x=0} \tag{2.48}$$

$$= \exp(-\frac{\theta}{\mu_x})\cdot\sum_{k=0}^{(PRT-1)}\frac{(\theta/\mu_x)^k}{k!}|_{x=0}. \tag{2.49}$$

2.3.2.4 PDF Based Approach in MC-DS-CDMA

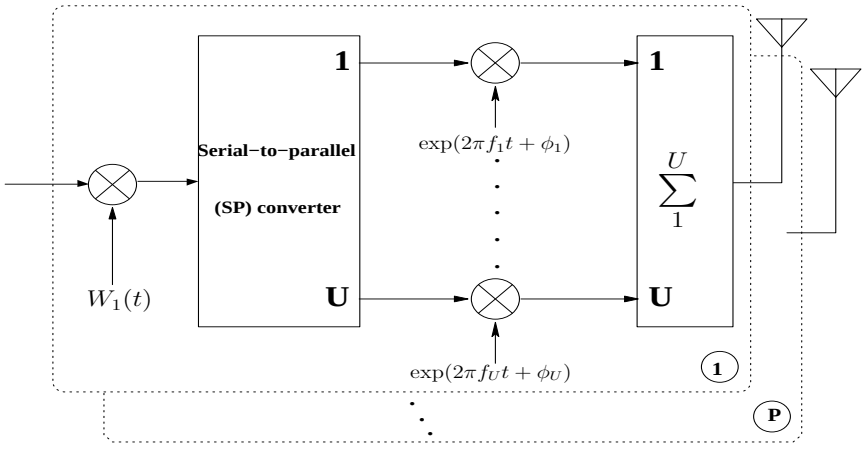

Figure 2.6: Transmitter schematic of the MC-DS-CDMA DL having both P antennas and U subcarriers.

The assumptions stipulated for the MC-DS-CDMA system considered here are exactly the same as those of Section 2.3.2.2. The signal transmitted by the BS having P transmit antennas and U subcarriers can be expressed as

$$S_{tot}(t) = \sum_{m=1}^{P}\sum_{u=1}^{U}[\sqrt{\frac{E_c}{PT_c}}\,b(t)\;C(t)\;w_m(t)\cdot\exp(2\pi f_u t + \phi_u)], \tag{2.50}$$

where P indicates the number of transmit antennas, U is the number of subcarriers, $b(t)$ represents the pilot data sequence assuming a value of binary '1' [3], $C(t)$ denotes a common PN sequence having a cell-specific code-phase offset, $w_m(t)$ identifies the specific Walsh code assigned to the m^{th} transmit antenna, E_c denotes the pilot signal energy per PN code chip, T_c indicates the chip duration, f_u is the u^{th} subcarrier frequency and ϕ_u denotes the u^{th} subcarrier phase of the modulator. Figure 2.6 depicts the schematic diagram of the transmitter used in the MC-DS-CDMA DL having both P antennas and U subcarriers. The total allocated power is equally shared by the P transmit antennas. The spacing of the multiple transmit antennas at the BS and the multiple receive antennas at the MS are assumed to be 10 λ and 0.5 λ, respectively. It is also assumed that the BS antennas have a high elevation. Further details on the calculation of the total interference may be found in [3, 15]. The signal of the MIMO-assisted MC-DS-CDMA DL received over the multi-path Rayleigh fading channel of Section 2.2.1 may be formulated as

$$r_{tot}(t) = \sum_{l=1}^{L}\sum_{m=1}^{P}\sum_{n=1}^{R}\sum_{u=1}^{U}[\alpha_{(l,m,n,u)}\sqrt{\frac{E_c}{PT_c}}\, b(t+dT_c+\tau_l)\, C(t+dT_c+\tau_l) \cdot w_m(t+dT_c+\tau_l)\exp(2\pi f_u^{'}t+\phi_{(l,m,n,u)}) + I_{(l,m,n,u)}(t)], \tag{2.51}$$

where L is the number of multi-path signals received, R is the number of receive antennas, $\alpha_{(l,m,n,u)}$ represents the envelope of the $(l,m,n,u)^{th}$ received signal path obeying the Rayleigh distribution, $f_u^{'}$ is the u^{th} subcarrier frequency distorted by the clock-drift-induced frequency mismatch, whilst d is the code phase offset with respect to the phase of the local code, while the integral dwell time is given by $\tau_D{=}N{\cdot}T_c$ and N is defined as τ_D/T_c. Furthermore, $I_{(l,m,n,u)}(t)$ is the complex-valued AWGN having a double-sided power spectral density of I_0, which contaminates the $(l,m,n,u)^{th}$ path. The total amount of channel-induced impairments imposed on the DL is constituted by the superposition of the background noise, plus the serving-cell interference imposed by the multi-path signals and the other users as well as the other-cell interference plus the inter-subcarrier interference. Figure 2.7 depicts the receiver's schematic designed for our MC-DS-CDMA code acquisition scheme using MIMO, which generates the decision variable by accumulating $(P{\cdot}R{\cdot}U)$ number of independently faded signals observed over a time interval of τ_D.

By employing the procedures proposed in [18], the outputs of the MFs are multiplied by a factor $\frac{1}{\sqrt{2}}{\cdot}\sqrt{\frac{4E_c}{NI_0P}}$ in order to normalise the noise variance. In the context of the receiver structure of Figure 2.7, the final decision variable obeying the AWGN channel may

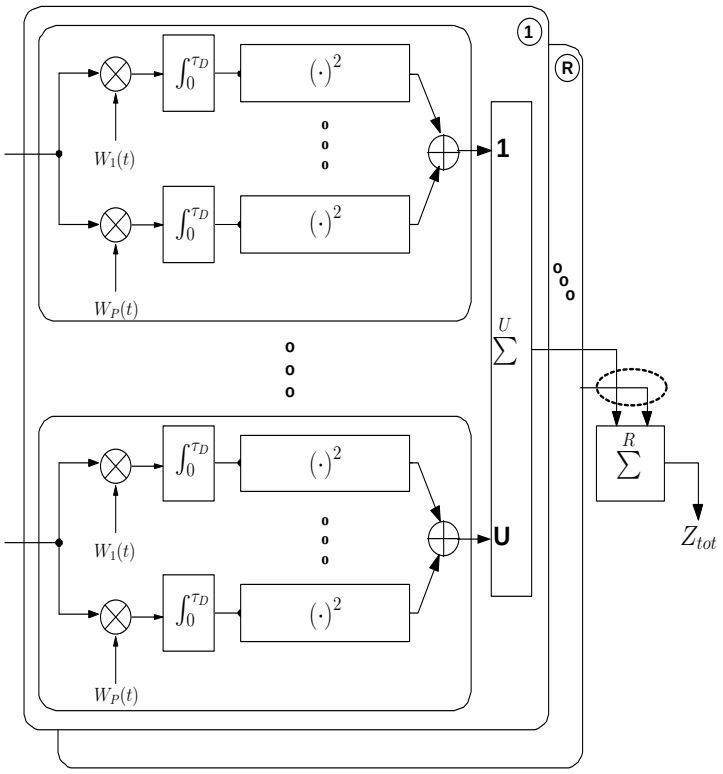

Figure 2.7: Receiver schematic of a MC-DS-CDMA code acquisition employing both R receive antennas and U subcarriers.

be expressed with the aid of the procedures suggested in [18] as follows

$$Z_\zeta = \sum_{m=1}^{P}\sum_{n=1}^{R}\sum_{u=1}^{U}\left\| \frac{1}{\sqrt{2}}\cdot\left(\sqrt{\frac{4E_c}{NI_0P}}\cdot S_{\zeta(m,n,u)} + I_{\zeta(m,n,u)}\right)\right\|^2, \tag{2.52}$$

where ζ denotes the ζ^{th} chip's sampling instant, $S_{\zeta(m,n,u)} = \frac{1}{T_c}\int_0^{NT_c} c(t)c(t+dT_c+kT_c)\cdot exp(j2\pi N\Delta f_t)dt$. If the PN codes have ideal ACFs, where the ACF has identical sidelobes to those of maximum length shift register sequences [3], $S_{\zeta(m,n,u)}$ can be expressed as $N\cdot exp(j2\pi N\Delta f_t)$ for the signal being present H_1 ($x=1$). On the other hand, in case of the signal being absent H_0 ($x=0$), it can be shown to be $-1\cdot exp(j2\pi N\Delta f_t)$. Therefore, $S_{\zeta(m,n,u)}$ becomes deterministic [18], while $I_{\zeta(m,n,u)}$ is the complex-valued AWGN having zero means and variances of σ^2=2 for both their real and imaginary parts, as shown in [18], while $\|\cdot\|^2$ represents the Eucledian norm of the complex-valued argument in Equation 2.52. The factor of $1/\sqrt{2}$ is employed in order to normalise according to the noise variance. It is worth noting that the outputs of the squaring operation invoked for both the in-phase and the quadrature branch of $Z_{\zeta(m,n,u)}$ in Figure 2.5 are modelled as the square of the Gaussian random variable, respectively. Accordingly, the decision variable $Z_{\zeta(m,n,u)}$ of each path obeys a non-central chi-square PDF with two degrees of freedom [22] and having a

non-centrality parameter of λ_x, which is either $\frac{2N}{P}(\frac{E_c}{I_0})$ for the hypothesis of the desired signal being present H_1 $(x = 1)$ or $\frac{2}{NP}(\frac{E_c}{I_0})$ for it being absent H_0 $(x = 0)$ [18]. This PDF is given by [93]

$$p_{Z_{\zeta(m,n,u)}(z|H_x)} = \frac{1}{2} \cdot exp\left[-\frac{(z + \lambda_x)}{2}\right] \cdot \mathcal{I}_0\left(\sqrt{z \cdot \lambda_x}\right), \tag{2.53}$$

where we have $z \geq 0$, $x = 0\,\text{or}\,1$, while $\mathcal{I}_0(\cdot)$ is the *zero*-order modified Bessel function. Our aim is now that of expressing the PDF of a desired user's signal at the output of the acquisition scheme conditioned on the presence of the desired signal in $p_{Z_\zeta}(z|H_x)$ derived for transmission over a spatially uncorrelated Rayleigh channel. In this scenario E_c is multiplied by the square of the Rayleigh-distributed fading amplitude, β, which exhibits a chi-square distribution having two degrees of freedom and it is hence expressed as $p(\beta) = \frac{e^{-\beta/\sigma^2}}{\sigma^2}$, where σ^2 is the variance of the constituent Gaussian distribution. Then, the average pilot signal energy $\overline{E_c}$ per PN code chip can be expressed as $\overline{E_c} = \overline{\beta} E_c = \sigma^2 E_c$ [3]. Hence, first the PDF $p_{Z_{\zeta(m,n,u)}}(z|H_x, \beta)$ corresponding to β conditioned on the hypothesis of the desired signal being transmitted over an AWGN channel having this specific SINR is weighted by the probability of occurrence $p(\beta)$ of encountering β, as quantified by the PDF. The resultant product is then averaged over its legitimate range of $-\infty \sim \infty$, yielding:

$$\begin{aligned}
p_{Z_{\zeta(m,n,u)}}(z|H_x) &= \int_{-\infty}^{\infty} p(\beta) \cdot p_{Z_{\zeta(m,n,u)}}(z|H_x, \beta) d\beta && (2.54)\\
&= \int_{0}^{\infty} \left(\frac{e^{-\beta/\sigma^2}}{\sigma^2}\right) \cdot \frac{\exp[-(z + \beta\lambda_x)/2]}{2} \cdot \mathcal{I}_0\left(\frac{2\sqrt{\beta\lambda_x z}}{2}\right) d\beta && (2.55)\\
&= \frac{\exp[-z/(2 + \lambda_x\sigma^2)]}{(2 + \lambda_x\sigma^2)} && (2.56)\\
&\equiv \frac{\exp[-z/(2 + \overline{\lambda_x})]}{(2 + \overline{\lambda_x})}, && (2.57)
\end{aligned}$$

where $\overline{(E_c/I_0)'}$ is defined as $\overline{(E_c/I_0)'} = \overline{(E_c/I_0)} \cdot sinc^2(\frac{\tau}{T_c}) \cdot sinc^2(N\Delta f_t T_c)$, where the second multiplicative term of this definition represents the square of the autocorrelation function of the timing error, τ, while the third multiplicative term of the definition quantifies the signal energy reduction expressed as a function of the total frequency mismatch, Δf_t after the squaring operation seen in Figure 2.5. The corresponding non-centrality parameter of $\overline{\lambda_x} \equiv \lambda_x\sigma^2$ is either $\frac{2N}{P}(\overline{\frac{E_c}{I_0}})'$ for the hypothesis of the desired signal being present H_1 $(x = 1)$ or $\frac{2}{NP}(\overline{\frac{E_c}{I_0}})'$ for it being absent H_0 $(x = 0)$. For notational convenience we also define $\mu_x = (2 + \overline{\lambda_x})$, which physically represents a new biased non-centrality parameter. Finally, we arrive at the PDF of $Z_{k(m,n,u)}$ conditioned on the presence of the desired signal

in the form of:

$$p_{Z_{\zeta(m,n,u)}}(z|H_x) = \frac{1}{\mu_x} e^{-z/\mu_x}. \tag{2.58}$$

Assuming that the number of PDI stages is T, since the decision variable Z_ζ is constituted by the sum of $(P{\cdot}R{\cdot}U{\cdot}T)$ number of independent variables $(Z_\zeta = \sum_{m=1}^{P}\sum_{n=1}^{R}\sum_{u=1}^{U}\sum_{k=1}^{T} Z_{\zeta(m,n,u,k)})$, which has a PDF given by Equation. 2.58, we can derive the Laplace transform of each by raising them to the $(P{\cdot}R{\cdot}U{\cdot}T)^{th}$ power and then performing the inverse transform in order to generate the resultant PDF [3], leading to:

$$p_{Z_\zeta}(z|H_x) = \frac{z^{(PRUT-1)} e^{-z/\mu_x}}{\Gamma(PRUT){\cdot}{\mu_x}^{PRUT}}, \tag{2.59}$$

where $\Gamma(\cdot)$ is the Gamma function. In the case of MIMO using PDI, finally, the probability of correct detection corresponding to $x = 1$ is obtained as

$$P_D = \int_\theta^\infty p_{Z_\zeta}(z|H_x)dz|_{x=1} \tag{2.60}$$

$$= \exp(-\frac{\theta}{\mu_x}) \cdot \sum_{k=0}^{(PRUT-1)} \frac{(\theta/\mu_x)^k}{k!}|_{x=1}, \tag{2.61}$$

where θ is a threshold value. Similarly, the probability of false alarm corresponding to $x = 0$ is expressed as

$$P_F = \int_\theta^\infty p_{Z_\zeta}(z|H_x)dz|_{x=0} \tag{2.62}$$

$$= \exp(-\frac{\theta}{\mu_x}) \cdot \sum_{k=0}^{(PRUT-1)} \frac{(\theta/\mu_x)^k}{k!}|_{x=0}. \tag{2.63}$$

2.3.3 PDF of Co-located MIMO Aided DC Code Acquisition Scheme

2.3.3.1 PDF Based Approach in SC-DS-CDMA

The transmitted signal of the BS having P transmit antennas can be expressed as

$$S_{tot}(t) = \sum_{m=1}^{P} [\sqrt{\frac{E_c}{PT_c}}\, b(t)\; C(t)\; w_m(t) \cdot \exp(2\pi f t + \phi)], \tag{2.64}$$

where P indicates the number of transmit antennas, $b(t)$ represents the pilot data sequence assuming a value of binary '1' [3], $C(t)$ denotes a common PN sequence having a cell-specific code-phase offset, $w_m(t)$ identifies the specific Walsh code assigned to the m^{th} transmit antenna, E_c denotes the pilot signal energy per PN code chip, T_c indicates the chip duration, f is the carrier frequency and ϕ is the carrier phase of a specific user's

modulator. The signal of the MIMO-aided DS-CDMA DL received over the multi-path Rayleigh fading channel considered in Section 2.2.1 may be expressed as [18]

$$r_{tot}(t) = \sum_{l=1}^{L}\sum_{m=1}^{P}\sum_{n=1}^{R}[\alpha_{(l,m,n)}\sqrt{\frac{E_c}{PT_c}}\, b(t+dT_c+\tau_l)\, C(t+dT_c+\tau_l)\; w_m(t+dT_c+\tau_l) \cdot \exp(2\pi f^{'} t+\phi_{(l,m,n)}) + I_{(l,m,n)}(t)], \quad (2.65)$$

where L is the number of multi-path signals received, R is the number of receive antennas, $\alpha_{(l,m,n)}$ represents the complex-valued envelope of the $(l,m,n)^{th}$ signal path obeying the Rayleigh distribution, d is the code phase offset with respect to the phase of the local code, $f^{'}$ is the carrier frequency distorted by the clock-drift-induced frequency mismatch. Furthermore, $I_{(l,m,n)}(t)$ is the complex-valued AWGN having a double-sided power spectral density of I_0 at the $(l,m,n)^{th}$ path. Here the total allocated power is equally shared by the P transmit antennas. The spacing of the multiple transmit antennas at the BS and the multiple receive antennas at the MS are assumed to be 10 λ and 0.5 λ, respectively. It is also assumed that the BS antennas have a high elevation. The total amount of channel-induced impairments imposed on the DL is constituted by the superposition of the background noise, plus the serving-cell interference imposed by the multi-path signals and the other users as well as the other-cell interference. Further details on the calculation of the total interference may be found in [3, 15]. Figure 2.8 portrays the Differentially Coherent (DC) receiver's schematic designed for our code acquisition scheme using MIMO, where the timing hypothesis test is carried out for binary spreading. In the DC scheme of Figure 2.8, instead of squaring the summed energy as suggested by the procedures outlined in Section 2.3.2, the channel's output samples accumulated over a full spreading code period are multiplied by the conjugate of the N-chip-delayed samples [17, 18] and the integral dwell time is represented by $\tau_D = N{\cdot}T_c$, whilst N is defined as τ_D/T_c. A decision variable is generated by accumulating $(P{\cdot}R)$ number of independently faded received signals observed over a time interval for the sake of improving the correct detection probability in the mobile channel imposing both received signal fading and poor SINR conditions.

By employing the procedures proposed in [18], the outputs of the MFs are multiplied by a factor of $\sqrt{\frac{4E_c}{NI_0P}}$ in order to normalise the noise variance. The output r_ζ^{MF} of the MF assigned to each path is as follows:

$$r_\zeta^{MF} = \sqrt{\frac{4E_c}{NI_0P}} S_{\zeta(m,n)} e^{(j\phi_{(m,n)})} + I_{\zeta(m,n)}, \quad (2.66)$$

where ζ denotes the ζ^{th} chip's sampling instant, $S_{\zeta(m,n)} = \frac{1}{T_c}\int_0^{NT_c} C(t){\cdot}C(t+dT_c+\zeta T_c)dt$ and $I_{\zeta(m,n)} = \sqrt{\frac{4}{NI_0T_c}}\int_0^{NT_c} C(t){\cdot}I(t+\zeta T_c)dt$. Both $I_{\zeta(m,n)}$ and $I_{\zeta-N(m,n)}$ are independent

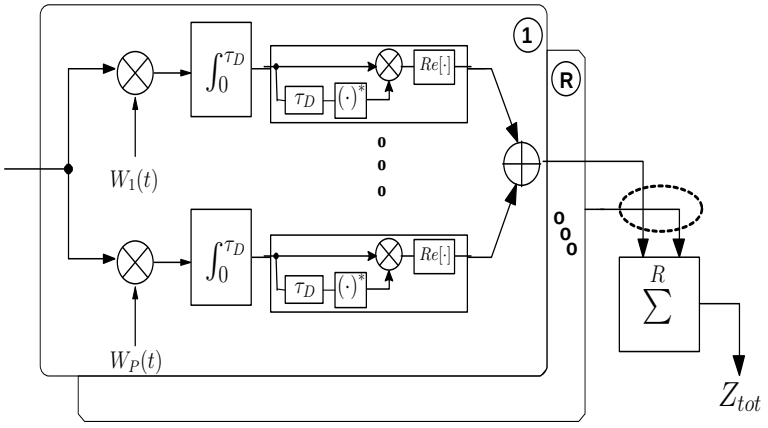

Figure 2.8: DC receiver schematic of a SC-DS-CDMA code acquisition employing R receive antennas.

complex-valued Gaussian random variables with zero means and variances of 2 for both their real and imaginary parts [18]. Here we assume that the autocorrelation function of the spreading sequences is the same as those of the sequences generated by maximum length shift register [3]. The value of $S_{\zeta(m,n)}$ is either N for the hypothesis of the desired signal being present H_1 ($x = 1$) or -1 for it being absent H_0 ($x = 0$). Therefore both $S_{\zeta(m,n)}$ and $S_{(\zeta-N)(m,n)}$ are considered to be a deterministic value, which depends on whether a signal is present or absent [18]. For notational simplicity we omit the subscripts of S, I and W. The decision variable Z_ζ, which is constituted by the real part of $(r_\zeta^{MF} \cdot {r_{(\zeta-N)}^{MF}}^*)$ might be expressed as

$$Z_\zeta = Re[(\sqrt{\frac{4E_c}{NI_0P}} S_\zeta e^{(j\phi)} + I_\zeta) \cdot (\sqrt{\frac{4E_c}{NI_0P}} S_{(\zeta-N)} e^{(j\phi)} + I_{(\zeta-N)})^*]. \tag{2.67}$$

By absorbing the multiplicative factor of $e^{(j\phi)}$ in the complex noise components, S_ζ is simplified to

$$Z_\zeta = (\sqrt{\frac{4E_c}{NI_0P}} S_\zeta + I_\zeta^{(r)}) \cdot (\sqrt{\frac{4E_c}{NI_0P}} S_{(\zeta-N)} + I_{(\zeta-N)}^{(r)}) + I_\zeta^{(\dot{\imath})} I_{(\zeta-N)}^{(\dot{\imath})} \tag{2.68}$$

Equation.2.68 may also be rewritten as

$$Z_\zeta = [\sqrt{\frac{4E_c}{NI_0P}} S_\zeta + W_{1,\zeta}]^2 + W_{3,\zeta}^2] - [W_{2,\zeta}^2 + W_{4,\zeta}^2], \tag{2.69}$$

where we have $I_\zeta^{(r)} = Re(I_\zeta)$, $I_\zeta^{(\dot{\imath})} = Im(I_\zeta)$, $I_{(\zeta-N)}^{(r)} = Re(I_{(\zeta-N)})$, $I_{(\zeta-N)}^{(\dot{\imath})} = Im(I_{(\zeta-N)})$, $W_{1,\zeta} = \frac{1}{2}(I_\zeta^{(r)} + I_{(\zeta-N)}^{(r)})$, $W_{2,\zeta} = \frac{1}{2}(I_\zeta^{(r)} - I_{(\zeta-N)}^{(r)})$, $W_{3,\zeta} = \frac{1}{2}(I_\zeta^{(\dot{\imath})} + I_{(\zeta-N)}^{(\dot{\imath})})$ and $W_{4,\zeta} = \frac{1}{2}(I_\zeta^{(\dot{\imath})} - I_{(\zeta-N)}^{(\dot{\imath})})$. Then, in the context of the DC receiver structure of Figure 2.8 employing MIMO, the final DC decision variable obeying the AWGN channel may be written as [18]

$$Z_\zeta^{dc} = \sum_{m=1}^{P} \sum_{n=1}^{R} [(\sqrt{\frac{4E_c}{NI_0P}} \cdot S_{\zeta(m,n)} + W_{1,\zeta(m,n)})^2 \tag{2.70}$$

$$+W^2_{3,\zeta(m,n)}] - \sum_{m=1}^{P}\sum_{n=1}^{R}[W^2_{2,\zeta(m,n)} + W^2_{4,\zeta(m,n)}],$$

where $S_{\zeta(m,n)}$ is assumed to be deterministic [18] and the definition of $W_{1,\zeta(m,n)}$, $W_{2,\zeta(m,n)}$, $W_{3,\zeta(m,n)}$ and $W_{4,\zeta(m,n)}$ is also the same as in [18], which are mutually independent Gaussian random variables having zero means and unit variances [18]. Let us now introduce a shorthand for the first and second terms of Equation. 2.70 as follows:

$$X_\zeta = \sum_{m=1}^{P}\sum_{n=1}^{R}[(\sqrt{\frac{4E_c}{NI_0P}}\cdot S_{\zeta(m,n)} + W_{1,\zeta(m,n)})^2 + W^2_{3,\zeta(m,n)}] \tag{2.71}$$

and

$$Y_\zeta = \sum_{m=1}^{P}\sum_{n=1}^{R}\left[W^2_{2,\zeta(m,n)} + W^2_{4,\zeta(m,n)}\right]. \tag{2.72}$$

Then the final decision variable of Equation.2.70 is obtained as $Z^{dc}_\zeta = X_\zeta - Y_\zeta$ $= \sum_{m=1}^{P}\sum_{n=1}^{R} X_{\zeta(m,n)} - \sum_{m=1}^{P}\sum_{n=1}^{R} Y_{\zeta(m,n)}$, where X_ζ obeys a noncentral chi-square PDF with $(2P\cdot R)$ degrees of freedom and having a non-centrality parameter of λ_x, which is either $\frac{4N}{P}(\frac{E_c}{I_0})'$, when the desired signal is deemed to be present ($x=1$) or $\frac{4}{NP}(\frac{E_c}{I_0})'$, when it is deemed to be absent ($x=0$) [18]. The effects of both timing errors and the total frequency mismatches are encapsulated by the definition of $(E_c/I_0)'$. In the spirit of [3], $(E_c/I_0)'$ is defined as $(E_c/I_0)' = (E_c/I_0)\cdot sinc^2(\frac{\tau}{T_c})\cdot sinc^2(N\Delta f_t T_c)$, where the second term of the definition is the square of the autocorrelation function imposed on the timing error, τ, the third term of the definition is the signal energy reduction expressed as a function of the total frequency mismatch, Δf_t after the squaring operation and N represents the number of chips accumulated over the duration of τ_D. Finally, Y_ζ is centrally chi-square distributed with $2P\cdot R$ degrees of freedom. It is also worth noting that the outputs of the squaring operation invoked for both the in-phase and the quadrature branches in Figure 2.8 are modelled as squares of Gaussian random variables, respectively. Accordingly, the decision variable $X_{\zeta(m,n)}$ of each path obeys a non-central chi-square PDF with two degrees of freedom [22], whereas $Y_{\zeta(m,n)}$ is centrally chi-square distributed with two degrees of freedom. These PDFs are given by [93] as follows:

$$p_{X_{\zeta(m,n)}}(z|H_x) = \frac{1}{2}\cdot exp\left[-\frac{(z+\lambda_x)}{2}\right]\cdot \mathcal{I}_0\left(\sqrt{z\cdot\lambda_x}\right), \tag{2.73}$$

and

$$p_{Y_{\zeta(m,n)}}(z|H_x) = \frac{1}{2}\cdot exp\left[-\frac{z}{2}\right], \tag{2.74}$$

respectively, where $z \geq 0$, $x = 0\,\text{or}\,1$, $\mathcal{I}_0(\cdot)$ is the *zero*-order modified Bessel function of the first kind. Let us now express the PDF of the desired user's signal at the output of the

DC acquisition scheme conditioned on the presence of the desired signal in $p_{X_{\zeta(m,n)}}(z|H_x)$, when communicating over a spatially uncorrelated Rayleigh channel. In this scenario E_c is multiplied by the square of the Rayleigh-distributed fading amplitude, namely β, which exhibits a chi-square distribution having two degrees of freedom and it is hence expressed as $p(\beta) = \frac{e^{-\beta/\sigma^2}}{\sigma^2}$, where σ^2 is the variance of the constituent Gaussian distribution. Then the average pilot signal energy $\overline{E_c}$ per PN code chip can be expressed as $\overline{E_c} = \overline{\beta}E_c = \sigma^2 E_c$ [3]. Therefore first the PDF $p_{Z_{\zeta(m,n)}}(z|H_x, \beta)$ corresponding to β conditioned on the hypothesis of the desired signal being transmitted over an AWGN channel having this specific SINR is weighted by the probability of occurrence $p(\beta)$ of encountering β, as quantified by the PDF. The resultant product is then averaged over its legitimate range of $-\infty \sim \infty$, yielding:

$$
\begin{aligned}
p_{X_{\zeta(m,n)}}(z|H_x) &= \int_{-\infty}^{\infty} p(\beta) \cdot p_{X_{\zeta(m,n)}}(z|H_x, \beta) d\beta && (2.75)\\
&= \int_{0}^{\infty} \left(\frac{e^{-\beta/\sigma^2}}{\sigma^2} \right) \cdot \frac{\exp[-(z + \beta\lambda_x)/2]}{2} \cdot \mathcal{I}_0 \left(\frac{2\sqrt{\beta\lambda_x z}}{2} \right) d\beta && (2.76)\\
&= \frac{\exp[-z/(2 + \lambda_x\sigma^2)]}{(2 + \lambda_x\sigma^2)} && (2.77)\\
&\equiv \frac{\exp[-z/(2 + \overline{\lambda_x})]}{\left(2 + \overline{\lambda_x}\right)}, && (2.78)
\end{aligned}
$$

where the corresponding non-centrality parameter of $\overline{\lambda_x} \equiv \lambda_x\sigma^2$ is either $\frac{4N}{P}(\frac{\overline{E_c}}{I_0})'$ when the desired signal is deemed to be present ($x = 1$) or $\frac{4}{NP}(\frac{\overline{E_c}}{I_0})'$ when it is deemed to be absent ($x = 0$). For notational convenience we also define a new biased non-centrality parameter $\mu_x = (2 + \overline{\lambda_x})$. Further details on the related calculations are found in [3, 18]. Finally, we arrive at the PDF of $X_{\zeta(m,n)}$ conditioned on the presence of the desired signal in the form of:

$$
p_{X_{\zeta(m,n)}}(z|H_x) = \frac{1}{\mu_x} e^{-z/\mu_x}. \tag{2.79}
$$

By contrast, the PDF of $p_{Y_{\zeta(m,n)}}(z|H_x)$ may be readily derived from Equation. 2.74, yielding

$$
p_{Y_{\zeta(m,n)}}(z|H_x) = \frac{1}{2} e^{-z/2}. \tag{2.80}
$$

The decision variables, X_ζ and Y_ζ are constituted by the sum of $(P{\cdot}R)$ number of independent variables ($X_\zeta = \sum_{m=1}^{P}\sum_{n=1}^{R} X_{\zeta(m,n)}$ and $Y_\zeta = \sum_{m=1}^{P}\sum_{n=1}^{R} Y_{\zeta(m,n)}$), each of which has a PDF given by Equation. 2.79 or Equation. 2.80, respectively. Both decision variables constitute independent Gamma variables, as mentioned in [3], leading to:

$$
p_{X_\zeta}(z|H_x) = \frac{z^{(PR-1)} e^{-z/\mu_x}}{\Gamma(PR) \cdot {\mu_x}^{PR}}, \tag{2.81}
$$

$$p_{Y_\zeta}(z|H_x) = \frac{z^{(PR-1)}e^{-z/2}}{\Gamma(PR)\cdot 2^{PR}}, \tag{2.82}$$

where we have $X_{tot}\sim g(P\cdot R, \mu_x)$ and $Y_{tot}\sim g(P\cdot R, 2)$. This short-hand indicates that both X_{tot} and Y_{tot} follow a Gamma distribution having the shape parameter of $(P\cdot R)$ and a scale parameter of either μ_x or 2, respectively, as outlined in [104]. Then, the PDF of $Z_\zeta^{dc} = X_\zeta - Y_\zeta$ can be computed by straightforward convolution of the PDFs of both X_ζ and Y_ζ, which results in the PDF of the difference between two independent Gamma variables. The convolution of the PDFs p_{X_ζ} and p_{Y_ζ} derived for calculating the PDF of Z_ζ^{dc} conditioned on the desired signal being present H_1 or absent H_0 is formulated as [104]:

$$p_{Z_\zeta^{dc}}(z|H_x) = \int_{-\infty}^{\infty} p_{X_\zeta}(\xi)\cdot p_{Y_\zeta}(\xi - z)d\xi \tag{2.83}$$

$$= \left(\frac{(1-c^2)^{a+\frac{1}{2}}\cdot|z|^a}{\sqrt{\pi}\cdot 2^a\cdot b^{a+1}\cdot\Gamma(a+\frac{1}{2})}\right)\cdot\exp(-\frac{c}{b}z)\cdot K_a\left(\frac{|z|}{b}\right), z\neq 0, \tag{2.84}$$

where $K_a(\cdot)$ is the modified Bessel function of the second kind and of order a. We note furthermore that $K_a(\cdot)$ is undefined, when the argument is equal to zero. However, this fact has a negligible impact on calculating the probability of correct detection and false alarm. Further details on the associated statements are detailed in [104]. Let us now define the following three parameters, namely $a = P\cdot R - 0.5$, $b = (4\mu_x)/(\mu_x + 2)$ and $c = -(\mu_x - 2)/(\mu_x + 2)$, which allow us to express the probability of correct detection according to $x = 1$, as follows [104]:

$$P_D^{dc} = \int_\theta^\infty p_{Z_\zeta^{dc}}(z|H_x)dz|_{x=1},\ \theta\neq 0, \tag{2.85}$$

where θ is a threshold value. Finally, the false alarm probability in the context of a H_0 hypothesis is expressed as

$$P_F^{dc} = \int_\theta^\infty p_{Z_\zeta^{dc}}(z|H_0)dz|_{x=0},\ \theta\neq 0. \tag{2.86}$$

2.3.3.2 PDF Based Approach in MC-DS-CDMA

The signal transmitted by the BS having P transmit antennas and U subcarriers can be expressed as

$$S_{tot}(t) = \sum_{m=1}^{P}\sum_{u=1}^{U}[\sqrt{\frac{E_c}{PT_c}}\,b(t)\ C(t)\ w_m(t)\cdot\exp(2\pi f_u t + \phi_u)], \tag{2.87}$$

where P denotes the number of transmit antennas, U indicates the number of subcarriers, $b(t)$ represents the pilot data sequence assuming a value of binary '1' [3], $C(t)$ is a common

PN sequence having a cell-specific code-phase offset, $w_m(t)$ identifies the specific Walsh code assigned to the m^{th} transmit antenna, E_c represents the pilot signal energy per PN code chip, T_c denotes the chip duration, f_u denotes the u^{th} subcarrier frequency, and ϕ_u is the u^{th} subcarrier phase of the modulator. Figure 2.9 depicts the schematic diagram of the transmitter used in the MC-DS-CDMA DL having both P antennas and U subcarriers. The total allocated power is equally shared by the P transmit antennas. The spacing of the multiple transmit antennas at the BS and the multiple receive antennas at the MS are assumed to be 10 λ and 0.5 λ, respectively. It is also assumed that the BS antennas have a high elevation.

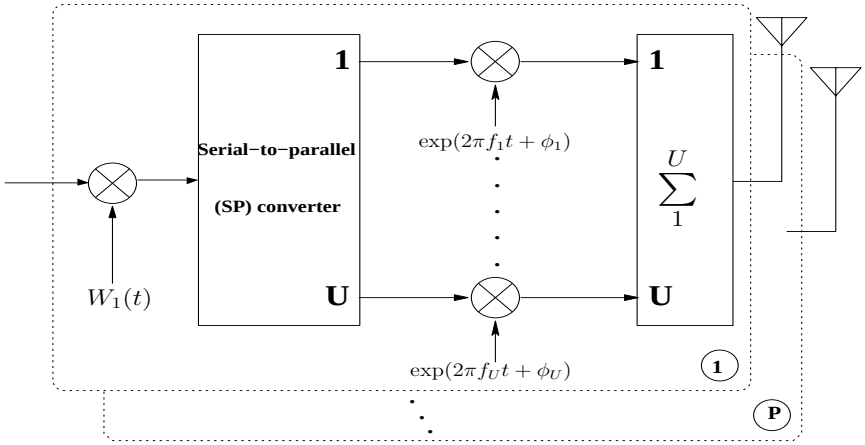

Figure 2.9: Transmitter schematic of the MC-DS-CDMA DL having both P antennas and U subcarriers.

The received signal of the MIMO-assisted MC-DS-CDMA DL over the multi-path Rayleigh fading channel of Section 2.2.1 may be written as

$$r_{tot}(t) = \sum_{l=1}^{L}\sum_{m=1}^{P}\sum_{n=1}^{R}\sum_{u=1}^{U}[\alpha_{(l,m,n,u)}\sqrt{\frac{E_c}{PT_c}}\, b(t+dT_c)\; C(t+dT_c)\; w_m(t+dT_c) \cdot \exp(2\pi f_u' t + \phi_{(l,m,n,u)}) + I_{(l,m,n,u)}(t)], \tag{2.88}$$

where L is the number of multi-path signals received, R denotes the number of receive antennas, $\alpha_{(l,m,n,u)}$ is the envelope of the $(l,m,n,u)^{th}$ received signal path obeying the Rayleigh distribution, f_u' is the u^{th} subcarrier frequency distorted by the clock-drift-induced frequency mismatch, whilst d indicates the code phase offset with respect to the phase of the local code. Furthermore, $I_{(l,m,n,u)}(t)$ is the complex-valued AWGN having a double-sided power spectral density of I_0, which contaminates the $(l,m,n,u)^{th}$ path. The total amount of channel-induced impairments imposed on the DL is constituted by the superposition of the background noise, plus the serving-cell interference imposed by the multi-path signals

and the other users as well as the other-cell interference plus the inter-subcarrier interference. Further details on the calculation of the total interference may be found in [3, 15]. Figure 2.10 portrays the DC receiver's schematic designed for our MC-DS-CDMA code acquisition scheme using MIMO, which generates the decision variable by accumulating $(P{\cdot}R{\cdot}U)$ number of independently faded signals observed over a time interval, where the integral dwell time is represented by $\tau_D = N{\cdot}T_c$ and N is defined as τ_D/T_c. In the DC scheme of Figure 2.10, instead of squaring the summed energy as suggested by the procedures outlined in Section 2.3.2, the channel's output samples accumulated over a full spreading code period are multiplied by the conjugate of the N-chip-delayed samples [17, 18].

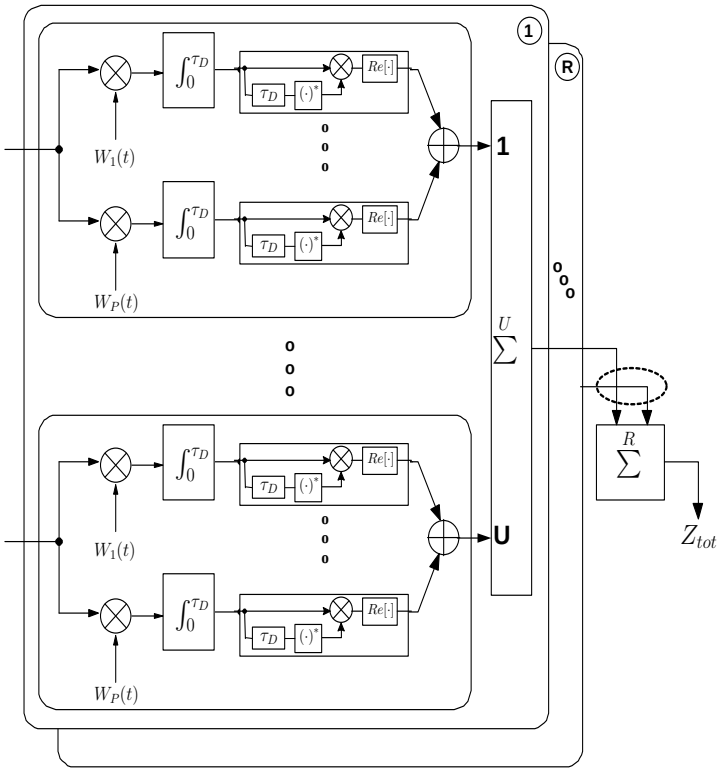

Figure 2.10: DC receiver schematic of a MC-DS-CDMA code acquisition employing both R receive antennas and U subcarriers.

Again, the decision variable is generated by accumulating $(P{\cdot}R{\cdot}U)$ number of independently faded received signals observed over a time interval of τ_D in order to improve the correct detection probability, when the mobile channel imposes both received signal fading and poor SINR conditions. Here we omitted formulating the final decision variable, which may be readily derived using the procedures proposed in the Section 2.3.3.1 in the context of the receiver structure of Figure 2.10. The final DC decision variable obeying the AWGN

may be expressed as [18]

$$Z_{\zeta}^{dc} = \sum_{m=1}^{P}\sum_{n=1}^{R}\sum_{u=1}^{U}[(\sqrt{\frac{4E_c}{NI_0P}}\cdot S_{\zeta(m,n,u)} + W_{1,\zeta(m,n,u)})^2 + W_{3,\zeta(m,n,u)}^2] - \sum_{m=1}^{P}\sum_{n=1}^{R}\sum_{u=1}^{U}\left[W_{2,\zeta(m,n,u)}^2 + W_{4,\zeta(m,n,u)}^2\right], \quad (2.89)$$

where ζ indicates the ζ^{th} chip's sampling instant, $S_{\zeta(m,n,u)}$ is assumed to be deterministic [18] and the definition of $W_{1,\zeta(m,n,u)}$, $W_{2,\zeta(m,n,u)}$, $W_{3,\zeta(m,n,u)}$ and $W_{4,\zeta(m,n,u)}$ is the same as in [18], which are mutually independent Gaussian random variables having zero means and unit variances [18]. Again, the definitions of all the symbols in Equation. 2.89 are readily inferred from Section 2.3.3.1. Let us now introduce a shorthand for the first and second terms of Equation. 2.89 as follows:

$$X_{\zeta} = \sum_{m=1}^{P}\sum_{n=1}^{R}\sum_{u=1}^{U}[(\sqrt{\frac{4E_c}{NI_0P}}\cdot S_{\zeta(m,n,u)} + W_{1,\zeta(m,n,u)})^2 + W_{3,\zeta(m,n,u)}^2] \quad (2.90)$$

and

$$Y_{\zeta} = \sum_{m=1}^{P}\sum_{n=1}^{R}\sum_{u=1}^{U}\left[W_{2,\zeta(m,n,u)}^2 + W_{4,\zeta(m,n,u)}^2\right]. \quad (2.91)$$

Then the final decision variable of Equation 2.89 is expressed as $Z_{\zeta}^{dc} = X_{\zeta} - Y_{\zeta} = \sum_{m=1}^{P}\sum_{n=1}^{R}\sum_{u=1}^{U} X_{\zeta(m,n,u)} - \sum_{m=1}^{P}\sum_{n=1}^{R}\sum_{u=1}^{U} Y_{\zeta(m,n,u)}$, where X_{ζ} is noncentrally chi-square distributed with $(2P{\cdot}R{\cdot}U)$ degrees of freedom and its non-centrality parameter λ_x is either $\frac{4N}{P}(\frac{E_c}{I_0})'$ for the hypothesis of the desired signal being present H_1 $(x=1)$ or $\frac{4}{NP}(\frac{E_c}{I_0})'$ for it being absent H_0 $(x=0)$ [18], while Y_k follows a central chi-square PDF with $(2P{\cdot}R{\cdot}U)$ degrees of freedom. The effects of both timing errors and the total frequency mismatches are encapsulated by the definition of $(E_c/I_0)'$. In the spirit of [3], $(E_c/I_0)'$ is defined as $(E_c/I_0)' = (E_c/I_0){\cdot}sinc^2(\frac{\tau}{T_c}){\cdot}sinc^2(N\Delta f_t T_c)$, where the second term of the definition is the square of the autocorrelation function imposed on the timing error, τ, the third term of the definition is the signal energy reduction expressed as a function of the total frequency mismatch, Δf_t after the squaring operation and N represents the number of chips accumulated over the duration of τ_D. Finally, Y_{ζ} is centrally chi-square distributed with $2P{\cdot}R$ degrees of freedom. It is also worth noting that the outputs of the squaring operation invoked for both the in-phase and the quadrature branches in Figure 2.10 are modelled as squares of Gaussian random variables, respectively. Accordingly, the decision variable $X_{\zeta(m,n,u)}$ of each path obeys a non-central chi-square PDF with two degrees of freedom [22], whereas $Y_{\zeta(m,n,u)}$ is centrally chi-square distributed with two degrees of freedom. These

PDFs are given by [93] as follows:

$$p_{X_{\zeta(m,n,u)}}(z|H_x) = \frac{1}{2}\cdot exp\left[-\frac{(z+\lambda_x)}{2}\right]\cdot \mathcal{I}_0\left(\sqrt{z\cdot\lambda_x}\right), \tag{2.92}$$

and

$$p_{Y_{\zeta(m,n,u)}}(z|H_x) = \frac{1}{2}\cdot exp\left[-\frac{z}{2}\right], \tag{2.93}$$

respectively, where $z \geq 0$, $x = 0\,\text{or}\,1$, $\mathcal{I}_0(\cdot)$ is the *zero*-order modified Bessel function of the first kind. Let us now express the PDF of the desired user's signal at the output of the DC acquisition scheme conditioned on the presence of the desired signal in $p_{X_{\zeta(m,n,u)}}(z|H_x)$, when communicating over a spatially uncorrelated Rayleigh channel. In this scenario E_c is multiplied by the square of the Rayleigh-distributed fading amplitude, namely β, which exhibits a chi-square distribution having two degrees of freedom and it is hence expressed as $p(\beta) = \frac{e^{-\beta/\sigma^2}}{\sigma^2}$, where σ^2 is the variance of the constituent Gaussian distribution. Then, the average pilot signal energy $\overline{E_c}$ per PN code chip can be expressed as $\overline{E_c} = \overline{\beta}E_c = \sigma^2 E_c$ [3]. Therefore, first the PDF $p_{Z_{\zeta(m,n,u)}}(z|H_x,\beta)$ corresponding to β conditioned on the hypothesis of the desired signal being transmitted over an AWGN channel having this specific SINR is weighted by the probability of occurrence $p(\beta)$ of encountering β, as quantified by the PDF. The resultant product is then averaged over its legitimate range of $-\infty \sim \infty$, yielding:

$$\begin{aligned}
p_{X_{\zeta(m,n,u)}}(z|H_x) &= \int_{-\infty}^{\infty} p(\beta)\cdot p_{X_{\zeta(m,n,u)}}(z|H_x,\beta)d\beta && (2.94)\\
&= \int_{0}^{\infty}\left(\frac{e^{-\beta/\sigma^2}}{\sigma^2}\right)\cdot\frac{\exp[-(z+\beta\lambda_x)/2]}{2}\cdot\mathcal{I}_0\left(\frac{2\sqrt{\beta\lambda_x z}}{2}\right)d\beta && (2.95)\\
&= \frac{\exp[-z/(2+\lambda_x\sigma^2)]}{(2+\lambda_x\sigma^2)} && (2.96)\\
&\equiv \frac{\exp[-z/(2+\overline{\lambda_x})]}{\left(2+\overline{\lambda_x}\right)}, && (2.97)
\end{aligned}$$

where the corresponding non-centrality parameter of $\overline{\lambda_x} \equiv \lambda_x\sigma^2$ is either $\frac{4N}{P}(\frac{\overline{E_c}}{I_0})'$ when the desired signal is deemed to be present ($x = 1$) or $\frac{4}{NP}(\frac{\overline{E_c}}{I_0})'$ when it is deemed to be absent ($x = 0$). For notational convenience we also define a new biased non-centrality parameter $\mu_x = (2+\overline{\lambda_x})$. Further details on the related derivations are provided in [3, 18]. Finally, we arrive at the PDF of $X_{\zeta(m,n,u)}$ conditioned on the presence of the desired signal in the form of:

$$p_{X_{\zeta(m,n,u)}}(z|H_x) = \frac{1}{\mu_x}e^{-z/\mu_x}. \tag{2.98}$$

By contrast, the PDF of $Y_{k(m,n,u)}$ may be readily derived from Equation. 2.93, leading to

$$p_{Y_{\zeta(m,n,u)}}(z|H_x) = \frac{1}{2}e^{-z/2}. \tag{2.99}$$

The decision variables, X_ζ and Y_ζ are expressed as the sum of $(P{\cdot}R{\cdot}U)$ number of independent variables ($X_\zeta = \sum_{m=1}^{P}\sum_{n=1}^{R}\sum_{u=1}^{U} X_{\zeta(m,n,u)}$ and $Y_\zeta = \sum_{m=1}^{P}\sum_{n=1}^{R}\sum_{u=1}^{U} Y_{\zeta(m,n,u)}$), each of which obeys a PDF given by either Equation. 2.98 or Equation. 2.99, respectively. Both decision variables constitute independent Gamma variables, as mentioned in [3], yielding:

$$p_{X_\zeta}(z|H_x) = \frac{z^{(PRU-1)}e^{-z/\mu_x}}{\Gamma(PRU)\cdot{\mu_x}^{PRU}}, \tag{2.100}$$

$$p_{Y_\zeta}(z|H_x) = \frac{z^{(PRU-1)}e^{-z/2}}{\Gamma(PRU)\cdot 2^{PRU}}. \tag{2.101}$$

Then, the PDF of $Z_\zeta^{dc} = X_\zeta - Y_\zeta$ can be calculated by straightforward convolution of the PDFs of both X_ζ and Y_ζ, which leads to the PDF of the difference between two independent Gamma variables. To elaborate a little further, we have $X_{tot}{\sim}g(P{\cdot}R{\cdot}U,\, \mu_x)$ and $Y_{tot}{\sim}g(P{\cdot}R{\cdot}U,\, 2)$, where this shorthand represents that both X_{tot} and Y_{tot} obey a Gamma distribution having the shape parameter of $(P{\cdot}R{\cdot}U)$ and the scale parameter of either μ_x or 2, respectively, as outlined in [104]. The convolution of the PDFs p_{X_ζ} and p_{Y_ζ} formulated in an effort to compute the PDF of Z_ζ^{dc} conditioned on the desired signal being present H_1 or absent H_0 is derived as [104]:

$$p_{Z_\zeta^{dc}}(z|H_x) = \int_{-\infty}^{\infty} p_{X_\zeta}(\xi)\cdot p_{Y_\zeta}(\xi - z)d\xi \tag{2.102}$$

$$= \left(\frac{(1-c^2)^{a+\frac{1}{2}}\cdot|z|^a}{\sqrt{\pi}\cdot 2^a\cdot b^{a+1}\cdot\Gamma(a+\frac{1}{2})}\right)\cdot\exp(-\frac{c}{b}z)\cdot K_a\left(\frac{|z|}{b}\right), z{\neq}0\,, \tag{2.103}$$

where $K_a(\cdot)$ indicates the modified Bessel function of the second kind and of order a. We note furthermore that $K_a(\cdot)$ is undefined, when the argument is equal to zero. However, this fact has a negligible impact on calculating the probability of correct detection and false alarm. Again, further details on the associated statements are found in [104]. Let us now define the parameters of $a = P{\cdot}R{\cdot}U - 0.5$, $b = (4\mu_x)/(\mu_x+2)$ and $c = -(\mu_x-2)/(\mu_x+2)$, which allow us to express the probability of correct detection according to $x = 1$, as follows [104]:

$$P_D^{dc} = \int_\theta^\infty p_{Z_\zeta^{dc}}(z|H_x)dz|_{x=1},\, \theta{\neq}0\,, \tag{2.104}$$

where θ is a threshold value. Finally, the false alarm probability in the context of a H_0 hypothesis is expressed as

$$P_F^{dc} = \int_\theta^\infty p_{Z_\zeta^{dc}}(z|H_0)dz|_{x=0},\, \theta{\neq}0\,. \tag{2.105}$$

In the following section both the probability of correct detection and false alarm expressions ill be exploited for creating the corresponding detection transfer functions encompassing all

branches of the relevant state diagram characterising the acquisition scheme in order to derive a formula for the MAT [3].

2.3.4 PDF of Cooperative MIMO Aided Non-Coherent Code Acquisition

2.3.4.1 PDF Based Approach for SC-DS-CDMA

The fixed Relay Station (RS)-aided DS-CDMA DL signal received over the multi-path Rayleigh fading channel considered may be expressed as [75]

$$r(t) = \sum_{p=1}^{P}\sum_{l=1}^{L}\sum_{r=1}^{R}[\alpha_{(p,l,r)}\sqrt{\frac{1}{P}}\sqrt{\frac{E_c}{T_c}}\,c(t+dT_c+\tau_p+\tau_l) \cdot w_p(t+dT_c+\tau_p+\tau_l)\cdot\exp(2\pi ft+\phi_{(p,l,r)})+I_{(p,l,r)}(t)], \tag{2.106}$$

where $p = P$ is the number of RSs and BS, $r = R$ is the number of receive antennas, and $\alpha_{(p,l,r)}$ represents the complex-valued envelope of the $(p,l,r)^{th}$ signal path obeying the Rayleigh distribution. Furthermore, E_c denotes the pilot signal energy per PN code chip, $c(t)$ represents a common PN sequence having a cell-specific code-phase offset, while d is the code phase offset with respect to the phase of the local code. Still considering Equation 2.106, $w_p(t)$ identifies the specific Walsh code assigned to the p^{th} RS, τ_p indicates the relative time difference of the signal received from a RS with respect to the signal received from the BS, f is the carrier frequency and finally, ϕ is the carrier phase of a specific user's modulator. Furthermore, $I_{(p,l,r)}(t)$ is the complex-valued AWGN having a double-sided power spectral density of I_0 at the $(p,l,r)^{th}$ path. It is also noted that in the normalised-power scenario a factor denoted as $\sqrt{\frac{1}{P}}$ must be included in Equation 2.106 due to equally sharing the total allocated power. On the other hand, this factor must be omitted in the increased-power scenario. For the sake of a fair comparison, it is assumed that in the absence of link imbalance, the total power received by the MS in RS-aided scenarios is the same as that of the corresponding multiple transmit antenna aided scenario for the normalised-power scenario. In the increased-power scenario, it is assumed that in the absence of a link imbalance, the total power received by the MS in RS-aided scenarios is the same as that of the corresponding multiple receive antenna assisted scenarios. Figure 2.11 depicts the block diagram of the non-coherent DS-CDMA DL receiver designed for our code acquisition scheme using R co-located receive antennas. The receiver generates a decision variable by accumulating R number of independently faded signals observed over a time interval for the sake of improving the P_D in the mobile channel imposing both fading and

poor SINR conditions. By employing the procedures proposed in Section 2.3.2 in the context of the receiver structure of Fig. 2.11, the final decision variable may be written as [18]

$$Z_{(k,p,l)} = \sum_{r=1}^{R} \left\| \frac{1}{\sqrt{2}} \cdot \left(\sqrt{\frac{4E_c}{NI_0}} \cdot S_{(k,p,l)(r)} + I_{(k,p,l)(r)} \right) \right\|^2, \tag{2.107}$$

where k denotes the k^{th} chip's sampling instant, $Z_{(k,p,l)}$ is a decision variable of the $(p,l)^{th}$ path, which constitutes an element of the final decision variables, $Z_1, ..., Z_P$ in Fig. 2.11, and $S_{(k,p,l)(r)} = \frac{1}{T_c} \int_0^{NT_c} c(t)c(t+dT_c+kT_c) \cdot \exp(j2\pi N\Delta f_t)dt$ as described in Section 2.3.2. If the PN codes have ideal AutoCorrelation Functions (ACFs), where the ACF has identical sidelobes to those of maximum length shift register sequences [3], $S_{(k,p,l)(r)}$ can be expressed as $N \cdot \exp(j2\pi N\Delta f_t)$ for the signal being present. On the other hand, in case of the signal being absent, it can be shown to be $-1 \cdot \exp(j2\pi N\Delta F_t)$. Therefore, $S_{(k,p,l)(r)}$ becomes deterministic [18, 75], while $I_{(k,p,l)(r)}$ is the complex-valued AWGN having zero means and variances of σ^2=2 for both their real and imaginary parts. Furthermore, $\|\cdot\|^2$ represents the Euclidean norm of the complex-valued argument and the factor of $1/\sqrt{2}$ is employed to appropriately normalise the noise variance. Accordingly, the decision variable $Z_{(k,p,l)}$ obeys a non-central chi-square PDF with $2R$ degrees of freedom, where the non-centrality parameter λ_x is either $2N(\frac{E_c}{I_0})$ for the hypothesis of the desired signal being present $(H_x, x = 1)$ or $\frac{2}{N}(\frac{E_c}{I_0})$ for it being absent $(H_x, x = 0)$ [75]. The effects of both timing errors and frequency mismatches are encapsulated by the definition of $(E_c/I_0)'$ [82] and the corresponding non-centrality parameter, $\overline{\lambda_x} \equiv \lambda_x \sigma^2$ is either $2N(\frac{\overline{E_c}}{I_0})'$ when the desired signal is deemed to be present $(x = 1)$ or $\frac{2}{N}(\frac{\overline{E_c}}{I_0})'$ when it is deemed to be absent $(x = 0)$. We also define $\mu_x = (2 + \overline{\lambda_x})$, which physically represents a new biased noncentrality parameter. Further details on the related calculations and derivations can be found in Sections 2.3.2 and 2.3.3. When using the procedures outlined in Section 2.3.2, finally, the decision variables $Z_{(k,p,l)}$ are constituted by the sum of R number of independent variables according to $Z_{(k,p,l)} = \sum_{r=1}^{R} Z_{(k,p,l)(r)}$, whilst the desired signal's PDF may be formulated using the procedure outlined in Sections 2.3.2 and 2.3.3 as:

$$f_{Z_{(k,p,l)}}(z|H_x) = \frac{z^{(R-1)} e^{-z/\mu_x}}{\Gamma(R) \cdot {\mu_x}^R}, \tag{2.108}$$

where $\Gamma(\cdot)$ is the Gamma function. Then, the P_D or P_F corresponding to $x = 1 \text{ or } 0$, respectively, may be expressed as

$$P|_{\xi=D \text{ or } F}|_{(cooperative)} = \int_{\theta}^{\infty} f_{Z_{(k,p,l)}}(z|H_x)dz \tag{2.109}$$

$$= \exp(-\frac{\theta}{\mu_x}) \cdot \sum_{r=0}^{R-1} \frac{(\theta/\mu_x)^r}{r!}, \tag{2.110}$$

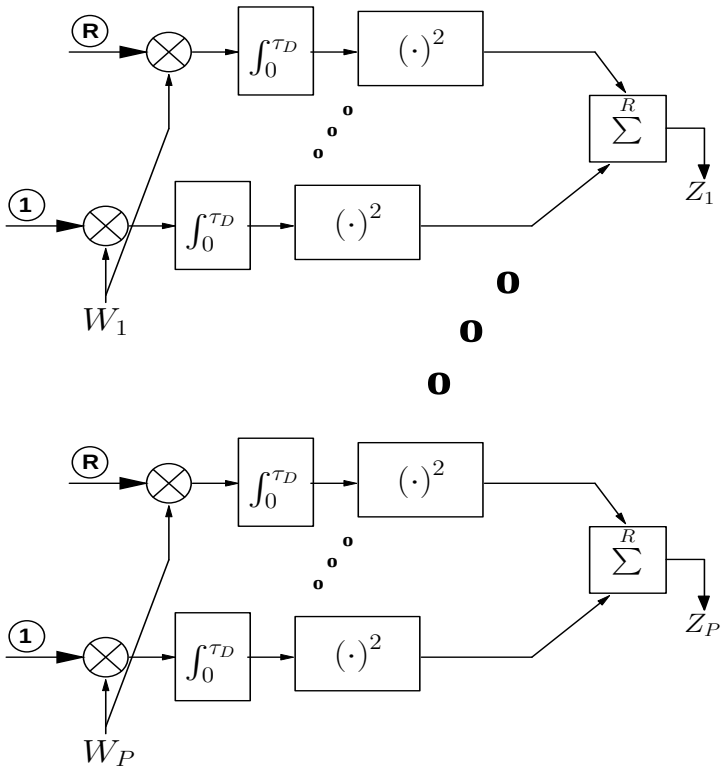

Figure 2.11: Receiver structure of a non-coherent code acquisition system employing R receive antennas in RS-aided scenarios

where θ is a threshold value. By employing Equation 2.110, the transfer functions required for calculating the achievable MAT of the fixed RS-aided scenarios considered will be derived in the forthcoming section.

2.4 Mean Acquisition Time

2.4.1 Single Dwell Serial Search for Co-located Transmission Scenario

2.4.1.1 Single-path Scenario

In [3, 14, 22], explicit Mean Acquisition Time (MAT) formulae were provided for a single-antenna aided serial search based code acquisition system. There is no procedural difference between a single-antenna aided scheme and a multiple-antenna assisted one in terms of analysing the associated MAT, except for deriving the correct detection and the false alarm probability based upon MIMO rather than a single transmit/single receive antenna. We will commence our discourse by illustrating the rudimentary concept of Section 1.4.3 in somewhat depth for the sake of augmenting the concept of Single Dwell Serial Search

(SDSS). The classic SDSS technique has been employed in scenarios, where the uncertainty region representing the search window width is quite wide. Hence in the context of SDSS the MAT is the vital performance criterion, as seen for example in the DL of the inter-cell synchronous CDMA-2000 system of [3, 15]. In this scheme, in the absence of any prior information such as a predetermined SDSS starting point, all the potential candidate code phases are serially searched, until the correct phase is determined. Determination of the correct code implies registering a sufficiently high correlator energy output exceeding a threshold value optimised in terms of the best possible MAT performance at the receiver. The associated trade-off is that a low threshold value may offer result in a high probability of exceeding the threshold owing to channel impairments or interference, which results in a so-called false alarm. In this case it takes a long time for the receiver to return to its search mode, hence substantially degrading the MAT. By contrast, an excessive threshold value results in a high miss probability, when the channel-contaminated reduced signal does not pass the correlation test. If the estimated code phase is deemed correct, despreading will be carried out. For the sake of better understanding the SDSS technique, let us introduce

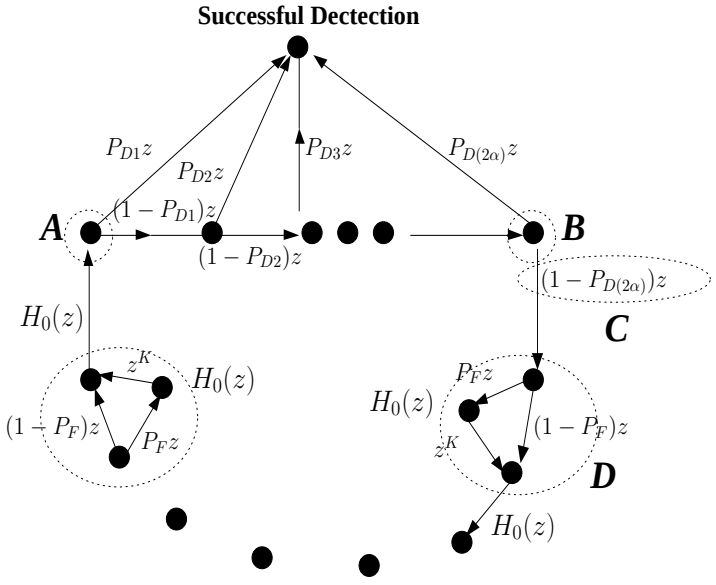

Figure 2.12: State diagram of single dwell serial search.

the circular diagram of the SDSS scheme in Figure 2.12, indicating that the code acquisition process will be repeated, when it has proceeded through all of its legitimate states (hypothesis) without attaining correct code phase acquisition.

We assume that in each chip duration T_c, α number of correct timing hypotheses are tested, which are spaced by T_c/α, and hence the total uncertainty region ν, namely the

number of phases to be tested is increased by a factor of α. [4]

All the resultant $(\nu - 2\alpha)$ states that may lead to a false alarm are expected to increase the MAT according to the corresponding penalty time, which is often assumed to be $1000 \cdot T_c$. The 2α number of legitimate locking states within a lag of one chip duration of the correct timing instant are taken into account in the MAT analysis. Combining all these 2α number of legitimate locking states into the total or accumulated correct detection transfer function, which encompasses all branches of the relevant state diagram seen in Figure 2.12 leads to the correct detection probability and the corresponding transfer function expressed as

$$H_D(z) = \sum_{j=1}^{2\alpha} P_{Dj} z \prod_{i=1}^{j-1} [(1 - P_{Di})z], \tag{2.111}$$

where P_{Dj} represents the probability of correct detection associated with testing the correlator's output for the j^{th} occasion, following $(j - 1)$ failed trials each resulting in a miss owing to the channel-impairments and where each probability of a miss in the corresponding total miss transfer function is given by $(1 - P_{Di})$. Furthermore, z indicates the unit-delay operator, where the unit-delay is determined by the time required by the correlator for testing a specific hypothesis and the exponent of z represents the time delay. Again, $H_0(z)$ in the dotted circles of Figure 2.12 denotes the probability of the desired user's signal at the output of the acquisition scheme being absent indicated by an insufficiently high correlator output or because the receiver is waiting for the penalty time to expire, which is expressed as

$$H_0(z) = (1 - P_F)z + P_F z^{K+1}, \tag{2.112}$$

where P_F represents the false alarm probability and K is the above-mentioned false locking penalty factor [3]. Finally, $H_M(z)$ represents the overall miss probability of a search run carried out across the entire uncertainty region, which may be formulated as the product of the individual miss probabilities associated with the 2α number of intervals tested, since

[4] Note 1: Let us now consider Figure 2.12 and commence other related discussions from the left-most state, namely A, of the row of 2α number of horizontally aligned states. There are α states per chip-interval, each of which has to be tested at both-sides of the current time instant. From the left-most state of Figure 2.12 we traverse to successful detection with a probability of P_{D1} and to the second of the 2α states with a probability of $(1 - P_{D1})$, etc. If we tested both the α number of dwell intervals left and right until the right-most state, namely B, and failed to satisfy the correlation threshold, the acquisition scheme traverses to state C of Figure 2.12 with a probability of $(1 - P_{D(2\alpha)})$. Since no acquisition success was declared so far, at this stage two more legitimate events have to be considered, namely either the false alarm event having a probability of P_F or the absence of false alarm having a probability of $(1 - P_F)$. Given that no successful detection or no false alarm took place or -alternatively- false alarm was encountered, the only conclusion that may be drawn is that the desired user's signal is indeed absent or it is deemed to be absent owing to interference and other channel impairments, leading to state D in Figure 2.12. The probability of the desired user being absent is denoted by $H_0(Z)$ and graphically portrayed in Figure 2.12. The acquisition scheme traverses an indefinite number of these desired user is absent states, until eventually assumes state A again.

these may be considered independent events, yielding

$$H_M(z) = z^{2\alpha} \prod_{j=1}^{2\alpha} (1 - P_{Dj}). \tag{2.113}$$

The above-mentioned three transfer functions of Equations. 2.111, 2.112 and 2.113 apply to all cases, except for the branches of Figure 2.12 emerging from the specific nodes at all the resultant 2α number of states of the diagram, which connect to the final correct destination node. Then the transfer function characterising the transition from an initial mode that is i branches down counterclockwise from the top of Figure 2.12 to the final correct destination mode is derived as follows:

$$\begin{aligned} U_i(z) &= H_0^i(z)H_D(z) + H_0^i(z)H_M(z)H_0^{(\nu-2\alpha)}(z)H_D(z) + H_0^i(z)H_M^2[H_0^{(\nu-2\alpha)}(z)]^2 H_D(z) + ... \\ &= H_0^i(z)H_M(z)\{1 + H_M(z)H_0^{(\nu-2\alpha)}(z) + [H_M(z)H_0^{(\nu-2\alpha)}(z)]^2 + ...\}. \end{aligned} \tag{2.114}$$

Then, following further manipulation, the final transfer function is obtained as

$$U_i(z) = \frac{H_0^i(z)H_D(z)}{[1 - H_M(z)H_0^{(\nu-2\alpha)}(z)]}. \tag{2.115}$$

Since all the nodes seen in Figure 2.12 are a priori equally likely, the resultant transfer function averaged over all the $(\nu - 2\alpha)$ root-nodes or starting-nodes becomes [3]

$$U(z) = \frac{1}{(\nu - 2\alpha)} \sum_{i=1}^{(\nu-2\alpha)} U_i(z) = \frac{H_D(z)H_0(z)[1 - H_0^{(\nu-2\alpha)}(z)]}{(\nu - 2\alpha)[1 - H_0(z)][1 - H_M(z)H_0^{(\nu-2\alpha)}(z)]}. \tag{2.116}$$

The function $U(z)$ may also be expressed after a polynomial division as

$$U(z) = \sum_{i=1}^{\infty} U_i \cdot z^i, \tag{2.117}$$

where U_i encompasses all the information regarding both the time instant and the probability of i^{th} path in the resultant transfer function. Hence it may be shown that the generalised expression derived for computing the MAT of the SDSS based code acquisition scheme considered is given by employing both Equation. 2.116 and Equation. 2.117:

$$\begin{aligned} E[T_{ACQ}] = \frac{dU(z)}{dz}|_{z=1} \cdot \tau_D = \frac{1}{H_D(1)}[H_D{}'(1) + H_M{}'(1) + \\ \{(\nu - 2\alpha)[1 - \frac{H_D(1)}{2}] + \frac{1}{2}H_D(1)\}H_0{}'(1)] \cdot \tau_D, \end{aligned} \tag{2.118}$$

where $H_x'(z)|_{x=D,\,M\,or\,0}$ is the derivative of $H_x(z)|_{x=D,\,M\,or\,0}$ and τ_D is the dwell time [3]. Therefore the MAT may be expressed as $N{\cdot}T{\cdot}T_c{\cdot}E[T_{ACQ}]$ seconds and characterises the overall system performance of the SDSS, where N denotes the coherent integration interval and T is the number of PDI stages, $E[T_{ACQ}]$ denotes the mean acquisition time given by Equation 2.118, while τ_D represents $N{\cdot}T{\cdot}T_c$.

2.4.1.2 Multi-path Scenario

We assume that in each chip duration T_c, α number of correct timing hypotheses are tested, which are spaced by T_c/α. Hence the total number of timing positions within the uncertainty region is increased by a factor of α. Moreover, as mentioned in Section 2.2.1, when the L multi-path signals arrive with a time delay τ_l having a tap-spacing of one chip-duration, then the relative frequency of the signal being present H_1 is increased L-fold. Therefore, in light of both α and L, the total number of timing positions within the entire uncertainty region is finally increased by a factor of $\alpha \cdot L$. The required transfer functions [14] are defined as follows. The entire successful detection function $H_D(z)$ encompasses all the possible branches of successful detection, which was increased by a factor of L in the state diagram of Figure 2.12 [3]. Furthermore, $H_0(z)$ indicates the absence of the desired user's signal at the output of the acquisition scheme, whilst $H_M(z)$ represents the overall miss probability of a search run carried out across the entire uncertainty region. Other related processes are the same as detailed for the single-path scenario of SDSS in Section 2.4.1.1. Then, it may be shown that the generalised expression derived for computing the MAT of the serial search based code acquisition scheme is given by Equation. 2.118 in Section 2.4.1.1:

$$E[T_{ACQ}] = \frac{1}{H_D(1)}[H_D{}'(1) + H_M{}'(1) + \{(\nu - 2\alpha L)[1 - \frac{H_D(1)}{2}] + \frac{1}{2}H_D(1)\}H_0{}'(1)] \cdot \tau_{D1} \tag{2.119}$$

which may be simplified to

$$E[T_{ACQ}] \approx \frac{(1 + H_M(1)) \cdot H_0{}'(1)}{2 \cdot (1 - H_M(1))} \cdot (\nu \cdot \tau_D), \tag{2.120}$$

where $H_x^{'}(z)|_{x=D,\,M\,or\,0}$ is a derivative of $H_x(z)|_{x=D,\,M\,or\,0}$ and τ_D denotes the dwell time. The exact MAT formula given by Equation. 2.119 can be simplified, as described in Equation. 2.120, if the total number of states ν is significantly higher than the number of H_1 states, where H_1 represents that the signal may be deemed to be present [22]. In order to perform our numerical performance analysis, we adopted the specific approximation of the exact MAT expression proposed in [22]. More explicitly, since each resolvable path contributes two hypotheses and because the average correct detection probability associated with these two hypotheses is the same, the overall miss probabilities of the SDSS scheme may be expressed as:

$$H_M(z) = z^{2L\alpha} \prod_{l=1}^{L} \prod_{\zeta=1}^{2\alpha} (1 - P_{D(l,\zeta)}), \tag{2.121}$$

where $P_{D(l,\zeta)}$ represents the correct detection probability of the SDSS scheme. The $H_0(z)$ value of the SDSS scheme is expressed as

$$H_0(z) = (1 - P_F)z + P_F z^{K+1}, \tag{2.122}$$

where K denotes the false locking penalty factor expressed in terms of the number of chip intervals required by an auxiliary device for recognising that the code-tracking loop is still unlocked and P_F is the false alarm probability of the SDSS scheme.

2.4.2 Double Dwell Serial Search for Co-located Transmission Scenario

2.4.2.1 Single-path Scenario

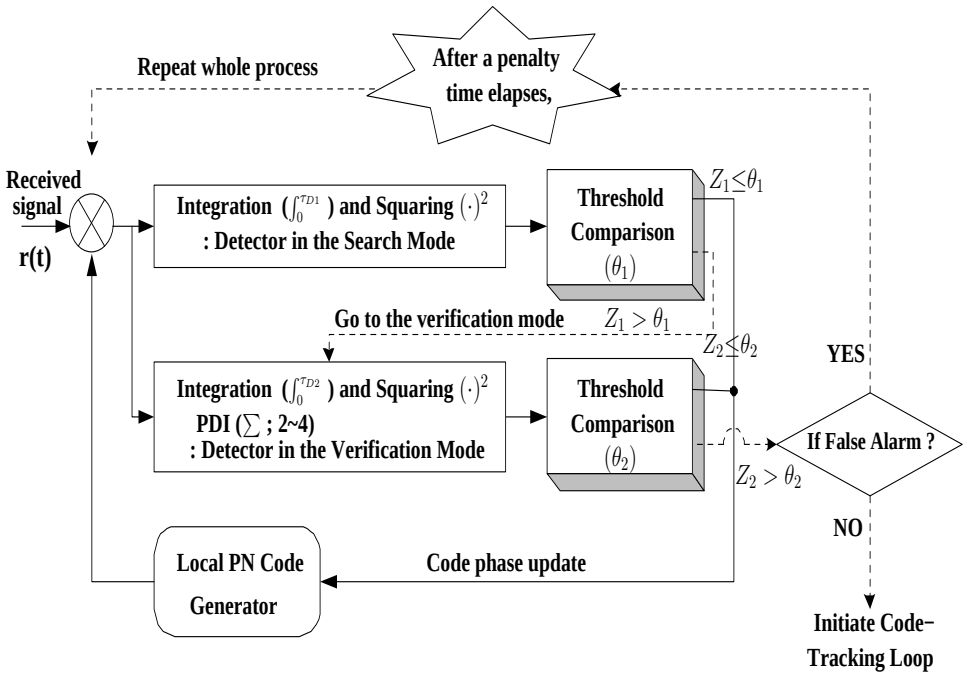

Figure 2.13: Schematic diagram of double dwell serial search.

An appealing approach to minimising the achievable MAT performance of the serial search based code acquisition scheme is to perform consecutive tests in conjunction with multiple dwell times [3, 4, 5]. Since most of the cells searched correspond to incorrect alignments, eliminating them quickly leads to a significant reduction in the MAT. The resultant multiple dwell based search system may be considered a generalisation of the single dwell based one. Double dwell based serial search has been widely used in practice [3, 5, 15], because it strikes an attractive compromise between the achievable MAT performance and an increased hardware complexity. Figure 2.13 portrays the schematic of Double Dwell Serial Search

(DDSS), where the block-diagram shows both the search mode and the verification mode. More explicitly, if the correlation-test of $Z_1 > \theta_1$ is satisfied, the result of the search mode in the upper branch is confirmed in the verification mode of the lower branch using the second integer dwell time τ_{D2} and the correlator threshold of $Z_2 > Z_1$. The first integration dwell time (τ_{D1}) seen in the upper branch of Figure 2.14 is defined as the time required for testing each hypothesis in the search mode which is typically on the order of 64 chips. If the estimated code phase is deemed correct in the search mode, the verification mode is activated in order to confirm, whether H_D the previous decision is correct or not. For the sake of achieving a high-reliability decision, both the coherent integration interval and the number of PDI stages should be optimised [5]. If the decision is confirmed in the verification mode, the corresponding code phase can be deemed the correct code phase of the received signal. Otherwise, the search mode will be reactivated, until the correct code phase will be obtained and confirmed. In a scenario, where false alarm was encountered, after a penalty time, the search mode will be reactivated. The operation of the DDSS is also illustrated in the state diagram of Figure 2.14. Similarly, to the assumption of the preceding SDSS scenario, we postulate that in each chip duration T_c, α number of correct timing hypotheses are tested, which are spaced by T_c/α, and hence the total uncertainty region ν is increased by a factor of α [6]. All the resultant $(\nu - 2\alpha)$ states that may lead to a false alarm are expected to increase the MAT according to the corresponding penalty time. The 2α number of legitimate locking states within a lag of one chip duration of the correct timing instant extending in both directions are taken into account in the MAT analysis. Combining all these 2α number of legitimate locking states into the correct detection transfer function

[5]Selection of the optimised value of the coherent integration interval is highly dependent upon the performance degradation of the carrier frequency mismatch between the BS's transmitter and the MS's receiver and a specific number of PDI stages must be determined by satisfying a pair of targeted correct detection and false alarm probabilities in terms of minimised MAT.

[6]Note 2: Let us now consider Figure 2.14 and commence other related discussions from the left-most state, namely A, of the row of 2α number of horizontally aligned states. There are α states per chip-interval, each of which has to be tested at both-sides of the current time instant. From the left-most state of Figure 2.14 we traverse to successful detection with a probability pair of $P_{D1}^{(1)}$ and $P_{D1}^{(2)}$ and to the second of the 2α states either with a probability of $(1 - P_{D1}^{(1)})$ or with a probability pair of $P_{D1}^{(1)}$ and $(1 - P_{D1}^{(2)})$, etc. If we tested both the α number of dwell intervals left and right until the right-most state, namely B, and failed to exceed the correlation threshold, the acquisition scheme traverses to state C of Figure 2.14, namely $H_0(z)$. Since no acquisition success was declared so far, at this stage three more legitimate events have to be considered, namely the false alarm event having a probability pair of $P_F^{(1)}$ and $P_F^{(2)}$, the absence of false alarm having a probability pair of $P_F^{(1)}$ and $1 - P_F^{(1)}$, or the absence of false alarm having a probability of $(1 - P_F^{(1)})$. Given that no successful detection or no false alarm took place or - alternatively - false alarm was encountered, the only conclusion that may be drawn is that the desired user's signal is indeed absent or it is deemed to be absent owing to interference and other channel impairments, leading to state C in Figure 2.14. The probability of the desired user being absent is denoted by $H_0(Z)$ and graphically portrayed in Figure 2.14. The acquisition scheme then traverses an indefinite number of these 'desired user is absent states', until eventually assumes state A again.

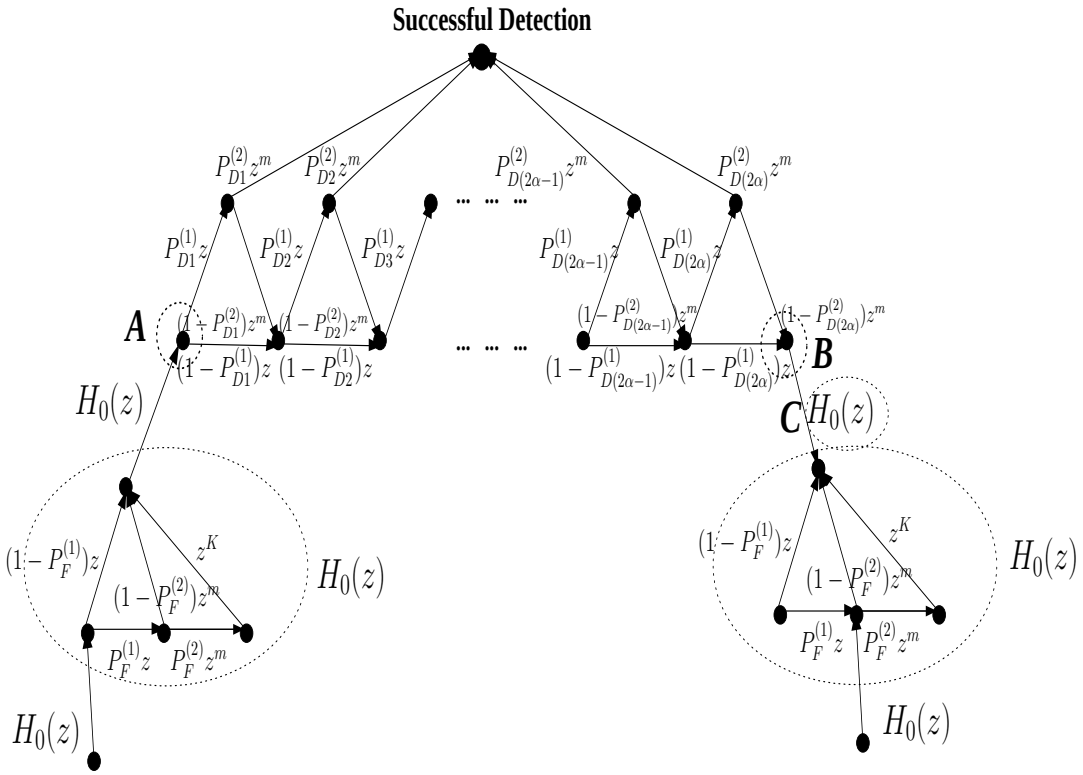

Figure 2.14: Sate diagram of double dwell serial search.

encompassing all branches of the relevant state diagram in Figure 2.14 leads to the correct detection transfer function expressed as [14]

$$H_D(z) = \sum_{j=1}^{2\alpha} P_{Dj}^{(1)} P_{Dj}^{(2)} z^{m+1} \prod_{i=1}^{j-1} \left[(1-P_{Di}^{(1)})z + P_{Di}^{(1)}(1-P_{Di}^{(2)})z^{m+1} \right], \tag{2.123}$$

where $P_{Dj}^{(1)}$ and $P_{Dj}^{(2)}$ represent the correct detection probability associated with the j^{th} testing of the first and second integration dwell interval, respectively, following $(j-1)$ failed trials, each resulting in a miss and where each probability of a miss in the corresponding total miss transfer function is given by $(1-P_{Di}^{(1)})$ or $P_{Di}^{(1)}(1-P_{Di}^{(2)})$. Furthermore, z indicates the unit-delay operator and m represents the exponent of z in the verification mode, while $H_0(z)$ in a dotted circle of the Figure 2.14 denotes the probability of the desired user's signal being absent at the output of the acquisition scheme, which is expressed as

$$H_0(z) = (1-P_F^{(1)})z + P_F^{(1)}(1-P_F^{(2)})z^{m+1} + P_F^{(1)}P_F^{(2)}z^{K+m+1}, \tag{2.124}$$

where $P_F^{(1)}$ and $P_F^{(2)}$ represent the false alarm probability of the first and second dwell, respectively, and K is the false locking penalty factor [3]. Finally, $H_M(z)$ represents the overall probability of miss during a search run carried out across the entire uncertainty

region, which may be formulated as the product of the summation of the two individual miss probabilities of the first and second integral dwell interval, since these may be considered independent events, yielding

$$H_M(z) = \prod_{j=1}^{2\alpha}[(1 - P_{Dj}^{(1)})z + P_{Dj}^{(1)}(1 - P_{Dj}^{(2)})z^{m+1}]. \tag{2.125}$$

Similarly, to the procedures used for SDSS in Equation. 2.118 of Section 2.4.1.1 it may be shown that the generalised expression derived for computing the MAT of the DDSS based code acquisition scheme considered is given by employing both Equation. 2.116 and Equation. 2.117 of Section 2.4.1.1:

$$E[T_{ACQ}] = \frac{dU(z)}{dz}|_{z=1}\cdot\tau_{D1} = \frac{1}{H_D(1)}[H_D{}'(1) + H_M{}'(1) + \{(\nu - 2\alpha)[1 - \frac{H_D(1)}{2}] + \frac{1}{2}H_D(1)\}H_0{}'(1)]\cdot\tau_{D1}, \tag{2.126}$$

where $H_x^{'}(z)|_{x=D,\,M\,or\,0}$ is the derivative of $H_x(z)|_{x=D,\,M\,or\,0}$ and τ_{D1} is the first dwell time [3]. Therefore the MAT may be expressed as $N{\cdot}T{\cdot}T_c{\cdot}E[T_{ACQ}]$ seconds and represents the overall system performance of the DDSS, where N denotes a coherent integration interval and T is the number of PDI stages, $E[T_{ACQ}]$ denotes the mean acquisition time given by Equation 2.126, while τ_{D1} represents $N{\cdot}T{\cdot}T_c$.

2.4.2.2 Multi-path Scenario

As illustrated in the Multi-path scenario of SDSS, we assume that in each chip duration T_c, α number of correct timing hypotheses are tested, which are spaced by T_c/α. Hence the total number of timing positions within the uncertainty region is increased by a factor of α. When the L multi-path signals arrive with a time delay τ_l having a tap-spacing of one chip-duration, then the relative frequency of the signal being present H_1 is increased L-fold. Therefore, in light of both α and L the total number of timing positions within the entire uncertainty region is finally increased by a factor of $\alpha{\cdot}L$. The required transfer functions [14, 15], are defined as follows. The entire successful detection function $H_D(z)$ encompasses all the possible branches of successful detection, which was increased by a factor of L in the state diagram of Figure 2.14 [14]. Furthermore, $H_0(z)$ indicates the absence of the desired user's signal at the output of the acquisition scheme, while $H_M(z)$ represents the overall miss probability of a search run carried out across the entire uncertainty region. Other related processes are the same as detailed for the single-path scenario of DDSS in Section 2.4.2.1.

Then, it may be shown that the generalised expression derived for computing the MAT of the serial search based code acquisition scheme is given by Equation 2.118 in Section 2.4.1.1:

$$E[T_{ACQ}] = \frac{1}{H_D(1)}[H_D{}'(1) + H_M{}'(1) + \{(\nu - 2\alpha L)[1 - \frac{H_D(1)}{2}] + \frac{1}{2}H_D(1)\}H_0{}'(1)] \cdot \tau_{D1}, \tag{2.127}$$

while the corresponding simplified expression is formulated as

$$E[T_{ACQ}] \approx \frac{(1 + H_M(1)) \cdot H_0{}'(1)}{2 \cdot (1 - H_M(1))} \cdot (\nu \cdot \tau_{D1}), \tag{2.128}$$

where $H_x^{'}(z)|_{x=D,\,M\,or\,0}$ is a derivative of $H_x(z)|_{x=D,\,M\,or\,0}$ and τ_{D1} denotes the dwell time[7]. The exact MAT formula given by Equation 2.127 can be simplified, as seen in Equation 2.128, if the total number of states ν is significantly higher than the number of H_D states [22]. More explicitly, when considering $\nu >> 2\alpha L$, $\nu - 2\alpha L$ is approximated by ν, then only the term $[1 - \frac{H_D(1)}{2}]$ of Equation 2.127 is retained, because the effects of others are negligible in terms of calculating the MAT. In order to carry our numerical analysis, we adopted the approximation for the exact MAT expression of Equation. 2.127, as proposed in [22]. Since each resolvable path contributes two hypotheses and because the average correct detection probability associated with these two hypotheses is the same, the overall miss probabilities of the DDSS scheme may be expressed as:

$$H_M(z) = \prod_{l=1}^{L} \prod_{\zeta=1}^{2\alpha} [(1 - P_{D(l,\zeta)}^{(1)})z + P_{D(l,\zeta)}^{(1)} \cdot (1 - P_{D(l,\zeta)}^{(2)}) z^{m+1}], \tag{2.129}$$

where $P_{D(l,\zeta)}^{(x)}|_{x=1,\,or\,2}$ are the correct detection probability of both the search and the verification modes of the DDSS arrangements, respectively. The $H_0(z)$ value of the DDSS scheme can be expressed as

$$H_0(z) = (1 - P_F^{(1)})z + P_F^{(1)}(1 - P_F^{(2)})z^{m+1} + P_F^{(1)}P_F^{(2)}z^{K+m+1}, \tag{2.130}$$

where K denotes the false locking penalty factor expressed in terms of the number of chip intervals required by an auxiliary device for recognising that the code-tracking loop is still unlocked. Furthermore, $P_F^{(x)}|_{x=1,\,or\,2}$ represents the false alarm probability of both the search and the verification mode of the DDSS scheme, respectively and m is the exponent of z in the verification mode.

[7]The dwell time is defined as the time-interval, during which the acquisition scheme 'dwells' in the interval $\tau_D \equiv NT_c$ accumulating the correlation contributions, which quantify the similarity of the locally stored and received spreading sequence.

2.4.3 Double Dwell Serial Search for Cooperative Transmission Scenario

2.4.3.1 Multi-path Scenario

There is a difference between a single- and co-located MIMO-aided schemes as well as a RS-assisted one in terms of analysing the MAT, because a signal received from a RS is a time delayed version of that directly received from the BS. Hence the independently fading multiple signal replicas received from RSs cannot be directly combined, as opposed to the co-located MIMO-element scenarios, as described in Sections 2.4.1 and 2.4.2. The groups of multi-path components received from a BS and RS(s) may or may not overlap, depending on the path delays experienced. However, for the sake of simplifying our analysis, we assume that every group of multi-path components is non-overlapping and each arrives with a time delay that is an integer multiple of the chip-duration τ_p, because the derivation of the exact MAT formula can be simplified without grave inaccuracies, when the uncertainty region may be assumed to be substantially wide, such as $(2^{15}-1)$ chips [8]. In terms of deriving both the P_D and the P_F based upon invoking multiple receive antennas, we will commence our discourse by analysing the MAT performance of code acquisition schemes employing DDSS [15]. We assume that in each chip duration T_c, α number of correct timing hypotheses are tested instead of just a single one, which are spaced by T_c/α. Hence the uncertainty region's total time-duration remains the same, but the number of legitimate locking positions to be tested is increased by a factor of α. Moreover, when the L multi-path signals arrive at time delays, which are integer multiples of the chip-duration τ_l, then the relative frequency of the signal being present is increased L-fold. Similarly, the relative frequency of the signal being present is increased by a factor of P, which is proportional to the total number of RSs and BS, P. The required transfer functions [3, 15], are defined as follows. The entire successful detection related transfer function $H_D(z)$ encompasses all the branches of a state diagram [3, 15], which lead to successful detection. Furthermore, $H_0(z)$ indicates the absence of the desired user's signal at the output of the acquisition scheme, whilst $H_M(z)$ represents the overall miss probability of a search run carried out across the entire uncertainty region. The related processes were detailed for DDSS in Section 2.4.2. Then, it may be shown that the generalised expression derived for computing the MAT of the DDSS scheme is given by

[8] To elaborate a little further, when the uncertainty region is $(2^{15}-1)$ chip durations, the ratio between the number of chips in the uncertainty region and that of the legitimate locking positions corresponding to the signal being absent and present, respectively, is at most on the order of 10^{-4}, which allows us to employ our aforementioned assumptions in the derivation of the MAT formula.

[3, 22]:

$$E[T_{ACQ}] = \frac{1}{H_D(1)}[H_D{}'(1) + H_M{}'(1) + \{(\nu - 2\alpha LP)[1 - \frac{H_D(1)}{2}] + \frac{1}{2}H_D(1)\}H_0{}'(1)] \cdot \tau_{D1} \quad (2.131)$$

$$\approx \frac{(1 + H_M(1))\cdot H_0{}'(1)}{2\cdot(1 - H_M(1))}\cdot(\nu\cdot\tau_{D1}), \quad (2.132)$$

where $H_x^{'}(z)|_{x=D,\,M\,or\,0}$ is a derivative of $H_x(z)|_{x=D,\,M\,or\,0}$, ν represents the total number of uncertainty positions to be searched and τ_{D1} denotes the 1^{st} dwell time. Again, the exact MAT formula can be simplified, if ν is significantly higher than the number of H_1 states, where H_1 represents that the signal may be deemed to be present [22]. Therefore, in order to simplify our numerical performance analysis, we adopted the specific approximation of the exact MAT expression proposed in [22], as shown in Equation. 2.132. Explicitly, since each resolvable path contributes two H_1 hypotheses and because the average P_D associated with these two hypotheses is the same, the overall miss probability of the DDSS scheme in the fixed RS-aided scenario may be expressed as:

$$H_M(1)|_{(cooperative)} = \prod_{p=1}^{P}\prod_{l=1}^{L}\prod_{\zeta=1}^{\alpha}[(1 - P_{D1(p,l,\zeta)}) + P_{D1(p,l,\zeta)}\cdot(1 - P_{D2(p,l,\zeta)})]^2, \quad (2.133)$$

where $P_{Dx(p,l,\zeta)}|_{x=1,\,or\,2}$ represent the correct detection probability of both the search and the verification modes of the DDSS arrangements, respectively. The $H_0{}'(1)$ value of the DDSS scheme is expressed as:

$$H_0{}'(1) = 1 + m\cdot P_{F1} + K\cdot P_{F1}\cdot P_{F2}, \quad (2.134)$$

where K denotes the false locking penalty factor expressed in terms of the number of chip intervals required by an auxiliary device for recognising that the code-tracking loop is still unlocked and m represents the exponent of z in the verification mode. Furthermore, $P_{Fx}|_{x=1,\,or\,2}$ represent the false alarm probability in both the search and in the verification mode of the DDSS scheme, respectively.

2.5 Analysis of E_c/I_0 for DS-CDMA Systems

In this section we investigate the E_c/I_0 distribution in the DL of the inter-cell synchronous CDMA system for the sake of analysing serial search based code acquisition in multiple transmit antenna aided DS-CDMA. Let us commence this section by considering the definition of E_c/I_0 and how it impacts the performance of the DS-CDMA systems.

First of all, we assumed having the transmitted powers for the CDMA-2000 system [72], which are summarised in Table 2.2.

Hence the total allocated power at the BS is highly dependent on the number of the active

Table 2.2: Transmitted Powers for the CDMA-2000 System

BS's transmit power	10 [W]
Pilot channel power	1.5 [W]
Paging and synchronisation channel power	0.9 [W]
Traffic channel power	0.25 [W]
Total power of 10 traffic channels	2.53 [W]
Total power of 20 traffic channels	5.07 [W]
Total power of 30 traffic channels	7.6 [W]

users in each sector. When assuming that the number of active users is 30, the total power assigned is 10 [W] = 40 [dBm]. Then, the total amount of channel-induced impairments on the DL is constituted by the superposition of the background noise, plus the serving-cell interference imposed by both the multi-path signals, the other intra-cell users and the other-cell interference [3, 15, 72].

The total amount of serving-cell interference on the DL is expressed as $I_{SC(Total)} = I_{SC1}(1-\beta_1) + I_{SC2}(1-\alpha_1)$, where I_{SC1} is the serving-cell interference imposed by the multi-path signals, while β_1 represents the fraction of the first received path's power and a fixed value of 0.57, which represents the fraction of the Line-Of-Sight (LOS) path's power of a single-path scenario as in [15]. Then I_{SC2} denotes the serving-cell interference imposed by the other intra-cell users, whilst α_1 is the orthogonality factor of (0.4 – 1)[9] [105]. Furthermore, the other-cell interference imposed by the remaining 56 sectors is denoted as I_{OC} [72] and the received noise power is denoted as $N_0 \cdot W$, where N_0 represents the power spectral density of the thermal noise and W is the bandwidth allocated. Accordingly, the total amount of channel-induced impairments imposed on the DL is defined as $I_{(Total)} = I_{SC1}(1-\beta_1) + I_{SC2}(1-\alpha) + I_{OC} + N_0 \cdot W$. The total link loss is expressed as the product of the antenna gain, path loss and the lognormal shadow-fading coefficient. Therefore, the received signal power is obtained as the product of the transmitted pilot power and the link loss. In our

[9]The orthogonality factor is defined as the particular fraction of other-cell interference, which contaminates the serving cell's desired signal as a result of the asynchronous interference.

scenario the cellular structure consists of 19 hexagonal cells. The six neighbouring cells of the first tier and the 12 neighbouring cells of the second tier surround the centre cell. Each cell has three sectors. The cell layout is wrapped-around to form a toroidal surface in order to achieve shorter simulation run times. A toroidal surface is chosen, because it can be readily formed from a rhombus by joining the opposing edges [106, 107, 108].

Let us now consider the definition of E_c/I_0 for the DL pilot channel. The SINR per chip denoted as E_c/I_0 may be expressed as [72, 105]

$$(\frac{E_c}{I_0})_{(pilot)} = \frac{\beta_1 \cdot P_{Total} \cdot \varsigma_p \cdot L_1}{I_{SC1}(1-\beta_1) + I_{SC2}(1-\alpha_1) + I_{OC} + N_0 \cdot W}, \tag{2.135}$$

where P_{Total} is the total transmit power allocated at the BS, ς_p represents the fraction of the transmitted pilot power with respect to the total allocated transmit power, while L_1 denotes the link loss. Table 2.3 portrays the orthogonality factor set used in our simulations. In the macro-cellular scenario considering a range spanning from 1 to 0.5 is appropriate for our simulations depending upon the environmental conditions associated with the cell size considered [105]. Table 2.4 represents the general system level parameters used in our

Table 2.3: Orthogonality Factor Set Parameterised by Received Pilot Signal Strength

Orthogonality Factor	Pilot Signal Strength
1	... -55 [dBm]
0.95	... -60 [dBm]
0.9	... -65 [dBm]
0.85	... -70 [dBm]
0.8	... -75 [dBm]
0.75	... -80 [dBm]
0.7	... -85 [dBm]
0.65	... -90 [dBm]
0.6	... -95 [dBm]
0.55	... -100 [dBm]
0.5	Less than -100 [dBm]

simulations.

We also assume operating in the range of 'finger locking', which may be considered to be the range between E_c/I_0 = -17 and -13 dB, as suggested in [72, 110]. In our scenario it is simply assumed that the pilot channel's required E_c/I_0 value is -15 dB [72]. Based on Table 2.4, we analysed the distribution of E_c/I_0 depending on the number of MSs supported. For the simplicity of this analysis we only considered a single-input single-output scenario. In these investigations, we analysed the distribution of E_c/I_0 in the DL of

Table 2.4: General Downlink System Level Simulation Parameters

Parameter	Explanation	Comments
Carrier Frequency	1.9 GHz	
Cellular Layout	Hexagonal grid, 3-sector, Wrap around method	[106, 107, 108]
Number of cells	57 sectors	2 rings [106, 107]
Site to site distance	2000 m	Macro cell [109]
Antenna horizontal pattern	70 deg (-3 dB) with 20 dB front-to-back ratio	[106, 107]
Antenna Orientation	0 degree horizontal azimuth is East(main lobe)	No loss is assumed on the vertical azimuth [106]
Propagation model	L_1=128.6+35log10(dist.)dB (BS Ant. Ht=32m, MS=1.5m)	[106] (dB scale and dist. in km)
Std. of slow fading	8 [dB]	Log-normal shadowing [72, 106, 107]
BS total power	10 [W] (= 40 [dBm])	[72]
Overhead channel DL power usage	Pilot(0.15), Paging and Sync(0.09)	[72]
Received noise power	-105 [dBm]	[72]
Pilot $(E_c/I_0)_{req}$	-15 [dB]	Threshold of finger locking [72]
Delay spread model	Relative power ratio: 0.7 and 0.3; 0.57,0.29 and 0.14; 0.45 and the others not defined	(0.25,0.5 and 0.25, respectively) Two paths [106, 107]; Three paths [15]; Four paths [106, 107]
Active set size	Up to 3	2- and 3-way soft handover considered [106, 107]
Soft handove parameters	WindowADD=4[dB]	[72, 107]
Orthogonality factor	[1 0.85 0.65 0.5]	See Table 2.3 [105]
Number of MS	10,20 and 30	Actual allocated transmit power in BS is 6,8,10 [W], respectively depending on the number of MS (10,20 and 30, respectively) [72]
Length of coherent summation	1 symbol (128 chips)	

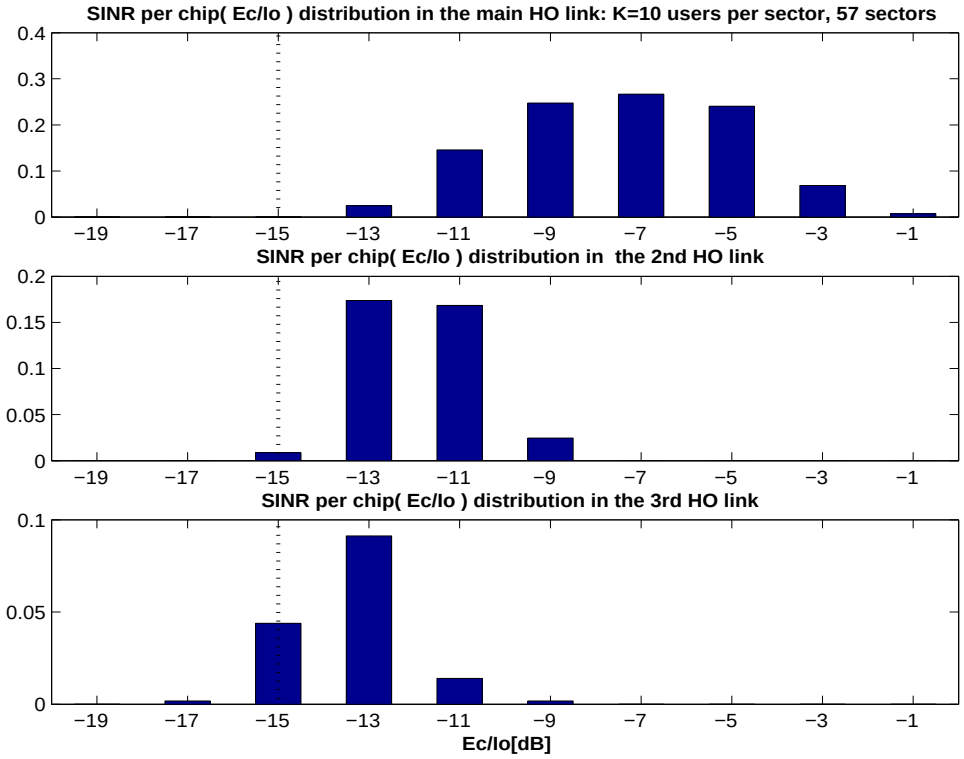

Figure 2.15: Distribution of E_c/I_0 when supporting K = 10 mobile stations per sector.

the inter-cell synchronous CDMA-2000 system with the aid of our system level simulations, in order to characterise the relationship between the value of E_c/I_0 and the achievable MAT performance in Chapters 3 and 4. This will allow us to characterise the effects of using both transmit diversity and frequency diversity in multi-user scenarios in terms of the attainable MAT performance.

Figure 2.15 illustrates the distribution of E_c/I_0 for the pilot channel, when supporting K = 10 MSs per sector. The sub-figure situated at the top of this figure explicitly shows the distribution of E_c/I_0 recorded for the currently activated HandOver (HO) link, when the MS benefits from soft-HO. All the recorded values are higher than the predetermined value of the threshold required for finger locking. Accordingly, the achievable MAT performance may not be gravely affected, although employing transmit diversity, frequency diversity or both in multi-user scenario may lead to the degradation of the MAT performance. By contrast, when considering the E_c/I_0 distribution of the 3rd HO link in a soft-HO scenario, considerable fraction of the MSs will experience an E_c/I_0 value close to the minimum required threshold. Hence, when considering the effects of using both transmit diversity and frequency diversity, the MAT performance of the post-initial acquisition scheme may be

significantly deteriorated. This phenomenon may lead to a HO performance degradation. Figures 2.16 and 2.17 demonstrate the E_c/I_0 distribution of the pilot signal received, when supporting $K = 20$ and $K = 30$ MSs per sector, respectively. These scenarios corresponds to a highly loaded cellular network. All the three sub-figures suggest that the E_c/I_0 distributions are shifted to the lower E_c/I_0 region in comparison to the scenario of $K = 10$ MSs per sector. This suggests that a further degraded MAT performance may be experienced. Accordingly, it may be concluded from Figures 2.15, 2.16 and 2.17 that in the scenarios of 3-way soft HO the number of MSs to be supported by the BS of a given sector increases, the E_c/I_0 ratio may dip below -15 dB for a high portion of the 2nd- and 3rd-best target handover links, where -15 dB is the minimum required E_c/I_0 value of the pilot channel [72]. Therefore the results of our in-depth analysis suggest that both the achievable MAT performance and the HO performance may be seriously degraded.

The three figures were generated by the following procedures:

1) The distance from any MS to any BS can be obtained from the following calculations. Define a coordinate system so that the centre of cell 1 is at (0,0), the distance of a mobile at (x,y) from a base-station at (a,b) is computed as the minimum in the set seen below[10].

A. Distance between (x, y) and (a, b),

B. Distance between (x, y) and $(a + 3\tilde{R}, b + 8\sqrt{3}\tilde{R}/2)$,

C. Distance between (x, y) and $(a - 3\tilde{R}, b - 8\sqrt{3}\tilde{R}/2)$,

D. Distance between (x, y) and $(a + 4.5\tilde{R}, b - 7\sqrt{3}\tilde{R}/2)$,

E. Distance between (x, y) and $(a - 4.5\tilde{R}, b + 7\sqrt{3}\tilde{R}/2)$,

F. Distance between (x, y) and $(a + 7.5\tilde{R}, b + \sqrt{3}\tilde{R}/2)$ and

G. Distance between (x, y) and $(a - 7.5\tilde{R}, b - \sqrt{3}\tilde{R}/2)$,

where $\tilde{R}$ is the radius of a circle which connects the six vertices of the hexagon.

2) MSs are randomly dropped over the 57 sectors so that each cell has the required number of users. A user shall be assigned to a sector of any cell, if the sector is in the Active Set (with a maximum size of three) of the user. All sectors of the system shall continue to accept users, until the desired fixed number of users per sector is achieved everywhere.

3) The fading signal and fading interference are computed for each MS roaming in each sector.

When considering multiple transmit antennas and multiple subcarriers, the number of MSs having an E_c/I_0 ratio below -15 dB may increase further. Details on the MAT analysis of

[10]To simplify our simulations, only three-way handovers were employed. A MS engaged in a three-way soft handover acts as a user in the sector having the smallest total path loss defined as the sum of the path loss and shadowing in the Active Set of MS.

the above-mentioned scenario will be provided in Chapters 3 and 4.

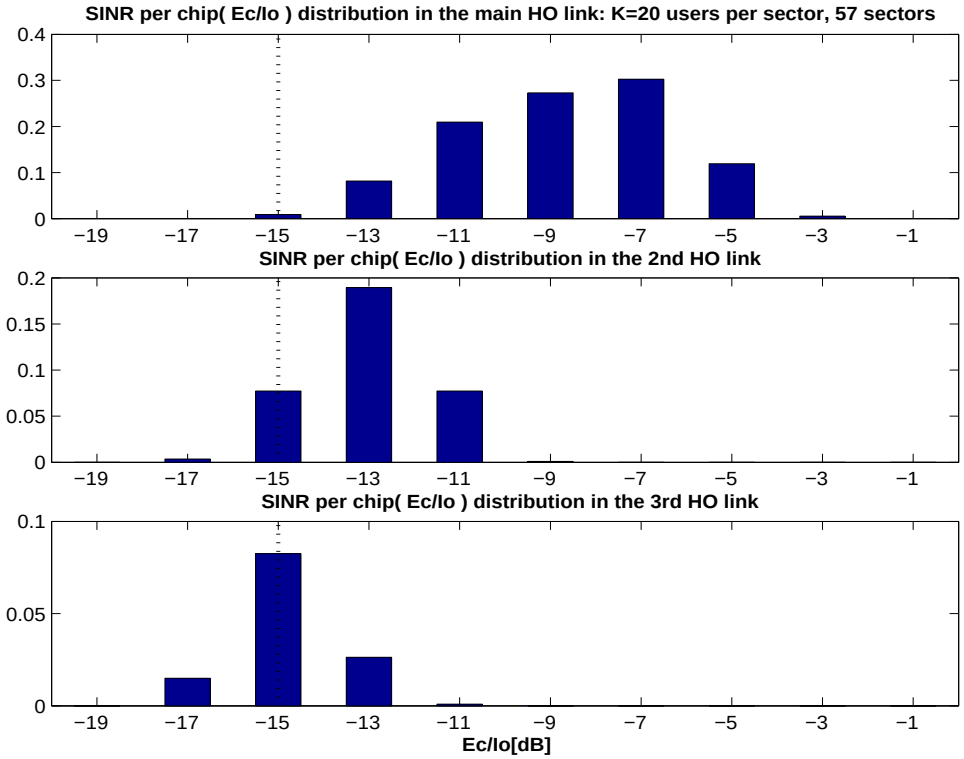

Figure 2.16: Distribution of E_c/I_0 when supporting K = 20 mobile stations per sector.

2.6 Chapter Summary and Conclusions

In this chapter, we have provided a detailed study of serial search based code acquisition schemes. Following a brief introduction in Section 2.1, we continued by describing our single- and multi-path channel model, the fading conditions as well as the effects of both spatial and inter-subcarrier fading correlation for our performance analysis provided in Section 2.2. Furthermore, the four most wide-spread MIMO types were briefly summarised in Table 2.1. It was noted that code acquisition schemes specifically designed for scenarios of both SDM and Space-Time Coding MIMOs are considered. Then the underlying formulae of both the correct detection and false alarm probabilities in co-located scenario were derived in Section 2.3. The Neyman-Pearson criterion was introduced in Section 2.3.1, followed by the derivation of the decision variable PDFs of a co-located MIMO aided NC code acquisition scheme designed for both the SC-DS-CDMA and MC-DS-CDMA DL, when communicating over a spatially uncorrelated Rayleigh channel in Section 2.3.2 in terms of using both a

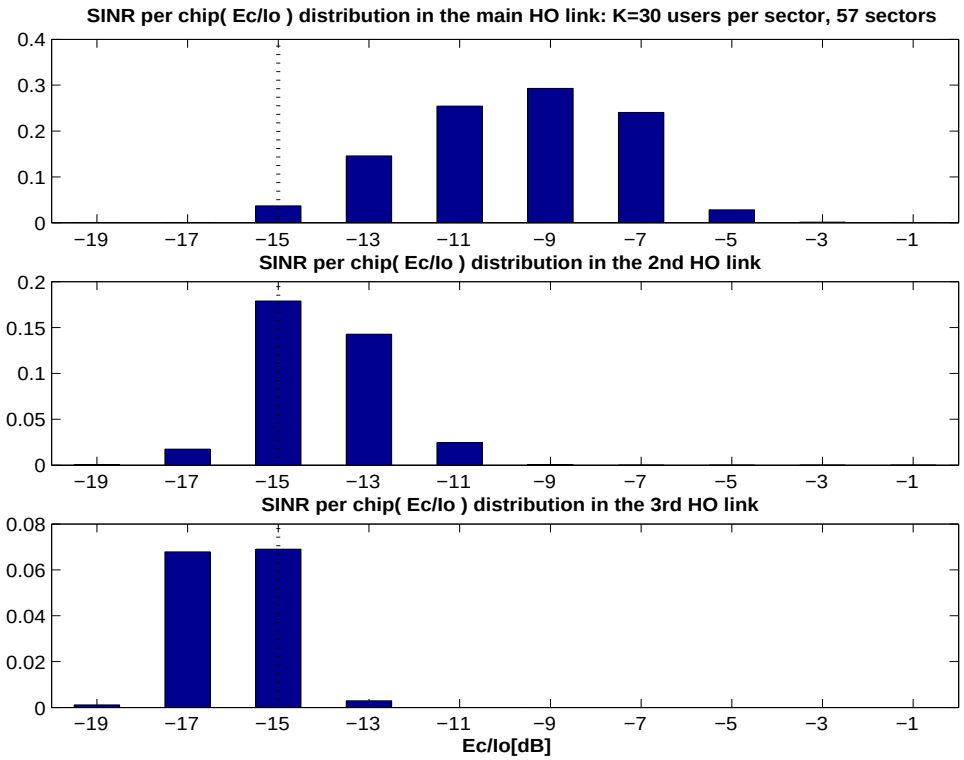

Figure 2.17: Distribution of E_c/I_0 when supporting K = 30 mobile stations per sector.

direct approach and a PDF based one. In Section 2.3.3 the decision variable PDFs of an co-located MIMO aided DC code acquisition scheme used for both the SC-DS-CDMA and MC-DS-CDMA DL, when communicating over a spatially uncorrelated Rayleigh channel were investigated. Finally, the decision variable PDFs of a cooperative MIMO aided NC code acquisition scheme designed for the SC-DS-CDMA DL in Section 2.3.4 in terms of using a PDF based one were derived. The MAT analysis of both SDSS and DDSS employed in our code acquisition schemes was provided for both single- and multi-path scenarios in Section 2.4. Finally, the specific definition of E_c/I_0 with respect to a DS-CDMA system was introduced and then the in-depth relationship between the E_c/I_0 distribution and the number of users per sector was analysed in Section 2.5. Based on the above-mentioned experimental results of Section 2.2, as well as on the formulae of Sections 2.3 and 2.4 derived for supporting the analysis provided in Chapters 4 as well as 5, and finally, the analysis of E_c/I_0 in Section 2.5 the specific characteristics of both co-located and cooperative NC MIMO aided schemes will be analysed in the forthcoming chapters.

Chapter 3

Performance Analysis of Co-located versus Cooperative MIMO Aided Non-Coherent Code Acquisition

3.1 Introduction

In this chapter, we will provide a quantitative performance analysis for serial search based code acquisition in the co-located and cooperative MIMO aided SC- and MC- DS-CDMA DL. In Section 3.2 we will commence the chapter with the performance analysis of the correct detection versus false alarm probability for serial search based code acquisition employed in the co-located MIMO aided SC-DS-CDMA DL with the aid of Sections 2.3.2 and 2.4.1. Based on the formulae in Sections 2.3.2, 2.4.1 and 2.4.2, this section is followed by a discussion on both initial and post-initial acquisition in the serial search based co-located NC MIMO aided SC-DS-CDMA DL in Section 3.3. We will analyse the performance of code acquisition in the co-located MIMO aided MC-DS-CDMA DL in Section 3.4 with the aid of Sections 2.3.2, 2.4.1 and 2.4.2. Finally, based on the formulae in Sections 2.3.4 and 2.4.3, we will also investigate the performance of the serial search based cooperative NC MIMO aided SC-DS-CDMA DL in Section 4.5. Furthermore, based on the above-mentioned results justified by information theoretic considerations, our acquisition design guidelines applicable to diverse NC MIMO aided scenarios will be summarised.

3.2 Correct Detection versus False Alarm Probability Performance in Co-located Scenario

3.2.1 System Parameters

Figure 2.2 depicts the block diagram of the NC receiver designed for our code acquisition scheme using MIMO. The MAT formulae provided for the single-path scenario of SDSS in Section 2.4.1.1 are also employed for the performance analysis of the NC scheme of this section. The system parameters employed are summarised in Table 3.1. In Table 3.2 we outlined the maximum SINR degradation imposed by both the Doppler shift and the clock-drift-induced frequency mismatch between the transmitter and receiver in conjunction with a coherent integration interval of N chip durations. The length of the PN sequence in our system was assumed to be $(2^{15}-1)\cdot T_c = 65534\cdot T_c$, where the chip-duration is $T_c = 1/1.2288\mu s$. It may be deemed sufficient at this point to integrate the detector output seen in Figure 2.2 over $N = 256$ chips, which is equivalent to two 128-chip modulated symbols used for coherent accumulation. This value was calculated by using Equation. 2.9 provided for determining the performance degradation owing to both the Doppler shift and the frequency mismatch. The spreading factor of the Walsh code to be acquired was selected to be 128. The frequency mismatch was assumed to be 1000 Hz [3], while the carrier frequency was 1.9 GHz. As an example of a high mobile speed, it is reasonable to postulate 160 km/h. We also assumed that the sampling inaccuracy caused by having a finite search step size of $\Delta = 1/2T_c$ was -0.91 dB, which is a typical value for the search step size [3, 15]. Accordingly, we considered three performance degradation factors, which encompassed the clock-drift-induced frequency mismatch, the Doppler shift and the effects of the finite sampling distance. All these imperfections were taken into account, when calculating the correct detection probability. Finally, two additional parameters have to be stipulated for the analysis of SDSS. Specifically, the total uncertainty region was assumed to entail 65,534 hypotheses, and in the spirit of [15], the false locking penalty factor was assumed to be 1000 chip-durations.

3.2.2 System Performance Results

Figure 3.1 illustrates the correct detection probability versus false alarm probability, parameterised by both the number of transmit antennas for P = 1,2 as well as 4 and the

Table 3.1: System Parameters

Bandwidth		1.25 MHz
Carrier frequency		1.9 GHz
Spreading factor		128
Diversity:	Transmit	1,2,4,6,8,10
	Receive	1,2,4
Frequency mismatch		1000 Hz
Mobile speed		160km/h
Coherent integration interval		256chips
Total uncertainty region		65,534
False locking penalty factor		1000 chip-durations

Table 3.2: Maximum SINR degradation inflicted by both the Doppler shift and a 1000 Hz frequency mismatch in conjunction with the coherent integration interval of N chip durations at a carrier frequency of 1.9 GHz

N (Chips)	64	128	256	384	512
Degradation (dB)	0.061	0.2449	0.9969	2.3144	4.3213

E_c/I_0 value. In case of E_c/I_0 = -10 dB, the achievable performance enhancement gradually saturates, as the transmit diversity order is increased from $P = 1$ to 4. By contrast, P_D decreases as the number of transmit antennas P increases, when the mobile station experiences a relatively low E_c/I_0 value of -19 dB, as evidenced by the three curves corresponding to the relatively low P_D values in Figure 3.1. Figures 3.2 and 3.3 characterise the correct detection probability versus false alarm probability, parameterised by both the number of transmit antennas for P = 1,2 as well as 4 in conjunction with both $R = 2$ (Figure 3.2) and $R = 4$ (Figure 3.3) receive antennas as a function of the E_c/I_0 value.

When having $R = 2$ receive antennas as portrayed in Figure 3.2, the results show similar trends to those of Figure 3.1. By contrast, in the scenario of $R = 4$ receive antennas as seen in Figure 3.3, there is a sufficiently high spatial diversity gain, which has beneficial effects on the achievable acquisition performance P_D. However, as seen in Figure 3.3, increasing the transmit diversity order imposes a degradation of the achievable P_D performance. The specific E_c/I_0 abscissa values used in Figures 3.1 to 3.3 were chosen to exemplify the typical achievable values. In all the remaining figures we will assume an operation in the range of 'finger locking', which may be considered to be the range between E_c/I_0 = -17 and -13 dB, as suggested in [72, 110]. Therefore, in Figure 3.4 and Figure 3.5

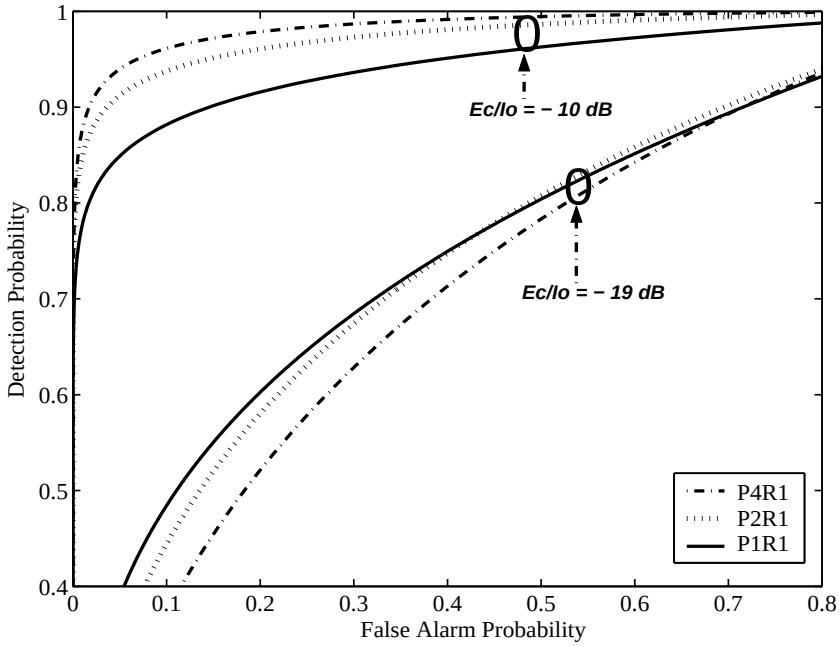

Figure 3.1: Correct detection versus false alarm probability for $P = 1,2$ and 4 transmit antennas in conjunction with $R = 1$ receive antenna, when using the schematic of Figure 2.2 and Table 3.1.

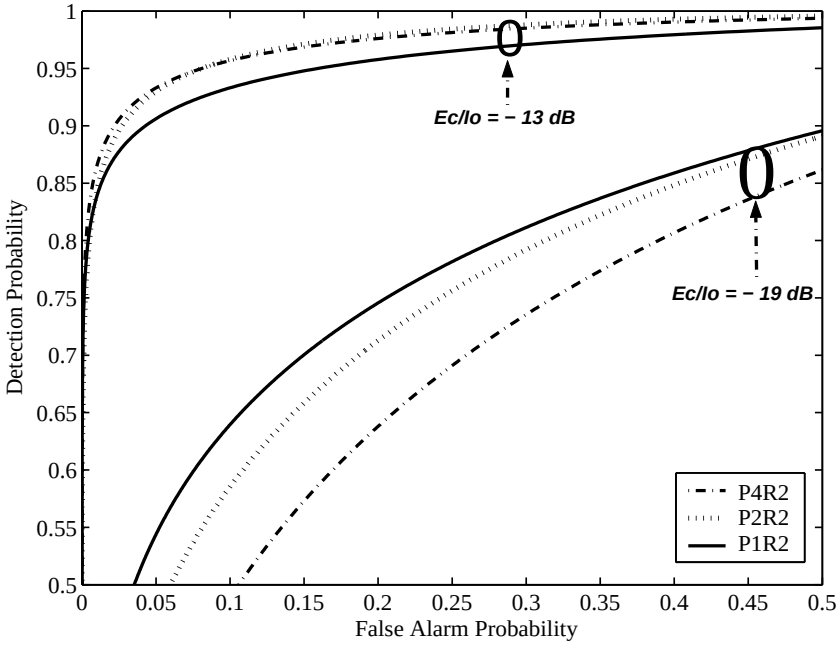

Figure 3.2: Correct detection versus false alarm probability for $P = 1,2$ and 4 transmit antennas in conjunction with $R = 2$ receive antennas, when using the schematic of Figure 2.2 and Table 3.1.

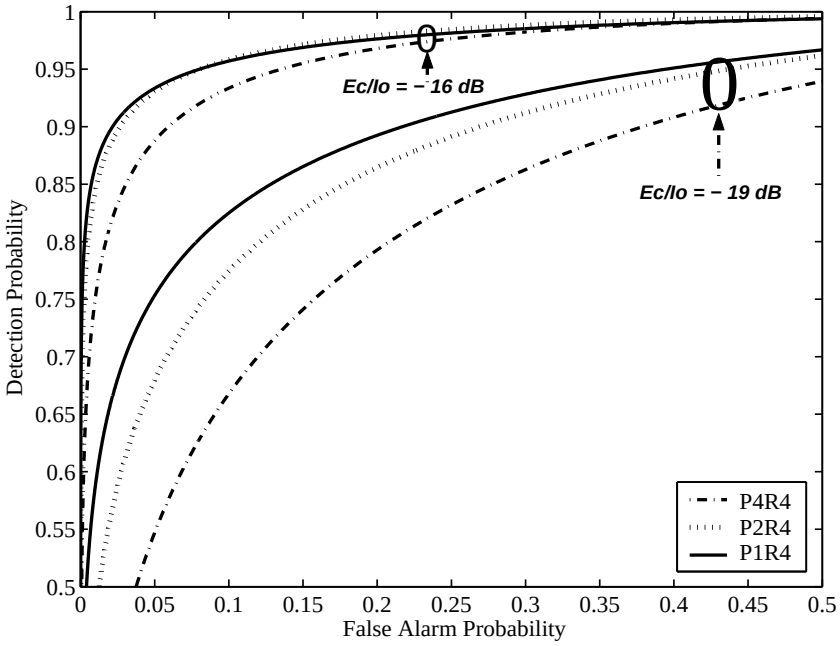

Figure 3.3: Correct detection versus false alarm probability for P= 1,2 and 4 transmit antennas in conjunction with R= 4 receive antennas, when using the schematic of Figure 2.2 and Table 3.1.

we will investigate in more detail the somewhat unexpected phenomenon of experiencing a degraded acquisition performance in the presence of multiple transmit antennas. The correct detection probabilities seen in Figure 3.4 and Figure 3.5 were obtained assuming a false locking probability of $P_F = 0.1$ for all scenarios considered, where $'S'$ denotes the simulation results, whilst $'A'$ presents the numerical analysis results calculated from both Equations. 2.28 and 2.29. The simulations always represent a slightly better correct detection probability than the analysis at the same false alarm probability. This is because in the analysis a constant Doppler shift value was added to the total frequency mismatch in Equation. 2.9, which was calculated for the high mobile speed scenario. However, in a practical scenario, the Doppler shift may have either a positive or a negative impact on the P_D performance, depending upon the specific conditions encountered.

In Figures 3.4 and 3.5, the relationship between P_D and the number of transmit antennas is portrayed both with and without multiple receive antennas for different values of E_c/I_0, respectively. More explicitly, Figure 3.4 portrays the correct detection probability versus the number of transmit antennas, parameterised by the pilot channel's E_c/I_0 value. At E_c/I_0 = -10 dB a slight P_D improvement is observed upon increasing the number of transmit antennas, although again, at low E_c/I_0 values typically the opposite is true. Figure 3.5

characterises the correct detection probability versus both the number of MIMO, parameterised by the pilot channel's E_c/I_0 value. The left illustration of Figure 3.5 characterises the scenario of $R = 2$ receive antennas, while the one at the right was valid for $R = 4$ receive antennas. The curve recorded for E_c/I_0 = -10 dB at the right of Figure 3.5 overlapped with that plotted for E_c/I_0 = -13 dB, because all the achievable detection probabilities were $P_D \approx 1$. Both Figures 3.4 and 3.5 illustrate that P_D tends to decrease, as the number of transmit antennas increases, especially when the MS experiences a low E_c/I_0 value. We can observe in both Figure 3.4 and Figure 3.5 that the highest detection probabilities marked by circles were achieved, when the per-branch E_c/I_0 value was -19 dB for a given total E_c/I_0 value in the range of 'finger locking'. Owing to the above-mentioned facts, the range of the minimum E_c/I_0 values required for reaching 'finger locking' may vary, depending upon the number of transmit antennas.

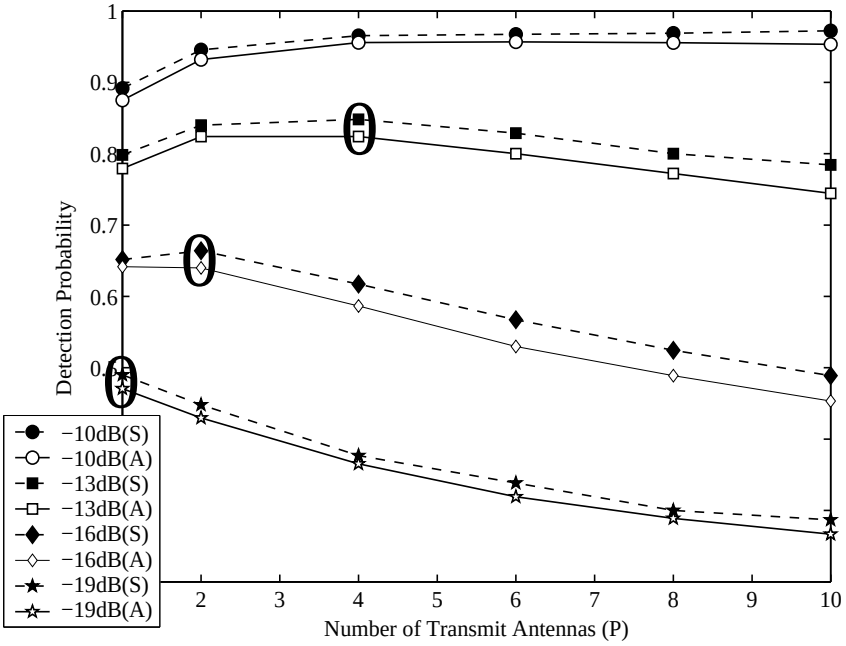

Figure 3.4: Correct detection probability versus the number of transmit antennas for P = 1,2,4,6,8 and 10, parameterised by the pilot channel's E_c/I_0 value, when using the schematic of Figure 2.2 and Table 3.1.

Let us now proceed by defining the MAT gain as the quotient of the MAT achieved by a particular MIMO configuration and that attained by the conventional $[P = 1, R = 1] = P1R1$ scheme. However, the transmit power reduction imposed by using multiple transmit antennas can be partially compensated for with the aid of multiple receive antennas. In this case it is more appropriate to use the MAT of the $P1R2$ or $P1R4$ schemes. Figure 3.6 characterises the MAT gain/degradation as a function of the E_c/I_0 values considered. Here

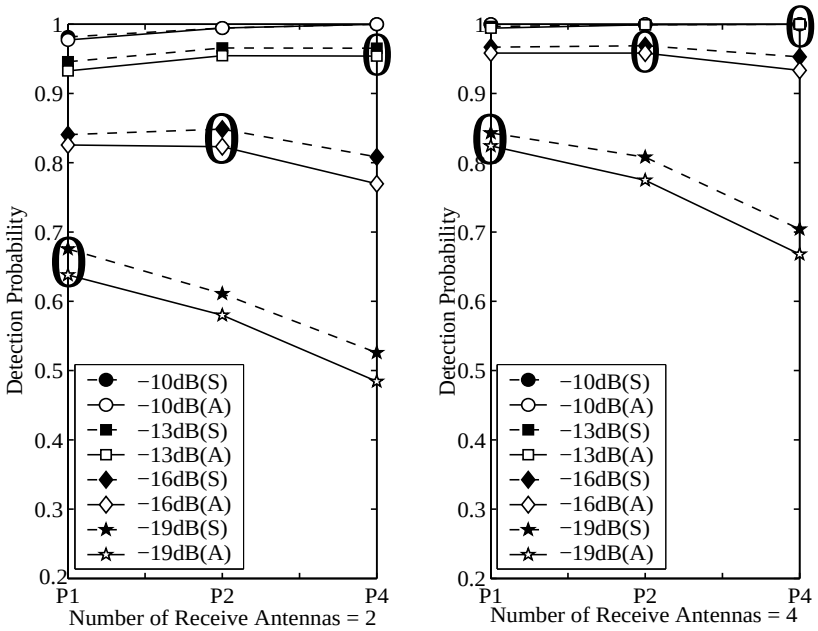

Figure 3.5: Correct detection probability versus the number of transmit antennas for $P =$ 1,2 as well as 4 and the number of receive antennas for both $R = 2$ (Left figure) and $R = 4$ (Right figure), parameterised by the pilot channel's E_c/I_0 value, when using the schematic of Figure 2.2 and Table 3.1.

the MAT gain/degradation recorded for the different scenarios was presented by defining the MAT ratios of the scenarios ($P1R1/PxR1$), ($P1R2/PxR2$) and ($P1R4/PxR4$), where we have $x = 2$ or 4. To elaborate a little further, there would have been some benefit in using the same normalisation factor such as the MAT of the single receiver system $R1$ for all the different scenarios, but we found that the above-mentioned definitions were more suitable for explicitly demonstrating the impact of the number of transmit antennas. As shown in Figure 3.6, for example the $P2R1$ and $P2R2$ scenarios exhibit a modest MAT gain for E_c/I_0 values between -11 and -8 dB and between -12 and -9 dB, respectively, but in the rest of the SINR region a MAT degradation is experienced. Here all the performance curves have been generated at the threshold value of E_c/I_0 = -13 dB, which was considered as the minimum value required for reliable finger locking. More quantatively, observe in Figure 3.6 that in order to achieve the MAT ratio of unity, corresponding to no transmit-antenna-induced MAT loss, we need about 2 dB more power for the $P2R1$ scenario. Alternatively, the cell radius would have to be reduced by an appropriate path-loss-dependent factor, if no transmit-antenna-induced MAT degradation can be tolerated. Therefore the employment of MIMO may lead to the reduction of the attainable cell size, since no communications are possible until code acquisition has been completed.

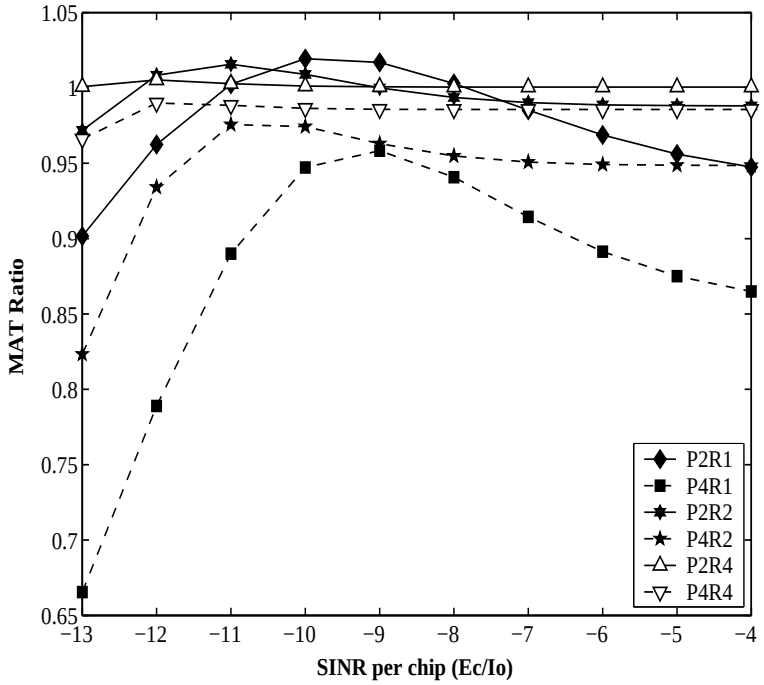

Figure 3.6: MAT ratio versus E_c/I_0 value, when using the schematic of Figure 2.2 and Table 3.1.

In summary, multiple transmit antennas constitute an efficient means of improving the attainable diversity gain, and/or system throughput, when communicating over mobile channels. However, for the sake of fair comparisons, the total signal power transmitted from the multiple transmit antennas must be fixed, regardless of their number. In other words, the total transmit power must be equally shared by all the transmit antennas. This implies that an excessively low level of per-branch received signal strength would lead to a low acquisition performance, even if the transmit multiplexing/diversity gain is high. In other words, a high diversity order effectively results in an acquisition performance loss, as a consequence of the insufficiently high transmit signal strength per branch. In case of employing both multiple transmit and receive antennas, this trend is still observable, although using two or four receive antennas has the potential of mitigating the associated acquisition performance degradation imposed by the low per-branch E_c/I_0 values encountered.

3.2.3 Conclusion

In this section, we analysed the MIMO aided initial acquisition performance of the inter-cell synchronous CDMA DL. Ironically, our findings suggest that increasing the number of transmit antennas results in combining the low-energy, noise-contaminated signals of the

transmit antennas, which ultimately reduces the correct detection probability, as evidenced by Figures 3.1 to 3.5. However, it is extremely undesirable to degrade the achievable acquisition performance, when the system is capable of attaining its target bit error rate performance at reduced SINR values, as a benefit of employing multiple transmit antennas. It may be concluded that the achievable cell coverage determined by the received pilot channel power may be reduced, as observed in Figure 3.6, as the number of transmit antennas is increased, which is a highly undesirable phenomenon, since it has grave repercussions in terms of having to tolerate a high number of handovers per cell.

3.3 Initial and Post-Initial Acquisition in Co-located Scenario

3.3.1 Concept of Initial and Post-Initial Acquisition

The classic serial search techniques designed for initial acquisition [3] have been traditionally employed in specific scenarios, where the uncertainty region (or search window width) is quite wide (i.e. $2^{15} - 1$) and hence in the context of serial search it is the MAT, which constitutes the most pertinent performance criterion, as seen for example in the DL of the inter-cell synchronous CDMA-2000 system [3]. In the case of initial acquisition contrived for DS-CDMA, the main design goal is to acquire accurate timing of the first received signal path impinging at the receiver, since this timing information is used as that of the reference finger of the Rake receiver. By contrast, the post-initial acquisition procedure that extracts the accurate timing positions of the remaining delayed paths and identifies the appropriate paths earmarked for processing by the Maximum Ratio Combining (MRC) scheme of the Rake receiver, has a major impact on the performance of the Rake receiver [8]. There are two main differences between the initial and post-initial acquisition procedures. First of all, once the first Rake finger is synchronised, the uncertainty region that has to be explored will be shrunk to $\pm\xi$ hypotheses surrounding the time-instant, where the first received path was found. This reduced interval will be referred to as the 'reduced uncertainty region' to be explored after the initial acquisition [7]. This search window width is defined by both the dispersion of the multipath propagation environment encountered as well as by the appearance and disappearance of propagation paths [111]. Secondly, the post-initial acquisition procedure commences after the Automatic Frequency Control (AFC) operation was activated for the sake of fine tracking, following the successful initial acquisition. Hence,

the performance degradation imposed by the associated frequency mismatch is considerably reduced compared to that immediately after the initial acquisition. Accordingly, these two factors are taken into account in our forthcoming analysis.

3.3.2 System Parameters

Figure 2.5 depicts the block diagram of the NC receiver designed for our code acquisition scheme using MIMO. The MAT formulae of both the SDSS and DDSS provided in Sections 2.4.1 and 2.4.2 are also employed for the performance analysis of this section. The associated system parameters are summarised in Table 3.3. In Tables 3.4 and 3.5 we outlined the maximum SINR degradation imposed by both the Doppler shift and the clock-drift-induced frequency mismatch between the transmitter and receiver in conjunction with the coherent integration interval of N chip durations seen in Figure 2.5 for both initial and post-initial acquisition. The length of the PN sequence in our system was assumed to be $(2^{15}-1)\cdot T_c$, where the chip-duration was $T_c = 1/1.2288\mu s$. In the case of the initial

Table 3.3: System Parameters

Bandwidth		1.25 MHz
Carrier frequency		1.9 GHz
Spreading factor		128
Diversity:	Transmit	1,2,4
	Receive	1,2,4
Frequency mismatch (Initial)		1000 Hz
Frequency mismatch (Post-Initial)		200 Hz
Mobile speed		160km/h
Num. of chip	SDSS	128 chips
	DDSS	32 and 256 (or 128) chips
Total uncertainty region (Initial)		65,534 hypotheses
Total uncertainty region (Post-Initial)		124 hypotheses
False locking penalty factor		1000 chip-durations
Number of paths		single and three path(s)

acquisition scheme of Figure 2.5, it was found to be sufficient to integrate the detector output seen in Figure 2.5 over N =128 chips for the sake of analysing SDSS, while the number of chips over which the accumulator Σ of Figure 2.5 sums the $(\cdot)^2$ envelope detector's

Table 3.4: Maximum SINR degradation inflicted by both the Doppler shift and a 1000 Hz frequency mismatch in conjunction with the coherent integration interval of N chip durations at a carrier frequency of 1.9 GHz

N(Chips)	64	128	256	384	512
Degradation(dB)	0.061	0.2449	0.9969	2.3144	4.3213

Table 3.5: Maximum SINR degradation inflicted by both the Doppler shift and a 200 Hz frequency mismatch in conjunction with the coherent integration interval of N chip durations at a carrier frequency of 1.9 GHz

N(Chips)	128	256	384	512	640	768
Degradation(dB)	0.032	0.128	0.289	0.5159	0.812	1.179

output in both the search and the verification modes of DDSS are assumed to be 32 and 256 in the $R = 1$ receive antenna scenarios or 128 in the $R = 4$ receive antenna scenario, respectively. By contrast, in the case of the post-initial acquisition scheme of Figure 2.5, the optimised length of coherent summation of the detector output values invoked for the sake of analysing SDSS is given in Table 3.6, whilst 64 is selected as the length of coherent summation in the search mode of DDSS. Finally, the optimised intervals of the coherent summation used in the verification mode of DDSS are portrayed in Table 3.7. The numbers seen in $(\cdot)$ in both Tables 3.6 and 3.7 can be used as an alternative. Its basic operation is identical for both the initial and post-initial acquisition schemes, except for using different coherent summation intervals necessitated by the different frequency mismatch of the two schemes. These optimised parameter values were calculated by using the formulae of the probability of the correct detection and false alarm in Section 2.3.2.3, the MAT expression of Section 2.4 as well as Equation. 2.9 of Section 2.3.2.1 provided for determining the performance degradation owing to both the Doppler shift and the frequency mismatch. The spreading factor of the Walsh code to be acquired was selected to be 128. The frequency mismatch was assumed to be 1000 Hz for the initial acquisition [3] and 200 Hz for the post-initial acquisition phases [8], while the carrier frequency was 1.9 GHz. As an example of a high mobile speed, it is reasonable to postulate 160 km/h. We also assumed that the sampling inaccuracy caused by having a finite, rather than infinitesimally low search step size of $\Delta = T_c/2$ was -0.91 dB, which is a typical value for the search step size [3]. The total uncertainty region of initial and post-initial acquisition were assumed to entail 65,534 and 124 hypotheses, respectively. Finally, in the spirit of [15], the false locking penalty

factor was assumed to be 1000 chip-durations. Finally, both single-path and multi-path scenarios were considered. In this scenario both a single-path and a group of three paths arriving with a relative time delay of one chip were considered. Both CIRs had the same magnitude for the first received path as well as 3 dB lower for the second and 6 dB lower for the third received paths, respectively, compared to the LOS path of a single-path scenario. All the performance curves, except for Figures 3.12 and 3.13, have been obtained at the optimum decision threshold of $E_c/I_0 = -13\,dB$ designed for the initial acquisition scheme and at $E_c/I_0 = -19\,dB$ invoked for the post-initial acquisition scheme, respectively. The operational range of the post-initial acquisition scheme was assumed to be 6 dB lower than that of the initial acquisition arrangement, because the signal power of the delayed paths is typically lower than that of the first received path.

Table 3.6: Optimised length of coherent summation of the detector outputs invoked for the sake of analysing SDSS in post-initial acquisition

Transmit/Receive	P1R1	P2R1	P4R1	Transmit/Receive	P1R4	P2R4	P4R4
Length (Chips)	512	512	640	Length (Chips)	256 (128)	256 (384)	384

Table 3.7: Optimised length of coherent summation of the detector outputs invoked in the verification mode for the sake of analysing DDSS in post-initial acquisition

Transmit/Receive	P1R1	P2R1	P4R1	Transmit/Receive	P1R4	P2R4	P4R4
Length (Chips)	384	640	768	Length (Chips)	256 (384)	384	512

3.3.3 System Performance Results

Figure 3.7 illustrates the achievable MAT versus SINR per chip performance for our SDSS aided initial acquisition scheme as a function of the number of transmit antennas for $P = 1$, 2 as well as 4 and that of the number of receive antennas for $R = 1$ and 4. In the results of Figures 3.7 to 3.11, except for Figure 3.9, the bold lines indicate the scenario of receiving three paths (denoted as $M3$ in Figures 3.7 to 3.11, except for Figure 3.9), whereas the thinner lines represent a single-path scenario (denoted as $M1$ in Figures 3.7

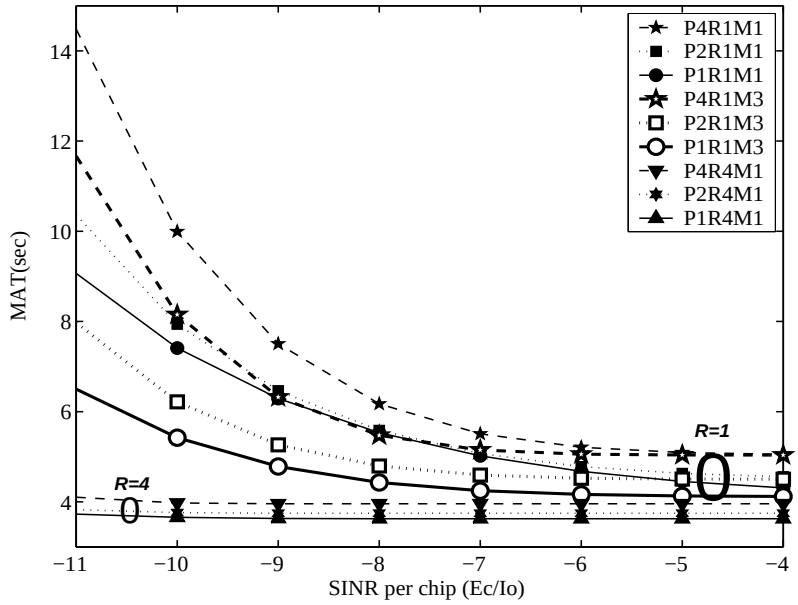

Figure 3.7: MAT versus SINR per chip performance of the initial acquisition scheme for SDSS parameterised with both the number of transmit and receive antennas, when employing the schematic of Figure 2.5 and Table 3.3.

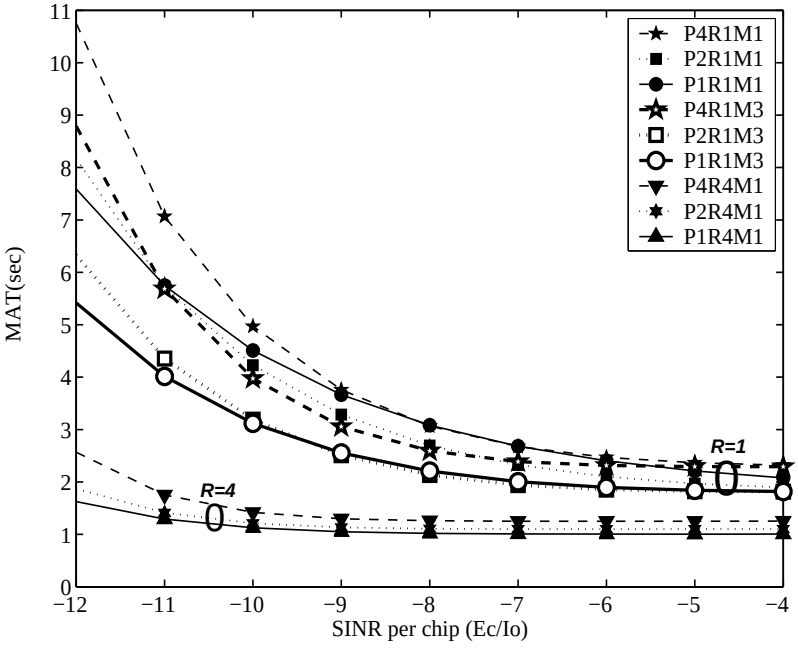

Figure 3.8: MAT versus SINR per chip performance of the initial acquisition scheme for DDSS parameterised with both the number of transmit and receive antennas, when employing the schematic of Figure 2.5 and Table 3.3.

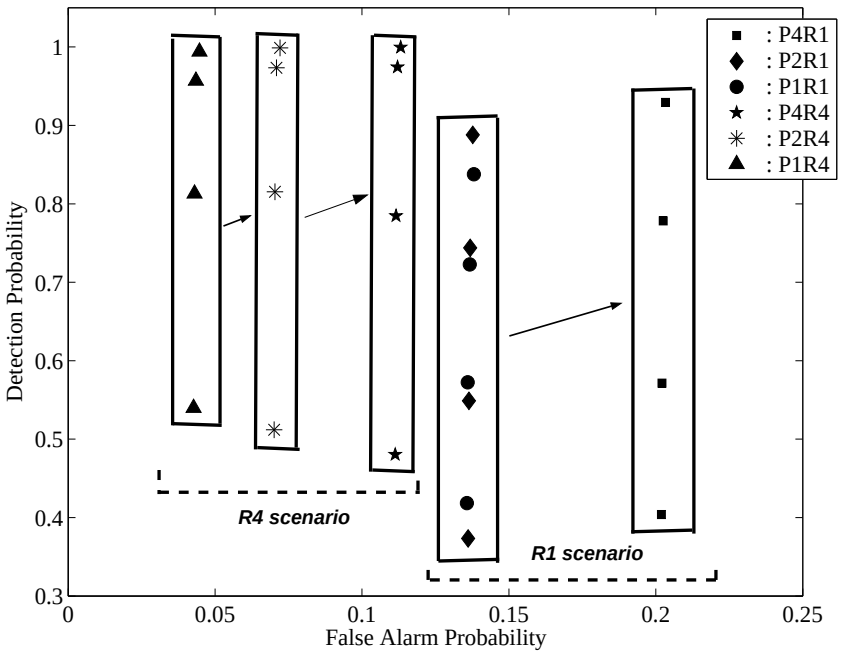

Figure 3.9: Operating ranges in the search mode of the initial acquisition scheme for the sake of obtaining the best possible MAT performance. The four vertically stacked points seen in the figure correspond to E_c/I_0 = -4, -7, -10 and -13 dB, respectively, from the top to the bottom, when employing the schematic of Figure 2.5 and Table 3.3.

to 3.11, except for Figure 3.9). Observe in Figure 3.7 that somewhat surprisingly, as the number of transmit antennas is decreased, despite the potentially reduced transmit diversity gain, we experience an improved MAT performance for both the single-path and multi-path scenarios. Since the number of the successfully detected states was increased by a factor of three, the MAT performance of this scenario becomes better than that of the single-path one. In the case of $R = 4$ receivers the performance improvements due to having multiple paths become marginal, because the receive diversity gain is already sufficiently high for having a near-Gaussian MAT-performance. Hence the results of the multi-path scenario of $R = 4$ were omitted in order to avoid obfuscating details. For comparison, Figure 3.8 characterises the MAT versus SINR per chip performance of DDSS for the initial acquisition arrangement as a function of the number of transmit antennas for $P = 1$, 2 as well as 4 and that of the number of receive antennas for $R = 1$ and 4. Similarly to the conclusions of Figure 3.7, as the number of transmit antennas is decreased, all the curves seen in Figure 3.8 illustrate an improved MAT performance, except that a useful transmit diversity gain is experienced only for the case of $'P2R1'$, and even this gain was limited to the specific SINR range of -4 and -11 dB in the single-path scenario. In the case of DDSS, the performance improvements obtained for the three-path scenario are less than those of SDSS. It is worth

mentioning that although not explicitly shown in Figures 3.7, 3.8, 3.10 and 3.11 for avoiding obfuscating details, the operating range of $R = 2$ receive antennas was found to be between that corresponding to the $R = 1$ and $R = 4$ receive antenna scenario. To illustrate the above fact a little further, in the case of $'P2R1'$ the DDSS scheme exhibits a better MAT performance in comparison to the $'P1R1'$ arrangement across the specific SINR range shown in Figure 3.8. This is because in the case of DDSS the reliable operational ranges expressed in terms of both the correct detection and the false alarm probability are quite different from those of SDSS. More explicitly, the reliable operational range of SDSS associated with the best possible MAT performance is around a false alarm probability of 10^{-4}. On the other hand, the reliable operation of DDSS may be maintained at as high a false alarm probability, as 0.2 when the number of transmit antennas is increased from $P = 1$ to $P = 4$ in conjunction with $R = 1$ receive antenna, as demonstrated in Figure 3.9. Furthermore, in case of $R = 4$ receive antennas, similar trends are observed, even though the region of the reliable DDSS operation is shifted to the left with respect to the case of a single receive antenna, as seen in Figure 3.9. It is worth mentioning that the operating range of $R = 2$ receive antennas is in between that corresponding to $R = 1$ and $R = 4$ receive antennas, for the sake of avoiding obfuscating points in the figure, the $R = 2$ scenario was omitted. Accordingly, while the reliable operational range of SDSS is around a false alarm probability of 10^{-4}, that of DDSS in the search mode varies more widely, namely across the range spanning from 0.04 to just over 0.2, depending on the specific number of transmit and receive antennas. This manifests itself also in terms of having detection threshold values in the search mode of DDSS, which are substantially lower than those of SDSS, when optimised for the sake of attaining the best possible MAT performance. This clearly implies that DDSS benefits from a significantly higher diversity gain than SDSS. The performance degradation imposed by employing multiple antennas becomes more drastic, as the number of transmit antennas is increased for both the SDSS and DDSS schemes in the initial acquisition scenario. Furthermore, the associated MAT performance discrepancy between the SDSS and DDSS schemes becomes more drastic. In case of employing both multiple transmit and multiple receive antennas, similar trends are observable, although using two or four receive antennas has the potential of mitigating the associated acquisition performance degradation imposed by the low per-branch E_c/I_0 values associated with the employment of multiple transmitters.

Figure 3.10 and 3.11 characterise the achievable MAT versus SINR per chip performance of post-initial acquisition. The results are parameterised by both the number of transmit

antennas for P = 1,2 as well as 4 and by the number of receive antennas for $R = 1$ as well as 4 for both the SDSS (Figure 3.10) and for the DDSS schemes (Figure 3.11), respectively. Even though the optimised coherent summation intervals determined for the sake of obtaining the best possible MAT performance are quite different, as the number of transmit antennas is decreased, all the curves seen in both Figures 3.10 and 3.11 indicate an improved MAT performance, as we observed in the case of initial acquisition in both Figures 3.7 and 3.8. This trend explicitly indicates that the DDSS scheme also degrades the achievable MAT performance as a consequence of the low per-antenna power imposed by employing multiple transmit antennas for the sake of attaining a transmit diversity gain. However, the MAT performance degradation imposed is less severe than that of the SDSS scheme. Moreover, the performance improvements of the initial acquisition scheme recorded for SDSS in Figure 3.7 as a benefit of having multiple paths is more significant than those of the post-initial acquisition arrangement shown for SDSS in Figure 3.10. The initial acquisition scheme having multiple received paths contributes to the attainable performance improvements. On the other hand, observe in Figure 3.11 that in the case of DDSS, the performance improvements obtained for the three-path scenario are lower than those of SDSS in both the initial and post-initial acquisition scenarios. The performance improvements due to having multiple paths become the lowest for the post-initial acquisition arrangement using DDSS in Figure 3.11. Both Figures 3.12 and 3.13 illustrate the achievable MAT versus the detection threshold value for DDSS of both the initial and post-initial acquisition schemes, respectively, parameterised by both the number of transmit antennas for P = 1,2 as well as 4 in conjunction with $R = 1$ receive antenna and by the SINR per chip values seen in the legends. As seen in Figures 3.12 and 3.13, the sensitivity with respect to the detection threshold value becomes significantly higher as the value of E_c/I_0 is decreased, although the degree of the sensitivity is quite different depending upon the number of transmit antennas. Similarly, the associated MAT performance difference observed in Figures 3.12 and 3.13 also become quite dramatic in case of the initial acquisition scheme for E_c/I_0 = -13 dB and for the post-initial acquisition arrangement at -19 dB. The results of Figure 3.12 explicitly demonstrate that the MAT experienced at -13 dB exceeds 10 sec, a value which is in excess of the useful practical operational range of the system. In conclusion, the sensitivity of the MAT performance with respect to the detection threshold value depends on both the number of transmit as well as receive antennas. Accordingly, to interpret all the above results a little further, a low level of per-branch received signal strength would lead to a low acquisition performance, despite achieving a high transmit diversity gain. In other words,

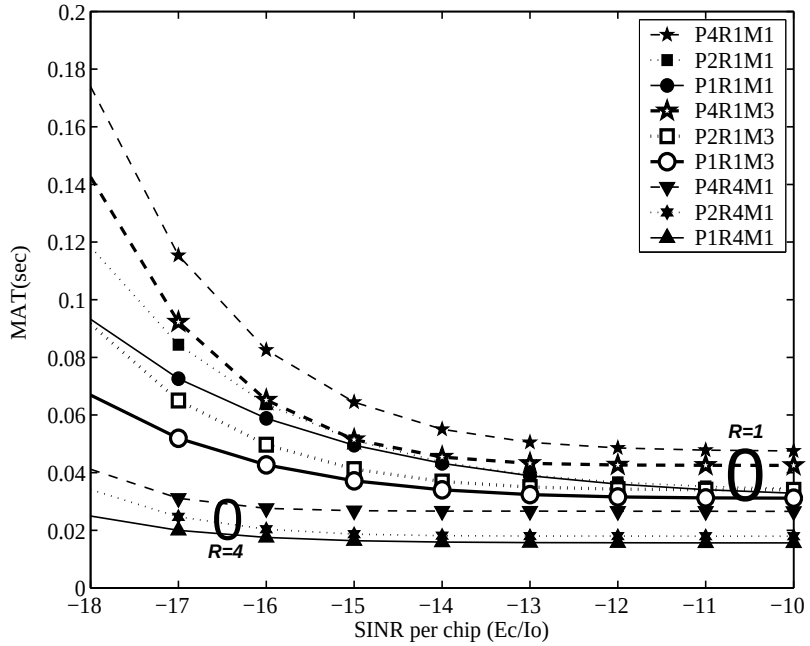

Figure 3.10: MAT versus SINR per chip performance of the post-initial acquisition scheme for SDSS parameterised with both the number of transmit and receive antennas, when employing the schematic of Figure 2.5 and Table 3.3.

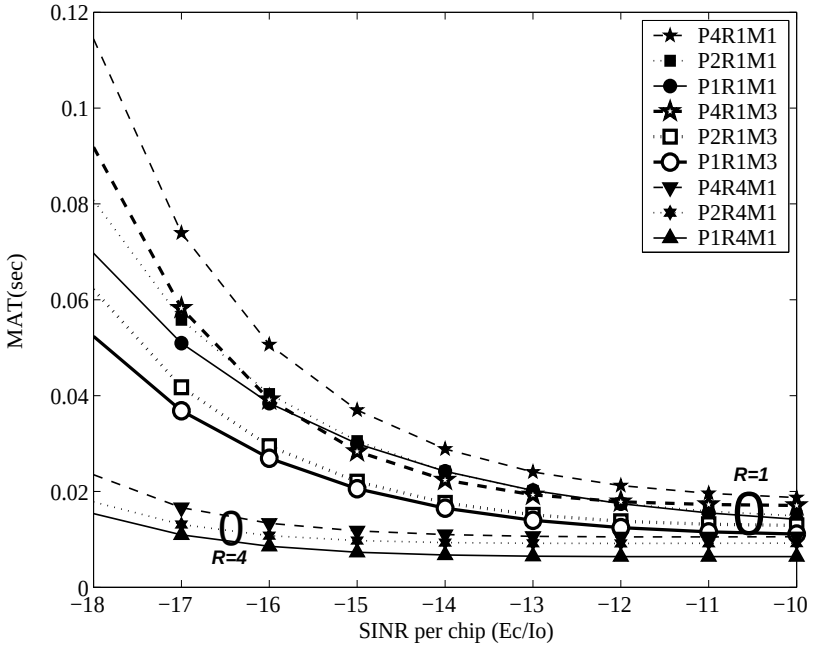

Figure 3.11: MAT versus SINR per chip performance of the post-initial acquisition scheme for DDSS parameterised with both the number of transmit and receive antennas, when employing the schematic of Figure 2.5 and Table 3.3.

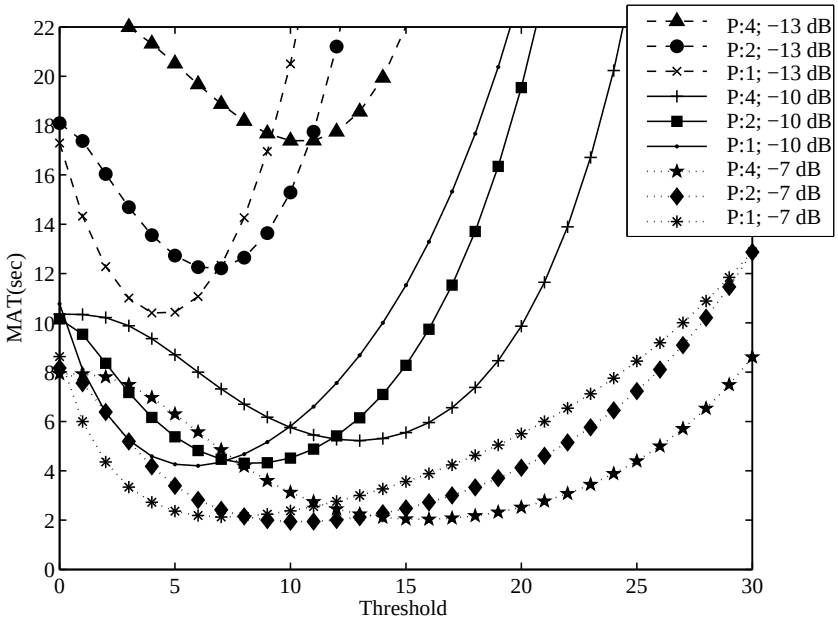

Figure 3.12: MAT versus the detection threshold value of the initial acquisition scheme for DDSS parameterised with $P = 1, 2$ as well as 4 transmit antennas in conjunction with $R = 1$ receive antenna for transmission over uncorrelated Rayleigh channels, when employing the schematic of Figure 2.5 and Table 3.3.

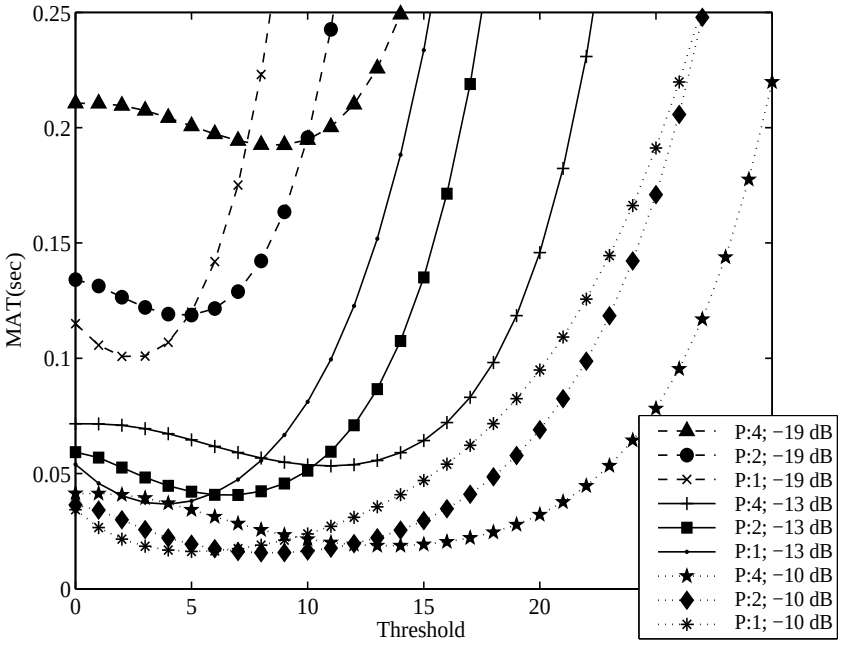

Figure 3.13: MAT versus the detection threshold value of the post-initial acquisition scheme for DDSS parameterised with $P = 1, 2$ as well as 4 transmit antennas in conjunction with $R = 1$ receive antenna for transmission over uncorrelated Rayleigh channels, when employing the schematic of Figure 2.5 and Table 3.3.

a high transmit diversity order effectively results in an acquisition performance loss, as a consequence of the insufficiently high signal strength per transmit antenna branch.

The main reasons for the above-mentioned performance trends may be further justified by information theoretic considerations in the NC MIMO aided scenarios considered [112, 113, 114]. The characteristics of the NC MIMO aided scenarios may be summarised as follows:
Wireless systems employing MIMO exhibit a high capacity, provided that the channel is known to the receiver [95]. By contrast, a NC MIMO aided scheme, which does not rely on any channel knowledge has a lower capacity [112, 113, 114]. However, it was argued in [113] that there is no reason for using more than $T_{sym}/2$ number of transmit antennas, where $T_{sym} = 2$ was the specific number of symbols over which integration was carried out when generating the results of both Tables 3.4 and 3.5, because the number of degrees of freedom increases with $T_{sym}/2$, but only until the number of transmit antennas P approaches $T_{sym}/2$ [113]. Furthermore, at low SINRs the mutual information between the transmitter and receiver is maximised by using a single transmit antenna, because the mutual information bounds were shown to be decreasing functions of P [114]. This implies that using multiple transmit antennas provides no MAT performance gain in the low SINR region, in fact, rather surprisingly, it leads to an MAT performance degradation. Finally, in the medium SINR range a maximum of T_{sym} transmit antennas is worth employing for the sake of achieving an MAT performance gain, because the capacity achieved for $P > T_{sym}$ is the same as that achieved for $P = T_{sym}$ [112]. This indicates that $P = 2$ transmit antennas are capable of achieving an improved MAT performance in the SINR region of -4 and -11 dB, as demonstrated for the single-path scenario of Figure 3.8.

Accordingly, when considering the design of MIMO aided code acquisition schemes, the following guidelines may be inferred from Figures 3.7 to 3.13:

a) Using multiple transmit antennas typically leads to an MAT performance degradation, except for the $'P2R1'$ scenario encoutering a single-path environment, as evidenced by Figures 3.7, 3.8, 3.10 and 3.11. Using a relatively low number of chips, over which integration or accumulation is carried out imposes further limits on the attainable benefits of MIMO. In the multi-path scenarios considered all the schemes fail to show a transmit diversity gain, as observed in Figures 3.7, 3.8, 3.10 and 3.11. Therefore, employing a single transmit antenna might be recommended for maximising the achievable performance of both the initial and post-initial acquisition schemes investigated. Furthermore, using a sufficiently high number

of Post-Detection Integration (PDI) stages is also beneficial for minimising the MAT [1].

b) Using multiple receive antennas increases the achievable receiver diversity gain and has the potential of compensating for the MAT degradation imposed by the low per-branch power of multiple transmitters, as demonstrated by $R = 4$ receive antenna scenario in Figures 3.7, 3.8, 3.10 and 3.11.

c) For the sake of acquiring the exact timing information of the received paths, specifically designed preambles, such as that of the Primary Synchronization Channel (P-SCH) of W-CDMA [115] combined with Time-Switched Transmit Diversity (TSTD) [116] might be recommended, which is capable of achieving a diversity gain with the aid of a single transmit antenna [113, 114]. In practical scenarios, the received path timing differences of the signals arriving from multiple transmit antennas might be distributed within a fraction of a chip duration [117], although they may vary owing to the time-variant propagation delay, hence using multiple transmit antennas may further degrade the attainable performance. In addition to initial acquisition, the classic pilot channel may also be used for carrier frequency error correction and channel estimation [118].

3.3.4 Conclusion

In this section, we analysed the MIMO aided diversity effects on the performance of both initial and post-initial acquisition schemes in the inter-cell synchronous CDMA DL. Ironically, our findings suggest that increasing the number of transmit antennas in a MIMO-aided CDMA system results in combining the low-energy, noise-contaminated signals of the transmit antennas, which ultimately degrades the achievable MAT performance, when the SINR is relatively low, regardless whether single-path or multi-path scenarios are considered, as evidenced by Figures 3.7, 3.8, 3.10 and 3.11. This phenomenon has a detrimental effect on the attainable performance of Rake receiver based synchronisation, when the perfectly synchronised system is capable of attaining its target bit error rate performance at reduced SINR values, as a benefit of employing multiple transmit antennas. Based on the above-mentioned results justified by information theoretic considerations, our acquisition design guidelines are applicable to diverse NC MIMO aided scenarios.

[1]The underlying philosophy of PDI is that a decision variable is generated by accumulating T consecutive N-spaced signal samples observed over multiple N-spaced time intervals to improve the P_D in the mobile channel imposing both fading and poor SINR conditions. This specific number must be determined by satisfying a pair of targeted P_D and P_F values for the sake of minimising the MAT.

3.4 Co-located MIMO Aided Code Acquisition in the MC-DS-CDMA Downlink

3.4.1 System Architecture and System Parameters

Figure 2.6 illustrates the schematic diagram of the transmitter used in the MC-DS-CDMA DL having both P antennas and U subcarriers. Figure 2.7 depicts the block diagram of the NC receiver designed for our MC-DS-CDMA code acquisition scheme using MIMO. The MAT formulae of both the SDSS and DDSS in Sections 2.4.1 and 2.4.2 are also employed for the performance analysis. Our performance comparison between the SC-DS-CDMA system ($U = 1$) and various MC-DS-CDMA ($U = 2$ and 4) systems using different number of subcarriers is based upon the assumptions that these systems employ the same total transmitted energy per chip. Furthermore, it is assumed that the integral dwell time, τ_D, is the same for all the scenarios considered here. The associated system parameters are summarised in Table 3.8. In Table 3.9 we outlined the maximum SINR degradation imposed by both the Doppler shift and the clock-drift-induced frequency mismatch between the transmitter and receiver in conjunction with the coherent integration interval of τ_D durations, as seen in Figure 2.7. The length of the PN sequence in our system was assumed to be $(2^{15} - 1) \cdot T_c (or T_{c1})$, where the chip-durations employed here for $U = 1, 2$ and 4 are $T_{c1} = 1/2.4576 \mu s$, $T_c = 1/1.2288 \mu s$ and $T_c = 1/0.6144 \mu s$, respectively. Based on [25], when communicating over various fading channels having delay spreads in the range of [0.1μs,3μs], the fading processes of the adjacent subcarriers in our MC-DS-CDMA system are considered to be uncorrelated. The number of chips over which the accumulator Σ of Figure 2.7 sums the $(\cdot)^2$ envelope detector's output in both the search and the verification modes of DDSS is assumed to be 128 and 512 in the SC scheme of $U = 1$. By contrast, the number of chips over which the accumulator summed the envelope detector's output is 64 and 256 in the $U = 2$ based MC-DS-CDMA arrangement, while 32 and 128 in the $U = 4$ scenarios, respectively. These optimised parameter values were calculated by using both the probability of correct detection and false alarm. Furthermore, the MAT formula of Equation 2.126 derived for a single-path scenario and Equation 2.128 valid for the multi-path scenario of Section 2.4.2 as well as Equation. 2.9 of Section 2.3.2.1 were used, which were provided for quantifying the performance degradation owing to both the Doppler shift and the frequency mismatch encountered. The spreading factor of the Walsh code to be acquired was selected to be 128. The frequency mismatch was assumed to be 1000 Hz

[3], while the carrier frequency was 1.9 GHz. As an example of a high mobile speed, it is reasonable to postulate 160 km/h. We also assumed that the sampling inaccuracy caused by having a finite, rather than infinitesimally low search step size of $\Delta = T_c/2$ was -0.91 dB, which is a typical value for this particular search step size [3, 14]. The total uncertainty region of code acquisition was assumed to entail 65,534 hypotheses. Finally, in the spirit of [15], the false locking penalty factor was assumed to be 1000 chip-durations. Finally, both single-path and multi-path scenarios were considered. In the $U = 1$ scenario both a single-path and a three-path scenario were considered. Each of the two delayed paths arrived with a relative time delay of one chip and a 3 dB lower magnitude for the first received path as well as 6 dB lower for both the second and the third received paths, respectively, when compared to the LOS path of a single-path scenario. On the other hand, in the $U = 4$ scenario, only a single received signal path is encountered in a given search window. All the performance curves in Figures 3.14 and 3.15 have been obtained at the value of E_c/I_0 = -16 dB. This is a threshold value in the range of 'finger locking', which may be considered to be the range between E_c/I_0 = -17 and -13 dB [72, 110].

Table 3.8: System Parameters

Bandwidth	$U = 1$	2.5 MHz
	$U = 4$	4×0.625 MHz
Carrier frequency		1.9 GHz
Spreading factor		128
Diversity	Transmit	1,2,4
	Receive	1,2,4
	Subcarrier	1,2,4
Frequency mismatch		1000 Hz
Mobile speed		160km/h
Schemes selected		Number of chip
SDSS	$U = 1$	512 chips
	$U = 2$	256 chips
	$U = 4$	128 chips
DDSS	$U = 1$	128 and 512 chips
	$U = 2$	64 and 256 chips
	$U = 4$	32 and 128 chips
Total uncertainty region		65,534 hypotheses
False locking penalty factor		1000 chip-durations
Number of paths		single and three path(s)

Table 3.9: Maximum SINR degradation inflicted by both the Doppler shift and a 1000 Hz frequency mismatch in comparison to a stationary receiver having no frequency drift for the coherent integration interval of N chip durations at a carrier frequency of 1.9 GHz as a function of the number of subcarriers ($U = 1, 2$ and 4)

N(Chips): U=1	**128**	256	**512**	768	1024
N(Chips): U=2	**64**	128	**256**	384	512
N(Chips): U=4	**32**	64	**128**	192	256
Degradation(dB)	**0.061**	0.2449	**0.9969**	2.3144	4.3213

3.4.2 System Performance Results

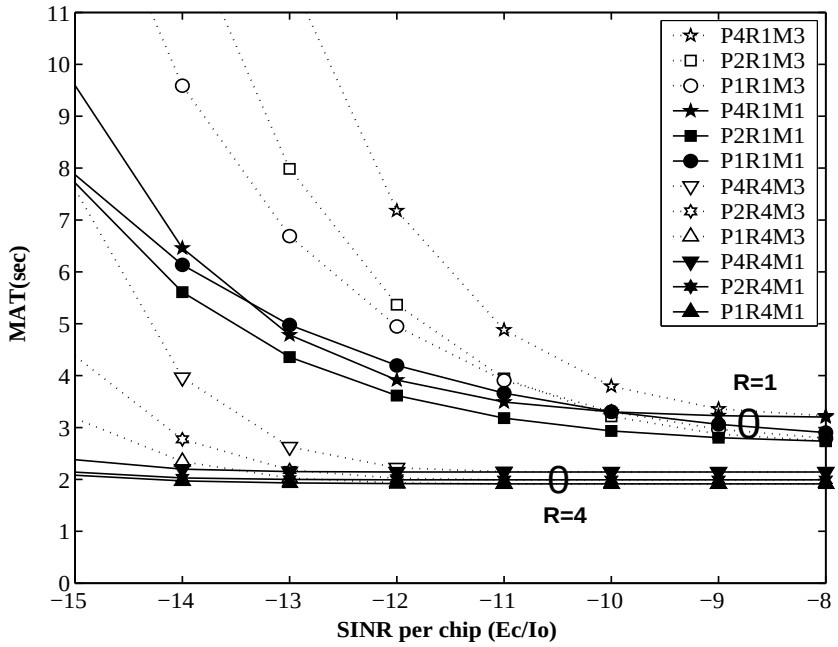

Figure 3.14: MAT versus E_c/I_0 performance of the DDSS-aided SC-DS-CDMA code acquisition scheme parameterised with both the number of transmit and receive antennas, when using the schematic of Figures 2.6 and 2.7 as well as Table 3.8.

Figure 3.14 characterises the MAT versus E_c/I_0 performance of DDSS for the SC-DS-CDMA code acquisition arrangement as a function of the number of transmit antennas for $P = 1$,2 as well as 4 and that of the number of receive antennas for the specific values of $R =$ 1 and 4. In the results of Figures 3.14 and 3.15, the solid lines indicate a single-path scenario (denoted as $M1$ in Figures 3.14 and 3.15), whereas the dotted lines represent the scenario of receiving three paths (denoted as $M3$ in Figure 3.14). It is worth mentioning that although not explicitly shown in Figures 3.14 and 3.15 for avoiding obfuscating details, the operating range of $R = 2$ receive antennas was found to be between that corresponding to the $R = 1$

and $R = 4$ receive antenna scenarios. As the number of transmit antennas was decreased, all the curves seen in Figure 3.14 illustrated an improved MAT performance for the systems exploiting $R = 4$ receive antennas in both the single-path and multi-path scenarios. Similar trends were observed also in the $R = 1$ receive antenna aided multi-path scenario, except for $R = 1$ in the specific E_c/I_0 range of the single-path system characterised in Figure 3.14. To elaborate on the above fact a little further, the $'P2R1'$ and $'P4R1'$ scheme communicating over a single-path channel exhibits a better MAT performance in comparison to the $'P1R1'$ arrangement across the specific E_c/I_0 range considered. In other words, this clearly implies that the scheme employing $R = 1$ receive antenna benefits from a higher diversity gain in the SC-DS-CDMA scenario having a sufficiently wider bandwidth. By contrast, even though the number of the successfully detected states was increased by a factor of three, the MAT performance of the multi-path scenario became worse than that of the single-path one. This is because a low 'per-path-power' would lead to a low acquisition performance in the multi-path scenario. Furthermore, the performance degradation imposed by employing multiple transmit antennas becomes more drastic in the low E_c/I_0 range, as the number of transmit antennas is increased in the scenario. In case of employing both multiple transmit and multiple receive antennas, similar trends are observable, although using two or four receive antennas has the potential of mitigating the associated acquisition performance degradation imposed by the low per-branch E_c/I_0 values associated with the employment of multiple transmitters. In the case of $R = 4$ receivers the performance degradations imposed by multiple paths become significantly lower than those in the $R = 1$ receive antenna scenario, because the receive diversity gain is already sufficiently high for achieving a near-Gaussian MAT-performance, provided that an E_c/I_0 in excess of -12 dB is maintained for both the single-path and multi-path scenarios. The $R = 4$ and $R = 1$ scenarios might be viewed as practical upper and lower bounds of the achievable MAT performances encountered. On the other hand, Figure 3.15 illustrates the achievable MAT versus E_c/I_0 performance of the DDSS-aided MC-DS-CDMA code acquisition scheme parameterised with the number of antennas, when using $U = 4$ subcarriers. In the case of the MC-DS-CDMA system, the scheme has an unnecessarily high diversity order, which is determined by the number of subcarriers used. It is also assumed that the total transmitted energy per chip is the same in all the scenarios considered. Accordingly, the effect of the inherent frequency diversity is the same as that of the multiple transmit antenna aided diversity, as documented in Section 2.3.2.1. This fact indicates that employing multi-carrier transmissions based on the DS-CDMA principle leads to exactly the same detrimental effect on the achievable

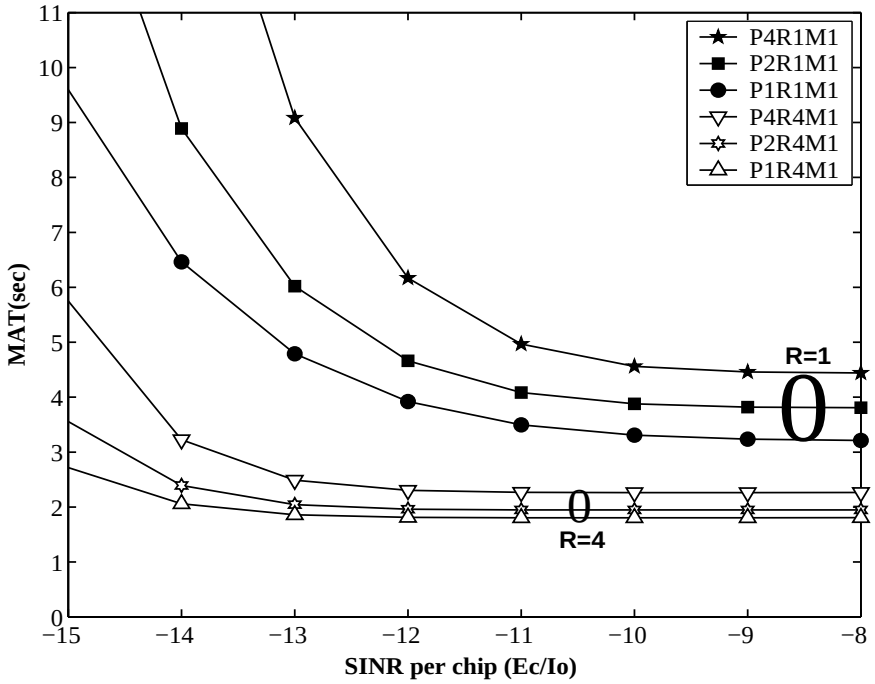

Figure 3.15: MAT versus E_c/I_0 performance of the DDSS-aided MC-DS-CDMA code acquisition scheme parameterised with both the number of transmit and receive antennas for $U = 4$ subcarriers, when using the schematic of Figures 2.6 and 2.7 as well as Table 3.8.

MAT performance as that imposed by employing the multiple transmit antennas. The results of Figure 3.15 are parameterised by both the number of transmit antennas for P = 1,2 as well as 4 and by the number of receive antennas for $R = 1$ as well as 4. As the number of transmit antennas is decreased, all the curves seen in Figure 3.15 indicate an improved MAT performance. This trend explicitly illustrates that the performance of the MC-DS-CDMA acquisition scheme becomes significantly worse than that of SC-DS-CDMA encountering a single-path. This is a consequence of both the low per-antenna power imposed by employing a transmit diversity gain and the low per-subcarrier power imposed by using a frequency diversity gain. To interpret the above results a little further, a low level of per-branch and/or per-subcarrier received signal strength would lead to a low acquisition performance, despite achieving a high transmit- and frequency-diversity gain, as a result of the insufficiently high signal strength per transmit antenna and per subcarrier. When comparing the results of Figures 3.14 and 3.15, the performance of the MC-DS-CDMA code acquisition scheme encountering a single-path is marginally better than that of the SC-DS-CDMA code acquisition scheme encountering three paths. It also suggests that a low level of per-path received signal strength would result in a low acquisition performance, despite having a four times higher number of accumulated chips over the same integral dwell

time.

Figure 3.16 documents the relationship between P_D and the number of transmit antennas required by the DDSS-aided code acquisition scheme for approaching their lowest possible MAT versus the number of subcarriers ($U = 1$ and 4), parameterised with both the number of transmit antennas and different values of E_c/I_0. The correct detection probabilities seen in Figure 3.16 were obtained assuming a false locking probability of $P_F = 10^{-3}$ for all scenarios considered, since the reliable operational range in the verification mode of the DDSS-aided code acquisition scheme is a false alarm probability spanning from 10^{-3} to 10^{-4}. The left illustration of Figure 3.16 characterises the scenario of $U = 1$, while the one at the right of Figure 3.16 is valid for the arrangememt having $U = 4$. When increasing the number of transmit antennas, the curves recorded for E_c/I_0 values spanning from -7 to -13 dB at the left of Figure 3.16 indicate a P_D improvement, although at low E_c/I_0 values, i.e. at E_c/I_0 = -16 dB, the opposite is true. On the other hand, the results at the right of Figure 3.16 indicate that P_D tends to decrease, as both the number of transmit antennas and the number of subcarriers increases, when typical E_c/I_0 values are encountered.

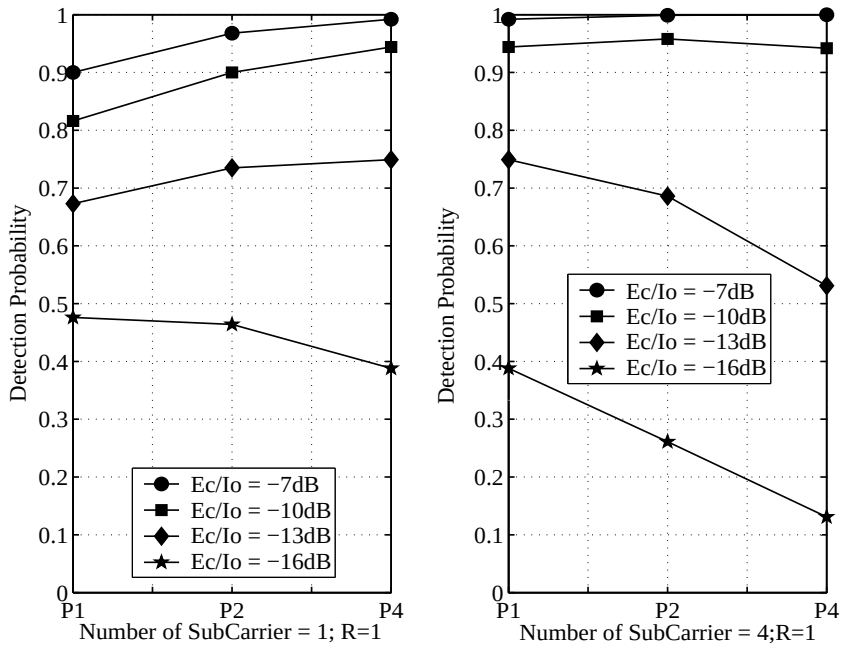

Figure 3.16: P_D versus the number of transmit antennas for P = 1,2 as well as 4, the number of receive antennas for P= 1 as well as the number of subcarriers for both $U = 1$ (Left figure) and $U = 4$ (Right figure) parameterised by the E_c/I_0, when using the schematic of Figures 2.6 and 2.7 as well as Table 3.8.

Figure 3.17 describes the relationship between the SINR per chip required by the DDSS-aided initial code acquisition scheme for approaching their lowest possible MAT versus the number of subcarriers ($U = 1, 2$ and 4) parameterised with both the number of transmit and receive antennas. More explicitly, for $R = 1$ and $R = 2$ receive antennas, the required E_c/I_0 values are compared at MAT = 6 and 4 seconds, respectively. As either the number of transmit antennas or the number of subcarriers is increased, the value of the required E_c/I_0 is also increased, except for the $'P1R1'$ scenario, benefiting from the positive effect of the increased frequency diversity gain. It is also worth mentioning that according to Figure 3.17 the required E_c/I_0 value tends to increase, as the number of subcarriers is increased, on provided that there exists no spectral overlap between the spectral main lobes of two adjacent subcarriers in the MC-DS-CDMA system considered [23]. Since the reliable operational range in the verification mode of the DDSS-aided initial code acquisition scheme is a false alarm probability spanning from 10^{-3} to 10^{-4}, as the number of subcarriers is increased, the correct detection probability considerably decreases according to the relationship between the correct detection versus false alarm probability formulated in Section 2.3.2.4. The main reasons for the above-mentioned performance trends may also be

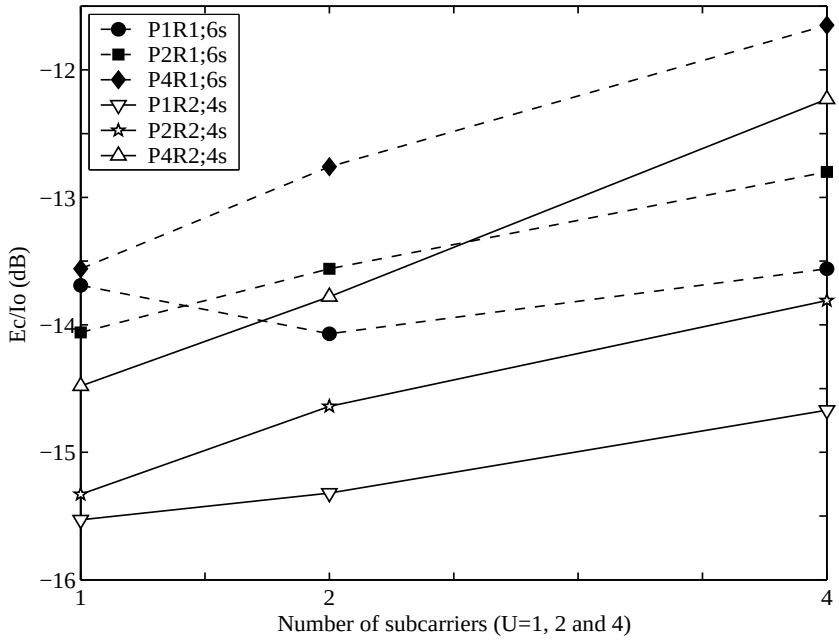

Figure 3.17: E_c/I_0 performance versus the number of subcarriers ($U = 1, 2$ and 4) of the DDSS-aided MC-DS-CDMA code acquisition scheme parameterised with both the number of transmit and receive antennas, when using the schematic of Figures 2.6 and 2.7 as well as Table 3.8.

further justified by the information theoretic considerations derived for NC MIMO aided

scenarios in [112, 113, 119]. Finally, when considering the design of MIMO aided code acquisition schemes, the following guidelines may be inferred from Figures 3.14, 3.15, 3.16 and 3.17:

a) As evidenced by Figures 3.14, 3.15 and 3.17, using multiple transmit antennas typically leads to an MAT performance degradation, owing to the reduced per-antenna transmit power, except for specific scenarios, when encountering a single-path environment, also depending on the allocated bandwidth. Using a relatively low number of chips, over which integration or accumulation is carried out, imposes further limits on the attainable benefits of MIMO [112, 113]. Furthermore, in the multi-path scenarios considered all the schemes of Figure 3.14 fail to show a transmit diversity gain. Therefore, activating only a single transmit antenna might be recommended for the sake of maximising the achievable MAT performance of the code acquisition scheme investigated before correct code acquisition is confirmed.

b) As seen in Figures 3.14, 3.15 and 3.17, employing multiple receive antennas increases the achievable receiver diversity gain and has the potential of compensating for the MAT degradation imposed by the low per-branch power of both multiple transmitters and multiple subcarriers.

c) In order to acquire the exact timing information of the received paths without any potential performance degradation that might be imposed on NC MIMO aided scenarios, specifically designed preambles, such as that of the primary synchronization channel of W-CDMA [115] combined with TSTD [116] might be recommended, which is capable of achieving a diversity gain with the aid of a single transmit antenna [113, 114]. The conventional pilot channel may also be used for other purposes, such as frequency error correction and channel estimation so as to support coherent MIMO aided scenarios [118].

3.4.3 Conclusion

In this section, we analysed the MIMO aided diversity effects on the performance of the code acquisition scheme of the inter-cell synchronous MC-DS-CDMA DL. Unexpectedly, our results suggest that increasing both the number of transmit antennas and that of the subcarriers in a MIMO-aided MC-DS-CDMA system results in combining the low-energy, noise-contaminated signals of both the transmit antennas and the subcarriers, which may degrade the MAT by an order of magnitude, when the SINR is relatively low, as evidenced

by Figures 3.14, 3.15, 3.16 and 3.17. This phenomenon imposes a grave degradation on the performance of Rake receiver aided initial code acquisition schemes, when the perfectly synchronised idealised system is capable of attaining its target bit error rate performance at reduced SINR values, as a benefit of exploiting both multiple transmit antennas and frequency diversity. Furthermore, communicating in a multi-path scenario also degrades the attainable performance. Based on the above-mentioned results, which are also corroborated by the information theoretic considerations of [113], our acquisition design guidelines are applicable to diverse NC MIMO aided scenarios.

3.5 Cooperative MIMO Aided Non-Coherent Code Acquisition

3.5.1 Cooperative Scenarios

In wireless networks, fading constitutes one of the main sources of channel-induced impairments. A powerful technique of overcoming the fading imposed by multi-path propagation is constituted by spatial diversity invoking MIMO, which has attracted substantial research interests [33, 34, 97]. Furthermore, the substantial appeal of MIMOs is that their capacity increases linearly with the Signal-to-Interference plus Noise Ratio (SINR), as opposed to the more modest logarithmic increment of the classic Shannon-Hartley law, which may be readily elucidated by assigning the increased transmit power to an additional antenna and therefore linearly increasing the throughput [35]. However, in realistic propagation environments, the multiple antenna's signals typically become correlated owing to the size-limitation of the MS and BS. Hence the spatial diversity gain of independently faded signals is often eroded. This phenomenon is typically imposed by shadow fading. In order to cope with this problem, various cooperative and Relay Station (RS)-aided transmission schemes have been proposed [120, 121, 122]. In low-complexity cooperative systems a MS receives the two-hop DL signal via the RS as well as the directly detected DL signal of the BS. Since these two signals generally arrive through completely different -rather than correlated- propagation paths, cooperative transmission becomes capable of mitigating the above-mentioned correlated shadow fading effects. Furthermore, exploiting the intermediate RS, cooperative transmission has the potential of extending the cell area and/or of improving the quality of cell-edge coverage, which results in requiring a reduced number of BSs. The RS in cooperative systems filters the signal received from the BS and retransmits it to the MS. The

relaying schemes are commonly classified into two types: Amplify-and-Forward (AF) as well as Decode-and-Forward (DF) regimes [121, 122]. In the AF scheme, the RS simply retransmits the scaled version of the encountered signal and hence the noise component may also be amplified. By contrast, the DF aided RS fully decodes the received signal and forwards the re-encoded version in order to avoid the noise amplification. However, the DF strategy undoubtedly increases the complexity of RSs. In cooperative or distributed MIMO aided scenarios, the RS may be constituted by an intermediate MS that is currently not engaged in active communication or by a fixed RS that is installed at a specific position in a cell. However, for the sake of creating high-reliability RSs, we consider fixed RSs as the master of a specific RS-aided network [122]. It is also assumed that there is a LOS path between the master RSs as well as the BS [122].

Our detailed scenario is demonstrated in Figure 3.18. Figure 3.18 illustrates our three-stage code acquisition scenario encountered in fixed RS-aided environments, when considering several RSs located in a cell, where (1) represents a BS, (2) indicates a RS being the master of the RS-aided network, (3) is a slave RS of the RS-aided network, (4) represents another slave RS of the RS-aided network, (5) indicates a MS travelling at low speed, (6) is another MS roaming at low speed and (7) represents a MS moving at high speed. The traffic cell is divided into three sectors and a fixed RS is employed in each sector. We assume that both the BS and the RS have a single transmit antenna. It is also assumed that the BS is capable of supporting all the functions required. Furthermore, both the BS and master RSs are capable of supporting handover functionalities, whilst the master RS supports both AF, DF as well as pilot transmission. We also assume that some of the slave RSs support AF, DF as well as signalling message transmission for the RS-aided cluster, while other slave RSs may only support AF and signalling message transmission. Only MSs travelling at low speed can be included in a cluster supported by slave RSs. It is worth noting that a substantial cell-size extension may be achieved by fixed master RSs. Furthermore, both the master and slave RSs are capable of achieving an improved throughput and a cooperative diversity gain. In Figure 3.18 the bold mark **[1]** suggests that Global Positioning System (GPS) aided synchronisation is employed for both the BS and fixed master RSs, the bold mark **[2]** indicates the required initial control procedures to be carried out between the BS and fixed RSs, whilst the bold mark **[3]** portrays the procedures associated with a specific master and the slaves in a RS-aided temporary cluster. Finally, the bold mark **[4]** illustrates the communication procedures employed by the RSs and a specific MS. The

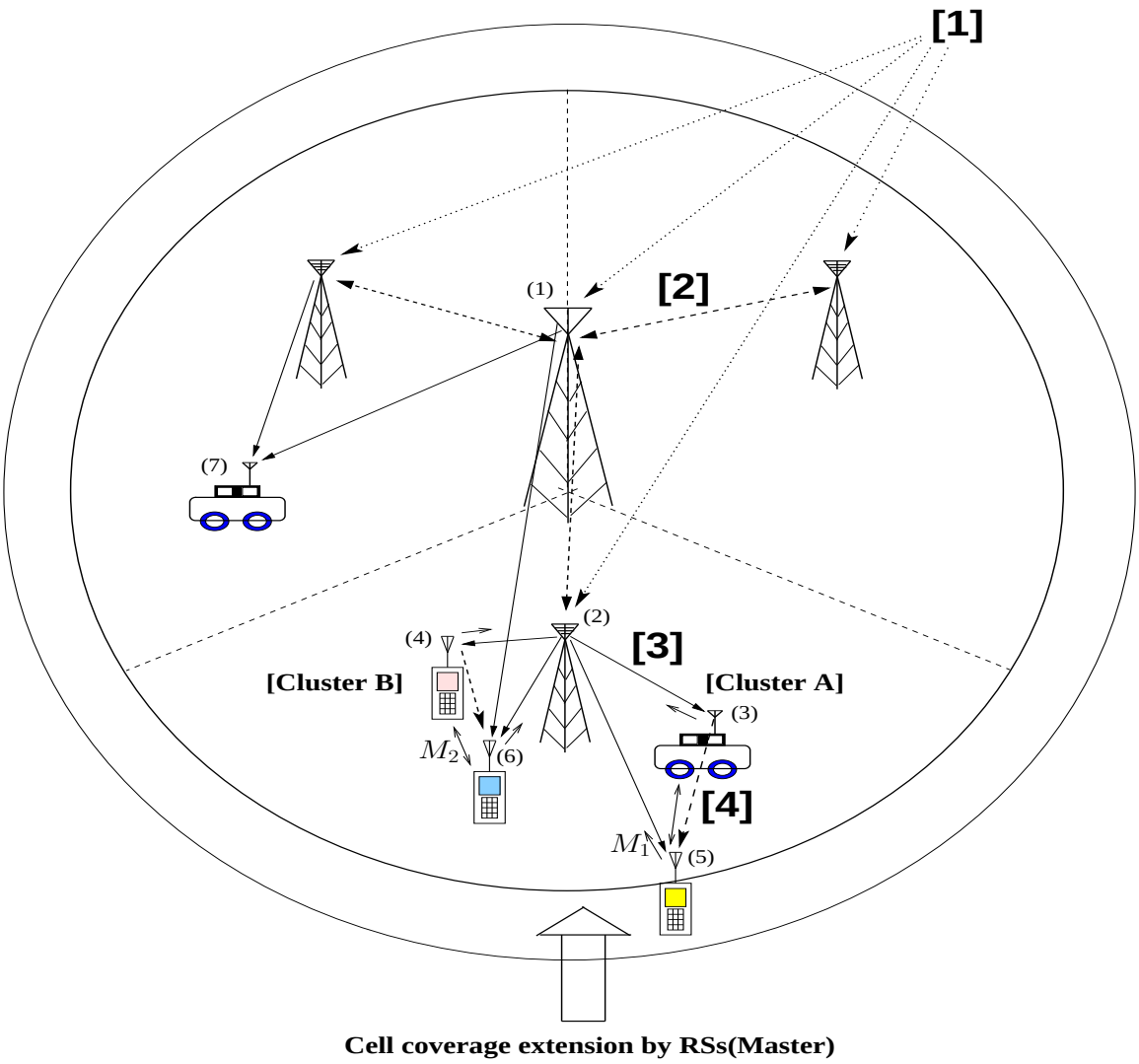

Figure 3.18: Code acquisition scenario in cooperative MIMO environments, which constitutes three stages when considering a couple of RSs.

bottom sector of Figure 3.18 depicts two clusters represented as Cluster A and B, respectively. Cluster A exemplifies a scenario, where only pilot transmission from a master RS is used for code acquisition in support of a MS located at the extended cell edge, while cluster B represents a scenario, where the BS transmits pilots in order to support the code acquisition and the master RSs also contribute towards supporting the code acquisition procedure. Within each cluster, the small dashed arrow indicates that only control information associated with a specific RS-aided cluster is sent without employing pilot transmission. Furthermore, the arrow M_1 of Figure 3.18 represents the signalling message, which is a specific PN code based preamble and provides MS identifier information in the UL in order to register both the slaves and the MSs. Finally, the arrow M_2 of Figure 3.18 represents another signalling message, which is another specific PN code based preamble and provides MS identifier information in a specific RS-aided cluster for the sake of acquiring timing information between the slaves and the MSs. The top left sector of Figure 3.18 depicts a scenario, when considering a MS roaming at high speed, in which the employment of fixed RSs is only possible, because the high speed of the MS does not allow a RS-aided cluster to be established. To illustrate this scenario a little further, a PN sequence having the same code phase offset is used by both the BS and the fixed master RSs in order to acquire GPS aided synchronisation. Different Walsh codes are assigned to both the BS and the fixed master RSs, respectively, where the BS and master RSs are fixed at a specific position.

Based on the above elaborations, our three-stage code acquisition scheme designed for RS-aided inter-cell synchronous DS-CDMA DL systems is summarised as follows:

- 1) **First stage:** Timing acquisition between the BS and master RSs $\Rightarrow$ Both are capable of extracting timing information from the received signal because they are fixed and it is already known which one was assigned a specific Walsh code for its future communications.
- 2) **Second stage:** Timing acquisition between the BS and master RSs as well as MSs. $\Rightarrow$ In this scenario, the MSs are capable of benefitting from cooperative diversity. We will analyse this particular scenario in detail.
- 3) **Third stage:** Timing acquisition among the RSs (master and slave) and MSs. $\Rightarrow$ By employing the M_1 message of Figure 3.18 in the UL, the slave RSs and the MSs are registered with a specific master RS. When using the M_2 message of Figure 3.18 among the slave RSs and the MSs, timing acquisition is accomplished within a previously established cluster. A new broadcast downlink channel is used for distributing

the cluster assignment or grouping information. More specifically, the grouping information includes assignment of slave RSs and unique identification information for each element of the cluster. Based on the information provided by the broadcast channel, the M_2 messages of Figure 3.18 are exchanged in order to establish timing acquisition among the constituents of a specific cluster.

Our analysis in this thesis is essentially confined to the second stage designed for employment in an RS-aided code acquisition scheme. Figure 3.19 illustrates a number of code acquisition

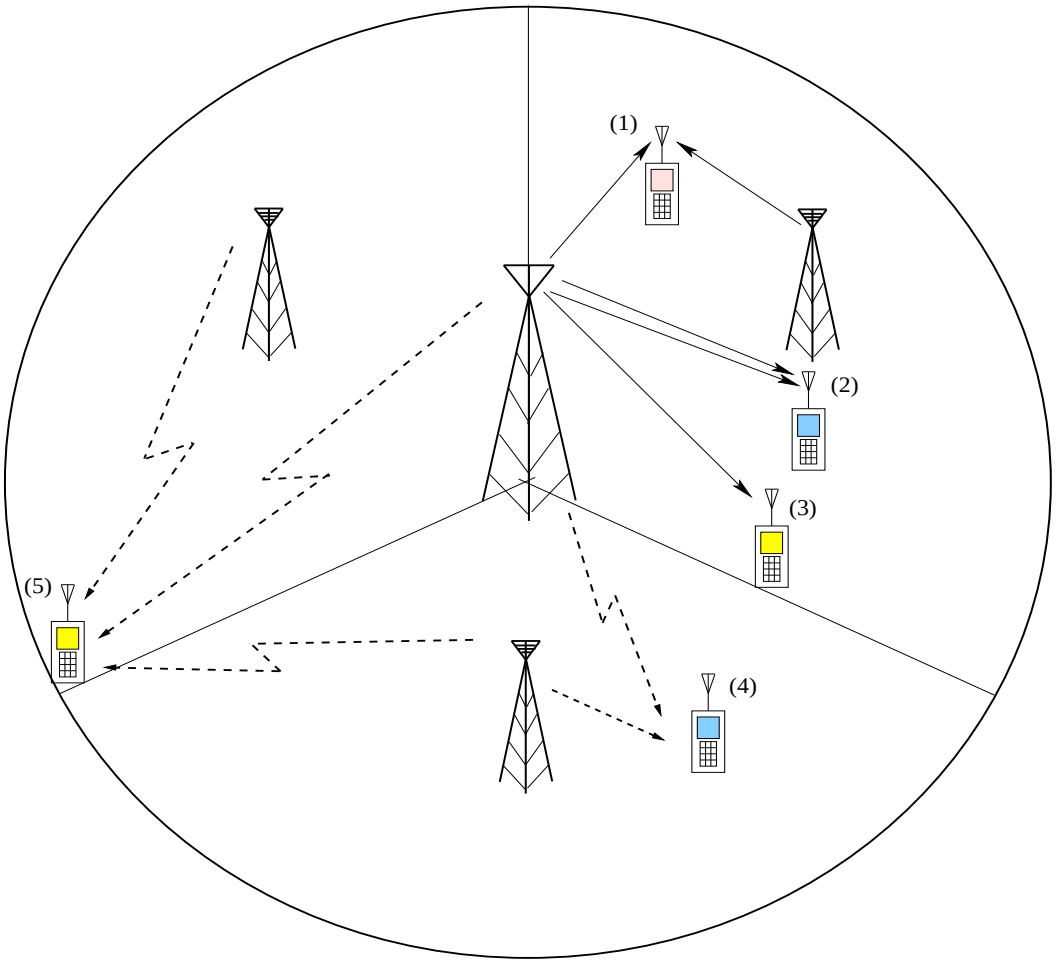

Figure 3.19: Code acquisition scenarios in cooperative MIMO environments, which encompasses three normalised-power scenarios (denoted as (1), (2) and (3)) and two increased-power ones (denoted as (4) and (5)) when considering one or two RSs.

scenarios encountered in fixed RS-aided environments, when considering one or two RSs. The traffic cell is divided into three sectors and a fixed RS is employed in each sector. We assume that both the BS and the RS have a single transmit antenna, except for a co-located scenario having two transmit antennas. The top right sector of Figure 3.19 depicts three

scenarios, where the total allocated power is equally shared by the transmit antennas in both the co-located and cooperative transmission scenarios (termed as 'normalised-power scenario') as follows:

- First scenario (denoted as (1) in Figure 3.19) : The MS receives the DL signals from both the RS located at the same sector's centre as well as from the BS and processes them in order to attain reliable code acquisition.
- Second scenario (denoted as (2) in Figure 3.19) : A co-located scenario having two transmit antennas is considered.
- Third scenario (denoted as (3) in Figure 3.19) : A SISO scenario is used as a benchmarker.

By contrast, in both the fourth and fifth scenarios it is assumed that the total allocated power is also proportionately increased according to the number of RSs (referred to as 'increased-power scenario'), as detailed below:

- Fourth scenario (denoted as (4) in Figure 3.19) : It is exactly the same as the first one, except for its different power allocation.
- Fifth scenario (denoted as (5) in Figure 3.19) : When the MS is located at the edge of the top left sector of Figure 3.19, the signal received from the RS at the adjacent sector's centre seen at the bottom of Figure 3.19 also arrives at the MS with a substantial signal strength.

Furthermore, in the fifth case, this particular MS has to combine the signals received from all the three transmitters for the sake of reliable code acquisition. The average strength of the RS' signal varies depending on the location of the MS. Explicitly, when the MS is located near the cell-edge, the signal received from the RS generally has a higher signal strength with respect to that of the BS, which results in the phenomenon often referred to as link imbalance between the signals received by the MS.

3.5.2 System Parameters

Figure 2.11 depicts the block diagram of the NC receiver designed for our code acquisition scheme employing R co-located receive antennas in RS-aided scenarios. The receiver

generates a decision variable by accumulating R number of independently faded signals observed over a time interval for the sake of improving the P_D in the mobile channel imposing both fading and poor SINR conditions. In order to simplify the receiver's structure, we omitted the front-end down converter, the chip-matched filter, as well as the sampler and descrambler of the PN code. Further details on the related schemes may be found in [18]. The MAT formula of DDSS provided in Section 2.4.3 is also employed for the performance analysis of this section. The associated system parameters are summarised in Table 3.10.

Table 3.10: System Parameters

Bandwidth		1.25 MHz
Carrier frequency		1.9 GHz
Spreading factor		128
Diversity:	Transmit	1,2,3
	Receive	1,2,4
Frequency mismatch		1000 Hz
Mobile speed		160km/h
Number of chip (DDSS)		64 and 256 chips
Total uncertainty region		65,534 hypotheses
False locking penalty factor		1000 chip-durations
Number of paths		single and three path(s)
Values of link imbalance		0,3 and 6 dB

Table 3.11: Maximum SINR degradation inflicted by both the Doppler shift and a 1000Hz frequency drift in conjunction with the coherent integration interval of N chip durations at a carrier frequency of 1.9GHz

N(Chips)	64	128	256	384	512
Degradation(dB)	0.061	0.2449	0.9969	2.3144	4.3213

In Table 3.11 we outlined the maximum SINR degradation imposed by both the Doppler shift and the frequency drift between the transmitter and receiver oscillators in conjunction with the coherent integration interval durations τ_D seen in the code acquisition schematic of Figure 2.11. The number of chips over which the integrator of Figure 2.11 sums the square of the envelope detector's output in both the search and the verification modes of DDSS is assumed to be 64 and 256 in the scenarios having $P = 1$ and 2 RSs as well as $R = 1, 2$ and

4 receive antennas. In the co-located MIMO scenario we assume having the same number of chips in both the search and the verification modes. The values of the link imbalance between the BS as well as the one RS or two RSs aided scenario is assumed to be $0, 3$ and 6 dB. Additionally, we assumed that there is no link imbalance between the two RSs. The spreading factor of the Walsh code to be acquired was selected to be 128. The frequency drift was assumed to be 1000Hz [3], whilst the carrier frequency was 1.9GHz. As an example of a high mobile speed, it is reasonable to postulate 160 km/h. We also assumed that the sampling inaccuracy caused by having a finite, rather than infinitesimally low search step size of $\Delta = T_c/2$ was -0.91 dB, which is a typical value for the search step size [3]. Furthermore, in case of $\Delta = T_c/2$, the effect of cell correlation becomes modest [123], hence it is reasonable to assume that two consecutive cells are uncorrelated. The total uncertainty region of code acquisition was assumed to entail $2 * (2^{15} - 1) = 65{,}534$ hypotheses. Finally, in the spirit of [15], the false locking penalty factor was assumed to be 1000 chip-durations. Both single-path and multi-path scenarios were considered. Each of the three paths of the multi-path scenario arrived with a relative time delay of one chip and they had a 3dB lower magnitude for the first received path as well as 6dB lower magnitude for the second and the third received paths than the LOS path of the single-path scenario, respectively. All paths were assumed to be present in a given search window. All the performance curves have been obtained at the optimum decision threshold of $E_c/I_0 = -13$ dB designed for the code acquisition scheme. The operational range of the two-RS scenario was assumed to be 3 dB lower than that of the single-RS one, because it is highly likely that the former may be situated near the cell-edge.

3.5.3 System Performance Results

Figure 3.20 characterises the MAT versus E_c/I_0 performance of the DDSS code acquisition arrangement parameterised with the number of paths for a single RS and for $P = 2$ co-located transmit antennas. A BS having a single transmit antenna is also considered to be a benchmarker. In Figure 3.20 to 3.24, '$M1$' denotes a single-path scenario, whilst '$M3$' presents the scenario of encountering three paths. When considering Figure 3.20, '$P2R1Mx|_{x=1or3} : 0dB$' represents a cooperative transmission scenario, whereas '$P2R1Mx|_{x=1or3}$' indicates a co-located transmission scenario. Furthermore, in Figures 3.21 to 3.24, the solid lines indicate the MAT curves recorded for RS-aided transmissions, whereas the dotted lines represent the MAT curves of our benchmarker. The effects of the different

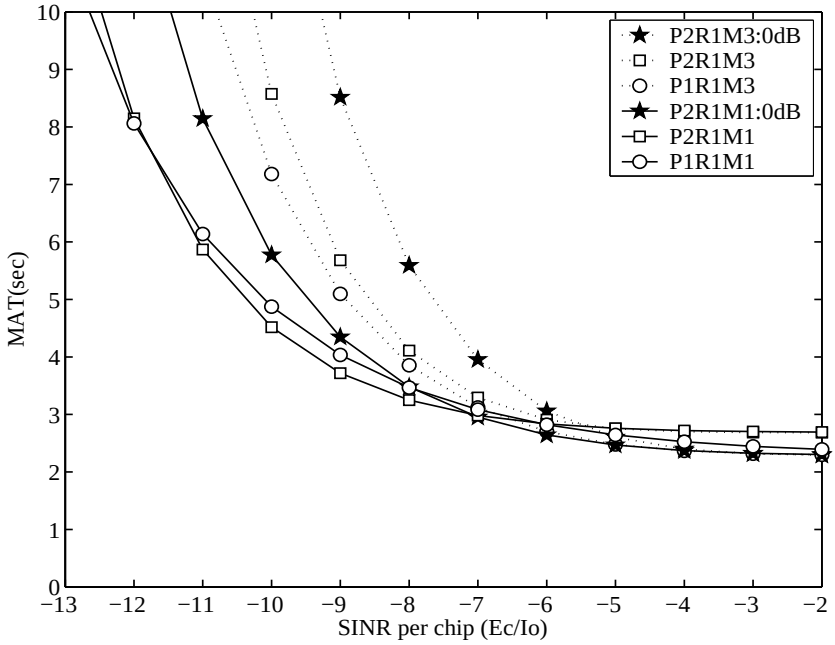

Figure 3.20: MAT versus SINR per chip performance of the code acquisition system for DDSS parameterised with the number of paths for one RS as well as for co-located $P = 1$ and 2 transmit antennas (normalised-power scenario), when employing the schematic of Figure 2.11 and the scenarios of Figure 3.19 as well as Table 3.10.

link imbalance values of $0, 3$, and 6 dB are clearly visible in all the figures. When considering the normalised-power scenario, the solid line denoted as '$P2R1M1$' in Figure 3.20 illustrates a similar MAT performance to the '$P1R1M1$' arrangement right across the entire E_c/I_0 range. The solid line denoted as '$P2R1M1 : 0dB$' indicates the worst MAT performance among all the three cases considered, suggesting that the multi-path diversity does not lead to any MAT performance gain. In case of the three-path scenario, the number of successful detection states was increased by a factor of three, but despite of this, the MAT performance of this three-path scenario became worse than that of the single-path one. The dotted line denoted as '$P1R1M3$' in Figure 3.20 exhibits the best achievable MAT performance among all the three cases. This is because a low 'per-path-power' of the $P = 2$ transmitter scenario leads to a low acquisition performance in the multi-path scenario. Even in case of '$P2R1M3$' we attain no diversity gain, because the performance degradation imposed by the low per-branch-power of both transmit and multi-path diversity becomes more drastic. Similarly to the single-path case, the '$P2R1M3 : 0dB$' scenario represents the worst performance. Accordingly, in the normalised-power scenario, sharing a given total transmit power at the BS by multiple transmit antennas becomes detrimental in terms of the MAT performance, in most practical scenarios. The increased-power scenarios are

analysed in Figures 3.21 to 3.24. Figure 3.21 illustrates the achievable MAT versus SINR

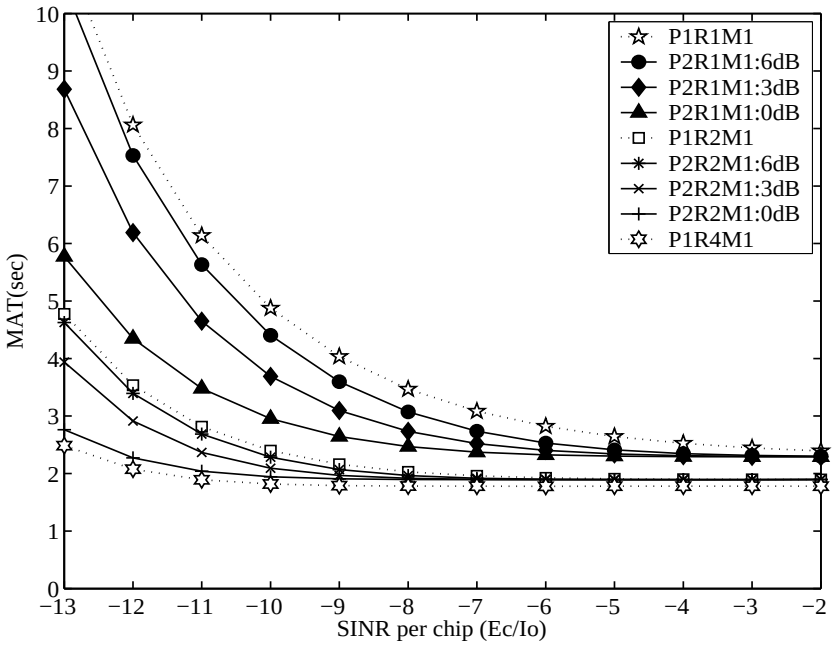

Figure 3.21: MAT versus SINR per chip performance of the code acquisition system for DDSS parameterised with link imbalance and the number of receive antennas for one RS and a single path (increased-power scenario), when employing the schematic of Figure 2.11 and the scenarios of Figure 3.19 as well as Table 3.10.

per chip performance of the DDSS code acquisition scheme parameterised with both the grade of link imbalance and with the number of receive antennas for a single RS and a single propagation path. Observe in Figure 3.21 that when the link imbalance is decreased, we experience an improved MAT performance. In a case of having no link imbalance, the MAT performance approaches that of having two receive antennas. On the other hand, in case of having a 6 dB imbalance, only a marginal diversity gain is achieved, hence the attainable MAT performance improvement also becomes negligible. Figure 3.22 characterises the MAT versus SINR per chip performance of the code acquisition scheme having exactly the same parameters as those considered in Figure 3.21, except for the scenario having three paths. Similarly to the conclusions of Figure 3.21, as the link imbalance is decreased, all the curves seen in Figure 3.22 indicate an improved MAT performance and vice versa. The above-mentioned conclusions explicitly demonstrate that employing a single RS is beneficial in terms of the achievable MAT performance, and as expected, the achievable improvements depend on the value of the link imbalance, regardless whether single-path or multi-path scenarios are considered. However, using a single RS cannot guarantee maintaining a high diversity gain due to the fluctuation of the RS's link quality.

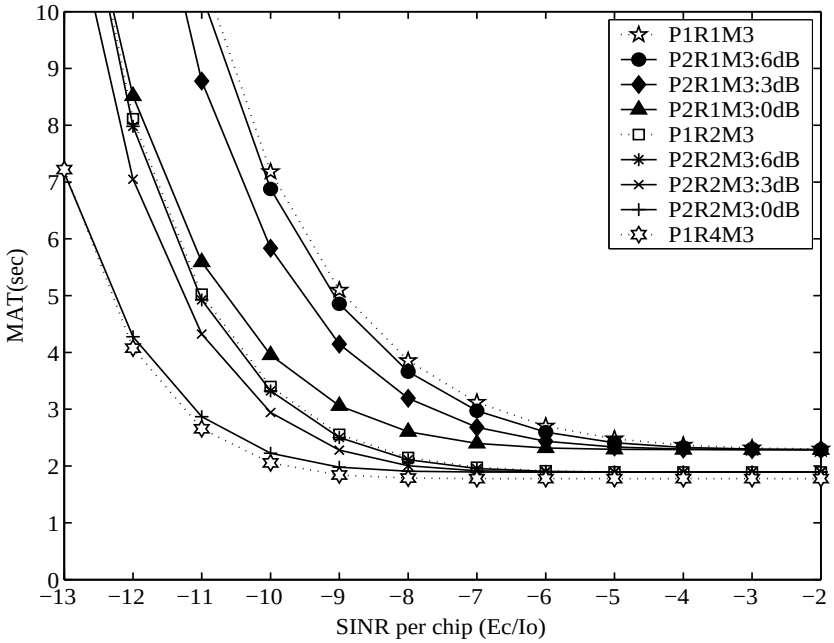

Figure 3.22: MAT versus SINR per chip performance of the code acquisition system for DDSS parameterised with link imbalance and the number of receive antennas for one RS and three paths (increased-power scenario), when employing the schematic of Figure 2.11 and the scenarios of Figure 3.19 as well as Table 3.10.

For comparison, Figures 3.23 and 3.24 characterise the achievable MAT versus SINR per chip performance of the DDSS code acquisition scheme parameterised with both the value of link imbalance and the number of receive antennas, when considering two RSs in both a single-path (Figure 3.23) and in a three-path scenario (Figure 3.24), respectively. The results of Figures 3.23 and 3.24 also exhibit similar MAT performance trends, as shown in Figures 3.21 and 3.22, although the degree of achievable performance improvements is higher than that of the single-RS scenario. To elaborate on the above results a little further, in case of having a 0 dB imbalance the MAT performance attained becomes better than that of the benchmarker supported by $R = 2$ or 4 receive antennas but no RS. Even a link imbalance of 6 dB is capable of ensuring a similar performance to that of the benchmarker. Therefore, owing to the random fluctuation of the link quality, the employment of two RSs might be beneficial in order to achieve a substantial performance improvement in RS-aided scenarios. In comparison to the detrimental effects of distributing the total transmit power over both several co-located and cooperative transmit antennas, as shown in Figure 3.20 and in previous sections, based upon Figures 3.21 to 3.24 characterising the increased-power scenario, we infer that RS-aided scenarios benefit from higher multi-path diversity gains. In case of employing multiple co-located receive antennas at the MS, an additional receiver

diversity gain is also achieved. Accordingly, by exploiting an appropriate combination of RS-aided transmissions and multiple co-located MS receive antennas, in the scenarios considered our scheme is capable of attaining a better performance than the benchmarker scheme benefiting from having four co-located MS receive antennas. It is worth mentioning furthermore that increasing the number of RSs used explicitly increases the number of independently fading multi-path components by a factor of P. However, this assumption implicitly expects that the extra transmit power required can indeed be provided by the RS. It is also noted that in practice the size-limitation of the MS restricts the number of DL receive antennas. In order to exploit the beneficial characteristics of cooperative transmissions, assigning additional power to each additional transmit antenna becomes inevitable during the initial code acquisition stage. The importance of post-initial acquisition - which is capable of identifying the timing instants of the affordable-complexity-dependent number of delayed and independently fading received signal paths to be combined by a Rake receiver - is also worth exploring further. This is particularly so in the code acquisition schemes designed for ultra-wide band systems, owing to the inherent presence of an extremely high number of multi-path components [63].

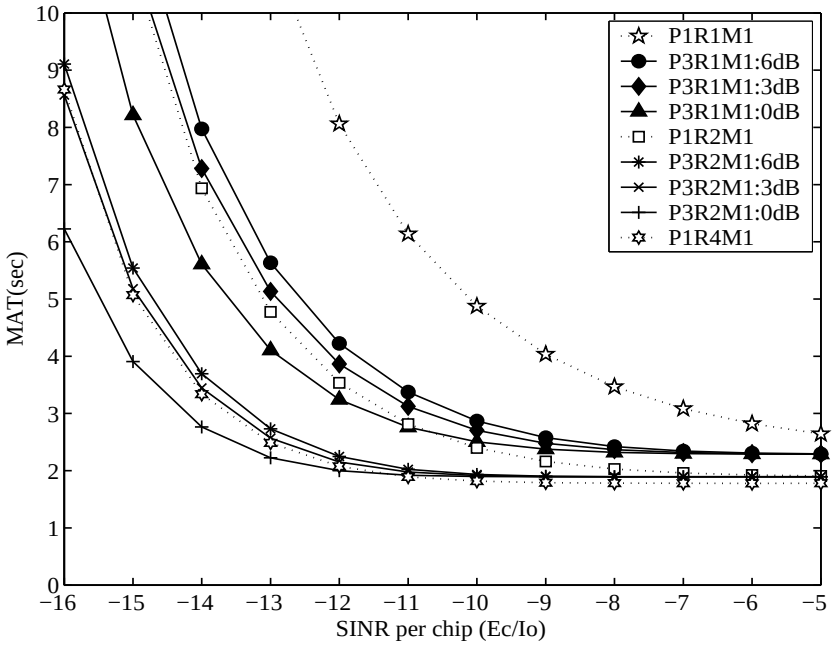

Figure 3.23: MAT versus SINR per chip performance of the code acquisition system for DDSS parameterised with link imbalance and the number of receive antennas for two RSs and a single path (increased-power scenario), when employing the schematic of Figure 2.11 and the scenarios of Figure 3.19 as well as Table 3.10.

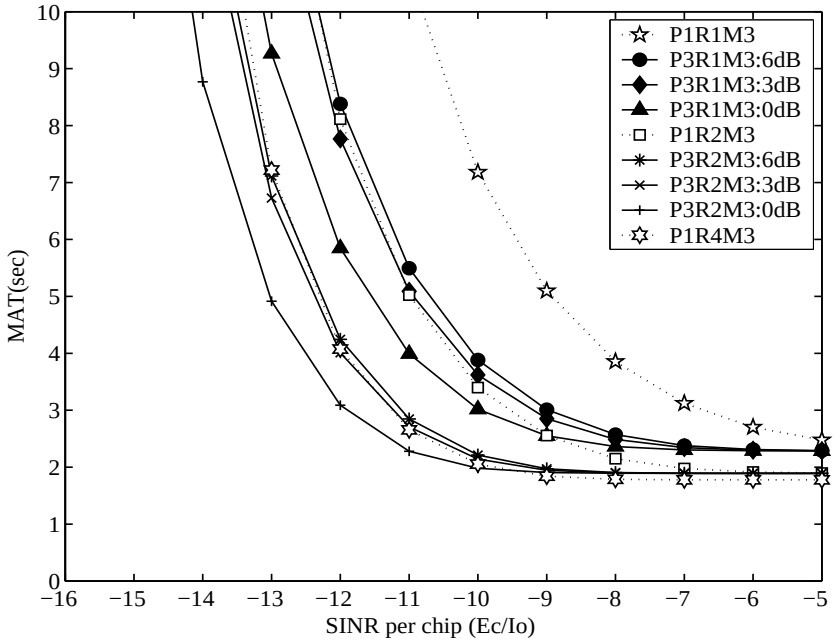

Figure 3.24: MAT versus SINR per chip performance of the code acquisition system for DDSS parameterised with link imbalance and the number of receive antennas for two RSs and three paths (increased-power scenario), when employing the schematic of Figure 2.11 and the scenarios of Figure 3.19 as well as Table 3.10.

3.5.4 Conclusion

In this section we considered RS-aided distributed DL MIMOs and the benefits of receive diversity in code acquisition schemes operating in the inter-cell synchronous CDMA DL. In contrast to the detrimental effects of sharing the total transmit power across multiple transmit antennas in both co-located and cooperative MIMO element based scenarios, as described in Figure 3.20 and in Sections 3.2 to 3.4, our analysis explicitly shows that in the absence of link imbalance, the achievable MAT performance of RS-aided distributed DL MIMOs approaches that of classic receive diversity schemes benefiting from having multiple independently fading MS receive antenna elements, when considering the same total diversity order, as evidenced by Figures 3.21, 3.22, 3.23 and 3.24. Naturally, the performance of the acquisition schemes employing multiple co-located transmit antenna elements erodes in the presence of correlated shadow fading, whilst that of the RS-aided scheme is expected to remain unaffected, provided that the RS is sufficiently far from the MS. On the other hand, in a scenario of having a high link imbalance, only marginal MAT performance gains may be achieved, regardless whether single-path or multi-path propagation scenarios are considered, as portrayed by Figures 3.21, 3.22, 3.23 and 3.24. Hence, for the sake

of exploiting the diversity benefits of RS-aided transmissions, the employment of at least two RSs might be recommended. When additionally invoking multiple co-located and yet independently fading receive antennas at the MS, further diversity gains may be achieved.

3.6 Chapter Summary and Conclusions

In this chapter, we have analysed the performance of serial search based code acquisition in the co-located MIMO aided SC- and MC-DS-CDMA DL as well as of the cooperative MIMO aided SC-DS-CDMA DL. We commenced the chapter by a brief introduction in Section 3.1, followed by the correct detection versus false alarm probability analysis of serial search based code acquisition employed in the co-located MIMO aided SC-DS-CDMA DL in Section 3.2. This was followed by a discussion of both initial and post-initial acquisition in the serial search based co-located NC MIMO aided SC-DS-CDMA DL in Section 3.3. We analysed the performance of code acquisition in the co-located MIMO aided MC-DS-CDMA DL in Section 3.4. Furthermore, we also investigated the performance of code acquisition in the cooperative NC MIMO assisted SC-DS-CDMA DL in Section 3.5.

In order to highlight our investigations of both the co-located and cooperative NC MIMO aided schemes, the characteristics of the co-located and cooperative NC MIMO aided code acquisition schemes is again emphasised in terms of the achievable MAT performance in Figures 3.25 and 3.26, respectively. Figure 3.25 illustrates the attainable MAT versus E_c/I_0 performance of the NC-based DDSS and SDSS code acquisition schemes as a function of the number of transmit antennas for $P = 1$, 2 and 4 as well as that of the number of receive antennas for $R = 1$. In the results of Figure 3.25, the solid lines indicate the performance curves of the DDSS schemes, whereas the dashed lines represent the performance curves of the SDSS schemes. Observe in Figure 3.25 that as the number of transmit antennas is decreased, despite the potentially reduced transmit diversity gain, we experience an improved MAT performance for the single-path scenario of the SDSS scheme. Similarly to the conclusions of the SDSS scenario, as the number of transmit antennas is decreased, all the curves seen in Figure 3.25 for the single-path scenario of the DDSS scheme illustrate an improved MAT performance. However, a useful transmit diversity gain is experienced only for the case of $'P2R1'$, and even this gain was limited to the specific SINR range of -4 and -11 dB. To illustrate the above fact a little further, in the case of $'P2R1'$ the DDSS scheme exhibits a better MAT performance in comparison to the $'P1R1'$ arrangement across the

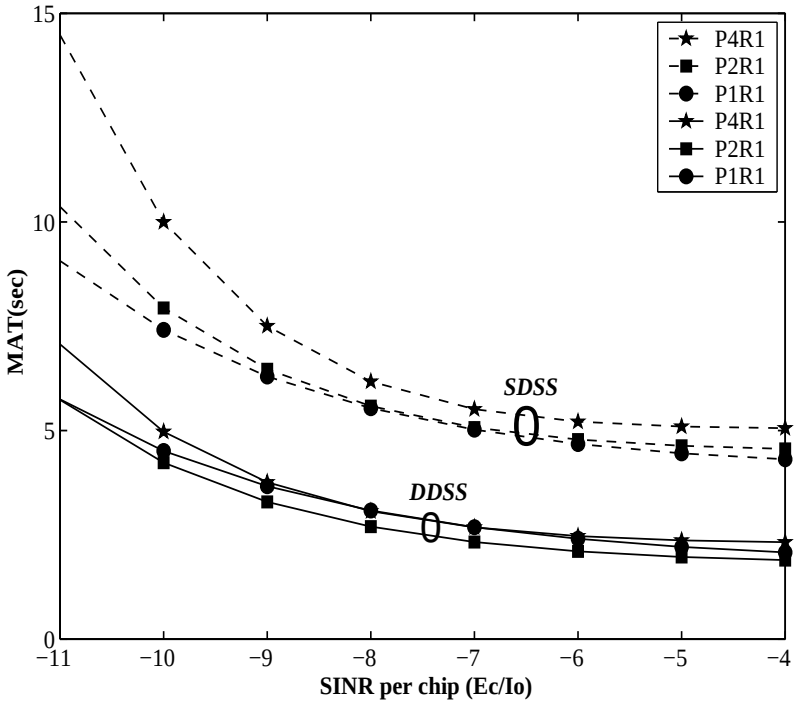

Figure 3.25: MAT versus E_c/I_0 performance comparison between the NC-based DDSS and SDSS code acquisition schemes parameterised with the number of transmit antennas, when using the schematic of Figure 2.5 and Table 3.3.

specific SINR range shown in Figure 3.25. It is worth noting that the total uncertainty region of this scenario was assumed to entail 65,534 hypotheses for Figure 3.25. This fact clearly implies that DDSS benefits from a significantly higher diversity gain than SDSS. The performance degradation imposed by employing multiple antennas becomes more drastic, as the number of transmit antennas is increased for both the SDSS and DDSS schemes, since the length of coherent summation is limited by the clock-drift-induced frequency mismatch. Furthermore, the associated MAT performance discrepancy between the SDSS and DDSS schemes becomes more drastic.

Figure 3.26 illustrates the achievable MAT versus SINR per chip performance of the DDSS code acquisition scheme parameterised with both the grade of link imbalance and with the number of receive antennas for a single RS and a single propagation path, when considering the increased-power scenario defined in Section 3.5.1. Observe in Figure 3.26 that when the link imbalance is decreased, we experience an improved MAT performance. When there is no link imbalance, the MAT performance approaches that of having two receive antennas. On the other hand, in case of having a 6 dB imbalance, only a marginal diversity gain is achieved, hence the attainable MAT performance improvement also becomes negligible. The

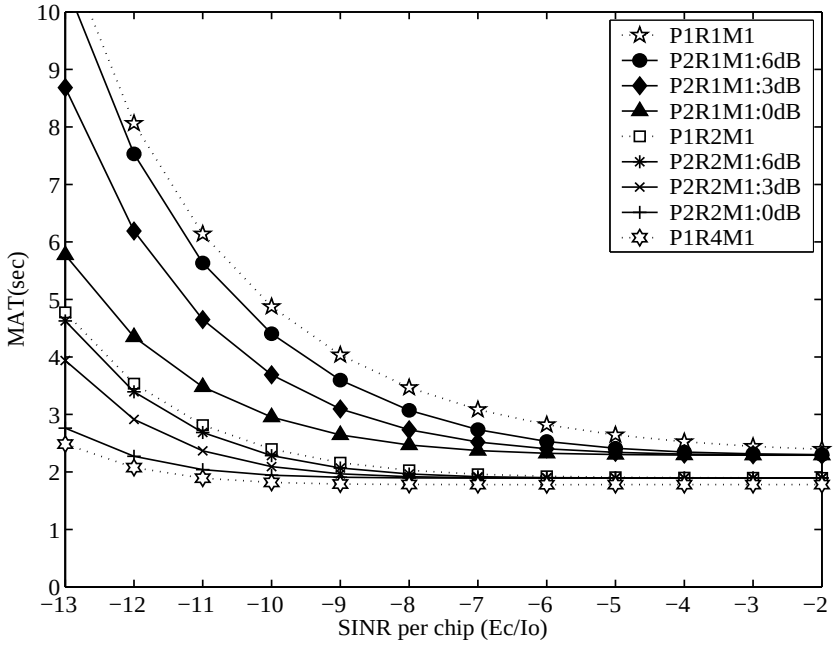

Figure 3.26: MAT versus SINR per chip performance of the code acquisition system for DDSS parameterised with link imbalance and the number of receive antennas for one RS and a single path (increased-power scenario), when employing the schematic of Figure 2.11 and the scenarios of Figure 3.19 as well as Table 3.10.

above-mentioned conclusions explicitly demonstrate that employing a single RS is beneficial in terms of the achievable MAT performance, and as expected, the achievable improvements depend on the value of the link imbalance. However, employing a single RS cannot guarantee maintaining a high diversity gain due to the fluctuation of the RS's link quality.

Ironically, our findings suggest that increasing the number of transmit antennas in a co-located MIMO-aided SC-DS-CDMA system results in combining the low-energy, noise-contaminated signals of the transmit antennas, as seen in Figures 3.14, 3.15, 3.16 and 3.17. Furthermore, increasing both the number of transmit antennas and that of the subcarriers in a co-located MIMO-aided MC-DS-CDMA system also results in combining the low-energy, noise-contaminated signals of both the transmit antennas and the subcarriers. This fact ultimately reduces the correct detection probability, and accordingly increases the MAT by an order of magnitude, when the SINR is relatively low. However, it is extremely undesirable to degrade the achievable acquisition performance, when the system is capable of attaining its target BER performance at reduced SINR values. This phenomenon also has a detrimental effect on the performance of Rake receiver based synchronisation, when the perfectly synchronised system is capable of attaining its target bit error rate performance at reduced SINR values, as a benefit of employing multiple transmit antennas and/or frequency

diversity. Hence it may be concluded that the achievable cell coverage determined by the received pilot channel power may be reduced, as the number of transmit antennas is increased, which is a highly undesirable phenomenon, since it has grave repercussions in terms of having to tolerate a high number of handovers per cell. Based on the above-mentioned results justified by information theoretic considerations, our acquisition design guidelines are applicable to diverse co-located NC MIMO aided scenarios.

In contrast to the detrimental effects of sharing the total transmit power across multiple transmit antennas in the co-located and cooperative MIMO based scenarios, characterised in Figure 3.20 and in Sections 3.2 to 3.4, our findings suggest that employing distributed MIMO elements acting as RSs combined with multiple receive antennas leads to an improved MAT performance, as evidenced by Figures 3.21, 3.22, 3.23 and 3.24. However, these gains are only achievable, if the RSs can afford to contribute toward supplying the extra power used in the 'increased-power-scenario' of Section 3.5. By contrast, when having a high link imbalance, as in Figure 3.21, 3.22, 3.23 and 3.24 only marginal MAT performance gains may be achieved, regardless whether single-path or multi-path propagation scenarios are considered. Therefore, in order to efficiently exploit the diversity benefits of RS-aided transmissions, the employment of at least two RSs might be recommended. When additionally invoking multiple co-located receive antennas at the MS, further diversity gains may be achieved.

Chapter 4

Performance Analysis of Co-located MIMO Aided Differentially Coherent Code Acquisition

4.1 Introduction

In this chapter, we will analyse both DC and NC serial search based code acquisition in both the co-located MIMO aided SC- and MC- DS-CDMA DL. We will commence our discourse by analysing the achievable code acquisition performance in the co-located MIMO aided SC-DS-CDMA DL in Section 4.2 with the aid of Sections 2.3.3, 2.4.1 and 2.4.2. Based on the formulae in Sections 2.3.3, 2.4.1 and 2.4.2, this will be followed by a discussion on the attainable code acquisition performance in the co-located MIMO aided MC-DS-CDMA DL in Section 4.3. Furthermore, based on the above-mentioned results justified by information theoretic considerations, our acquisition design guidelines applicable to diverse co-located DC MIMO aided scenarios will be summarised in Sections 4.2.2 and 4.3.2.

4.2 Co-located MIMO Aided Code Acquisition in the SC-DS-CDMA Downlink

4.2.1 System Architecture and System Parameters

Figure 4.1 portrays both the DC and the NC receiver's schematic designed for our code acquisition scheme using MIMOs, where the NC module generates its decision variable by accumulating $(P{\cdot}R)$ number of independently faded signals observed over a given time interval. In the DC scheme of Figure 4.1, instead of squaring the summed energy as suggested by the procedures outlined in [3], the channel's output samples accumulated over a full spreading code period are multiplied by the conjugate of the N-chip-delayed samples [17, 18] and τ_D represents the integral dwell time. The MAT formulae of both the SDSS and DDSS in Section 2.4 are also employed for the performance analysis. When analysing the MAT per-

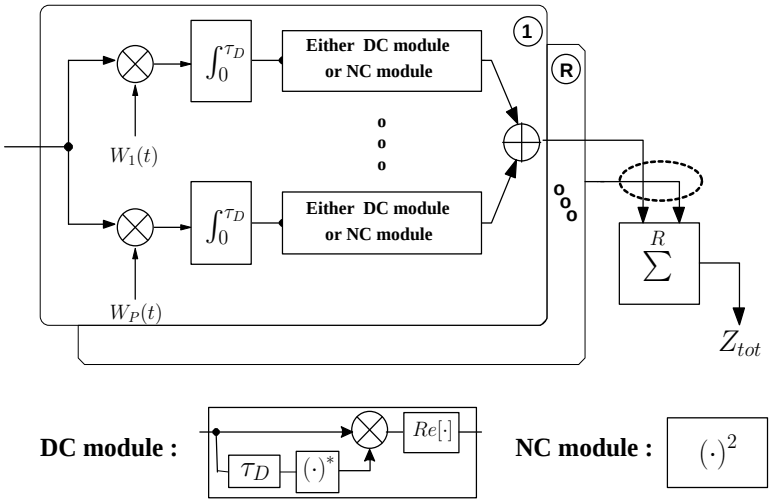

Figure 4.1: Receiver structure of both differentially coherent and non-coherent code acquisition using R receive antennas. In the context of the search mode constituting the SDSS scheme using the threshold θ_1 in Fig. 4.2 only NC detection is possible, while in the verification mode employing the threshold θ_2 both NC and DC acquisition is possible.

formance of the SDSS technique [3], where the NC receiver structure of Figure 4.1 is used in the search mode constituting the SDSS scheme seen at the top of Figure 4.2[1], the decision statistics, Z_{tot} generated by the NC module of Figure 4.1 is compared to the threshold θ_1, which is optimised for a specific E_c/I_0 value[2]. This completes the single-step search-mode

[1]The term 'update' indicates that the acquisition scheme adjusts or updates the particular code-phase assumed during the current hypothesis test in its efforts to find the best possible alignment of the received and locally stored code, given the particular search step-size used.

[2]The specific value of E_c/I_0 depends on the operating environment.

of the SDSS scheme. By contrast, the DDSS technique [14] of Figure 4.2 invokes a two-step process. More explicitly, once the desired user's code was found in the search-mode of the DDSS scheme of Figure 4.2, the verification mode is activated. The verification mode may use either the DC or the NC modules of Figure 4.1, in order to confirm that the correct code-phase is indeed the one identified in the search mode. On the other hand, in the search mode, only the NC scheme can be used, as portrayed in Figure 4.2. The DC scheme is excluded from the search mode, because it requires further processing carried out within the DC module of Figure 4.1 and hence the complexity may be minimised by limiting the employment of the DC scheme to the verification mode. More explicitly, the NC scheme is employed in two consecutive decision processes, namely first in finding and then confirming the correct code phase in order to improve the reliability of SDSS, which results in the DDSS acquisition scheme. Figure 4.2 illustrates the schematic of the DDSS scheme, where θ_1 and θ_2 represent the acquisition thresholds of the search and verification mode, respectively. Furthermore, Z_1 and Z_2 denote the decision variables of the search and verification mode, respectively. In Figure 4.2 Z_1 is compared to θ_1 and if it exceeds the threshold, Z_2 generated by either DC or NC module is compared to θ_2. If successful code acquisition is declared, then the code tracking loop is enabled. Otherwise, the acquisition system reverts back to the search-stage, until the correct code and its phase are found. In our forthcoming analysis, four code acquisition arrangements are considered. Specifically, SDSS employing both DC and NC schemes as well as DDSS exploiting both DC and NC arrangements are invoked in the verification mode. However, in the search mode of the DDSS scheme only the NC scheme can be used. Further details on the related DDSS system can be found in [14, 68].

The associated system parameters are summarised in Table 4.1. In Table 4.2 we outlined the maximum SINR degradation imposed by both the Doppler shift and the clock-drift-induced frequency mismatch between the transmitter and receiver in conjunction with a coherent integration interval of N chip durations, where both represent the total frequency mismatch. The length of the PN sequence in our system was assumed to be $256 \cdot T_c$, where the chip-duration is $T_c = 1/1.2288 \mu s$. It was found to be sufficient to integrate the detector output seen in Figure 4.1 over N =256 chips, which is equivalent to two 128-chip direct-sequence modulated symbols used for coherent accumulation due to the adoption of the above-mentioned FPC scheme of [18] for analysing SDSS. In the DDSS case the number of chips, over which the accumulator in Figure 4.1 sums the envelope detector's output, is assumed to be 64 for the search mode and 256 for the verification mode in all the different

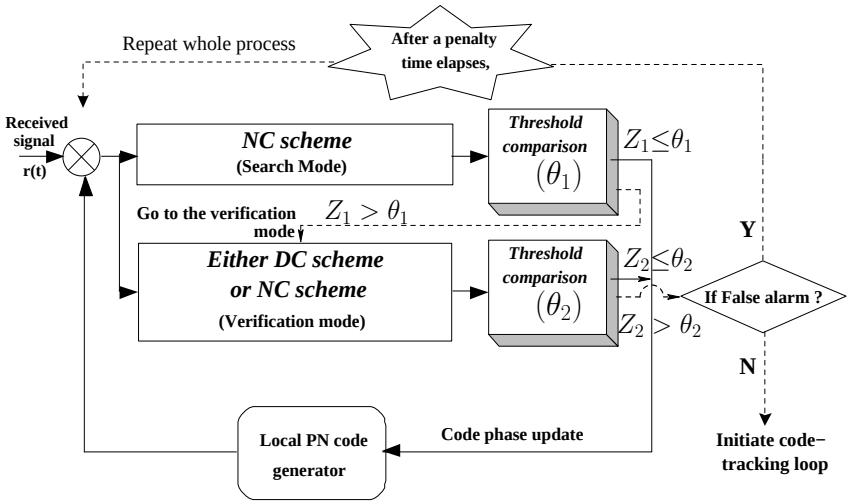

Figure 4.2: Receiver flowchart of our DDSS code acquisition scheme, where θ_1 and θ_2 represent the acquisition thresholds of the search and verification modes, respectively. The search mode constitutes the SDSS and consecutive search and verification modes represent the DDSS.

MIMO scenarios. This value was calculated by using Equation. 2.9 in Section 2.3.2.1 provided for determining the performance degradation owing to the total frequency mismatch imposed on both the Doppler shift and the clock drift. The spreading factor of the Walsh code to be acquired was selected to be 128. The frequency mismatch was assumed to be 1000 Hz [3], while the carrier frequency was 1.9 GHz. As an example of a high mobile speed, it is reasonable to postulate 160 km/h. We also assumed that the sampling inaccuracy caused by having a finite, rather than infinitesimally low, search step size of $\Delta = T_c/2$ was -0.91 dB[3], which is a typical value for the search step size [3]. The total uncertainty region was assumed to entail 512 hypotheses. In the spirit of [15], the false locking penalty factor was assumed to be 1000 chip-durations. Finally, it is assumed that both a single-path and a three-path scenario are considered. More specifically each of the three paths arrives with a relative time delay of one chip with respect to the previous one and has the same magnitude for the first received path as the single-path channel, as well as 3 dB lower for the second and 6 dB lower for the third received paths, respectively.

In all the remaining figures we assumed an operation in the range of 'finger locking', which may be considered to be the range between $E_c/I_0 = -17$ and $-13\,dB$, as suggested in [110]. All the performance curves - except when investigating the achievable MAT versus the detection threshold value - have been generated at the threshold value of $E_c/I_0 = -16\,dB$,

[3]A half-chip-duration timing error imposed on the single hypothesis test per chip is capable of causing an SINR loss of several dBs, when considering the achievable MAT performance which was deemed excessive. Hence we opted for testing two hypotheses per chip, which reduced the corresponding SINR loss to 0.91 dB.

which was considered as the minimum value required for finger locking.

Table 4.1: System Parameters

Bandwidth		1.25 MHz
Carrier frequency		1.9 GHz
Spreading factor		128
Diversity:	Transmit	1,2,4
	Receive	1,2,4
Frequency mismatch		1000 Hz
Mobile speed		160km/h
Num. of chip	SDSS	256 chips
	DDSS	64 and 256 chips
Total uncertainty region		512 hypotheses
False locking penalty factor		1000 chip-durations
Number of paths		single and three path(s)

Table 4.2: Maximum SINR degradation inflicted by both the Doppler shift and the clock drift in conjunction with the coherent integration interval of N chip durations at a carrier frequency of 1.9 GHz

N (Chips)	64	128	256	384	512
Degradation(dB)	0.061	0.2449	0.9969	2.3144	4.3213

4.2.2 System Performance Results

Throughout Figures 4.3 to 4.8, the sensitivity with respect to the detection threshold value becomes significantly higher as the value of E_c/I_0 is decreased and the NC scheme is employed, although the degree of the sensitivity is quite different depending upon the number of transmit antennas. The results for Figures 4.3 to 4.8 are generated by exploiting the SDSS technique in Section 2.4.1. Figure 4.3 illustrates the achievable MAT versus the detection threshold value for the DC code acquisition system as a function of both the number of transmit antennas for $P = 1$, 2 as well as 4 and that of the SINR per chip denoted as E_c/I_0. Observe in Figure 4.3 that surprisingly, as the number of transmit antennas is decreased, despite the potentially reduced transmit diversity gain, we experience an improved MAT performance at E_c/I_0 = -16 dB. However, observe in Figure 4.3 that in the case of E_c/I_0 = -13 and -10 dB, the performance degradation remains relatively low, as the transmit diversity order is increased from $P = 1$ to 4. For comparison, Figure 4.4 characterises the achievable

MAT versus the detection threshold value for the NC code acquisition arrangement as a function of the number of transmit antennas for $P = 1$,2 as well as 4 and that of the SINR per chip. Similarly to the conclusions of Figure 4.3, as the number of transmit antennas is decreased, all the curves seen in Figure 4.4 illustrate an improved MAT performance. However, unlike in the case of the DC scheme of Figure 4.3, the MAT performance degradation becomes further pronounced for E_c/I_0 values such as E_c/I_0 = -13 dB, as the transmit diversity order is increased from $P = 1$ to 4. This is because the DC scheme characterised in Figure 4.3 has a performance gain of just under 3 dB in comparison to the NC one. The MAT performance results of Figure 4.3 confirm the expected trends. Moreover, this explicitly indicates that the DC scheme also degrades the achievable MAT performance as a consequence of employing multiple transmit antennas for the sake of attaining a transmit diversity gain. However, the MAT performance degradation imposed is less severe than that of NC counterpart. Figure 4.5 and Figure 4.6 characterise the achievable MAT versus detection threshold performance, parameterised by both the number of transmit antennas for $P = 1$, 2 as well as 4 in conjunction with $R = 2$ receive antennas and by the E_c/I_0 ratio for both the DC code acquisition scheme (Figure 4.5) and for its NC counterpart (Figure 4.6). The achievable MAT versus detection threshold performance recorded for exactly the same parameters as in Figures 4.5 and 4.6 but using $R = 4$ receive antennas is characterised in Figures 4.7 and 4.8, respectively. When having $R = 2$ and $R = 4$ receive antennas, similar trends may be observed for both DC code acquisition schemes as portrayed in Figures 4.5 and 4.7, respectively. By contrast, as seen in Figures 4.6 and 4.8 for the same scenario of $R = 2$ and $R = 4$ receive antennas, respectively, the NC code acquisition scheme exhibited a more drastic MAT performance degradation at relatively low E_c/I_0 values such as -16 dB, compared to DC code acquisition, especially, as the number of transmit antennas was increased.

Throughout Figures 4.9 to 4.12, the achievable MAT versus SINR per chip performance of both the DC and NC code acquisition scheme employing SDSS and DDSS techniques is analysed in both single-path and multi-path scenarios. These investigations are then followed by the characterisation of the correct detection versus false alarm probability in Figure 4.13. The results of Figures 4.9 to 4.12 were generated by exploiting the techniques outlined in Sections 2.4.1 and 2.4.2. Figure 4.9 illustrates the achievable MAT versus SINR per chip performance of the DC SDSS code acquisition scheme as a function of the number of transmit antennas for $P = 1$,2 as well as 4 and that of the number of receive antennas for $R = 1$ and 4. In Figures 4.9 to 4.12, the solid lines indicate the scenario of receiving three

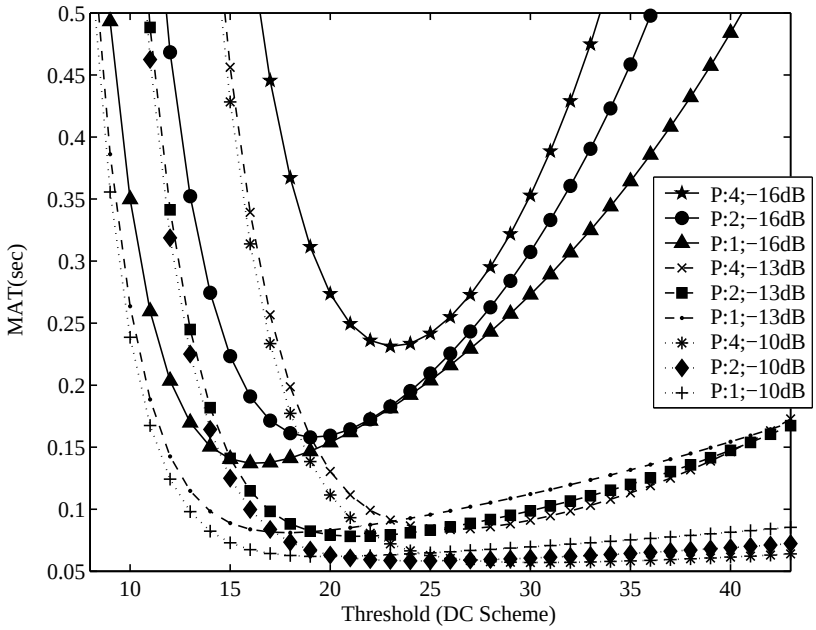

Figure 4.3: MAT versus the detection threshold value of the differentially coherent code acquisition system for $P = 1, 2$ as well as 4 transmit antennas in conjunction with $R = 1$ receive antenna for transmission over uncorrelated Rayleigh channels, when using the schematic of Figure 4.1 and Table 4.1.

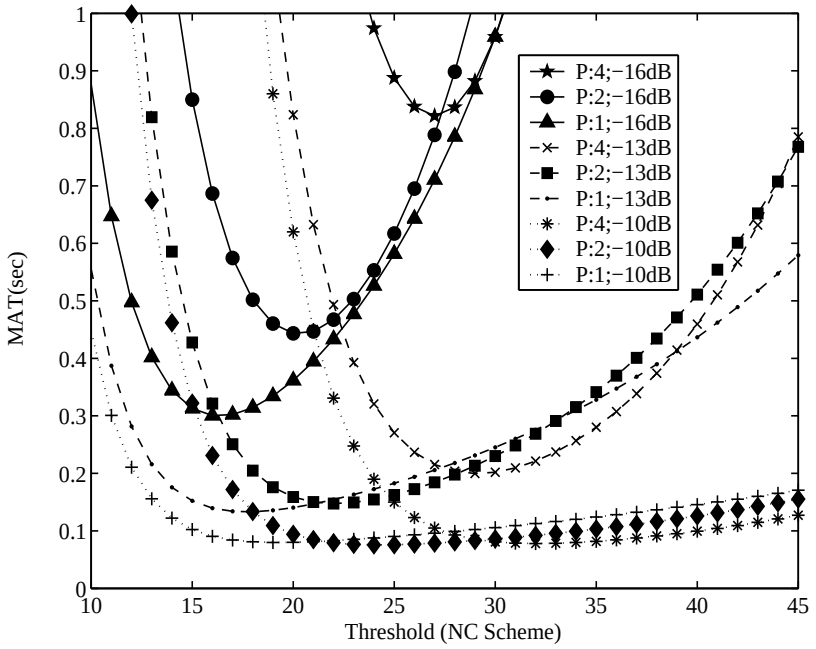

Figure 4.4: MAT versus the detection threshold value of the non-coherent code acquisition system for $P = 1, 2$ as well as 4 transmit antennas in conjunction with $R = 1$ receive antenna for transmission over uncorrelated Rayleigh channels, when using the schematic of Figure 4.1 and Table 4.1.

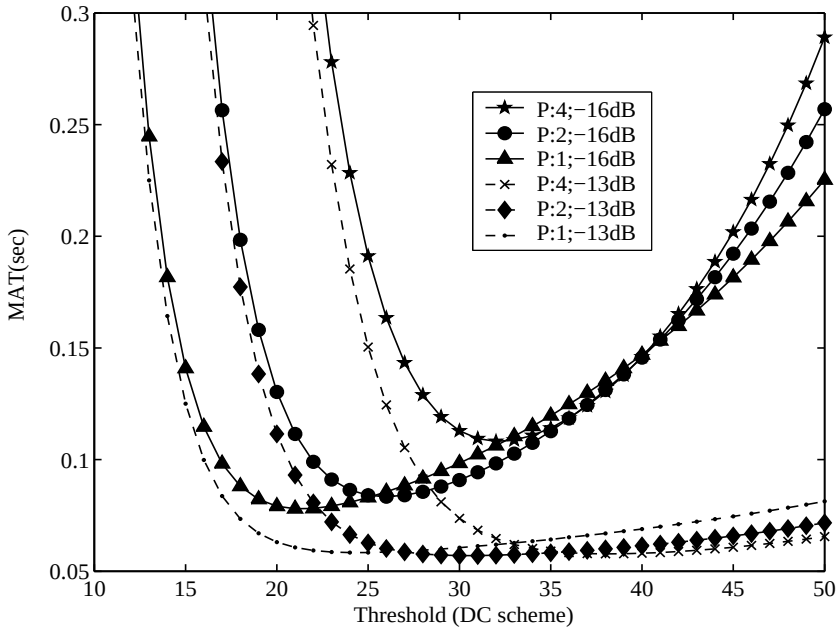

Figure 4.5: MAT versus the detection threshold value of the differentially coherent code acquisition system for $P = 1, 2$ as well as 4 transmit antennas in conjunction with $R = 2$ receive antenna for transmission over uncorrelated Rayleigh channels, when using the schematic of Figure 4.1 and Table 4.1.

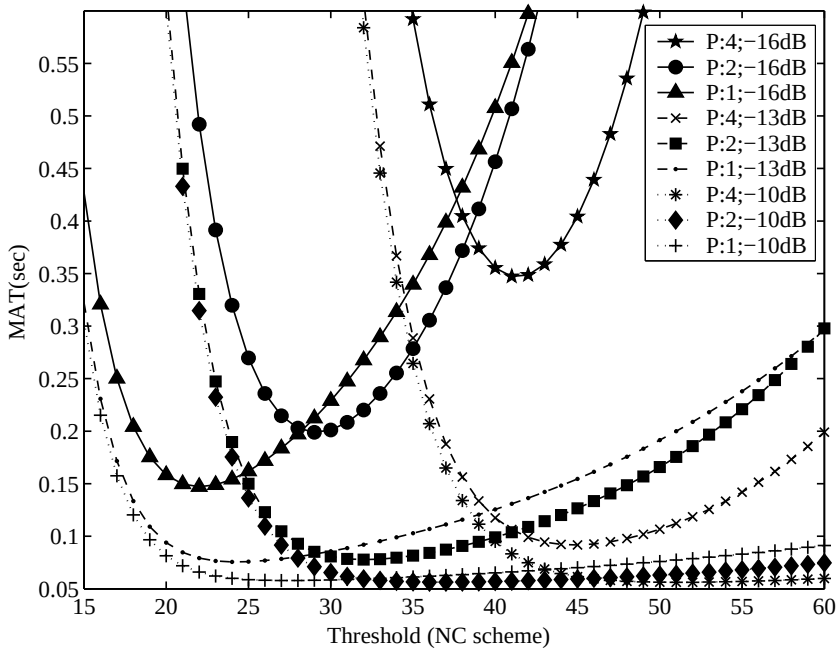

Figure 4.6: MAT versus the detection threshold value of the non-coherent code acquisition system for $P = 1, 2$ as well as 4 transmit antennas in conjunction with $R = 2$ receive antenna for transmission over uncorrelated Rayleigh channels, when using the schematic of Figure 4.1 and Table 4.1.

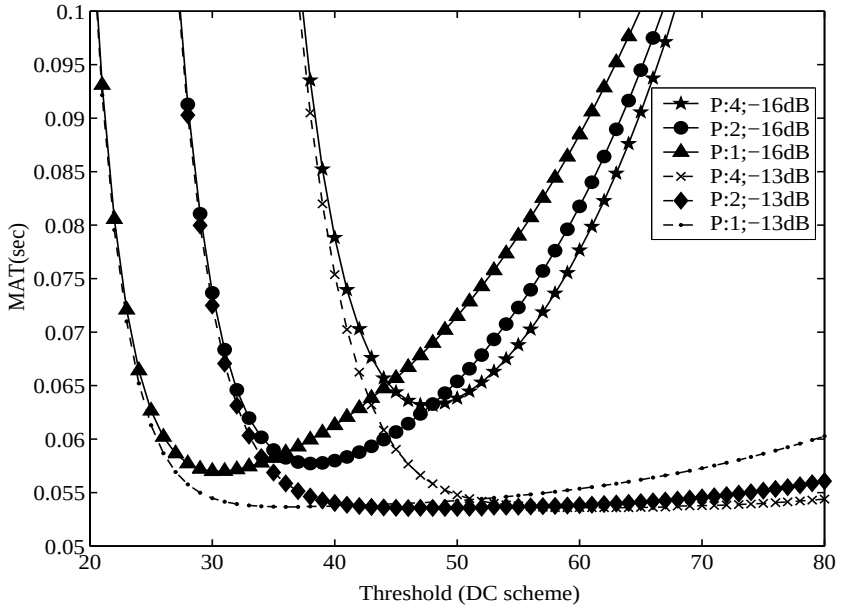

Figure 4.7: MAT versus the detection threshold value of the differentially coherent code acquisition system for $P = 1, 2$ as well as 4 transmit antennas in conjunction with $R = 4$ receive antenna for transmission over uncorrelated Rayleigh channels, when using the schematic of Figure 4.1 and Table 4.1.

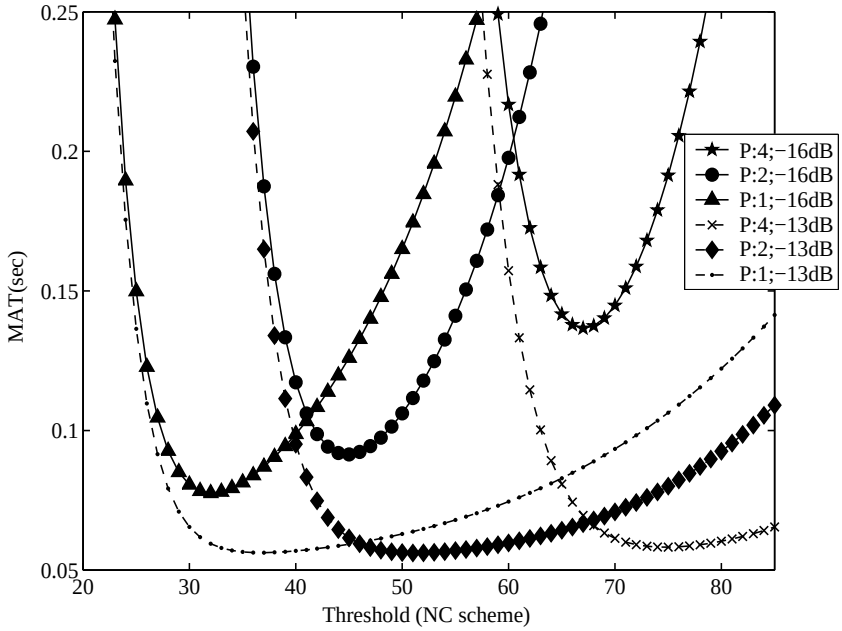

Figure 4.8: MAT versus the detection threshold value of the non-coherent code acquisition system for $P = 1, 2$ as well as 4 transmit antennas in conjunction with $R = 4$ receive antenna for transmission over uncorrelated Rayleigh channels, when using the schematic of Figure 4.1 and Table 4.1.

paths (denoted as $M3$), whereas the dashed lines represent a single-path scenario (denoted as $M1$). For the sake of compact notation, the scenario of using P = x, R = y and M = z is denoted as $PxRyMz$ in Figures 4.9 to 4.12.

Observe in Figure 4.9 that somewhat surprisingly, as the number of transmit antennas is decreased, we experience an improved MAT performance for both the single-path and multi-path scenarios. The main reasons for these performance trends will be further justified by information theoretic considerations in the NC MIMO antenna-aided scenarios at the end of the section. On the other hand, the MAT performance of the multi-path scenario became better than that of the single-path one, since the number of states where the signal was deemed to be present was increased by a factor of three. In the case of $R = 4$ receivers the performance improvements due to having multiple paths became marginal, because the receive diversity gain was already sufficiently high for approaching a Gaussian MAT-performance. A useful transmit diversity gain was achievable only for the $P = 2$ and $R =$ 1 scenario, and this was limited to the specific SINR range of -10 to -14 dB in the single-path scenario. For comparison, Figure 4.10 characterises the MAT versus SINR per chip performance of the NC SDSS code acquisition aided system as a function of the number of transmit antennas for P = 1,2 as well as 4 and that of the number of receive antennas for $R = 1$ and 4. Similarly, as the number of transmit antennas is decreased, all the curves illustrate an improved MAT performance. In particular, the MAT performance of the DC scheme clearly shows a better performance in comparison to the NC arrangement, since the DC scheme has a performance gain of approximately 3dB in comparison to the NC scheme. Furthermore, the DC scheme is more efficient in terms of reducing the effects of both the AWGN and the interference, than the NC one in the low SINR range [17] [4]. Hence, the DC scheme suffers from a less severe MAT performance degradation owing to employing multiple transmit antennas in comparison to its NC counterpart.

Figure 4.11 characterises the MAT versus SINR per chip performance of a DDSS system. More specifically, both the NC code acquisition aided system of Figure 4.1 used in the search mode and the DC code acquisition assisted scheme employed in the verification mode are characterised. Explicitly, their performance is quantified as a function of the number of transmit antennas for P = 1,2 as well as 4 and the number of receive antennas for $R = 1$ and 4 (denoted as $NCDC$ in Figure 4.1). By contrast, Figure 4.12 characterises the MAT versus SINR per chip performance of a DDSS system employing the NC code acquisition aided

[4] In the low SINR region, the false alarm probabilities of the DC and NC schemes differ by a factor of two. This fact leads to the superiority of the DC scheme over the NC arrangement.

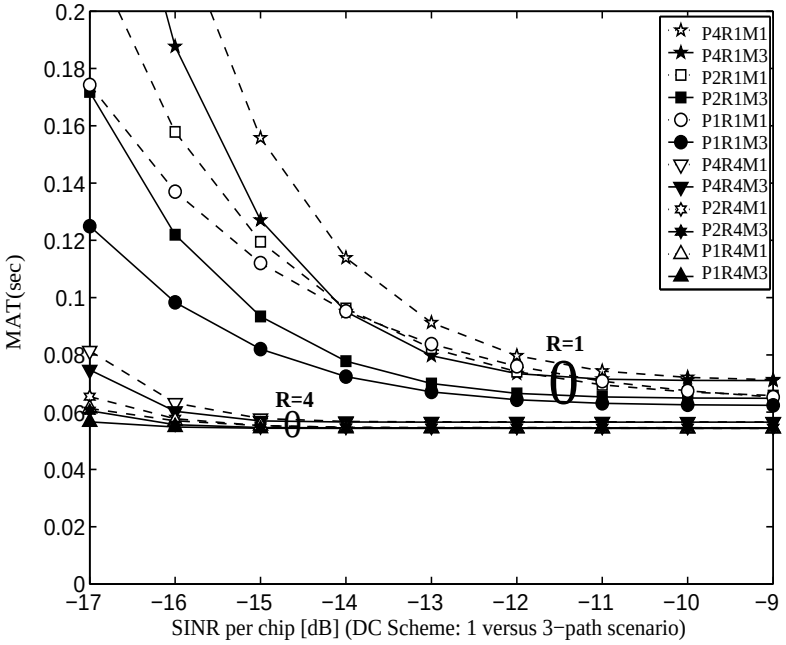

Figure 4.9: MAT versus SINR per chip performance of **the differentially coherent code acquisition system for SDSS** parameterised with both the number of transmit and receive antennas, when using the schematic of Figure 4.1 and Table 4.1.

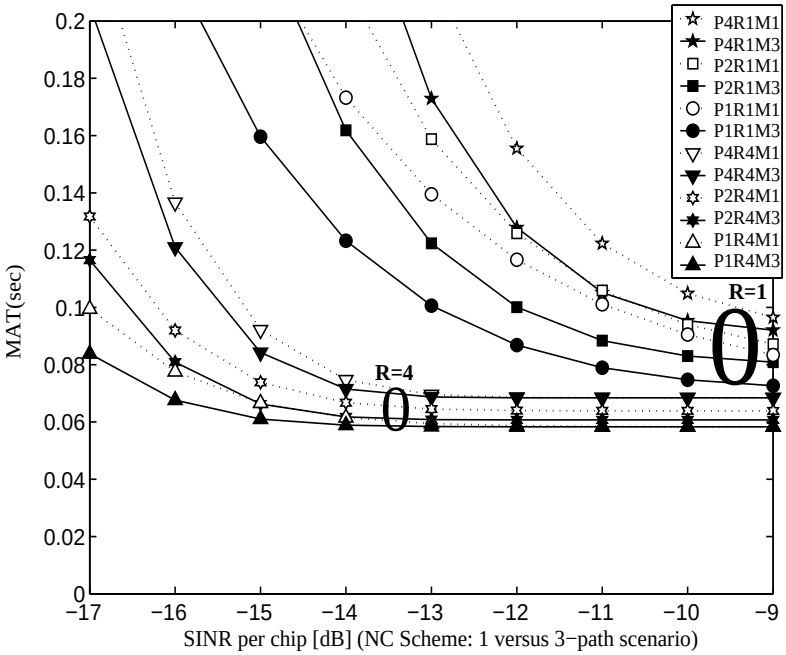

Figure 4.10: MAT versus SINR per chip performance of **the non-coherent code acquisition system for SDSS** parameterised with both the number of transmit and receive antennas, when using the schematic of Figure 4.1 and Table 4.1.

scheme of Figure 4.1 in both its search mode and verification mode (denoted as $NCNC$ in Figure 4.12). The results seen in Figure 4.11 suggest that the overall performance improvement of the DDSS system employing the DC scheme of Figure 4.1 in its verification mode is significantly higher than that of the DDSS system using the NC scheme of Figure 4.1, as seen in Figure 4.12. Similarly to the results of the SDSS scenario in both Figures 4.9 and 4.10, the MAT performance degradation becomes more drastic in Figures 4.11 and 4.12, when the number of transmit antennas is increased, as observed for the DC and NC schemes, respectively. Nonetheless, as expected, the overall performance of DDSS remains substantially higher than that of SDSS. In the case of DDSS, the performance improvement obtained for the three-path scenario is less than that of SDSS. It is worth mentioning that although not explicitly shown in Figures 4.9 to 4.12 for avoiding obfuscating details, the MAT operating range of $R = 2$ receive antennas was found to be between that corresponding to the $R = 1$ and $R = 4$ receive antenna scenario. Observe in Figures 4.9 to 4.12 that the associated MAT performance discrepancy between the SDSS and DDSS schemes becomes more drastic, when the number of transmit antennas is increased. In the multi-path scenarios all the schemes fail to show any transmit diversity gain, since the third-order receive diversity provided by the three paths approaches a Gaussian performance. Table 4.3 summaries the performance gains recorded in Figures 4.9 to 4.12 for the DC code acquisition scheme over the NC arrangement in the case of experiencing a single-path, when considering $P = 1$,2 and 4 number of transmit antennas invoked in conjunction with $R = 1$ receive antenna. Observe in this table, that the performance improvements achieved by employing the DC SDSS and DDSS schemes becomes significantly higher in the vicinity of SINR $= -15\,dB$, when the number of transmit antennas is increased.

Table 4.3: The MAT performance ratio between NC SDSS and DC SDSS as well as NC DDSS and DC DDSS at E_c/I_0 = -15 dB

	DC SDSS/ NC SDSS	DC DDSS/ NC DDSS
P4	3.2443	2.5727
P2	2.5	2.0704
P1	2.0208	1.7615

Figure 4.13 illustrates the correct detection versus false alarm probability, parameterised by the number of transmit antennas for $P = 1$,2 and 4 in the verification mode of both the DC and NC schemes at E_c/I_0 = -13 dB. In terms of the achievable MAT performance, the most efficient operational range of the false alarm probabilities for the verification mode and

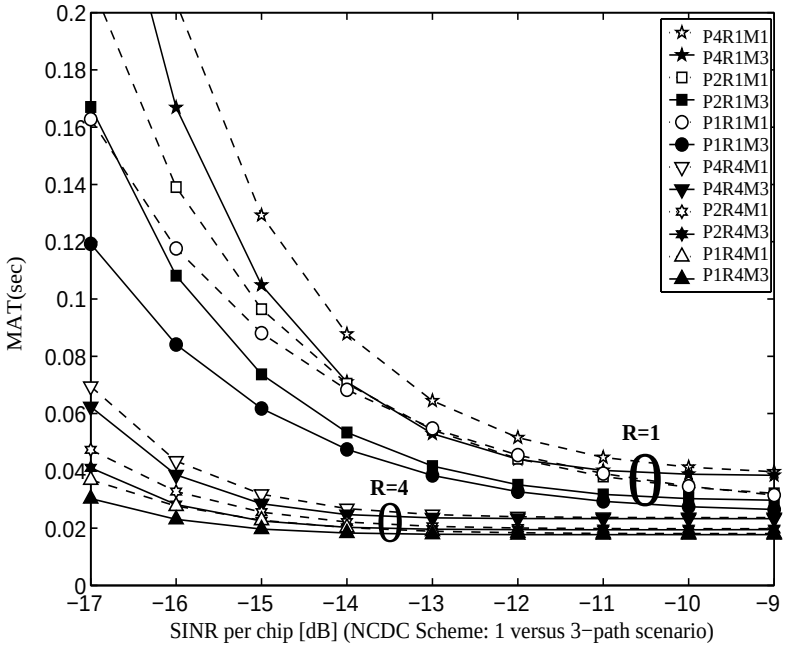

Figure 4.11: MAT versus SINR per chip performance for **a DDSS system constituted by both the non-coherent code acquisition aided system in the search mode and the differentially coherent code acquisition system in the verification mode** parameterised with both the number of transmit and receive antennas, when employing the schematics of Figures 4.1 and 4.2 as well as Table 4.1.

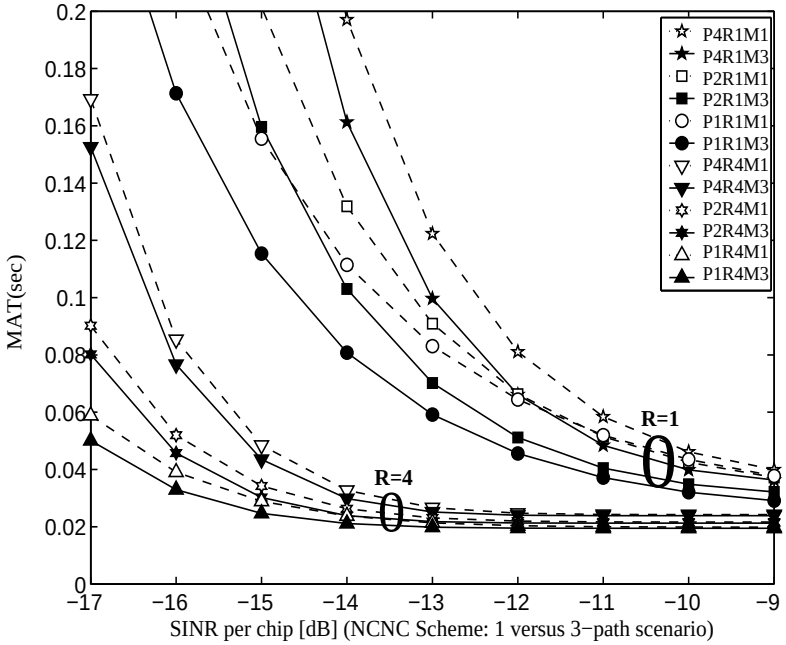

Figure 4.12: MAT versus SINR per chip performance of **the non-coherent code acquisition system for DDSS** parameterised with both the number of transmit and receive antennas, when employing the schematics of Figures 4.1 and 4.2 as well as Table 4.1.

for the search mode is in the range of 10^{-3} to 10^{-4}. In this range the values of the correct detection probability sharply decrease, as seen in Figure 4.13. The reason that the false alarm probability should be small is directly related to the value of the aforementioned false locking penalty associated with the false alarm event(s). A high value of the penalty factor leads to a further degraded MAT performance. Accordingly, a low false alarm probability results in the best possible MAT performance. Having a high correct detection probability would also impose the MAT, but finding the optimum of this probability may be challenging, whilst maintaining as low a false alarm probability as possible. Furthermore, observe in Figure 4.13 that the performance of $P = 4$ is the worst in the context of the NC DDSS scheme and $P = 1$ is the best, in particular at 10^{-3} and lower ranges of the false alarm probability. The DC scheme also exhibits similar trends for the DDSS scheme, although the degree of performance degradation is smaller than that of the NC scheme at E_c/I_0 values below those seen in Figure 4.13. More explicitly, the performance of the correct detection versus false alarm probability recorded for the DC scheme at E_c/I_0 = -16dB is similar to that of the NC scheme at E_c/I_0 = -13dB in Figure 4.13. Additionally, it is worth noting that the useful operational range of the false alarm probability for the search mode is 0.05 to 0.25 for values of $R = 1$ to 4. The correct detection probability increases rapidly over

this range of the probability of false alarm.

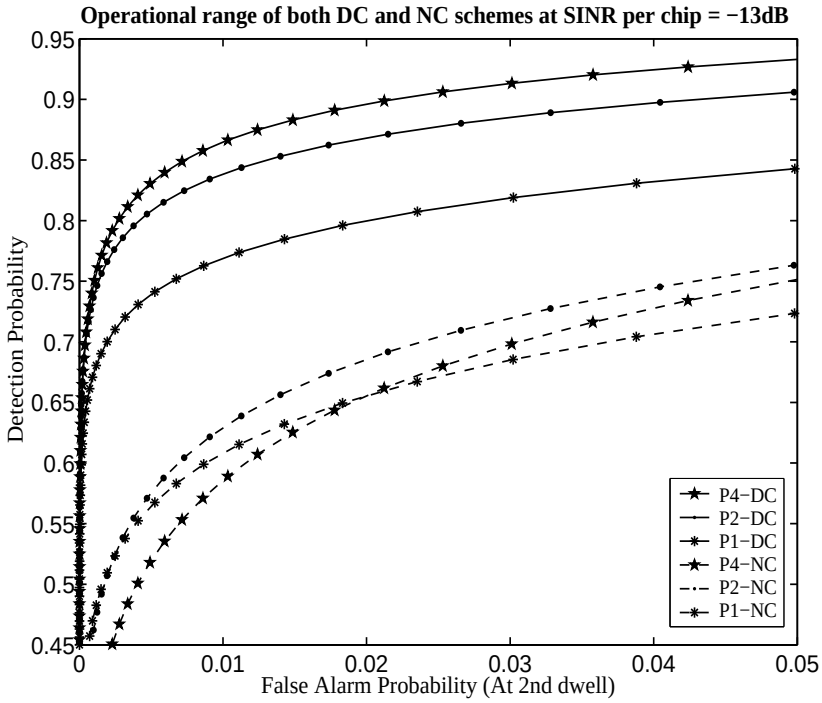

Figure 4.13: Correct detection versus false alarm probability of P= 1,2 and 4 transmit antennas for both differentially coherent and non-coherent code acquisition in the verification mode of our DDSS schemes, when employing the schematics of Figures 4.1 and 4.2 as well as Table 4.1.

The fact that multiple transmit antennas degrade the achievable MAT performance can be further explained as follows. A low level of per-branch received signal strength would lead to a low acquisition performance. In other words, a high diversity order effectively results in an acquisition performance loss, as a consequence of the insufficiently high transmit signal strength per branch. In case of employing both multiple transmit and multiple receive antennas, similar trends are observable, although using two or four receive antennas has the potential of mitigating the associated acquisition performance degradation imposed by the low per-branch E_c/I_0 values associated with the employment of multiple transmitters. The main reasons for the above-mentioned performance trends may be further justified by information theoretic considerations in the NC MIMO aided scenarios considered [112, 113].

The main reasons for the above-mentioned phenomenon are multifold, as inferred from Figures 4.3 to 4.13:

1) In general, coherently detected space-time transmission schemes benefit from having explicit knowledge of the channel's impulse response, which is unavailable during the

code-acquisition phase. Using a relatively low number of chips, over which integration or accumulation is carried out imposes further limits on the attainable benefits of MIMO schemes [112, 113]. Furthermore, the MIMO aided code-acquisition schemes are only capable of achieving a rather limited time diversity, even when 2 to 4 Post-Detection Integration (PDI) stages are used [3, 45].

2) Since no channel coding is used for the pilot signal, no time diversity gain associated with interleaving and channel coding can be achieved [124].

3) When the detection threshold θ_2 of Figure 4.2 is reduced, the resultant code phase estimate often cannot be confirmed by the verification stage of Figure 4.2 and hence the false alarm probability is increased. At the same time, the correct detection probability is also increased. However, when aiming for the best achievable MAT performance, the detection threshold optimisation has to strike a balance between increasing the false alarm probability and the correct detection probability, because after a false alarm event the system may require a high number of chip-durations to return to its search mode.

4) The effect of using a fixed threshold pair θ_1 and θ_2 in Figure 4.2, which is optimised for a specific E_c/I_0 value, also limits the attainable MAT performance, since the acquisition threshold should be optimised and controlled as a function of the E_c/I_0 value encountered.

4.2.3 Conclusion

In this section, we analysed the multiple antenna aided transmit/receive diversity effects on the code acquisition performance of both DC and NC code acquisition schemes in the inter-cell synchronous CDMA DL. Again, our results show that increasing the number of transmit antennas in a MIMO aided CDMA system usually results in a MAT performance degradation, regardless whether single-path or multi-path scenarios are considered. This fact suggests that employing a single transmit antenna might be recommended for maximising the achievable MAT performance. Furthermore, it is extremely undesirable to degrade the achievable code acquisition performance, when the idealised perfectly synchronised benchmark system is capable of attaining its target bit error rate performance at reduced SINR values, as a benefit of employing multiple transmit antennas. Hence it may be concluded that the achievable cell radius determined by the received pilot channel power is expected to be reduced, as the number of transmit antennas is increased, which is a highly undesirable phenomenon, since it has grave repercussions in terms of having to tolerate a high number

of handovers per cell.

4.3 Co-located MIMO Aided Code Acquisition in the MC-DS-CDMA Downlink

4.3.1 System Architecture and System Parameters

Figure 4.14 portrays both the DC and the NC receiver's schematic designed for our MC-DS-CDMA code acquisition scheme using MIMO, where the NC module generates its decision variable by accumulating $(P{\cdot}R{\cdot}U)$ number of independently faded signals observed over a given time interval. In the DC scheme of Figure 4.14, instead of squaring the summed energy as suggested by the procedures outlined in [3], the channel's output samples accumulated over a full spreading code period are multiplied by the conjugate of the N-chip-delayed samples [17, 18] and τ_D represents the integral dwell time. The MAT formulae of both the SDSS and DDSS in Section 2.4 are also employed for the performance analysis.

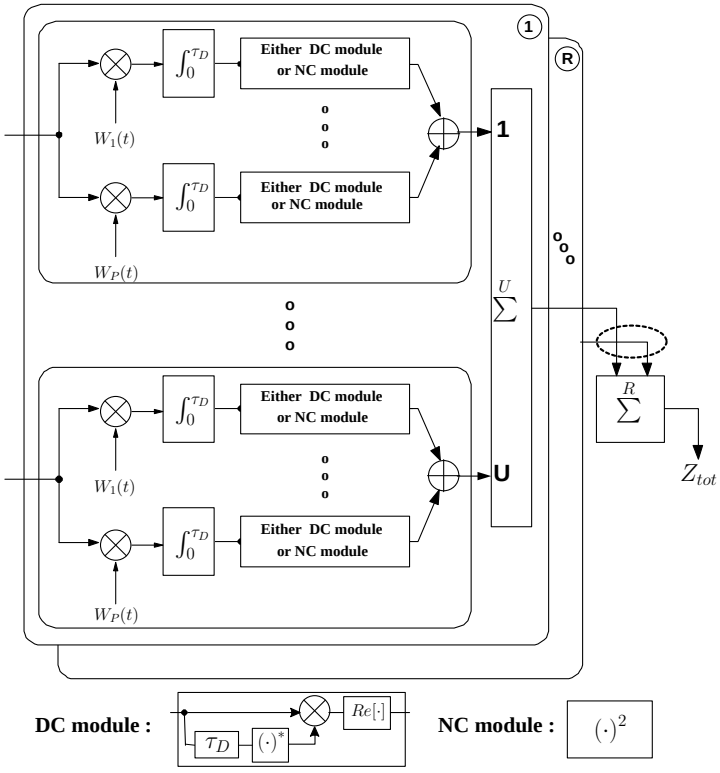

Figure 4.14: Receiver structure of either a differentially coherent or a non-coherent code acquisition scheme employing both R receive antennas and U subcarriers.

When analysing the MAT performance of the SDSS technique [3], where the NC receiver structure of Figure 4.14 is used in the search mode constituting the SDSS scheme seen at the top of Figure 4.15, the decision statistics, Z_{tot} generated by the NC module of Figure 4.14 is compared to the threshold θ_1, which is optimised for each specific E_c/I_0 value. This completes the single-step search-mode of the SDSS scheme. By contrast, the DDSS technique [14] of Figure 4.15 invokes a two-step process. More explicitly, once the desired user's code was found in the search mode of the DDSS scheme of Figure 4.15, the verification mode is activated, which may use either the DC or the NC modules of Figure 4.14, in order to confirm that the correct code-phase is indeed the one identified during the search mode. On the other hand, in the search mode of the DDSS scheme of Figure 4.15 preceding its verification mode, i.e. before the desired user's code was acquired, only the NC scheme can be used. More explicitly, the NC scheme is employed in two consecutive decision processes, namely first to find and then to confirm the correct code phase in order to improve the reliability of SDSS, which results in the DDSS acquisition scheme. Figure 4.15 illustrates the flow chart of the DDSS scheme, where θ_1 and θ_2 represent the acquisition thresholds of the search and verification mode, respectively. Furthermore, Z_1 and Z_2 denote the decision variables of the search and verification mode, respectively. In Figure 4.15 Z_1 is compared to θ_1 and if it exceeds the threshold, Z_2 generated by either DC or NC module is compared to θ_2. If successful code acquisition is declared, then the code tracking loop is enabled. Otherwise, the acquisition system reverts back to the search mode, until the correct code and its phase are found. In our forthcoming analysis, four code acquisition arrangements are considered. Specifically, SDSS employing both DC and NC schemes as well as DDSS exploiting both DC and NC arrangements are invoked in the verification mode. However, in the search mode of the DDSS scheme only the NC scheme can be used. Further details on the related DDSS system can be found in [14, 68].

Our performance comparison between the SC-DS-CDMA system ($U = 1$) and the MC-DS-CDMA system using $U = 4$ subcarriers is based upon the assumptions that these systems have the same total transmitted energy per chip. Furthermore, it is assumed that the integral dwell time, τ_D, is the same for all the scenarios considered here. The associated system parameters are summarised in Table 4.4. In Table 4.5 we summarised the maximum SINR degradation inflicted by both the Doppler shift and the clock-drift-induced frequency mismatch between the transmitter and receiver in conjunction with the coherent integration interval of τ_D duration, as seen in Figure 4.14. It was assumed that the length of the PN sequence in our system was $512 \cdot T_{c1}$ ($or\ 128 \cdot T_c$), where the chip-durations

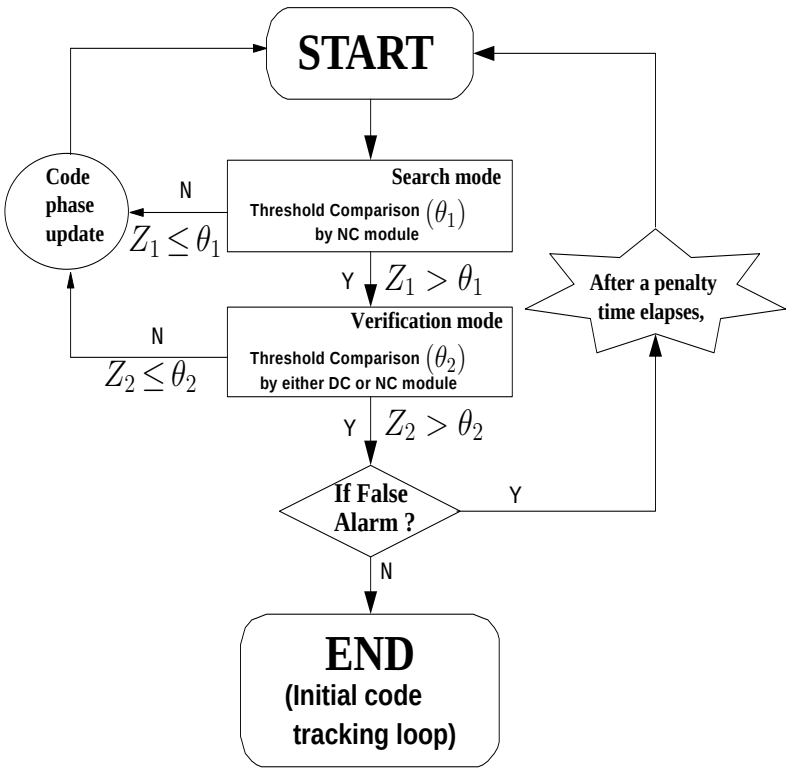

Figure 4.15: Flow chart of our DDSS code acquisition scheme.

chosen for $U = 1$ and 4 are $T_{c1} = 1/2.4576\mu s$ and $T_c = 1/0.6144\mu s$, respectively. In order to analyse the performance of the SDSS technique the accumulation was carried out over 512 chips in the SC scheme of $U = 1$ and over 128 chips in the $U = 4$ MC-DS-CDMA arrangement, respectively, whereas the number of chips over which the accumulator Σ sums the $(\cdot)^2$ envelope detector's output in both the search and the verification modes of DDSS are assumed to be 128 and 512 chips in the SC scheme of $U = 1$, while 32 and 128 chips in the $U = 4$ MC-DS-CDMA arrangement, respectively. These optimised parameter values were computed by using the probabilities of both the correct detection and false alarm in both DC and NC schemes as well as Equation. 2.9 in Section 2.3.2.1, which were provided for quantifying the performance degradation imposed by both the Doppler shift and the frequency mismatch encountered. The spreading factor of the Walsh code to be acquired was chosen to be 128. The carrier frequency was 1.9 GHz, whilst the frequency mismatch was postulated to be 1000 Hz [3]. As an example of a high mobile speed, it is reasonable to assume 160 km/h. We also assumed that the sampling inaccuracy caused by having a finite, rather than infinitesimally low search step size of $\Delta = 1/2T_c$ was -0.91 dB, which is a practically acceptable value for the specific search step size considered [3]. The entire uncertainty region of code acquisition was assumed to entail 512 hypotheses, which is the

uncertainty region of the $U = 2$ scenario, because the same uncertainty region is required for the sake of a fair comparison. Finally, in the spirit of [15], the false locking penalty factor was considered to be 1000 chip-durations. For simplicity, it was assumed that only a single received signal path is encountered in a given search window. All the performance curves have been generated at the threshold value of $E_c/I_0 = -19\,dB$, which was experimentally found for the specific code acquisition scheme considered.

Table 4.4: System Parameters

Bandwidth	$U = 1$	2.5 MHz
	$U = 4$	4×0.625 MHz
Carrier frequency		1.9 GHz
Spreading factor		128
Diversity	Transmit	1,2,4
	Receive	1,2,4
	Subcarrier	1,4
Frequency mismatch		1000 Hz
Mobile speed		160km/h
Schemes selected		Number of chip
SDSS	$U = 1$	512 chips
	$U = 4$	128 chips
DDSS	$U = 1$	128 and 512 chips
	$U = 4$	32 and 128 chips
Total uncertainty region		512 hypotheses
False locking penalty factor		1000 chip-durations

Table 4.5: Maximum SINR degradation inflicted by both the Doppler shift and a 1000 Hz frequency mismatch in comparison to a stationary receiver having no frequency drift for the coherent integration interval of N chip durations at a carrier frequency of 1.9 GHz as a function of the number of subcarriers ($U = 1$ and 4)

N(Chips): U=1	**128**	256	**512**	768	1024
N(Chips): U=4	**32**	64	**128**	192	256
Degradation(dB)	**0.061**	0.2449	**0.9969**	2.3144	4.3213

4.3.2 System Performance Results

Figure 4.16 illustrates the achievable MAT versus SINR per chip performance of SDSS for the DC SC-DS-CDMA code acquisition arrangement as a function of the number of transmit antennas for $P = 1$,2 as well as 4 and that of the number of receive antennas for $R = 1$ and 4. Observe in Figure 4.16 that unexpectedly, as the number of transmit antennas is decreased, all the curves explicitly indicate an improved MAT performance, except for the $'P2R1'$ scenario. To elaborate on the above observation a little further, a useful transmit diversity gain is only experienced for the case of $'P2R1'$, and even this was limited to the specific SINR range of -13 to -16 dB. For comparison, Figure 4.17 characterises the MAT versus SINR per chip performance of SDSS for the NC code acquisition scheme as a function of the number of transmit antennas for $P = 1$,2 as well as 4 and that of the number of receive antennas for $R = 1$ and 4. Similarly, as the number of transmit antennas is decreased, all the curves illustrate an improved MAT performance. Since the DC scheme has a performance gain of just under 3 dB over the NC one, when considering their correct detection probability and false alarm probability, hence we conclude that the MAT performance curves confirm the expected trends. Moreover, the DC scheme has an advantage over the NC one in the low SINR range in terms of reducing the effects of both the AWGN and interference. Hence, this indicates that the DC scheme experiences a lower MAT performance degradation owing to the employment of multiple transmit antennas than its NC counterpart.

Figures 4.18 and 4.19 illustrate the achievable MAT versus SINR per chip performance of the SDSS-aided MC-DS-CDMA code acquisition scheme in both DC and NC scenarios, respectively, when parameterised by both the number of transmit and receive antennas and using $U = 4$ subcarriers. In the case of the MC-DS-CDMA system, both schemes benefit from a specific diversity order, which is determined by the number of subcarriers used. It is also assumed that the total transmitted energy per chip is the same in all the scenarios considered. Accordingly, the achievable diversity order is determined by the product of the number of subcarriers and that of the number of transmit antennas. This phenomenon indicates that the employment of MC transmissions leads to exactly the same detrimental effect on the achievable MAT performance, as that imposed by employing multiple transmit antennas owing to the reduced 'per-diversity-branch' power, which further argued below. The results of Figures 4.18 and 4.19 are parameterised by both the number of transmit antennas for $P = 1, 2$ as well as 4 and by the number of receive antennas for $R = 1$ as well as 2. As the number of transmit antennas is decreased, all the curves of Figures 4.18

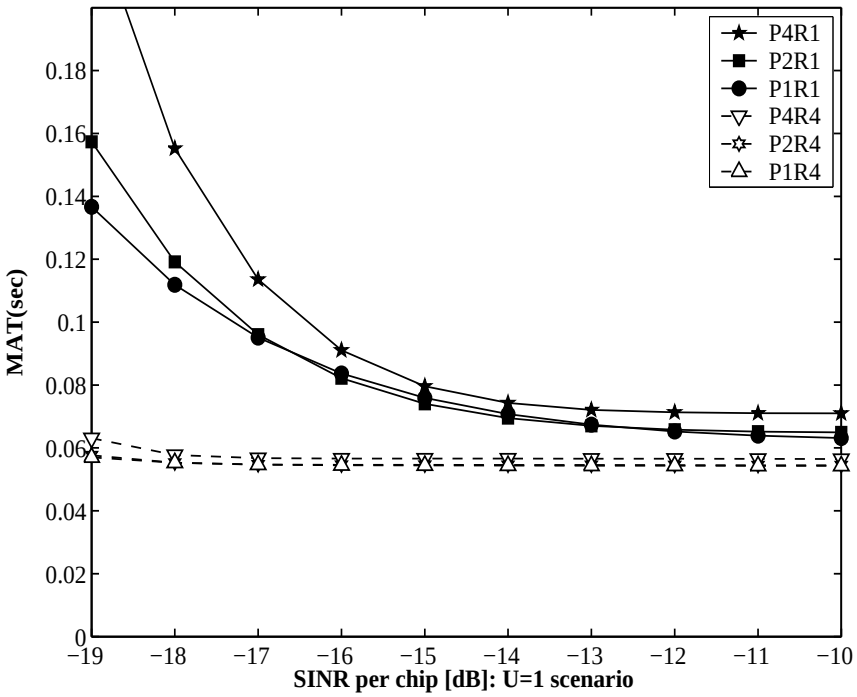

Figure 4.16: MAT versus SINR per chip performance of the SDSS-aided **differentially coherent code acquisition scheme** parameterised with both the number of transmit and receive antennas for $U = 1$ subcarriers, when employing the schematic of Figure 4.14 and Table 4.4.

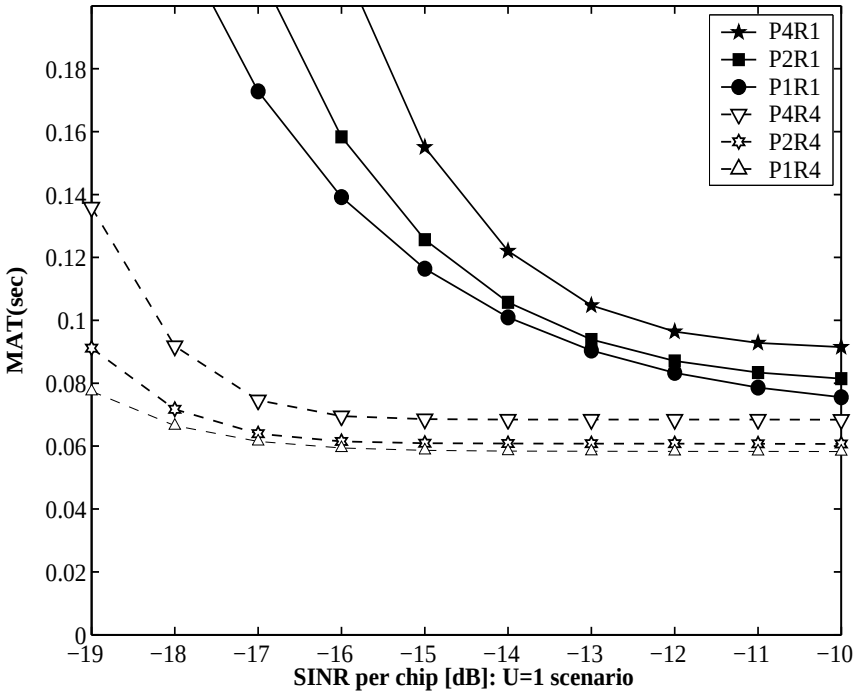

Figure 4.17: MAT versus SINR per chip performance of the SDSS-aided **non-coherent code acquisition scheme** parameterised with both the number of transmit and receive antennas for $U = 1$ subcarriers, when employing the schematic of Figure 4.14 and Table 4.4.

and 4.19 exhibit an improved MAT performance. Furthermore, as a benefit of the inherent performance gain of the DC scheme over the NC one, the overall MAT performance results of Figure 4.18 are better than those of Figure 4.19. This trend explicitly illustrates that the SDSS-aided MC-DS-CDMA code acquisition scheme considerably degrades the achievable MAT performance of SC-DS-CDMA. This is a consequence of both the low per-antenna power imposed by using multiple transmit antennas for the sake of achieving either a transmit diversity gain or a multiplexing gain as well as that of the low per-subcarrier power imposed by having multiple subcarriers in order to attain a frequency diversity gain. A low level of per-branch and/or per-subcarrier received signal strength is expected to result in a low acquisition performance, despite achieving a high transmit- and frequency-diversity gain.

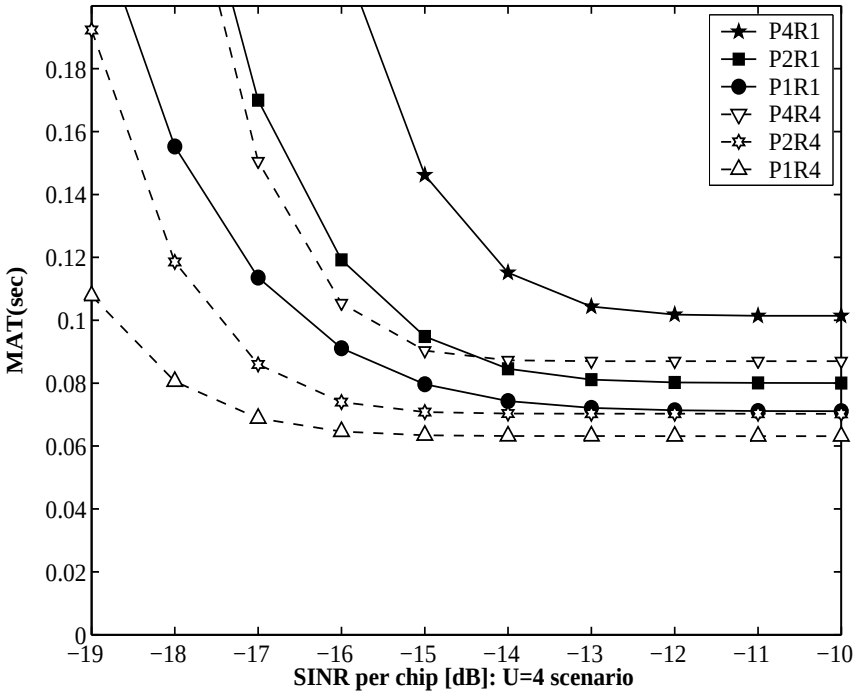

Figure 4.18: MAT versus SINR per chip performance of the SDSS-aided **differentially coherent code acquisition scheme** parameterised with both the number of transmit and receive antennas for $U = 4$ subcarriers, when employing the schematic of Figure 4.14 and Table 4.4.

Figure 4.20 illustrates the achievable MAT versus SINR per chip performance of the DDSS-aided SC-DS-CDMA code acquisition arrangement. More specifically, both the NC code acquisition assisted scheme used in the search mode and the DC code acquisition assisted arrangement employed in the verification mode are characterised as a function of both the number of transmit antennas for $P = 1$,2 as well as 4 and that of the number of

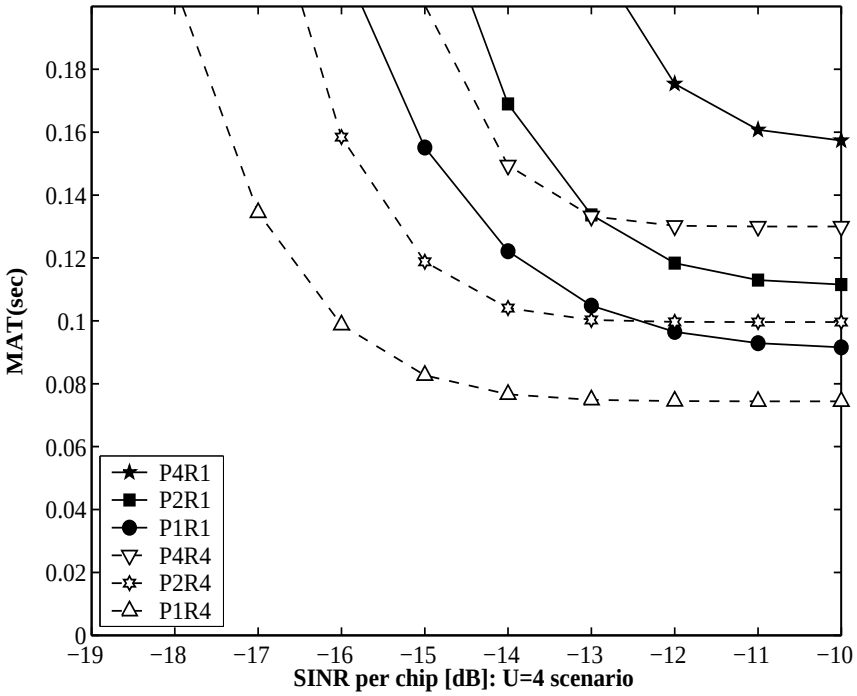

Figure 4.19: MAT versus SINR per chip performance of the SDSS-aided **non-coherent code acquisition scheme** parameterised with both the number of transmit and receive antennas for $U = 4$ subcarriers, when employing the schematic of Figure 4.14 and Table 4.4.

receive antennas for $R = 1$ and 4. By contrast, Figure 4.21 characterises the MAT versus SINR per chip performance of the DDSS aided NC code acquisition scheme, both in its search mode and verification mode. Observe in Figure 4.20 that unexpectedly, as the number of transmit antennas is decreased, all the curves explicitly indicate an improved MAT performance, except for the $'P2R1'$ scenario, as recorded for the specific SINR range between -13 and -16 dB. To elaborate on the above observation a little further, in the scenario of $'P2R1'$ the DDSS scheme exhibits a slightly better MAT performance in comparison to the $'P1R1'$ scenario right across the specific SINR range considered. Similarly, as the number of transmit antennas is decreased in Figure 4.21, all the MAT curves illustrate an improved performance, except for the $'P2R1'$ scenario, which constituted an exception also in Figure 4.20. The results seen in Figure 4.20 suggest that the overall performance improvement of the DDSS aided DC scheme of Figure 4.14 recorded in its verification mode is significantly higher than that of the DDSS assisted NC scheme of Figure 4.14, as seen in Figure 4.21. The DC scheme has a performance gain of just under 3 dB over the NC arrangement, when considering their correct detection probability and false alarm probability, hence we conclude that the MAT performance curves confirm the expected trends. Moreover, the DC scheme has an advantage over the NC one in the low SINR range [17] in

terms of reducing the effects of both the AWGN and interference [5]. Hence, this indicates that the MIMO-aided DC scheme experiences a lower MAT performance degradation owing to the reduced transmit power of the individual transmit antennas than its NC counterpart. It is worth mentioning that although not shown in Figure 4.20 and Figure 4.21 for reasons of avoiding obfuscating details, the reliable operating range of $R = 2$ receive antennas is situated in between that corresponding to the $R = 1$ and $R = 4$ receive antenna scenario.

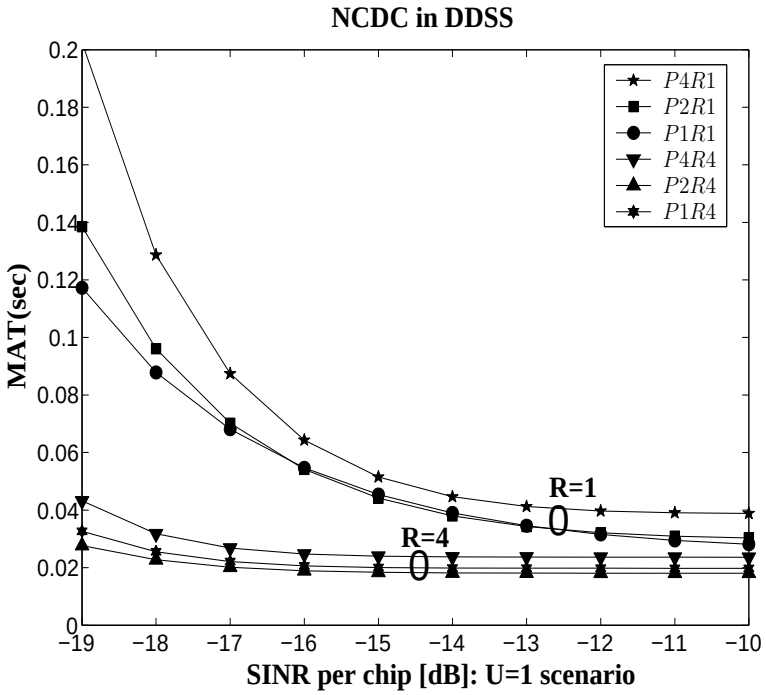

Figure 4.20: MAT versus SINR per chip performance for **a DDSS scheme constituted by both the non-coherent code acquisition assisted scheme in the search mode and the differentially coherent code acquisition scheme in the verification mode** parameterised with both the number of transmit and receive antennas for $'U = 1'$ subcarrier, when using the schematics of Figures 4.14 and 4.15 as well as Table 4.4.

Figure 4.22 illustrates the achievable MAT versus SINR per chip performance of the DDSS-assisted MC-DS-CDMA code acquisition scheme using NC code acquisition in its search mode and DC code acquisition in its verification mode. The MAT results are parameterised with both the number of transmit and receive antennas for $'U = 4'$ subcarriers. For the sake of comparison, Figure 4.23 characterises the MAT versus SINR per chip performance of the DDSS assisted NC code acquisition scheme in its search mode and verification mode parameterised with both the number of transmit and receive antennas for $'U = 4'$

[5] In the low-SINR region, the false alarm probability difference between the DC and NC schemes corresponds to a factor of two, indicating the superiority of the DC scheme over the NC one.

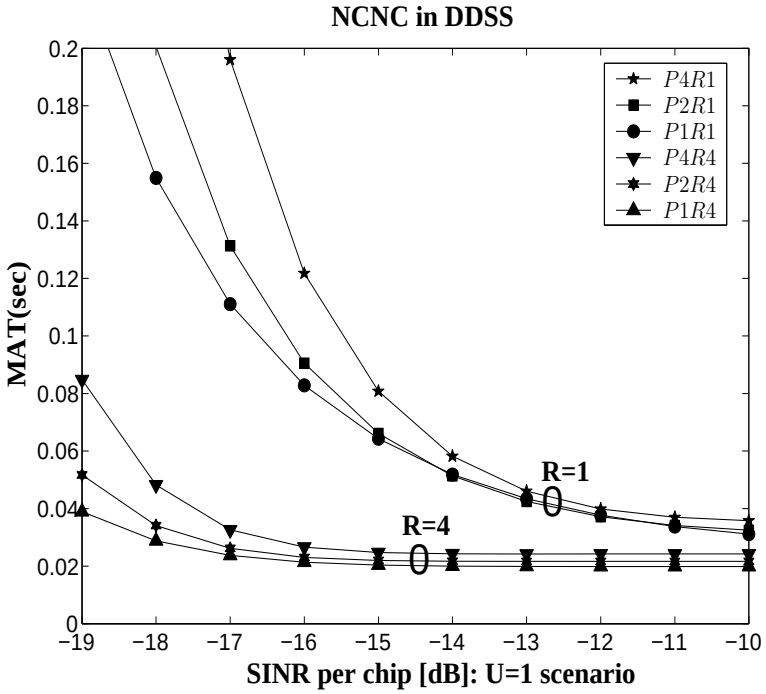

Figure 4.21: MAT versus SINR per chip performance of **the DDSS assisted non-coherent code acquisition scheme** parameterised with both the number of transmit and receive antennas for $'U = 1'$ subcarrier, when using the schematics of Figures 4.14 and 4.15 as well as Table 4.4.

subcarriers. In the case of the MC-DS-CDMA system, both schemes benefit from a specific diversity order, which is determined by the number of subcarriers used. It is also assumed that the total transmitted energy per chip is the same in all the scenarios considered. Accordingly, the achievable diversity order is determined by the product of the number of subcarriers and that of the number of transmit antennas. This phenomenon indicates that the employment of multi-carrier transmissions leads to exactly the same detrimental effect on the achievable MAT performance as that imposed by employing multiple transmit antennas owing to the reduced 'per-diversity-branch' power, as argued further below. The results of Figures 4.22 and 4.23 are parameterised by both the number of transmit antennas for $P = 1, 2$ as well as 4 and by the number of receive antennas for $R = 1$ as well as 2. As the number of transmit antennas is decreased, all the curves of Figures 4.22 and 4.23 exhibit an improved MAT performance. Furthermore, as a benefit of the inherent performance gain of the DC scheme over the NC one, the overall MAT performance results of Figure 4.22 are better than those of Figure 4.23. Although the results of the DDSS scenario characterised in both Figures 4.22 and 4.23 exhibit a similar trend as in both Figures 4.20 and 4.21, the performance degradation imposed by employing both multiple antennas and multiple subcarriers becomes more drastic in both Figures 4.22 and 4.23, when the number of transmit antennas is increased. This fact explicitly illustrates that the DDSS-assisted MC-DS-CDMA code acquisition scheme considerably degrades the achievable MAT performance of SC-DS-CDMA.

This is the consequence of two phenomena. Firstly, it is imposed by the low per-antenna power imposed by using multiple transmit antennas for the sake of achieving either a transmit diversity gain or a multiplexing gain. The second reason for the reduced MAT performance of MC-DS-CDMA is the low per-subcarrier power imposed by the introduction of multiple subcarriers in order to attain a frequency diversity gain. Nonetheless, we demonstrated that the employment of the DC scheme improves the achievable MAT performance. To elaborate on the above results a little further, a low level of per-branch and/or per-subcarrier received signal strength is expected to result in a low acquisition performance, despite achieving a high transmit- and frequency-diversity gain. In other words, a high transmit- and frequency-diversity order effectively leads to a code acquisition performance loss, as a consequence of the insufficiently high signal strength per transmit antenna and per subcarrier. When employing multiple receive antennas, similar trends are observable, although using multiple receive antennas has the potential of alleviating the acquisition performance degradation imposed by the low per-branch E_c/I_o values due to the employment

of multiple transmitters and multiple subcarriers. Both Figures 4.24 and 4.25 document

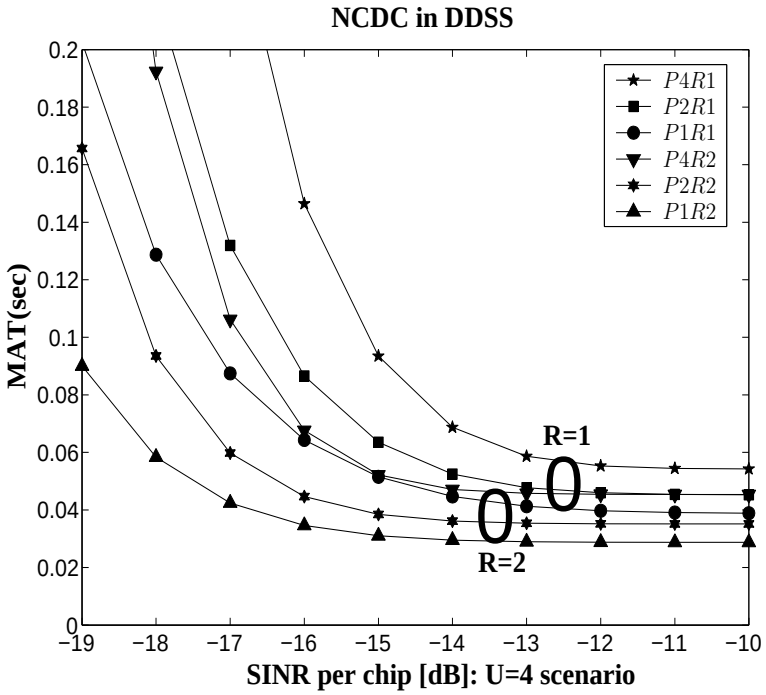

Figure 4.22: MAT versus SINR per chip performance for **a DDSS scheme constituted by both the non-coherent code acquisition assisted scheme in the search mode and the differentially coherent code acquisition scheme in the verification mode** parameterised with both the number of transmit and receive antennas for $'U = 4'$ subcarriers, when using the schematics of Figures 4.14 and 4.15 as well as Table 4.4.

the relationship between P_D and the number of transmit antennas required by both the DDSS-assisted DC and NC code acquisition schemes for approaching their lowest possible MAT. Explicitly, the results of Figures 4.24 and 4.25 were recorded versus the number of subcarriers ($U = 1$ and 4), parameterised with both the number of transmit antennas and with different values of E_c/I_0, respectively. The correct detection probabilities seen in both Figures 4.24 and 4.25 were obtained assuming a false locking probability of $P_F = 5{\times}10^{-4}$ for all scenarios considered, since the reliable operational range in the verification mode of the DDSS-assisted code acquisition scheme is a false alarm probability spanning from 10^{-3} to 10^{-4}. The left illustration of Figure 4.24 characterises the scenario of $U = 1$, while the one at the right of Figure 4.24 is valid for the arrangement having $U = 4$. When increasing the number of transmit antennas, the curves recorded for E_c/I_0 values spanning from -7 to -13 dB at the left of Figure 4.24 indicates a P_D improvement, although at low E_c/I_0 values, say at E_c/I_0 = -16 dB, the opposite is true. On the other hand, the results seen at the right of Figure 4.24 indicate that P_D tends to decrease, as both the number of transmit antennas

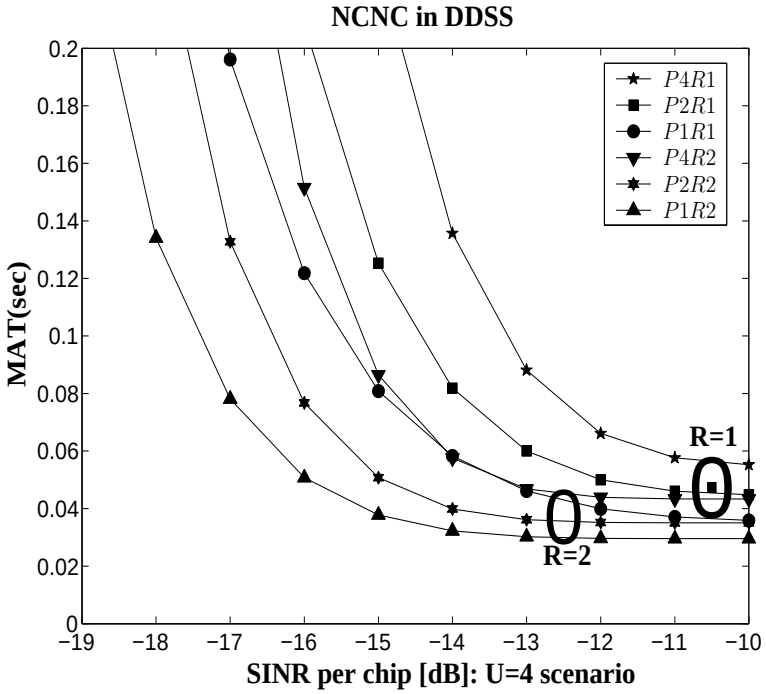

Figure 4.23: MAT versus SINR per chip performance of **the DDSS assisted non-coherent code acquisition scheme** parameterised with both the number of transmit and receive antennas for $'U = 4'$ subcarriers, when using the schematics of Figures 4.14 and 4.15 as well as Table 4.4.

and the number of subcarriers increases, when typical E_c/I_0 values are encountered. The results of Figure 4.25 also exhibit similar performance trends. However, due to the performance loss of the NC scheme in comparison to the DC arrangement, the achievable P_D performance further deteriorates over the E_c/I_0 values considered. The main reasons for

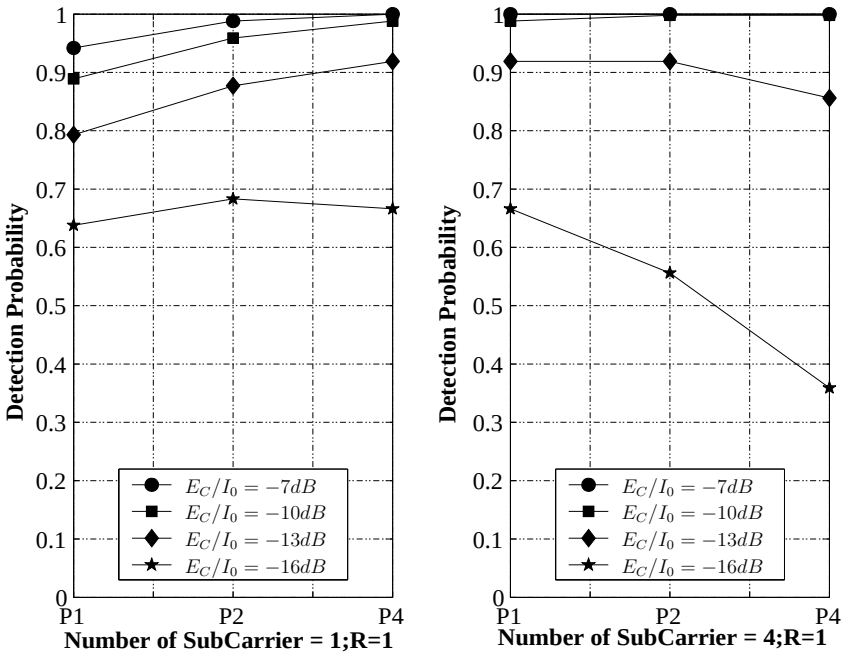

Figure 4.24: P_D of the differentially coherent scheme versus the number of transmit antennas for P = 1,2 as well as 4, the number of receive antennas for $P = 1$ as well as the number of subcarriers for both $U = 1$ (Left figure) and $U = 4$ (Right figure) parameterised by the E_c/I_0, when employing the schematic of Figure 4.14 and Table 4.4.

the above-mentioned performance trends may be further justified by information theoretic considerations in the NC MIMO aided scenarios considered [112, 113, 119]. Finally, when considering the design of MIMO aided code acquisition schemes, the following guidelines may be inferred from Figures 4.16 to 4.25:

1) In general, coherently detected space-time transmission schemes benefit from having explicit knowledge of the CIR, which is unavailable during the code-acquisition phase. Accordingly, exploiting multiple transmit antennas typically leads to an MAT performance degradation, as seen in Figures 4.16 to 4.25.

2) Using a relatively low number of chips, over which integration or accumulation is carried out imposes further limits on the attainable benefits of MIMO aided schemes [112, 113]. Furthermore, the MIMO aided code-acquisition schemes are only capable of achieving a

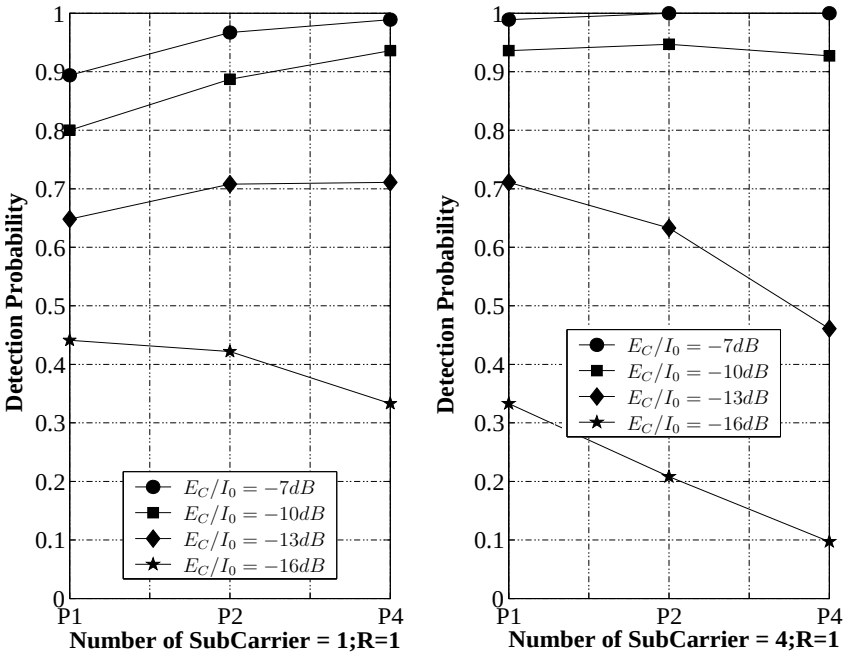

Figure 4.25: P_D of the non-coherent scheme versus the number of transmit antennas for $P = 1$,2 as well as 4, the number of receive antennas for $P = 1$ as well as the number of subcarriers for both $U = 1$ (Left figure) and $U = 4$ (Right figure) parameterised by the E_c/I_0, when employing the schematic of Figure 4.14 and Table 4.4.

rather limited time diversity, even when 2 to 4 PDI stages are used [3, 45].

3) Employing both DDSS and DC schemes may provide a rather limited diversity gain in comparison to using SDSS and NC schemes, as evidenced by Figures 4.16 to 4.25.

4) Using multiple receive antennas increases the achievable receiver diversity gain and has the potential of compensating for the MAT degradation imposed by the low per-branch power of multiple transmitters, as observed in Figures 4.16 to 4.23.

5) Since no channel coding is used for the pilot signal, no time diversity gain associated with interleaving and channel coding can be achieved [124].

6) When the detection threshold θ_2 of Figure 4.16 is reduced, the resultant code phase estimate often cannot be confirmed by the verification stage of Figure 4.16 and hence the false alarm probability is increased. At the same time, the correct detection probability is also increased. However, when aiming for the best achievable MAT performance, the detection threshold optimisation has to strike a balance between increasing the false alarm probability and the correct detection probability, because after a false alarm event the system may require 1000 chip-durations to return to its search mode.

7) The effect of using a pair of fixed thresholds of θ_1 and θ_2 in Figure 4.16, which are optimised for a specific E_c/I_0 value also limits the attainable MAT performance, since the acquisition threshold should be optimised and controlled as a function of the E_c/I_0 value encountered.

8) For the sake of acquiring the initial timing information of the received paths, specifically designed preambles, such as that of the P-SCH of W-CDMA [115] combined with TSTD [116] might be recommended, which is capable of achieving a diversity gain with the aid of a single transmit antenna [113, 114]. The pilot channel may also be used for other purposes, such as frequency error correction and channel estimation [118].

4.3.3 Conclusion

In this section, we characterised the MIMO aided diversity effects on the attainable code acquisition performance of both DC and NC code acquisition schemes in the inter-cell synchronous MC-DS-CDMA DL. Again, similarly to the conclusions of the previous chapter our results suggest that increasing both the number of transmit antennas and that of the subcarriers in a MIMO-assisted MC-DS-CDMA system leads to combining the low-energy signals of both the transmit antennas and the subcarriers, which may further increase the MAT by an order of magnitude, in particular in the critical scenario, when the SINR is relatively low, even though the MAT performance degradation imposed on the DC scheme is less severe than that of its NC counterpart, as observed in Figures 4.16 to 4.25. Based on the above-mentioned results justified by information theoretic considerations, our acquisition design guidelines are applicable to diverse NC MIMO aided scenarios, regardless whether any combinations of SC-DS-CDMA and multi carrier transmission schemes are considered.

4.4 Chapter Summary and Conclusions

In this chapter, we have provided details of the performance analysis for both DC and NC serial search based code acquisition in the co-located MIMO aided SC- and MC- DS-CDMA DL. We commenced the chapter by a brief introduction in Section 4.1. We then characterised the achievable performance of the code acquisition scheme in the co-located MIMO aided SC-DS-CDMA DL in Section 4.2. This was followed by a discussion on the performance of the code acquisition in the co-located MIMO aided MC-DS-CDMA DL in Section 4.3.

In order to highlight our investigations of the co-located DC MIMO aided schemes, the characteristics of the co-located DC MIMO aided code acquisition schemes is again emphasised in terms of the achievable MAT performance in Figures 4.26 and 4.27. Figure 4.26

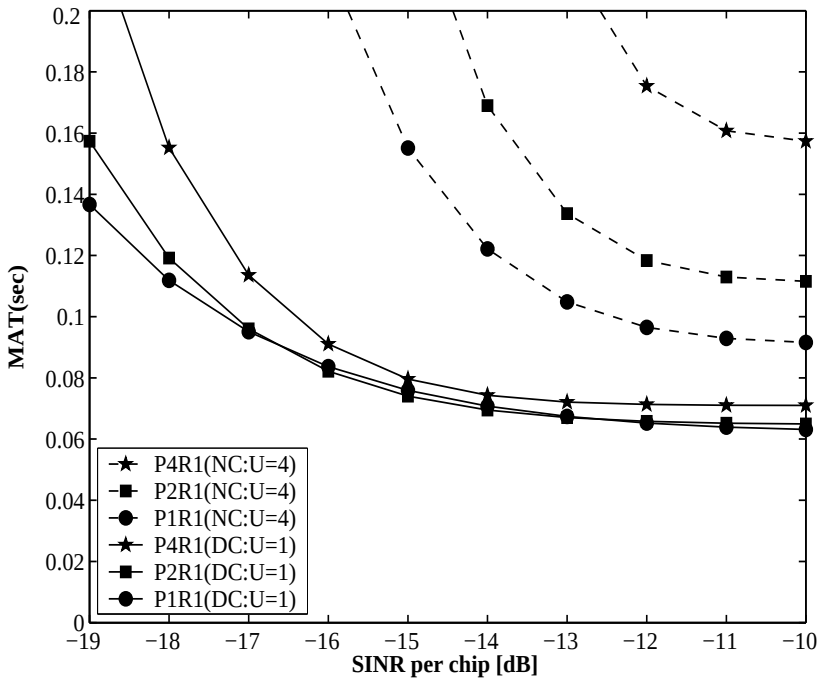

Figure 4.26: MAT versus E_c/I_0 performance comparison between the DC- and NC-based SDSS code acquisition schemes parameterised with the number of transmit antennas for $U = 1$ and $U = 4$ subcarriers, respectively, when employing the schematic of Figure 4.14 and Table 4.4.

illustrates the achievable MAT versus E_c/I_0 performance comparison between the DC- and NC-based SDSS code acquisition schemes parameterised with the number of transmit antennas for $U = 1$ and $U = 4$ subcarriers, respectively. In the results of Figure 4.26, the solid lines indicate the performance curves of the DC-based SDSS scheme for the $U = 1$ scenario,

whilst the dashed lines represent the performance curves of the NC-based SDSS scheme for the $U = 4$ scenario. It is worth mentioning that the operating range of both the NC-based SDSS scheme observed for $U = 1$ and that of the DC-based SDSS scheme recorded for $U = 4$ is between that corresponding to both schemes characterised in Figure 4.26. However, for the sake of avoiding obfuscating points in the figure, they were omitted. Similarly to the conclusions of the scenario of the co-located NC MIMOs, when the number of transmit antennas is decreased, all the curves explicitly indicate an improved MAT performance, except for the $'P2R1'$ scenario of the DC-based SDSS scheme recorded for $U = 1$. To elaborate on the above observations a little further, a useful transmit diversity gain is only experienced for the case of $'P2R1'$ in the single-path scenario, and even this was limited to the specific SINR range of -13 to -16 dB. In the case of the MC-DS-CDMA system, the NC SDSS scheme characterised for $U = 4$ in Figure 4.26 benefits from a specific diversity order, which is determined by the number of subcarriers used. It is also assumed that the total transmitted energy per chip is the same in all the scenarios considered. Accordingly, the achievable diversity order is determined by the product of the number of subcarriers and that of the number of transmit antennas. This phenomenon indicates that the employment of MC transmissions leads to exactly the same detrimental effect on the achievable MAT performance, as that imposed by employing multiple transmit antennas owing to the reduced 'per-diversity-branch' power, as argued further below. As the number of transmit antennas is decreased, all the curves of the NC SDSS scheme plotted for $U = 4$ in Figure 4.26 exhibit an improved MAT performance. Furthermore, as a benefit of the inherent performance gain of the DC scheme over the NC one, the overall MAT performance results recorded for the DC scenario of Figure 4.26 are significantly better than those of the NC arrangement. This trend explicitly illustrates that the SDSS-aided MC-DS-CDMA code acquisition scheme considerably degrades the achievable MAT performance of SC-DS-CDMA. This is a consequence of both the low per-antenna power imposed by using multiple transmit antennas for the sake of achieving either a transmit diversity gain or a multiplexing gain as well as that of the low per-subcarrier power imposed by having multiple subcarriers in order to attain a frequency diversity gain. A low level of per-branch and/or per-subcarrier received signal strength is expected to result in a low acquisition performance, despite achieving a high transmit- and frequency-diversity gain.

Figure 4.27 illustrates the achievable MAT versus E_c/I_0 performance of the NCDC and NCNC DDSS code acquisition schemes parameterised with the number of transmit antennas for $U = 1$ and $U = 4$ subcarriers, respectively. In the results of Figure 4.27, the solid

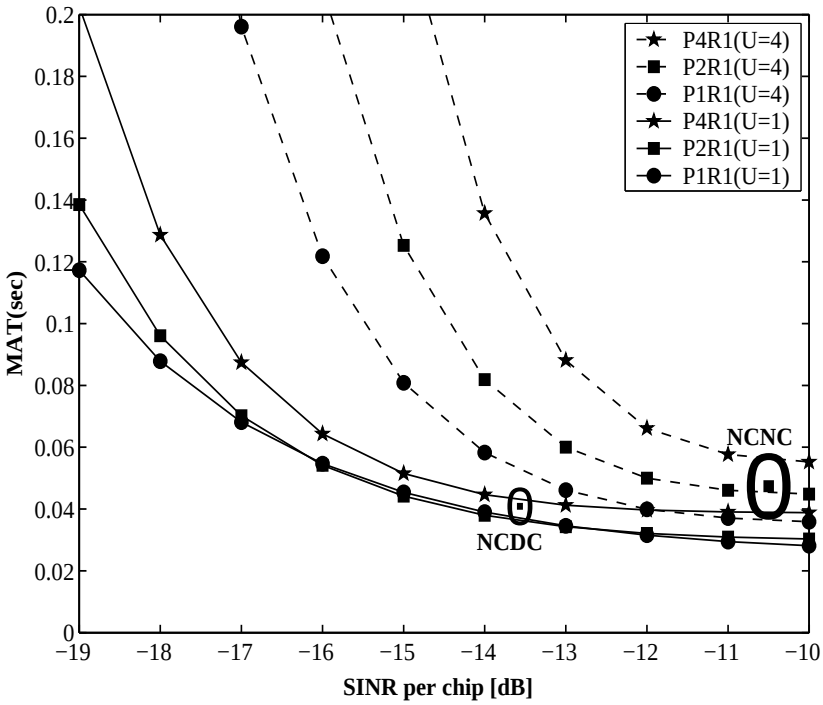

Figure 4.27: MAT versus E_c/I_0 performance comparison between the NCDC- and NCNC-based DDSS code acquisition schemes parameterised with the number of transmit antennas for $'U = 1'$ and $U = 4$ subcarriers, respectively, when using the schematics of Figures 4.14 and 4.15 as well as Table 4.4.

lines indicate the performance curves of the NCDC DDSS scheme for the $U = 1$ scenario, while the dashed lines represent the performance curves of the NCNC DDSS scheme for a $U = 4$ scenario. More specifically, the acronym $NCDC$ in Figure 4.27 indicates that both the NC code acquisition aided system used in the search mode and the DC code acquisition assisted scheme employed in the verification mode are characterised for $U = 1$. By contrast, the DDSS system denoted by the acronym $NCNC$ in Figure 4.27 employs the NC code acquisition aided scheme in both its search mode and verification mode for $U = 4$. It is worth mentioning that the operating range of both the NCNC-based DDSS scheme observed for $U = 1$ and that of the NCDC-based DDSS scheme recorded for $U = 4$ are in between that corresponding to both schemes of Figure 4.27. However, for the sake of avoiding obfuscating points in the figure, they were omitted. Similarly to the conclusions drawn for the scenarios of Figure 4.26, as the number of transmit antennas is decreased, all the curves explicitly indicate an improved MAT performance, except for the $'P2R1'$ scenario of the NCDC-based scheme in the single-path propagation environment, as recorded for the specific SINR range between -13 and -16 dB. To elaborate on the above observations a little further, in the scenario of $'P2R1'$ the DDSS scheme exhibits a slightly better MAT performance in comparison to the $'P1R1'$ scenario right across the specific SINR range considered. The results seen in Figure 4.27 also suggest that the overall performance improvement of the DC scheme in the verification mode is significantly higher than that of the DDSS assisted NC scheme. The DC scheme has a performance gain of just under 3 dB over the NC arrangement, when considering their correct detection probability and false alarm probability. Hence we conclude that the MAT performance curves confirm the expected trends. Moreover, the DC scheme has an advantage over the NC one in the low SINR range [17] in terms of reducing the effects of both the AWGN and interference. Hence, this indicates that the MIMO-aided NCDC scheme experiences a lower MAT performance degradation owing to the reduced transmit power of the individual transmit antennas than its NCNC counterpart. Furthermore, this result explicitly illustrates that the DDSS-assisted MC-DS-CDMA code acquisition scheme considerably degrades the achievable MAT performance of SC-DS-CDMA. Although the results of the DDSS scenarios characterised in Figure 4.27 exhibit a similar trend to those seen in Figure 4.26, the performance degradation imposed by employing both multiple antennas and multiple subcarriers becomes more drastic in Figure 4.26, when the number of transmit antennas is increased.

Throughout the above-mentioned two topics discussed in the context of the DC serial search based code acquisition in the co-located MIMO aided SC- and MC- DS-CDMA DL,

our findings suggest that increasing both the number of transmit antennas and that of the subcarriers in a co-located MIMO-aided MC-DS-CDMA system results in combining the low-energy, noise-contaminated signals of both the transmit antennas and the subcarriers. Furthermore, the MAT performance degradation imposed by the DC scheme is less severe than that of its NC counterpart, as seen in Figures 4.16 to 4.25. This fact ultimately reduces the correct detection probability, and accordingly increases the MAT by an order of magnitude, when the SINR is relatively low. It is extremely undesirable to degrade the achievable acquisition performance, when the system is capable of attaining its target BER performance at reduced SINR values. This phenomenon also has a detrimental effect on the performance of Rake receiver based synchronisation, when the perfectly synchronised system is capable of attaining its target BER performance at reduced SINR values, as a benefit of employing multiple transmit antennas and/or frequency diversity. Hence it may be concluded that the achievable cell coverage determined by the received pilot channel power may be reduced, as the number of transmit antennas is increased, which is a highly undesirable phenomenon, since it has grave repercussions in terms of having to tolerate a high number of handovers per cell. Furthermore, based on the above-mentioned results justified by information theoretic considerations, our acquisition design guidelines are applicable to diverse co-located DC MIMO aided scenarios.

Chapter 5

Code Acquisition Preliminaries for the Co-located SIMO DS-UWB Downlink

5.1 Introduction

A rudimentary introduction to code acquisition designed for the DS-UWB DL has been provided in Section 1.6. In this chapter, we will provide the necessary preliminaries for more sophisticated acquisition schemes contrived for the multiple receive antenna aided DS-UWB DL. We will commence the chapter with the portrayal of the UWB channel model, which exhibits both large-scale and small-scale fading. Furthermore, we will place much emphasis on the in-depth description of the Saleh-Valenzuela (S-V) model in Section 5.2. Further details on code acquisition for the DS-UWB DL will be presented in Section 5.3. More specifically, the characteristics of PN codes are highlighted in Section 5.3.1, followed by a detailed discussion on the so-called modulo-2 squaring operation in Section 5.3.2. An in-depth illustration of both the sum-product algorithm and offset-based min-sum algorithm will be the focus of Sections 5.3.3 and 5.3.4, respectively. In Section 5.3.5 the iterative message passing algorithm will be elucidated in detail.

Based on the above-mentioned facts, the detailed system description and a range of algorithms designed for both single- and two-stage iterative acquisition will be detailed in Sections 5.4.1 and 5.4.2, respectively. More explicitly, in Section 5.4.1, single-stage iterative

acquisition employing both a single- and multiple-component decoder will be described in Sections 5.4.1.1 and 5.4.1.2, respectively. Then the underlying formulas of both the correct detection and false alarm probabilities will be presented in Section 5.5. The MAT analysis of our proposed schemes will be provided for both the SISO and SIMO aided DS-UWB DL in Sections 5.6.1 and 5.6.2, respectively, when considering both single- and multi-path propagation environments. Finally, in Section 5.7 our summary and conclusions will be provided.

5.2 Channel Model

5.2.1 Modelling of UWB Channels

The UWB channel is a frequency-selective fading channel, which is different from classic cellular channels, as we will detail in this section. This is, because the bandwidth of the transmitted UWB signal is substantially wider than that of the conventional wireless channels. Based on classic Fourier theory, the wider the bandwidth of the channel, the higher the number of resolvable multi-path components. As an example, in practical Rake-receiver aided CDMA systems the number of resolvable multi-path components is $\lfloor \frac{T_m}{T_c} + 1 \rfloor$, where T_m and T_c are the maximum delay-spread of the communication channel and chip-duration, respectively. At such a high bandwidth the corresponding time-domain bins become extremely narrow and hence, there is a possibility that no multi-path component falls in a delay bin. Accordingly, in UWB channel modelling it is necessary to characterise the likelihood that an empty delay bin is followed by an 'occupied' one [62]. Naturally, the multi-path component occupying a specific delay bin is physically often constituted by the superposition of received paths, all arriving within a low delay difference of each other and given the current bandwidth, they cannot be distinguished within the delay bin. When the bandwidth is low and the delay bins are wide, a high number of components may be superimposed, which leads to having a complex-valued Gaussian, i.e. Rayleigh distribution for each delay bin. By contrast, for the UWB scenario the delay bins are narrow and hence the central limit theorem may no longer be valid. Therefore, the amplitude statistics of the signals of an UWB delay bin can no longer be modeled as Rayleigh or Rician distributed [62]. A more detailed investigation on this issue will be provided during our forthcoming discourse.

Having a low fading margin and the low power spectral density restrictions imposed by

government regulations make UWB systems eminently suitable for indoor wireless communications [125]. Recent results demonstrate that UWB systems constitute a viable candidate for short-range multiple-access communications in dense multi-path environments, since the UWB signals have the potential of benefiting from a high diversity order owing to the UWB signal's fine delay-resolution properties [126, 127]. Hence UWB communications have been used for supporting short-range high-speed wireless communications [125, 126, 127]. Extensive measurement campaigns have been performed for the sake of modelling the UWB indoor channels [62]. A detailed overview of the UWB indoor channel can be found in [128].

In this section an overview of the UWB channel models is provided. Similarly to conventional narrowband and wideband channels, UWB channels also exhibit both large- and small-scale fading as described in the next two sections. Small-scale fading plays a vital role in short-range indoor wireless communications.

5.2.1.1 Large-Scale Fading

The impact of the UWB channel on the signal transmitted over a relatively large distance (beyond 1m) is termed as 'large-scale fading'. It encompasses the path-loss-like average attenuation effects owing to the distance between the transmitter and receiver, as well as imposed by large objects that are blocking the Line-Of-Sight (LOS) propagation paths. In traditional propagation models, the large-scale fading is referred to as path loss and it is often modelled as [129, 130]

$$P_L(d) = \overline{P_L}(d_o) + 10\eta \log_{10}\left(\frac{d}{d_o}\right) + X_\sigma, \qquad d \geq d_o \tag{5.1}$$

where $P_L(d)$ represents the path-loss at a distance d, $\overline{P_L}(d_o)$ indicates the average path-loss at the so-called reference point just outside the antenna's near-field, i.e. at a distance of d_o, for example $d_o = 1m$, η is the path-loss exponent and X_σ represents a Gaussian distributed Random Variable (RV) having a standard deviation of σ (in dB) [129]. The path-loss $P_L(d_o)$ at the reference point, the path-loss exponent and the standard deviation of σ are statistically dependent on the communication environment. Hence, they are usually modelled as RVs obeying certain distributions [125]. The path-loss exponent η typically depends on the carrier frequency, the antenna height and the propagation environment. It is often considered to have a normal distribution $N[\mu_\eta, \sigma_\eta]$ and may be described as [125]

$$\eta = \mu_\eta + \eta_1 \sigma_\eta, \tag{5.2}$$

where η_1 represents a Gaussian RV having a mean of zero and a unit variance.

The shadow fading term X_σ of Equation 5.1 is a typically log-normally distributed environment-specific term, which can be modelled as [125]

$$X_\sigma = \eta_2(\mu_\sigma + \eta_3\sigma_\sigma), \tag{5.3}$$

where η_2 and η_3 also represent zero mean RVs and σ_σ is a unit-variance normal RV. It may be shown that the standard deviation σ_σ of the shadow fading is independent of the carrier frequency [131]. Upon inserting the above-mentioned parameters into Equation 5.1, we arrive at an expression for the propagation path-loss, which may be formulated as

$$P_L(d) = \overline{P_L}(d_o) + 10\mu_\eta \log_{10}\left(\frac{d}{d_o}\right) + 10\eta_1\sigma_\eta \log_{10}\left(\frac{d}{d_o}\right) + \eta_2\mu_\sigma + \eta_2\eta_3\sigma_\sigma. \tag{5.4}$$

It is worth noting that the first two terms in Equation 5.4 represent the median path-loss and the last three terms indicate the random variation around the median path-loss value [125].

5.2.1.2 Saleh-Valenzuela Model of Small-Scale Fading

'Small-scale fading' is caused by interferences among at least two or more delayed replicas of the transmitted signal, which arrive at the receiver with slightly different time delays [129]. The small-scale fading is that experienced within an area of $1m^2$ [132], and hence it becomes a vital parameter in indoor communications. The main small-scale fading model adopted for indoor UWB communications is the modified Saleh Valenzuela (S-V) model [62, 130].

It has been shown that the multi-path components arrive at the receiver in clusters [62, 133]. In wideband communications, generally, the number of resolvable multi-path components is related to the signal's bandwidth and to the propagation environment experienced [133], which can be formulated as

$$L = \lfloor WT_m \rfloor + 1, \tag{5.5}$$

where L represents the number of resolvable multi-path components, $W = 1/T$ indicates the signal bandwidth and T_m is the maximum delay-spread of the communication channel. The delay-spread spans several nanoseconds in time, which leads to Inter Symbol Interference (ISI), if the UWB signalling pulses are closely spaced in time [62]. However, the ISI may be mitigated by beneficially designing the signalling pulse waveform and/or by using equalisation algorithms [62].

The arrival of multi-path components may be grouped into two categories: a cluster-arrival and a ray-arrival within a cluster. Hence, four parameters are required to describe

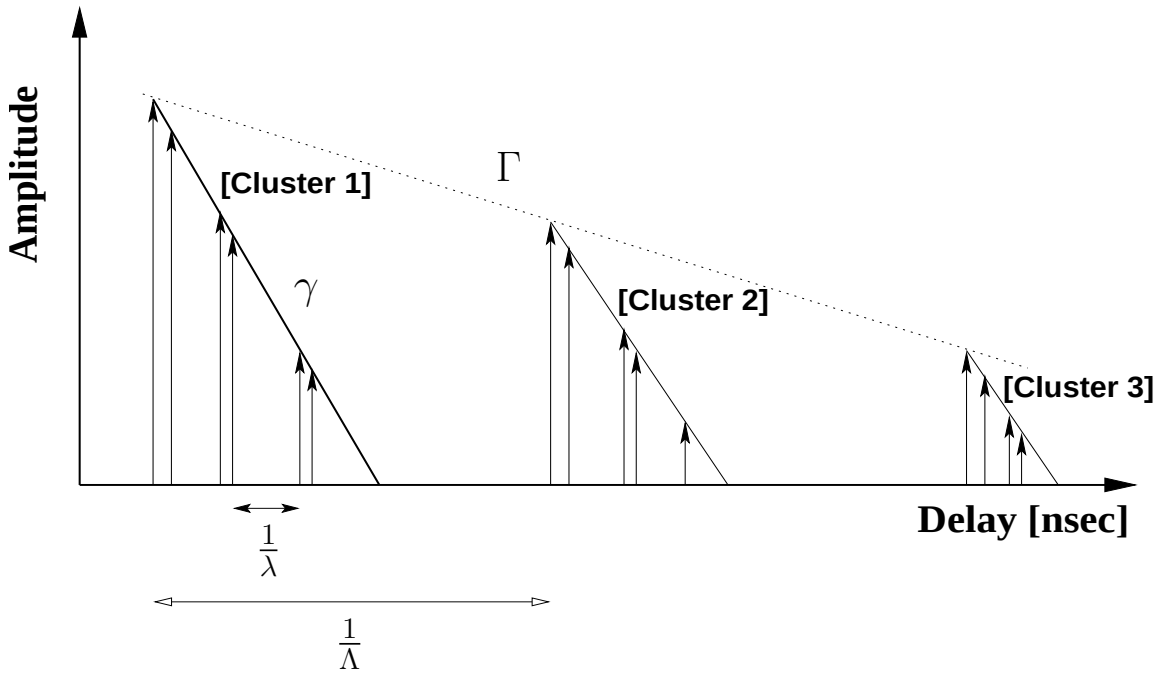

Figure 5.1: Stylised illustration of the Saleh Valenzuela (S-V) UWB channel model, which encompasses three clusters, where each cluster may have a different number of resolvable multi-path components.

the S-V channel model. These parameters provide a high flexibility and may be appropriately configured for different propagation environments. The four parameters associated with the S-V model are as follows:

- Cluster-arrival rate, Λ ;
- Ray-arrival rate within a cluster, λ ;
- Cluster-decay factor, Γ ;
- Ray-decay factor within a cluster, γ.

We will further discuss the above-mentioned parameters in our forthcoming discourse.

1. **Cluster-Arrival Rate (Λ):** The clusters seen in Figure 5.1 are formed by the constructing a so-called superstructure [134]. The cluster-arrival may be modelled with the aid of a Poisson process having a mean cluster-arrival rate of Λ. Hence, the probability of encountering v additional clusters at time instant T obeys the following

PDF [130, 133, 134]:

$$P(v \text{ additional clusters at instant T}) = \frac{(\Lambda T)^v}{v!} \exp(-\Lambda T). \tag{5.6}$$

The first cluster is always assumed to be present. In the context of a Poisson process, the interarrival time of clusters obeys a negative exponential RV, which is described by the following PDF:

$$p(T_v|T_{v-1}) = \Lambda \exp[-\Lambda(T_v - T_{v-1})], \quad v > 0 \tag{5.7}$$

where $1/\Lambda$ is typically within the range of 10 to 50ns [133].

2. **Ray-Arrival Rate within a Cluster (λ):** Rays portrayed in Figure 5.1 are generated by the objects within the vicinity of the transmitter and receiver [134]. The ray-arrival within a cluster may be described by another Poisson process, where the inter-arrival time of two adjacent rays is another negative exponentially distributed RV having the PDF of

$$P(\tau_{u,v}|\tau_{u-1,v}) = \lambda_v \exp[-\lambda_v(\tau_{u,v} - \tau_{u,v-1})], \quad u > 0 \tag{5.8}$$

where $\tau_{u,v}$ represents the arrival time of the uth multi-path component within the vth cluster, whilst λ_v indicates the mean multi-path arrival rate within the vth cluster. Typically, each cluster is constituted by a high number of multi-path components, i.e, we have $\lambda >> \Lambda$ [134]. In UWB communications environments, where the arrival rate of the later clusters becomes higher than that of the earlier clusters [133], the ray-arrival process may be modelled as a mixture of two Poisson processes, which is formulated as follows [130, 133, 134]:

$$\begin{aligned} P(\tau_{u,v}|\tau_{u-1,v}) &= \alpha\lambda_1 \exp[-\lambda_1(\tau_{u,v} - \tau_{u,v-1})] \\ &+ (1-\alpha)\lambda_2 \exp[-\lambda_2(\tau_{u,v} - \tau_{u,v-1})], \quad u > 0 \end{aligned} \tag{5.9}$$

where α represents the probability of the lower-arrival-rate clusters, whereas λ_1 and λ_2 are the ray-arrival rates of the first and second Poisson processes, respectively. The duration of the negative exponential process having a higher poissonian arrival rate typically becomes shorter than the negative exponential process related to a lower poissonian arrival rate. However, the former usually results in stronger multi-path components than the latter.

3. **Cluster-Decay Factor (Γ):** The decay factors shown in the stylised illustration of Figure 5.1 are calculated from the power decay profile observed [62]. In the S-V model,

the average power of the clusters is assumed to decay exponentially. The cluster decay factor, Γ typically increases, when the building walls become more reflective [134]. The factor Γ is determined as the exponential decay of the peak power of the delayed received clusters. For a block of data, the first arrived cluster may be normalised to an amplitude of unity and a time delay of zero. All the other clusters of the same block of data are expressed relative to the first cluster.

4. **Ray-Decay Factor within a Cluster (γ):** The average power of the multi-path components within a cluster decays exponentially as shown in Figure 5.1. The multi-path decay factor, which is synonymously referred to as the intra-cluster decay rate tends to be linearly proportional to the arrival time of the cluster, which is expressed as

$$\gamma_v \propto u_\gamma T_v + \gamma_o, \tag{5.10}$$

where u_γ represents a factor accounting for the increase of the decay rate as a function of the delay. The arrival time of the first ray in each cluster is set to zero, while its amplitude to one. All the other rays within a cluster are adjusted accordingly, relative to the first ray. Typically, $\Gamma > \gamma$ indicates that the expected power of the rays in a cluster decays faster than that of the first ray in the next cluster, as also above in the stylised Channel Impulse Response (CIR) of Figure 5.1.

The CIR of the UWB communications environment changes with time, owing to the relative motion between the transmitter and receiver. As the UWB channel is frequency-selective, it may be modelled by employing a tapped-delay line [132, 135]. Typically two types of UWB indoor channel models have been considered, which are derived from the Statistical Tapped-Delay-Line (STDL) channel model [132, 135]. More specifically, the indoor UWB channel model of [135] was constructed from propagation measurements, which were performed in typical office buildings. The model is based on the measurements performed within the frequency-range of 300 MHz to 1 GHz and on the UWB baseband pulse having a 2-ns delay resolution. Therefore, the resultant UWB channel model constitutes a typical models of the family of Low Frequency (LF) UWB systems. In the LF-UWB channel model [128], the measurements suggest that the direct LOS path is always the first resolvable path, which is usually also the strongest path. The energy of the subsequent resolvable paths decays exponentially with the delay. The analysis of the LF-UWB channel [135] suggest that the well-established tapped-delay-line model [136], where each tap obeys independent fading, accurately reflects the behaviour of the measured UWB channel. Furthermore, the

statistical analysis provided in [135] suggests that the best-fit distribution of the small-scale magnitude statistics is the Nakagami-m distribution, which corresponds to the Gamma distribution, when considering the distribution of the energy and hence that of the SINR. It has been also shown [135] that the parameters of the Gamma distribution vary from path to path. The Nakagami fading parameter value m_k ranges between 1 and 6, typically decreasing, when having an increased excess delay.

On the other hand, the measurement considered in [62] were carried out in the frequency band ranging from 3.1 GHz to 10.6 GHz. Therefore the corresponding UWB channel model may be termed as a High Frequency (HF) UWB channel. The measurements included both residential and office sites, where both LOS and non-LOS conditions were encountered and the delay spreads ranged from 5 ns to more than 40 ns. In contrast to the LF-UWB scenarios, analysis of the measurement data suggests that in the HF-UWB channel model the first resolvable multi-path component may not necessarily be the strongest one. The power delay profile becomes generally sparse, where some of the resolvable multi-path components do not carry any significant energy [62]. By contrast, in the HF-UWB channel model, the multi-path components arrive in clusters rather than as a continuum. Therefore a double exponential decay based model has been introduced for the sake of characterising the power delay profile of the HF-UWB channels. In the double exponential decay based UWB channel model, one of the exponential decay models corresponds to the decay of the clusters, whilst the other corresponds to the multi-path component decay within a cluster. Furthermore, the measurements conducted in the context of HF-UWB scenarios demonstrate that the amplitude of the UWB signal no longer obeys a Rayleigh distribution. Instead, either a lognormal or a Nakagami distribution may model the channel more accurately.

Based on the above-mentioned characteristics of UWB channels, the conventional STDL channel model will be modified for our investigations. More specifically, the S-V model will be adopted. The CIR of the S-V model is represented as [130, 132, 134]

$$h(t) = \sum_{v=1}^{\infty} \sum_{u=1}^{\infty} \beta_{u,v} \delta(t - T_v - \tau_{u,v}), \tag{5.11}$$

where $\beta_{u,v}$ represents the amplitude of the uth multi-path component within the vth cluster, T_v is the arrival time of the vth cluster and $\tau_{u,v}$ denotes the arrival time of the uth multi-path in vth cluster. Recall that all these variables may be interpreted with the aid of Figure 5.1. For the sake of capturing all or most of the transmitted signal energy, the receiver may have to process a high number of resolvable multi-path components. In order to reduce the detection complexity imposed, the selection of L multi-path components for detection

may achieve a BER performance close to that of a receiver that processes all the resolvable multi-path components, provided the value of L is sufficiently high. Practically, the UWB system can only process a limited number of clusters, where each cluster contains a limited number of resolvable multi-path components. Therefore the CIR of Equation 5.11 can be described as

$$h(t) = \sum_{v=1}^{V} \sum_{u=1}^{U} \beta_{u,v} \delta(t - T_v - \tau_{u,v}), \tag{5.12}$$

where V denotes the number of clusters and U represents the number of resolvable multi-path components in a cluster. Therefore the total number of resolvable multi-path components may be as high as $L = UV$. As mentioned before, the parameters $\beta_{u,v}$, T_v and $\tau_{u,v}$ are time varying owing to the motion of objects within the UWB communications environment. However, for the sake of convenience, we treat these parameters as time-invariant RVs, under the assumption that their variation is slow as compared to the signalling rate [134]. It is also assumed that the average power of a multi-path component at a given delay $T_v + \tau_{u,v}$ is related to the power of the first resolvable multi-path component according to

$$\overline{\beta_{u,v}^2} = \overline{\beta_{1,1}^2} \exp\left(-\frac{T_v}{\Gamma}\right) \exp\left(-\frac{\tau_{u,v}}{\gamma}\right), \tag{5.13}$$

where $\overline{\beta_{1,1}^2}$ represents the expected power of the first resolvable path of the received UWB signal. The total average received power of the received UWB signal is normalised to unity for the sake of convenient comparison to other wideband or narrowband systems [62]. Figure 5.1 illustrates the S-V UWB channel model, as described in [130, 133]. In contrast to the conventional S-V channel model, where the amplitude statistics were assumed to be Rayleigh distributed [134], the empirical distribution of the path gains differs significantly from the Rayleigh amplitude statistics [133]. This is because the received UWB signals exhibit a high resolution in the time delay domain and hence only a small number of the multi-path components may fall within a delay bin. Therefore, the complex-valued Gaussian approximation of the superimposed components of a bin may no longer satisfy the central limit theorem and hence may no longer obey the Rayleigh distribution. The measurement based propagation data matches more closely the lognormal or the Nakagami distribution, which has been shown using Kolmogorov-Smirnov testing at a significance level of 1% [62]. The PDF of the Nakagami-m distribution is given by [130, 136]

$$\begin{aligned} P(\beta_{u,v}) &= M\left(\beta_{u,v}, m, \Omega_{u,v}\right) \\ M\left(\beta_{u,v}, m, \Omega_{u,v}\right) &= \frac{2m^m \beta_{u,v}^{2m-1}}{\Gamma(m)\Omega_{u,v}^m} \exp(-m/\Omega_{u,v})\beta_{u,v}^2, \end{aligned} \tag{5.14}$$

where $m \geq 1/2$ represents the Nakagami-m fading factor, which is equal to $m = \mathbf{E}^2[(\beta_{u,v}^2)]$ $/\mathbf{Var}[(\beta_{u,v})^2]$, $\Gamma(m)$ is the Gamma function and $\Omega_{u,v} = \mathbf{E}[(\beta_{u,v})^2]$ denotes the second moment of the amplitude of the uth multi-path component in the vth cluster. In our forthcoming discourse, a specific type of the Nakagami distribution is used due to the following reasons:

1. The lognormal distribution can be approximated by the Nakagami distribution associated with a high value of the fading parameter [62].

2. The Rayleigh distribution may be valid in some communication environments even when the resolvable bin-width is low [133]. Rayleigh fading has been observed in industrial environments owing to dense multi-path scattering, where numerous multi-path components exist. The Nakagami-m distribution becomes identical to the Rayleigh distribution, when the fading parameter is set to $m = 1$.

3. The Nakagami-m distribution often gives the best fit to land-mobile and indoor-mobile multi-path propagation environments, as well as to scintillating ionospheric radio links. Different propagation scenarios may be accurately modelled by the Nakagami-m distribution by simply changing the value of m. Furthermore, the Nakagami-m distribution has advantages over the lognormal distribution in terms of its analytical convenience.

Furthermore, for the sake of fair comparison to all the results of [43, 59], a dispersive AWGN channel having multi-path components will also be investigated. This assumption was also considered in [42] along with a specific case of Nakagami-m fading.

Finally, Table 5.2.1 summaries the characteristics of four different UWB channel models [62, 130].

5.2.2 Summary of UWB Channel Models

In this section the modelling of UWB channels has been detailed. The main characteristics are summarised as follows:

- The modelling of UWB channels is substantially different from those of both narrowband and wideband cellular channels. Hence, the performance results which were derived for narrowband and wideband channels are no longer applicable for code acquisition in the context of UWB channels.

Channel Characteristics	CM-1	CM-2	CM-3	CM-4
Cluster-Arrival Rate Λ[1/nsec]	0.0233	0.4	0.0667	0.0667
Ray-Arrival Rate λ[1/nsec]	2.5	0.5	2.1	2.1
Cluster-Decay Factor Γ	7.1	5.5	14	24
Ray-Decay Factor γ	4.3	6.7	7.9	12
Models corresponding to the following channel measurements, respectively	LOS (0-4 m)	NLOS (0-4 m)	NLOS (4-10 m)	Extreme NLOS

Table 5.1: UWB Channel Characteristics

where CM is short for Channel Model, while LOS and NLOS represent Line-Of-Sight and Non-Line-Of-Sight scenarios, respectively.

- Both the average path-loss at the reference point and the path-loss exponent become environment-specific.
- Since UWB are only practical in indoor and short-range communications, the small-scale fading becomes a vital parameter of the interest. The widely known UWB channel model is the modified S-V model. The S-V channel model is based on a STDL model defined by four parameters, namely, the cluster-arrival rate (Λ), the ray-arrival rate within a cluster (λ), the cluster-decay factor (Γ) and the ray-decay factor within a cluster (γ), which were defined in the context of Figure 5.1.
- The amplitude statistics in UWB channels obey either the log-normal or the Nakagami-m distribution, and in some specific cases the Rayleigh distribution. The Nakagami-m distribution is preferred over the log-normal distribution, since both the Rayleigh and log-normal distributions may be approximated by the Nakagami-m distribution.

5.3 Preliminaries of Code Acquisition in the DS-UWB Downlink

5.3.1 Characteristics of PN Codes

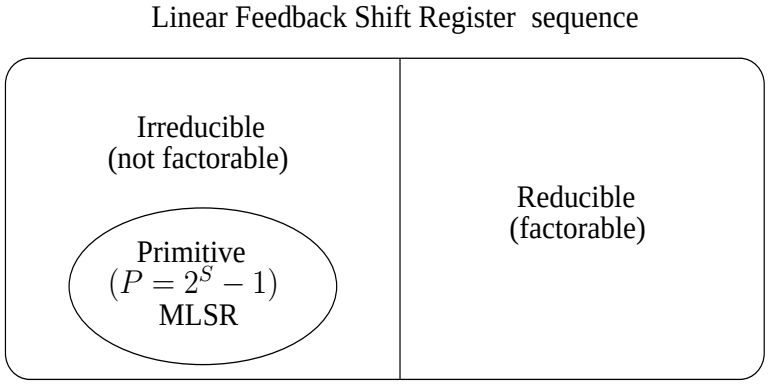

Figure 5.2: Classification of sequences generated by Linear Feedback Shift Registers

Let us define the function $G(D) = 1/g(D)$, where D is the delay unit and $g(D)$ denotes a Generator Polynomial (GP). Every output sequence of the Linear Feedback Shift Register (LFSR) is periodic with a period of $P \leq 2^S - 1$. If the polynomial $g(D)$ of degree S can be factorised into lower-order polynomials, it is referred to as '**reducible**'. On the other hand, if it cannot be further factorised, it is termed as '**irreducible**'. In terms of system design, we are interested in finding a subset of sequences, which leads to the definition of a Maximum Length (linear) Shift Register (MLSR) sequence [3]. Irreducible polynomials of degree S that generate an MLSR sequence of period $P = 2^S - 1$ for all non-zero initial vectors are referred to as '**primitive**' polynomials. Figure 5.2 illustrates a classification of LFSR sequences [3, 72].

By exploiting the available *a priori* knowledge about how PN codes are generated with the aid of LFSRs, the PN sequence is generated by feeding these S chips into the LFSR-based PN-code generator, which produces $(2^S - 1)$ chips. More explicitly, a $(2^S - 1)$-chip PN code can be generated with the aid of a LFSR using a specific Primitive Polynomial (PP), once the associated S-stage LFSR was filled with the S number of chip values [72]. This beneficial property can also be exploited by the initial acquisition scheme at the receiver, because once we estimated S number of channel-contaminated chip values, the acquisition scheme is capable of reconstructing the entire $(2^S - 1)$-chip code. Figure 5.3 portrays the LFSR structure for the PP $g(D) = D^{15} + D + 1$ [72].

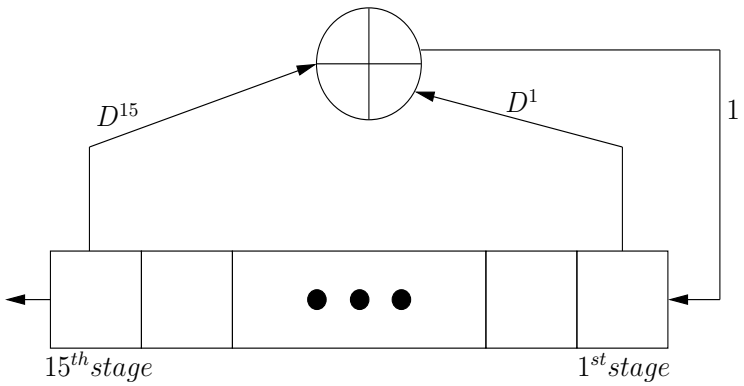

Figure 5.3: An example of LFSR sequence generator having $g(D) = D^{15} + D + 1$

5.3.2 Modulo-2 Squaring

If a sequence is represented by $G_1(D) = \frac{1}{g_1(D)}$, then the new sequence $G_2(D) = \frac{1}{g_2(D)} = [\frac{1}{g_1(D)}]^2$ generated using modulo-2 squaring represents the original sequence with a zero inserted between each pair of chips. For example, after modulo-2 squaring of $G_1(D) = \frac{1}{1+D^2+D^3} = 1\ 0\ 1\ 1\ 1\ 0\ 0\ \cdots$, we have $[G_1(D)]^2 = \frac{1}{1+D^4+D^6} = 1\mathbf{0}0\mathbf{0}1\mathbf{0}1\mathbf{0}1\mathbf{0}0\mathbf{0}0\mathbf{0}\cdots$. Then, modulo-2 squaring may be further exemplified as follows [72]:
$(1+D)^2 = 1+D^2$, $(1+D)^4 = 1+D^4$ and $(1+D)^{2n} = 1+D^{2n}$.
In our scenario, we selected the GP $g_1(D) = D^{15} + D + 1$ [43, 59], which is a PP. The detailed procedure of the modulo-2 squaring operation is as follows:

$$\begin{aligned} g_2(D) &= [g_1(D)]^2 = (D^{15} + D + 1)(D^{15} + D + 1) \\ &= D^{30} + D^{16} + D^{15} + D^{16} + D^2 + D + D^{15} + D + 1 \\ &= D^{30} + D^2 + 1. \end{aligned}$$

Higher order GPs are calculated by the repeated Modulo-2 squaring as follows:

$$\begin{aligned} g_1(D) &= D^{15} + D + 1. \\ g_2(D) &= D^{30} + D^2 + 1. \\ g_3(D) &= D^{60} + D^4 + 1. \\ g_4(D) &= D^{120} + D^8 + 1. \\ g_5(D) &= D^{240} + D^{16} + 1. \\ g_6(D) &= D^{480} + D^{32} + 1. \\ g_7(D) &= D^{960} + D^{64} + 1. \end{aligned}$$

Based upon the above-mentioned operation, finally, the operation is generalised as $g_n(D) = D^{15\cdot 2^{(n-1)}} + D^{2^{(n-1)}} + 1$, where n = 1,2,...

5.3.3 Sum-Product Algorithm

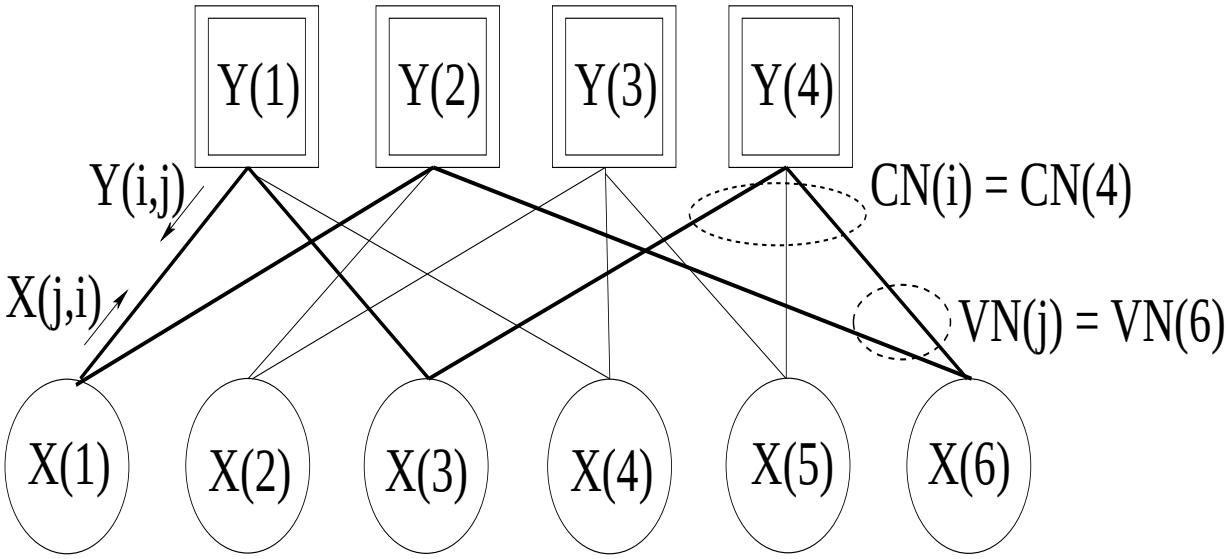

Figure 5.4: An example of the sum-product algorithm, where the squares and circles denote Check Nodes (CNs) and Variable Nodes (VNs), respectively, whilst the bold lines between the CNs and VNs represent a cycle length of 6.

The Sum-Product Algorithm (SPA) constitutes the basic decoding algorithm of arbitrary codes which can be described by graphs as exemplified in Figure 5.4. When all the operations of the SPA becomes local, it may be applied to graphs having cycles, which can also be portrayed in Figure 5.4. There have been various applications of the SPA [137, 138, 139]. More explicitly, the employment of the SPA has not only been limited to the decoding of Low Density Parity Check (LDPC) codes, it has been also applied for solving inference problems in artificial intelligence, computer vision and statistical physics [137]. In the context of statistical inference, it is referred to as the Belief Propagation (BP) algorithm [137], which constitutes an efficient iterative decoding technique guaranteeing low-complexity implementation [137]. The BP algorithm may also be considered to be a decentralised Message Passing (MP) algorithm, because each node communicates with the corresponding nodes connected to it. If the structure of the graph describing the detection/decoding problem considered is not a tree, the BP algorithm has no definite termination point. However, a popular detection termination rule selected is to make a hard decision after a predetermined

number of iterations. The application of the BP algorithm for the detection of certain systematic linear block codes having low-density parity check matrices leads to well known LDPC codes.

When considering graphs exhibiting cycles, there is no guarantee that the SPA will converge [138, 139, 140]. In practice, the SPA converges with a near-unity probability only if the code rate is below a certain value. Furthermore, even if the SPA does converge, there is no guarantee that it will converge to the correct decision. Generally speaking, the specific likelihoods associated with the most probable decisions may be too optimistic, since it is assumed that all the messages contributing to this decision are independent values, whilst in fact this is not entirely true, because the same messages are entered repeatedly into the sum-product update owing to graphs exhibiting cycles. Accordingly, the achievable decoding performance becomes sub-optimal. The results of the SPA applied to a factor graph having cycles cannot be interpreted as exact function summaries. Nonetheless, some of the most exciting applications of the SPA such as the decoding of LDPC codes have been shown to perform well even for codes operating over graphs exhibiting 'not-too-short' cycles [138]-[140].

The underlying decoding principle devised for LDPC[1] codes is to exchange messages between the Variable Nodes (VNs) and Check Nodes (CNs) of the code's Tanner graph based representation. The SPA has been routinely used in the design of LDPC decoders. We first briefly introduce the SPA with the aid of the specific message passing example of Figures 5.5 and 5.6 and then provide their more general description.

For the sake of describing the operations carried out in Figures 5.4 to 5.6 in more detail, a specific example of the Parity Check Matrix (PCM) was given in Equation 5.15.

$$\begin{pmatrix} 1 & 0 & 1 & 1 & 0 & 0 \\ 1 & 1 & 0 & 0 & 0 & 1 \\ 0 & 1 & 0 & 1 & 1 & 0 \\ 0 & 0 & 1 & 0 & 1 & 1 \end{pmatrix}. \tag{5.15}$$

The matrix of Equation 5.15 may be directly mapped to Figure 5.4, since it illustrates the

[1]LDPC codes constitute linear parity-check codes having a parity-check matrix, which encompasses a small number of ones. More explicitly, in order to find a correct codeword, every codeword C must satisfy $H \cdot C = 0$, where C represents an $(n \times 1)$-element binary vector and H denotes an $(n-k) \times n$ binary matrix, where it is assumed that k input bits are mapped to n coded bits using $(n-k)$ parity-check equations. The iterative decoding of LDPC codes is often based on the hard-decision aided bit-flipping algorithm or on the message-passing algorithm known as belief propagation. The message-passing algorithm is particularly popular due to its powerful decoding capability. Further details on the decoding of LDPC codes may be found in [141].

underlying principle of the SPA. More explicitly, in Figure 5.4, $X(j,i)$ represents the message passed from the j^{th} VN indicated by the circles to the i^{th} CN denoted by the squares, $Y(i,j)$ represents the message passed from the i^{th} CN to the j^{th} VN and $X(j)$ indicates the LLR of the soft value received from the AWGN channel. Furthermore, $VN(j)$ is the set of CNs linked to the j^{th} VN and $CN(i)$ represents the set of VNs connected to the i^{th} CN. To

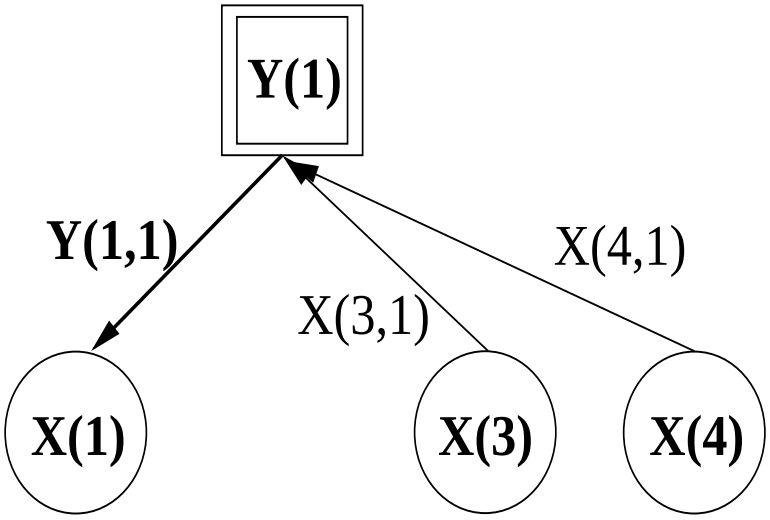

Figure 5.5: Message update in check-to-variable node message passing, where the circles represent VNs and the squares deonte CNs. It is also often termed as CN-processing.

elaborate a little further, Figure 5.5 elucidates the message update rule of the CN processing. Observe in Figure 5.5 that the message, $Y(1,1)$ is passed from the first CN to the first VN, which was calculated from the messages denoted as $X(3,1)$ and $X(4,1)$, respectively. More explicitly, we have $Y(1,1) = ln\left(\frac{1+tanh(X(3,1)/2)\cdot tanh(X(4,1)/2)}{1-tanh(X(3,1)/2)\cdot tanh(X(4,1)/2)}\right)$ [142, 143]. By contrast, in Figure 5.6, the VN-to-CN message passing update rule, which is also referred to as VN processing, is described in detail. A message, $X(1,1)$ is passed from the first VN to the first CN, which was generated by the VN message $Y(1,2)$ plus the estimate $X(1)$ of the soft signal received. More specifically, we have $X(1,1) = Y(1,2) + X(1)$.

When considering the PCM of Equation 5.15 having the corresponding Tanner graph based description of Figure 5.4, the following matrices can be defined:

$$\begin{pmatrix} Y(1,1) & 0 & Y(1,3) & Y(1,4) & 0 & 0 \\ Y(2,1) & Y(2,2) & 0 & 0 & 0 & Y(2,6) \\ 0 & Y(3,2) & 0 & Y(3,4) & Y(3,5) & 0 \\ 0 & 0 & Y(4,3) & 0 & Y(4,5) & Y(4,6) \end{pmatrix}, \tag{5.16}$$

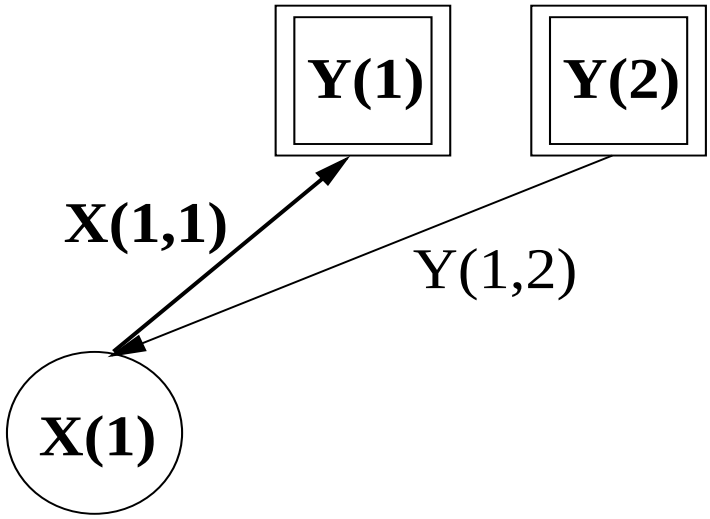

Figure 5.6: Message update in variable-to-check node message passing, which is also often referred to as VN-processing.

$$\begin{pmatrix} X(1,1) & 0 & X(3,1) & X(4,1) & 0 & 0 \\ X(1,2) & X(2,2) & 0 & 0 & 0 & X(6,2) \\ 0 & X(2,3) & 0 & X(4,3) & X(5,3) & 0 \\ 0 & 0 & X(3,4) & 0 & X(5,4) & X(6,4) \end{pmatrix}, \tag{5.17}$$

where the matrix of Equation 5.16 describes the extrinsic LLRs passed from the CNs to the VNs as dictated by the positions of logical ones in the PCM of Equation 5.15. Similarly, the matrix of Equation 5.17 represents the LLRs passed from the VNs to the CNs as dictated by the positions of logical ones in the PCM of Equation 5.15. By contrast, the zeros in the matrices of Equations 5.16 and 5.17 indicate the absence of connections among the CNs and the VNs.

Finally, the generalised operation of the SPA is as follows [142, 143]:

1. **Step 1: Initialisation of the log-likelihood ratio**

   As seen in Figure 5.4, the j^{th} VN passes the Log Likelihood Ratio (LLR) $X(j)$ of an estimate of the soft signal $r(j)$ received from the channel to the i^{th} corresponding CN in the set $VN(j)$. As shown in Figure 5.4, the soft-estimate $X(j,i)$ is expressed as $X(j,i) = X(j) = 4{\cdot}r(j){\cdot}\frac{E_c}{I_0}$ [58, 98] [2], where $X(j,i)$ represents the message passed

[2] After signal $s(j)$ was transmitted over an AWGN channel, we may calculate the LLR of $s(j)$ conditioned on $r(j)$ [58, 98] as $X(j;s|r) = ln\left(\frac{P(s=+1|r)}{P(s=-1|r)}\right) = ln\left(\frac{P(r|s=+1)P(s=+1)}{P(r|s=-1)P(s=-1)}\right)$. More specifically, $X(j;s|r)$ may also be expressed as $X(j;s|r) = ln\left(\frac{exp(-(E_c/I_0)(r-1)^2)}{exp(-(E_c/I_0)(r+1)^2)}\right) + ln\left(\frac{p(s=+1)}{p(s=-1)}\right)$. Finally, $X(j;s|r)$ becomes

from the j^{th} VN to the i^{th} CN and (E_c/I_0) is the Signal-to-Interference plus Noise Ratio (SINR) per chip. The channel was assumed to be an AWGN channel.

2. **Step 2: Horizontal step (Check-to-variable node message passing, also termed as Check Node (CN) processing)**
   As seen in Figure 5.4, the i^{th} CN forwards the extrinsic LLR to the j^{th} VN, which is described by [58] [3]

$$Y(i,j) = ln\left(\frac{1+\prod_{j'\in CN(i),j'\neq j} tanh[X(j',i)/2]}{1-\prod_{j'\in CN(i),j'\neq j} tanh[X(j',i)/2]}\right), \quad (5.18)$$

$$= 2{\cdot}artanh\left(\prod_{j'\in CN(i),j'\neq j} tanh[X(j',i)/2]\right). \quad (5.19)$$

   A specific example of Step 2 is portrayed in Figure 5.5.

3. **Step 3: Hard decision concerning the codeword generated**
   The summation of the extrinsic LLRs generated during Step 2 and the original intrinsic LLR value derived during Step 1 constitutes the resultant LLR to be subjected to a hard decision, which is expressed as $\Lambda' = \sum_{i\in VN(j)} Y(i,j) + X(j)$, where Λ' represents the *a posteriori* LLR of each VN. Then, a hard decision is performed for each chip based on the following rule:

$$\lambda'(j) = '1'\,(if\,\Lambda \leq 0)\ or\ '0'\,(if\,\Lambda > 0), \quad (5.20)$$

   where λ' represents the resultant logical value after a hard decision was performed. The SPA will be terminated if either the predefined number of iterations was completed or if the hard-decision based codeword $\lambda = [\lambda\,(1), \lambda\,(2), ..., \lambda\,(CN(i))]$ becomes a legitimate codeword and hence satisfies the parity check constraint equation associated with the PCM, namely, $H{\cdot}\lambda^T = 0$. A specific example of the PCM is portrayed in the matrix of Equation 5.15, where logical ones indicate the presence of connections among the CNs and the VNs.

$4{\cdot}r(j){\cdot}\frac{E_c}{I_0}$.

[3] The joint LLR described in Figure 5.5 may be expressed as $ln\left(\frac{(1+exp[X(3,1)]exp[X(4,1)])}{(exp[X(3,1)]+exp[X(4,1)])}\right)$ [58, 98]. By induction, the LLR is also equivalent to $ln\left(\frac{(exp[X(3,1)]+1)(exp[X(4,1)]+1)+(exp[X(3,1)]-1)(exp[X(4,1)]-1)}{(exp[X(3,1)]+1)(exp[X(4,1)]+1)-(exp[X(3,1)]-1)(exp[X(4,1)]-1)}\right)$. By employing the relationship $tanh(a/2) = \frac{(exp[a]-1)}{(exp[a]+1)}$ [58], where a is an arbitrary variable, finally we arrive at Y(1,1) = $ln\left(\frac{(1+tanh[X(3,1)/2]tanh[X(4,1)/2])}{(1-tanh[X(3,1)/2]tanh[X(4,1)/2])}\right)$, as portrayed in Figure 5.5.

4. **Step 4: Vertical step (Variable-to-check node message passing, also termed as Variable Node (VN) processing)**
   As seen in Figure 5.4, the j^{th} VN passes the message $X(j,i)$ to the i^{th} CN, but excludes the intrinsic message $Y(i,j)$ which is described as $X(j,i) = \sum_{i' \in VN(j), i' \neq i} Y(i^{'},j) + X(j)$. Then, the procedure will return to Step 2. A specific example of Step 4 is illustrated in Figure 5.6.

5.3.4 Offset-based Min-Sum Algorithm

When considering the SPA associated with the decoding of LDPC codes, the complexity of CN processing may become excessive. Therefore, in practice an efficient implementation of the SPA is highly recommended. In order to minimise the complexity of the MP algorithm, especially that of the CN processing, the corresponding calculations may be carried out in the log-likelihood domain, leading to the Min-Sum Algorithm (MSA), which has become a popular design alternative [139, 140, 143][4]. However, the performance of the MSA is about 0.5 dB worse than that of the SPA, depending on the propagation environment encountered [141]. Hence a variety of modified MSAs have been proposed in the literature [141, 144, 145, 146, 147, 148, 149, 150, 151, 152]. Here we briefly allude to some recent results, which are capable of partially closing the performance gap between the MSA and SPA based schemes.

The solutions proposed in [144]-[147] facilitated the employment of a corrective term at the output of the CNs in the MSA. More explicitly, in [144, 145] a performance degradation was reported for the MSA at low SINR values, since at high-SINRs the MSA can be interpreted as an approximation of the SPA. Therefore, finding more accurate approximations of the SPA that are valid even for low SNR values is desirable. For the sake of narrowing the performance difference between the MSA and SPA, the approximation of the correction term was further simplified[5]. Using a simple correction term in the context of CN processing is capable of eliminating the performance gap between the MSA and the SPA [144, 145], in fact,

[4] As shown in Figure 5.5, the joint LLR formulated in the context of the CN processing is expressed as $ln\left(\frac{(1+exp[X(3,1)]exp[X(4,1)])}{(exp[X(3,1)]+exp[X(4,1)])}\right)$ [58, 98], which can be approximated by $sgn[X(3,1)]sgn[X(4,1)]\cdot min(|X(3,1)|, |X(4,1)|)$ [58], where $sgn[\cdot]$ denotes the 'signum' function assuming values of either 1 or -1, and $min(\cdot)$ denotes an operator, which selects the smaller value of its two arguments.

[5] As an example of the MSA shown in [144], when considering only two messages in Step 2, the equation can be approximated by $sgn[X(3,1)]sgn[X(4,1)]\cdot min(|X(3,1)|, |X(4,1)|) + ln\left(\frac{1+exp[-|X(3,1)+X(4,1)|]}{1+exp[-|X(3,1)-X(4,1)|]}\right)$. The second term represents the original form of the correction term.

it may even become capable of providing a slight performance advantage for the modified MSA over the original SPA. By contrast, in [146, 147], look-up tables and a piecewise linear approximation were used for the correction term shown in [144]. Both methods resulted in a similar approximation of the correction term of [144, 145]. The employment of a piece-wise linear function approximating the correction term exhibits the best achievable performance, which appears to suffer an almost negligible loss of less than 0.05 dB at a modestly increased complexity [146].

In order to narrow the performance difference between the MSA and SPA, the approach of [148] was to normalise the output of the CN processing, whereas in [141, 149], the so-called offset-based MSA has been proposed. More explicitly, an optimised offset value was used for substituting the magnitude of the VNs' outputs in the graph. The normalised MSA slightly outperforms the offset-based MSA, but may also be slightly more complex to implement. The performance gap between the MSA and modified MSA is about 0.5 dB. However, by using either the normalised or offset-based MSA, the gap can be reduced to about 0.05 dB. In [150], the authors employed both conditional and unconditional correction terms for improving the performance of the offset-based MSA, where the unconditional correction term directly leads to the original offset-based MSA of [141]. Finally, in [151] both normalisation and a modified offset-based MSAs were also proposed. Similarly to the methods of [141], an optimised offset value was used for substituting the magnitude of the outputs of the VNs in the graph. However, the definition of the offset was different from that proposed in [141]. All the above-mentioned approaches [141]-[151] have been aiming for minimising the complexity of CN processing, while improving the achievable performance. Based on references [141]-[151], our goal is to design the best possible CN processing algorithm.

For a graph having short cycles, the incoming messages of a CN and VNs exhibit an interdependence throughout the iteration process, since the messages passed through the edges of the bipartite graph in the BP algorithm are statistically dependent. In this scenario, the BP algorithm is no longer optimal, because it mistakenly assumes having an increased reliability on average. In other words, this implies that the real reliability of these messages is lower than that derived by the BP algorithm under the assumption of having a cycle-free graph. Accordingly, the offset-based MSA is capable of compensating for the over-estimated reliabilities. By employing this, the performance of the BP algorithm can be enhanced by scaling down the log likelihood ratios [141].

From the range of the modified MSA found in the literature [141]- [152], we opted for a technique referred to as the offset-based MSA of CN processing [141], because it has the added benefit of a 0.5 dB gain compared to the pure MSA, which is achieved at a modest increase of the complexity. More specifically, during the CN processing shown in Figure 5.5, an optimised offset value was used for substituting the magnitude of the outputs of the VNs in the graph. This algorithm can be represented as [141]

$$X(j,i)^{'} = sgn\left[X(j,i)\right] \cdot max\left[|X(j,i)| - \beta, 0\right], \tag{5.21}$$

where $sgn\left[\cdot\right]$ denotes the 'signum' function assuming values of either 1 or -1, $X(j,i)$ represents a message passed from a VN to a CN across an edge connected to it in the graph and $max\left[\cdot\right]$ denotes an operator, which selects the largest value between two arguments. Finally, β is a nonnegative number selected by optimising a threshold of the offset-based MSA of Figure 2 seen in [141]. The optimum value was found to be $\beta = 0.15$. It is worth noting that all extrinsic messages having reliability values lower than β are set to 0, in order to ensure that no contribution is provided for the ensuing VN processing.

5.3.5 Decoding Procedure of the Iterative Message Passing Algorithm

In the field of engineering, many problems have been solved by 'divide-and-conquer' based approach. Similarly, a variety of problems may be solved by using MP algorithms, where the messages are passed back and forth among simple processors. After a sufficiently high number of information exchange steps we may approach the global solution of a problem. In this spirit, this MP algorithm requires amongst the processing nodes, which carry out simple operations such as storage and addition of integers. A popular graphical model derived for characterising diverse probability distributions is constituted by the Tanner graph [153]. The Tanner graph is a bipartite graph, which characterises the relationship of the symbols of a codeword and the code constraints for the sake of constructing a valid codeword. A factor graph is a straightforward generalisation of the Tanner graph [139]. The factor graph is also a bipartite graph, which has a VN for each variable and a CN for describing the corresponding relationship among these VNs. In probabilistic modelling of arbitrary systems, the factor graph may be used for representing the joint probability density of variables describing the system. Factorisation of this joint probability density function into individual density functions encompasses vital information regarding the statistical dependencies among these variables. The calculation of a conditional probability corresponds to the so-called marginalisation of the related messages entered to each node [138].

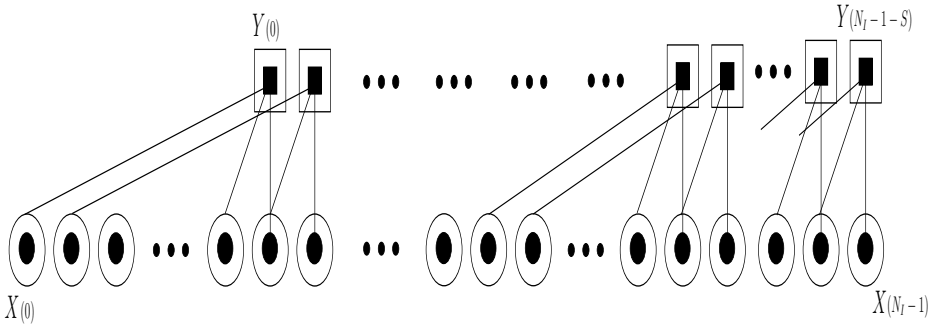

Figure 5.7: Tanner graph based acquisition structure for the PN sequence employing the GP of $g_1(D) = D^{15} + D + 1$. The squares and circles denote CNs and VNs, respectively.

The graphical model seen in Figures 5.7 and 5.8 can also be used for visualising the Parity-Check (P-C) constraints represented by connecting the VNs to the appropriate CNs. The simplest possible graphical model is based on a single CN, which checks the parity of the specific binary variables connected to it. When considering a MP algorithm that repeatedly passes messages across the Tanner graph's edges in both directions, the MP algorithm merges and marginalises the messages related to the VNs by taking into account the constraints imposed by the CNs. Similarly, each CN will collect soft-decision information from the VNs connected to it. This soft information gleaned from the VNs connected to a CN is then combined in order to generate soft-decision based estimates, which are then subjected to a hard-decision, once the affordable number of iterations has been exhausted.

Figure 5.7 depicts the schematic designed for PN sequences generated using the GP of $g_1(D) = D^{15} + D + 1$ [43, 59], whilst Figure 5.8 portrays the schematic designed for PN sequences generated using the GPs of $g_1(D) = D^{15} + D + 1$ and $g_3(D) = D^{60} + D^4 + 1$ [59], where the squares and circles represent CNs and VNs, respectively. Each CN in Figures 5.7 and 5.8 gleans soft-decision information from the three VNs connected to it. This constraint obeys the structure of $g_1(D)$ as well as either $g_1(D)$ or $g_3(D)$ for Figures 5.7 and 5.8, respectively. To elaborate a little further, in case of $g_1(D)$, the first CN $Y_{(0)}$ is directly connected to $X_{(0)}$, $X_{(14)}$ and $X_{(15)}$, corresponding to the terms of D^{15}, D and 1, respectively. Similarly, in Figure 5.8 $Z_{(0)}$ associated with $g_3(D)$ is mapped into $X_{(0)}$, $X_{(56)}$ and $X_{(60)}$, corresponding to the terms of D^{60}, D^4 and 1, respectively. Moreover, each node seen in Figures 5.7 and 5.8 represents a random variable, whereas each edge indicates probabilistic constraints among the nodes connected to it. The procedure of generating a (2^S-1)-chip PN sequence imposing redundancy according to the above-mentioned GPs may be considered to be equivalent to incorporating redundant P-Cs into the standard PCM of

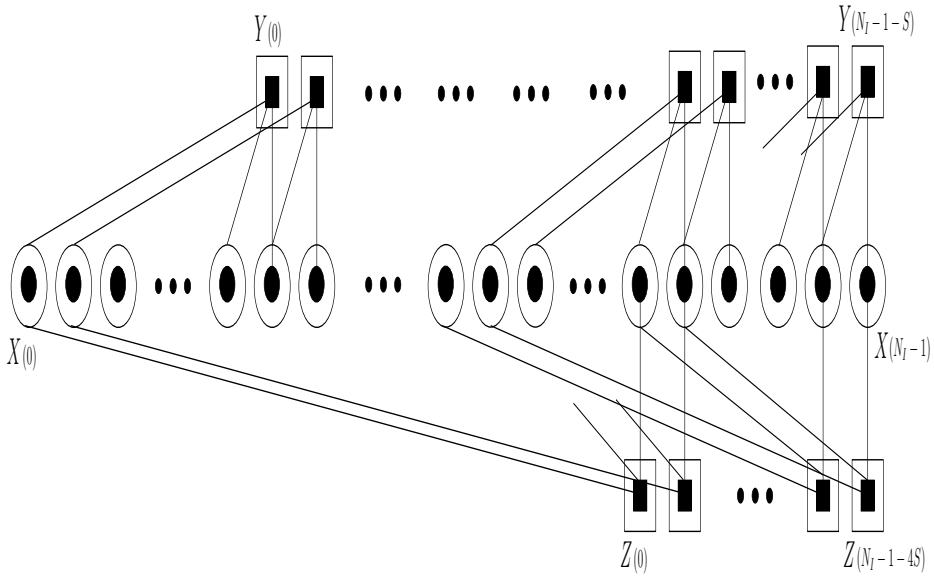

Figure 5.8: Tanner graph based acquisition structure for the PN sequence employing the GPs of $g_1(D) = D^{15} + D + 1$ and $g_3(D) = D^{60} + D^4 + 1$. The squares and circles denote CNs and VNs, respectively.

classic LDPC codes and a similar technique has been applied also for the soft decoding of classic channel codes in [154]. Each of the subgraphs corresponding to connections of the upper and the lower half of Figure 5.8 is based on a different GP, namely on $g_1(D)$ and $g_3(D)$, respectively. Mathematically, different reducible GPs may be used to generate the same PN sequence [59, 154]. Similarly to the notation used in Figure 5.4, we define the initial soft-decision based estimate in the form of $X(j)$ at the VN, where $X(j)$ represents an j^{th} chip-estimate of an N_I-chip soft-sequence received, where we have $j = 0, ..., (N_I - 1)$. The set of N_I-chip received signal estimates becomes the initial input of all the related CNs. Figure 5.8 can be also interpreted as a PCM in case of employing 1^{st} and 3^{rd} order GPs, as further described in Figure 5.9. Generally speaking, a graphical model such as the Tanner graph can be described by its corresponding PCM, which encompasses all the edges between its VNs and CNs, as shown in Figure 5.9. Namely, assuming that the j^{th} column directly corresponds to the j^{th} VN and that the i^{th} row is directly related to the i^{th} CN, the matrix element denoted as $h_{i,j}$ becomes 1 if and only if the i^{th} CN and the j^{th} VN are connected, otherwise we have $h_{i,j} = 0$. Accordingly, each GP-related connection can be identified as a subset of the corresponding PCM, which also constitutes a composite Tanner graph structure, again as shown in Figures 5.8 and 5.9. The composite PCM is represented by the vertical stacking of H_1 and H_3 corresponding to $g_1(D)$ and $g_3(D)$, respectively, where N_I is the number of columns, $(N_I - S)$ is the number of rows associated with $g_1(D) = D^{15} + D + 1$,

$(N_I - 4{\cdot}S)$ represents the number of rows associated with $g_3(D) = D^{60} + D^4 + 1$. In both H_1 and H_3 of Figure 5.9, every row encompasses a shifted version of the GP connection set denoted as either $[g_S, .g_s.., g_0]$ or $[g_{4\cdot S}, .g_s.., g_0]$, where g_s is the s^{th} coefficient of the GP assigned.

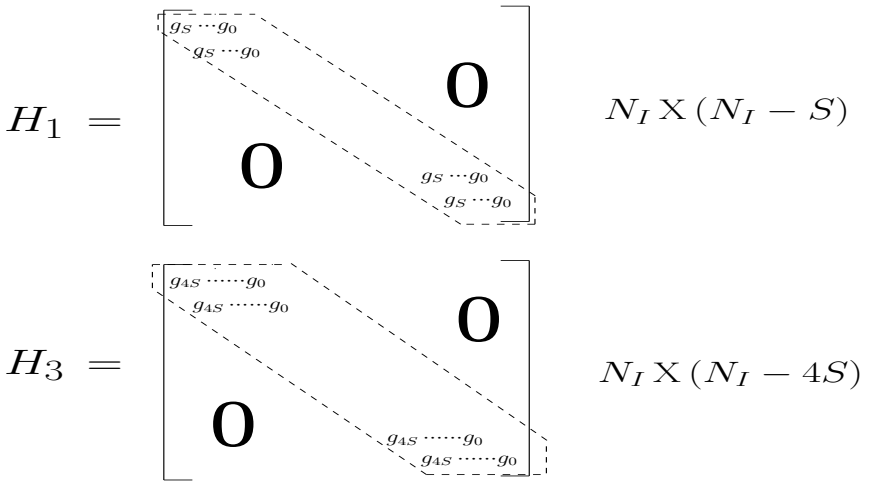

Figure 5.9: Structure of a parity check matrix in case of employing 1^{st} and 3^{rd} order GPs

The employment of higher-order GPs will provide further potential performance improvements at the cost of an increased hardware complexity. We will show in Chapter 6 that designing GPs for attaining the best possible P_D performance is achieved by investigating a plethora of different GPs in this system context. Then we will demonstrate that the achievable P_D performance may be improved by beneficially combining several GPs, such as 1^{st} and 3^{rd} as well as 1^{st}, 3^{rd} and 5^{th} order GPs, which will be denoted as a **13** and **135** GP constellation, respectively, where the bold numbers represent the order of the individual component GPs. We will demonstrate that a better performance may be achieved by the **135** GP combination, than in case of employing 1^{st}, 2^{nd} and 3^{rd} order GPs, where the latter combination is denoted by the acronym of **123**. We used a Tanner-graph based MP decoder for detecting the reception of PN sequences generated using different-order GPs. The rationale of our design choices is as follows: (i) This method facilitates the beneficial employment of the MP decoding algorithm originally derived for classic LDPC codes. (ii) The performance of the corresponding Tanner-graph based decoder using a lower-complexity MP algorithm approaches that of the Tanner-Wiberg graph based one [59] employing a higher-complexity MP algorithm, where there is only a modest power loss of about 0.3 dB [6] [59]. (iii) Furthermore, when the employment of several combined GPs is considered, the

[6]Moreover, this performance loss can be compensated by using the offset-based min-sum algorithm of

Tanner-Wiberg graph based decoder requires a quadrupled state metric memory [59]. We will demonstrate in Chapter 6 that the acquisition schemes based on the GPs **135** and **13** become our favourite choices for the $R = 1$ and 4 scenarios using one and four receive antennas, respectively, as a benefit of their improved performance in comparison to other GP combinations.

5.4 System Description and Algorithms

5.4.1 Single-Stage Iterative Acquisition

5.4.1.1 Single-Stage Iterative Acquisition Employing a Single Component Decoder

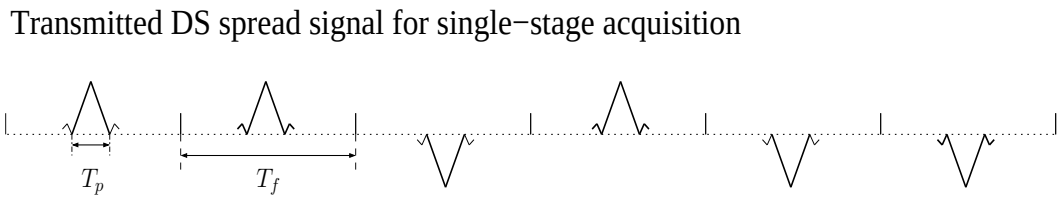

Figure 5.10: The transmitted UWB signal designed for single-stage acquisition.

Figure 5.10 portrays the transmitted UWB signal designed for single-stage acquisition using a single component decoder [43]. The transmitted UWB signal in Figure 5.10 are characterised by low-duty-cycle pulse trains, where each signalling pulse has a very narrow width [42, 43]. Depending on the logical value to be conveyed, a signalling impulse of T_p duration and of the required polarity is allocated at multiples of the frame duration T_f, where T_f is defined as the pulse repetition period, i.e. the time between two consecutive signalling pulses. The DS pulse train of the received DS-UWB DL signal is expressed as [43],

$$\sum_{r=1}^{R}\left[\sum_{n=0}^{(N_I-1)}\sqrt{E_c}\cdot(-1)^{x_n}\cdot\omega_r(t-nT_f-dT_p)\;+\;I_r(t)\right], \tag{5.22}$$

where this signal is generated by employing the PP $g_1(D) = D^{15} + D + 1$, $r = R$ is the number of receive antennas, N_I indicates the truncated PN sequence-length, E_c denotes the pilot signal energy per PN code chip, $x_n \in (-1, 1)$ represents the chip pattern of the PN sequence at the n^{th} position, $\omega_r(t)$ represents a chip waveform having a duration of T_p and d is the unknown time shift jointly imposed by the oscillator's frequency drift as well

[141].

as the receiver's mobility. Furthermore, $I_r(t)$ is the AWGN having a variance of $\frac{I_0}{2}$ at the r^{th} path.

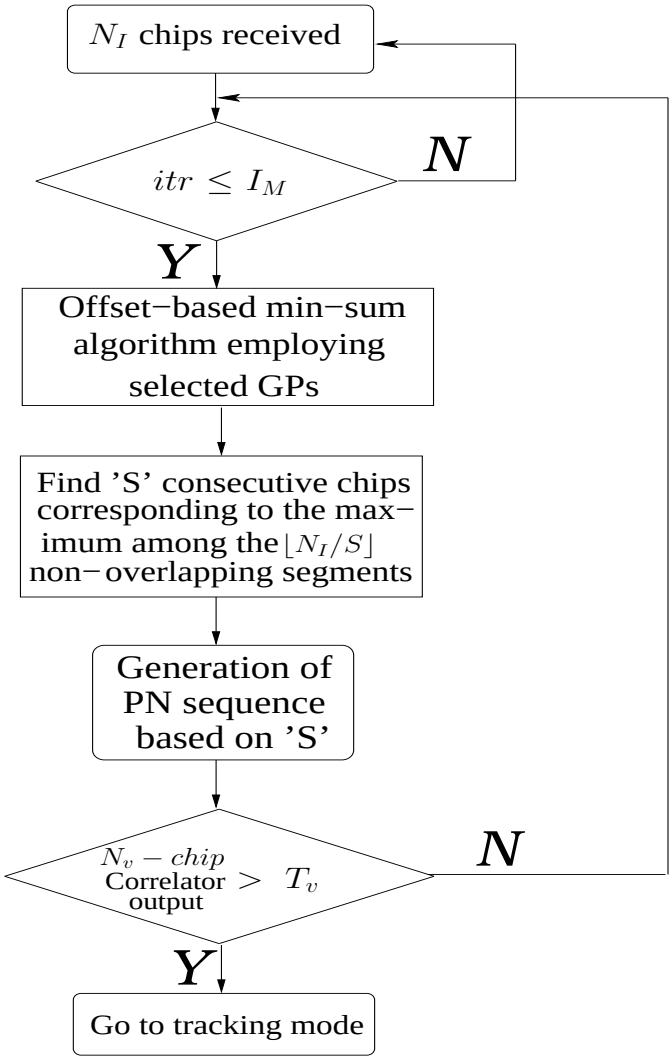

Figure 5.11: Flow chart of our proposed algorithm designed for single-stage acquisition scheme using a single component decoder, where the T_v is used for thresholding the correlation peaks.

Figure 5.11 illustrates our proposed algorithm exploiting the offset-based MSA and beneficially chosen higher-order GPs when using the single component decoder, where I_M represents the maximum allowable number of iterations, $\lfloor N_I/S \rfloor$ is the number of non-overlapping segments of S consecutive chips in the N_I-chip truncated PN sequence and T_v is a threshold value assigned to the verification mode [59]. The specific details of our iterative MP aided decoder were elucidated in Section 5.3.5. A single component decoder in

our proposed scheme constitutes the beneficially combined GPs, such as 1^{st} and 3^{rd} as well as 1^{st}, 3^{rd} and 5^{th} order GPs denoted as **13** and **135**, respectively, where the bold number represents the order of the individual component decoders. In our analysis we opted for invoking 'Algorithm 1' of [59] as a part of our basic iterative decoding MP algorithm, rather than that of [43], because this algorithm leads to significant reduction of the average number of iterations at the cost of a modest acquisition performance degradation. We also investigated a technique referred to as the offset-based MSA of CN processing [141], because it has the added benefit of a 0.5 dB gain compared to the pure min-sum one algorithm, which is obtained at a modest increase on the complexity. The offset-based MSA was also explained in Section 5.3.4. Hence the offset-based min-sum operation is invoked for our basic iterative MP decoding algorithm. During the CN processing of our proposed scheme, an optimised offset value was used for substituting the magnitude of the outputs of the VNs in the graph describing the acquisition scheme.

More specifically, as described in Figure 5.11, our decoder is constituted by the offset-based MSA [141], followed by a single correlator required for the verification of the S consecutive chips estimated. After performing an iteration of the MP scheme in order to obtain the N_I estimated chips, the particular PN code phase associated with the highest confidence is selected as the most likely correct phase from the non-overlapping segments of S consecutive chips in the N_I-chip-duration truncated PN-sequence. This code-phase is found by identifying the highest correlation peaks of N_v number of chips, since the S chips determine all the $(2^S - 1)$ PN code chips [59, 72]. More explicitly, the corresponding PN sequence is then generated by feeding these S chips into the LFSR-based PN-code generator, which produces $(2^S - 1)$ chips. Then, a single operation of the correlation between the received and locally generated N_v chip sequences confirms, whether the correct code phase of the PN sequence was indeed found or not by comparing the correlator output to the decision threshold of T_v.

5.4.1.2 Single-Stage Iterative Acquisition Using Multiple Component Decoders

Figure 5.10 also depicts the transmitted UWB signal designed for single-stage acquisition, when using multiple component decoders [43]. Further details of the transmitter were provided in Section 5.4.1.1. Here we also chose 'Algorithm 1' of [59] as a part of our basic iterative decoding algorithm, rather than that of [43], as shown in Section 5.4.1.1. The multiple component decoder constitutes a combination of several single component decoders.

The maximum affordable number of iterations is considered to be 15, while the P_D value of the verification stage is assumed to be 1.0 [59]. For example, a multiple component decoder is expressed as **13:135(3:12)**, where the value in **( )** represents the maximum affordable number of iterations. Explicitly, the **13:135(3:12)** represents a multiple component decoder, which activates the acquisition schemes using the GPs **13** and **135** for a maximum of three and 12 iterations, respectively. More specifically, the scheme employing the GPs **13** is activated up to three times and, then the decoder exploiting the GPs **135** is enabled for up to 12 iterations. Figure 5.12 illustrates our proposed algorithm exploiting the offset-based MSA and beneficially chosen higher-order GPs such as **13:135** when considering the employment of the multiple component decoder, where I_M represents the maximum allowable number of iterations, I_1 is the number of the maximum iteration assigned, $\lfloor N_I/S \rfloor$ is the number of non-overlapping segments of S consecutive chips in the N_I-chip truncated PN sequence and T_v is a threshold value assigned to the verification mode [59]. The remaining details of our proposed decoder are exactly the same as those described in Section 5.4.1.1.

5.4.2 Two-Stage Iterative Acquisition

Figure 5.13 illustrates the schematic of our proposed transmitter for two-stage acquisition [42, 70]. It transmits not only a periodic pulse train for Timing Acquisition (TA) but also a DS pulse train for PN Code Phase Acquisition (CPA).

Figure 5.14 portrays the transmitted UWB signal designed for two-stage acquisition, namely for the TA and CPA stages [42, 70]. The specifically designed training signal transmitted during the acquisition process is constituted by the superposition of the signals designed for supporting TA and CPA stages. Observe in Figure 5.14 that the top trace indicates a separate periodic pulse train used for supporting the TA stage, whilst the middle trace portrays a DS pulse train employed for assisting the CPA stage. The periodic pulse train designed for the TA stage at each receive antenna of the DS-UWB DL signal transmitted is expressed as [42, 70]

$$r_{(TA)|\xi}(t) = \sum_{n=0}^{(N_s-1)} \sqrt{E_c}\cdot\omega(t - 2nT_f - dT_p) + I_\xi(t), \tag{5.23}$$

where $\xi = R$ is the number of receive antennas, N_s is the number of chips used for the TA stage, E_c denotes the pilot signal energy per PN code chip, $\omega(t)$ represents a chip waveform having a duration of T_p, d is the unknown time shift jointly imposed by the oscillator's frequency drift as well as the receiver's mobility and $I_\xi(t)$ is the AWGN having a variance

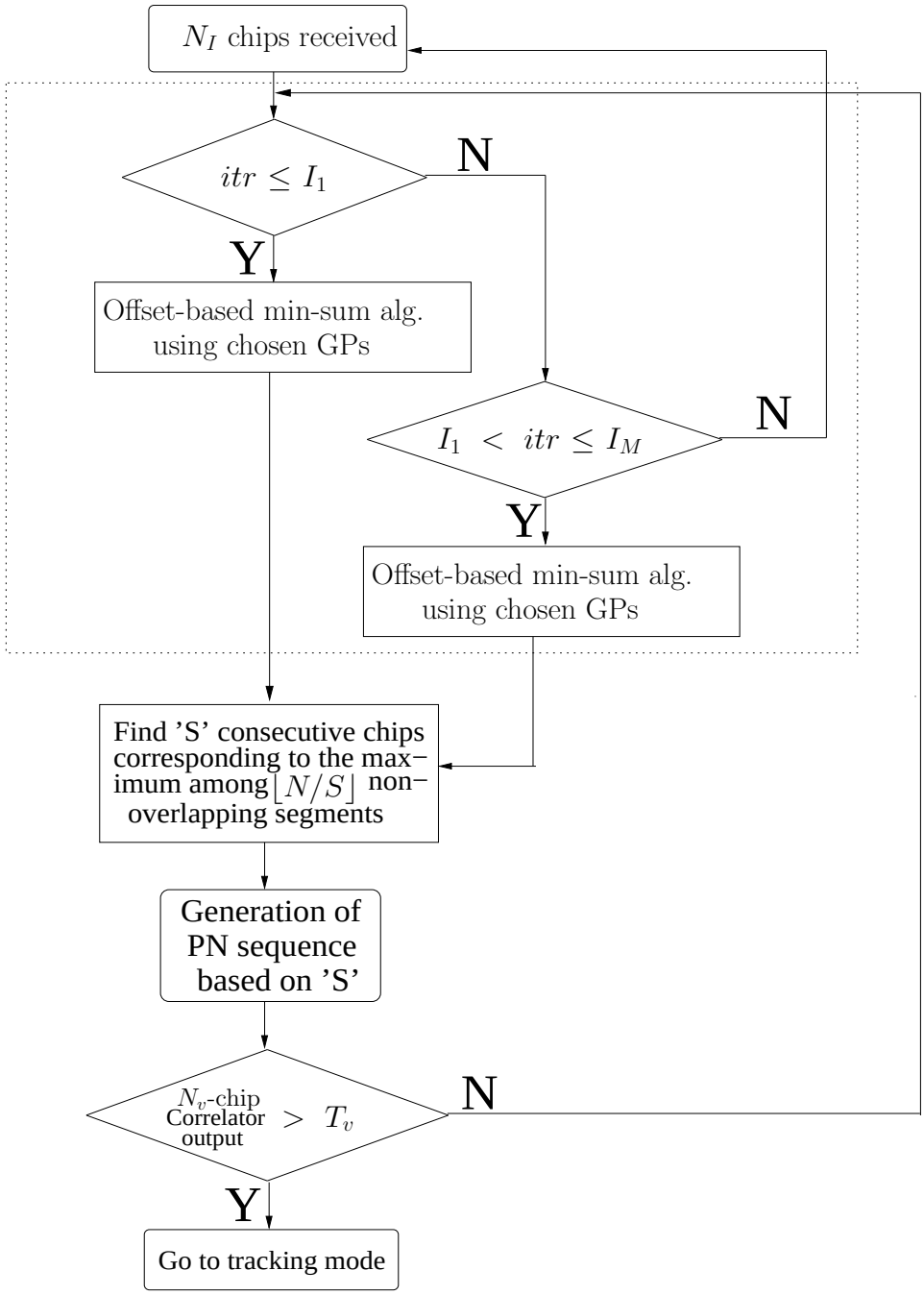

Figure 5.12: Flow chart of our proposed algorithm designed for single-stage acquisition scheme employing multiple component decoders, where the T_v is used for thresholding the correlation peaks.

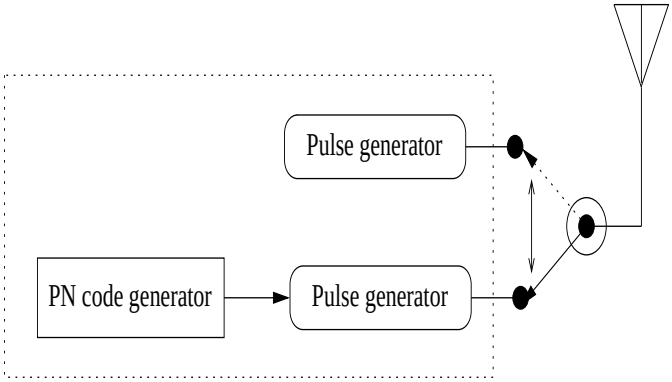

Figure 5.13: The schematic of our proposed transmitter for two-stage acquisition.

of $\frac{I_0}{2}$. Similarly, the DS pulse train of the received DS-UWB DL signal designed for the CPA stage is formulated as [43, 59]:

$$r_{(CPA)|\xi}(t) = \sum_{n=0}^{(N_I-1)} \sqrt{E_c}\cdot(-1)^{x_n}\cdot\omega(t-(2n+1)T_f - dT_p) + I_\xi(t), \tag{5.24}$$

where N_I indicates the truncated PN sequence-length used for the CPA stage and $x_n \in (-1, 1)$ represents the chip pattern of the PN sequence.

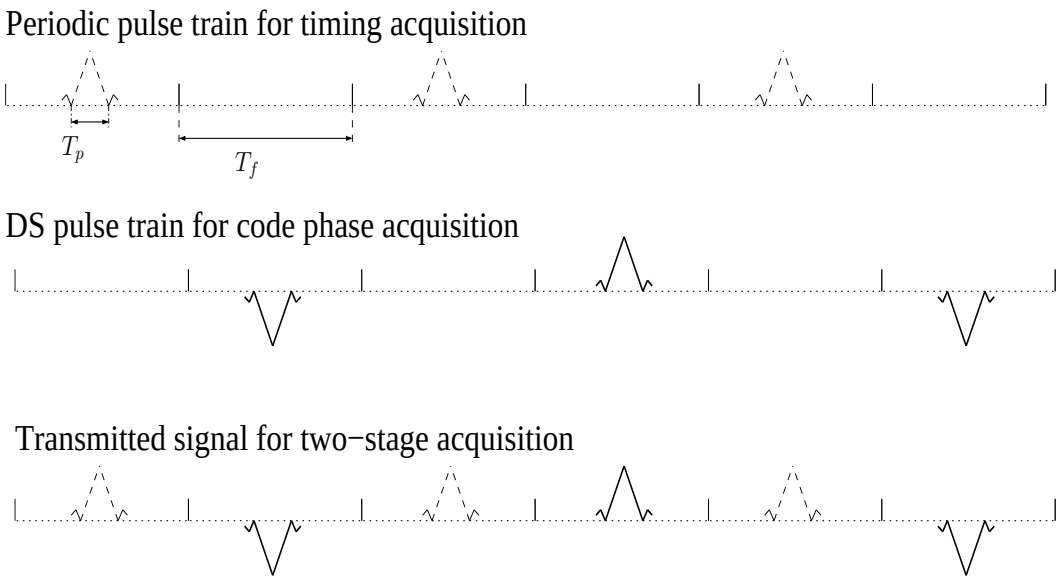

Figure 5.14: The transmitted UWB signal designed for two-stage acquisition, namely for TA and CPA stages.

The schematic of the proposed receiver designed for both Single Input Single Output (SISO) and Single Input Multiple Output (SIMO) scenarios is portrayed in Figures 5.15

and 5.16, respectively. These schemes are constituted by the amalgam of the sliding correlator used for the TA stage and the iterative CPA decoder, where T_{TA} is a threshold value assigned to the TA stage and T_{CPA} is another threshold assigned to the verification mode of the CPA stage [59, 70]. More specifically, the timing of the periodic pulse train at the TA stage is recovered by correlating the received signal with the receiver's own replica of the periodic pulse train over the entire uncertainty region, which is twice T_f [42, 70] and then comparing the correlator's output to the decision threshold of T_{TA}. More explicitly, we consider the random search technique described in Section 1.3.4 at the TA stage. Once the TA stage is completed, the chip boundaries of the DS pulse train have become known and the CPA stage has to search for the correct phase across a single PN sequence duration. The employment of both the MP decoding algorithm [43] originally derived for LDPC codes and a single correlation required for the verification of the $(2^S - S - 1)$ chips' expected values based on the S consecutive chips hypothesised are considered.

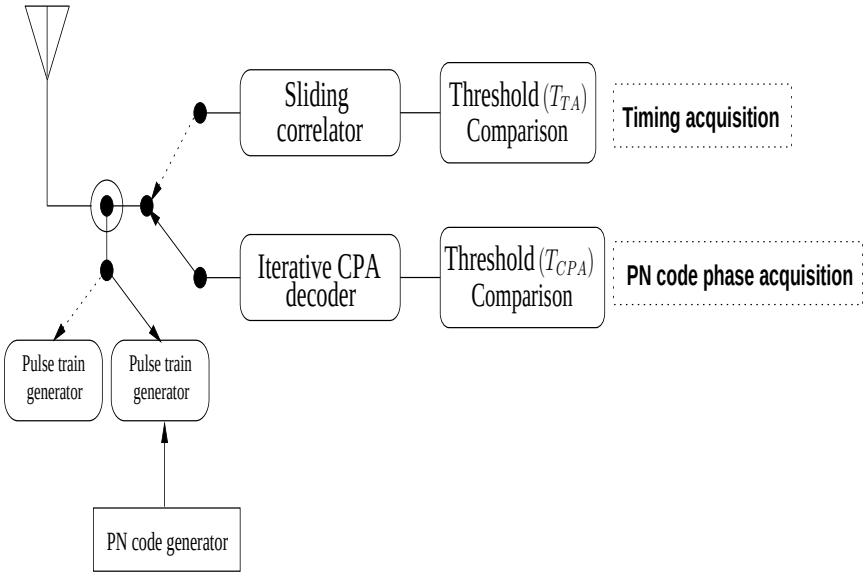

Figure 5.15: Schematic of our receiver proposed for a SISO scenario.

Similarly to the decoders described in Sections 5.4.1.1 and 5.4.1.2, we opted for invoking 'Algorithm 1' of [59] as a part of our basic iterative decoding algorithm, rather than that of [43]. This algorithm is used for the iterative CPA decoder. Figure 5.17 further illustrates our proposed algorithm designed for the two-stage detection aided acquisition scheme, where I_M represents the maximum affordable number of iterations and $\lfloor N_I/S \rfloor$ is the number of non-overlapping segments of S consecutive chips in the N_I-chip truncated PN-sequence used for the CPA stage. The offset-based MSA and other specific details of our iterative CPA decoder were provided in Sections 5.3.4 and 5.3.5, respectively. More explicitly, as

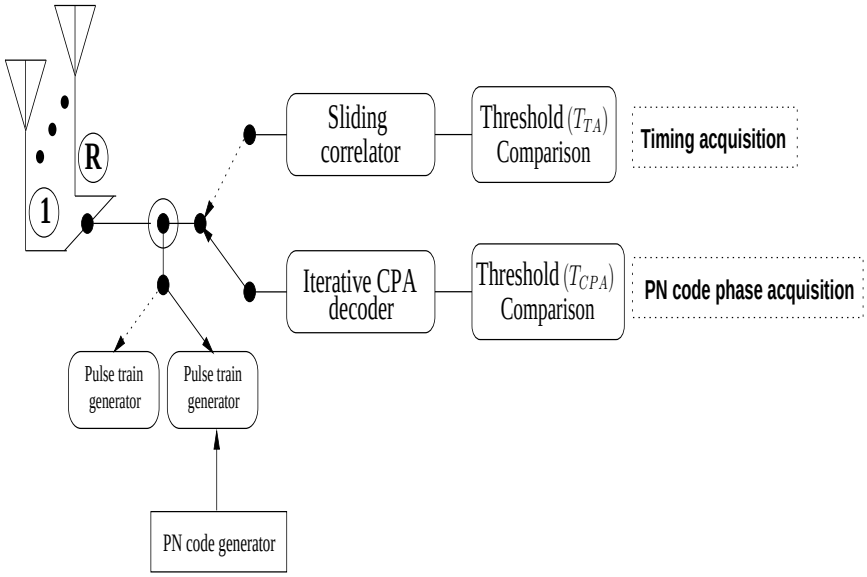

Figure 5.16: Schematic of our receiver proposed for a SIMO scenario.

described in Figure 5.17, our decoder designed for the CPA stage is constituted by the offset-based MSA [141], followed by a single correlator required for the verification of the S consecutive chips estimated. After performing an iteration of the MP scheme for the sake of obtaining the N_I estimated chips, the particular PN code phase associated with the highest confidence is chosen as the most likely correct phase from the non-overlapping segments of S consecutive chips in the N_I-chip-duration truncated PN-sequence. This code-phase is found by identifying the highest correlation peaks of N_v number of chips, since the S chips determine all the $(2^S - 1)$ PN code chips [59, 72]. More specifically, the corresponding PN sequence is then generated by feeding these S chips into the LFSR-based PN-code generator, which produces $(2^S - 1)$ chips. Then, a single correlation computation between the received and locally generated N_v chip sequences confirms, whether the correct code phase of the PN sequence was indeed found or not by comparing the correlator output to the decision threshold of T_{CPA}.

5.5 Correct Detection and False Alarm Probabilities

Having a realistic channel model, which encapsulates all the main characteristics of a specific channel becomes a crucial prerequisite for the system's analysis. The IEEE 802.15.3A standard's channel model is often used for DS-UWB systems, which is typically subdivided into four different models, depending on both the characteristics of the multi-path channel

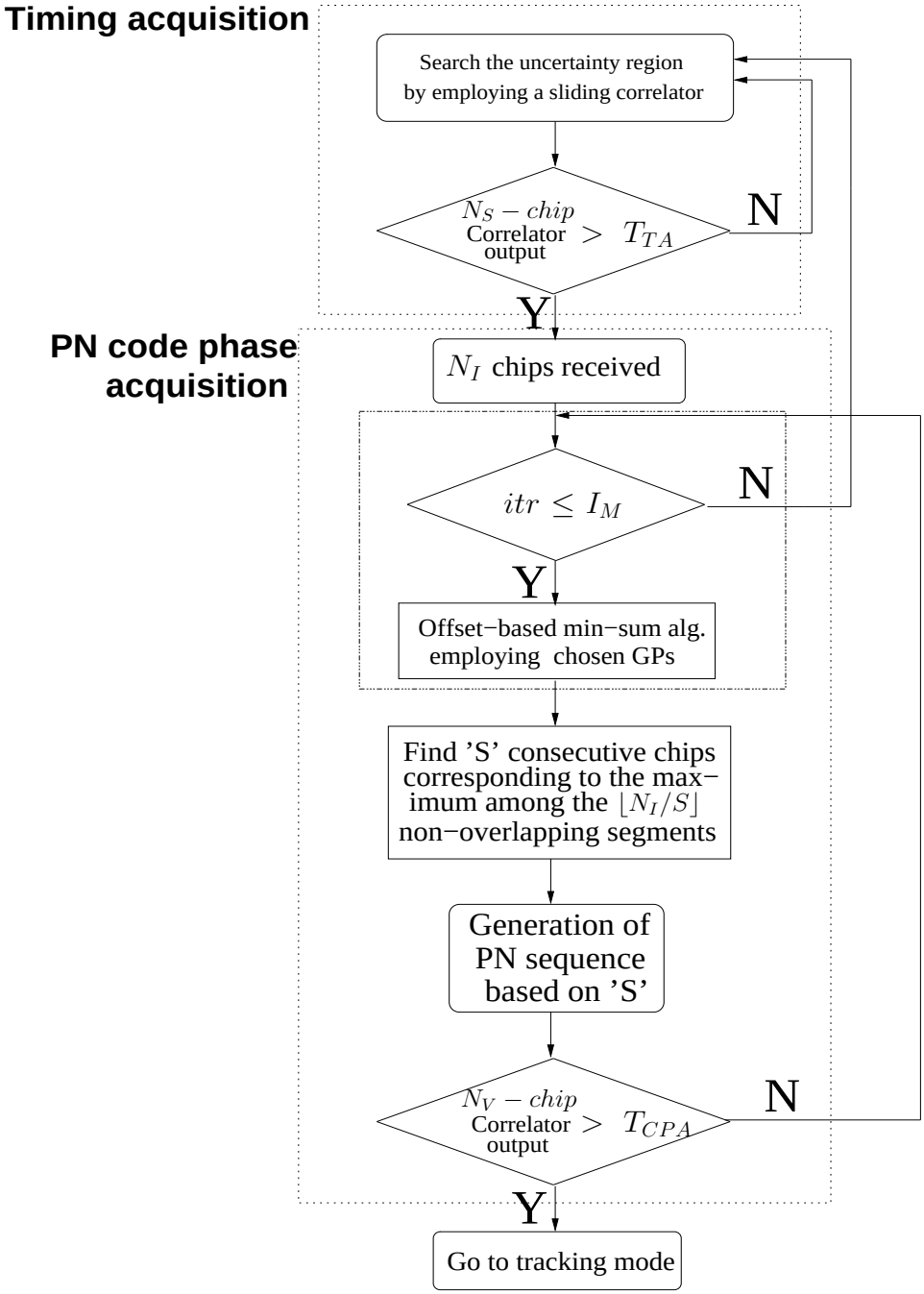

Figure 5.17: Flow chart of our proposed algorithm designed for two-stage acquisition scheme, where the T_{TA} and T_{CPA} are used for thresholding the correlation peaks.

and on the model parameters [62]. We will adopt some of the characteristics of the DS-UWB channel models in [62], which mimic the characteristics of multi-path indoor environments, as it was further illustrated in Section 5.2. When considering a realistic UWB channel, the numerical analysis of serial search based schemes becomes intractable for the CIR constituted by sparse clumps of multi-path components [62]. However, recently a random search aided scheme was proposed as a realistic alternative for the analysis of the UWB channel model [63], because the random search makes no particular assumption regarding the channel model and hence can be applied to arbitrary channel models. Furthermore, based on the results of Figure 6 in [63], the performance of the serial search based scheme approaches that of the random search. Accordingly, we will use the random search technique of [63] for our benchmarker as well as for the TA stage of our proposed scheme. The schematic of the random search aided receiver is exactly the same as that of the serial search based one seen in Figure 1.3 of Chapter 1, except that the search algorithm shifts the code phase of the local sequence by a random amount selected between 0 and $(\nu - 1)$, where ν represents the number of chips in the entire uncertainty region to be searched. Further details on the receiver schematic of the related scheme can be found in Figure 2 of [63]. It is also worth noting that the channel coefficients are assumed to be real-valued [43, 59, 62, 63]. Similarly to code acquisition in the DS-CDMA DL [3], that of the DS-UWB DL also dispenses with any prior information on channel knowledge at the receiver. The channel-induced impairments imposed on the DL are constituted by the superposition of the background noise, plus the serving-cell interference imposed by both the multi-path signals and the other users as well as the other-cell interference. Further details on the calculation of the total interference may be found in [3].

For the sake of deriving the Probability Density Function (PDF) conditioned on both the hypotheses of the desired signal being present and absent, let us assume that the amplitude is fixed [3]. The vector hosting the signal received via the single path considered of multi-path components may be expressed as $(r_1, r_2, ...r_{N_s})$. Then, we introduce the PDFs of each sample denoted as r_n, which may be expressed in the context of an AWGN channel [3] as

$$p_0(r_n) = \frac{1}{\sqrt{2\pi I_0}} \cdot \exp\left[-\frac{r_n^2}{2I_0}\right], \tag{5.25}$$

$$p_1(r_n) = \frac{1}{\sqrt{2\pi I_0}} \cdot \exp\left[-\frac{(r_n - \alpha_l\sqrt{E_c})^2}{2I_0}\right], \tag{5.26}$$

where the variance is $\frac{I_0}{2}$ and α_l represents the amplitude of the l^{th} multi-path component. We also need the likelihood functions based on the absolute value of the sum

$Y = |\sum_{n=1}^{N_s}(r_n)|$, because both P_D and P_F will be the complement of the cumulative distribution function corresponding to the normalised Gaussian RV derived. We arrive at the likelihood functions conditioned on both the hypothesis $p_0(Y)$ and $p_1(Y)$ of the desired signal being absent and present, respectively, in the context of an AWGN channel. Therefore, the likelihood function in the absence of the desired signal is expressed as

$$p_0(Y) = \frac{1}{\sqrt{2\pi N_s I_0}} \cdot \exp\left[-\frac{Y^2}{2N_s I_0}\right], \tag{5.27}$$

where the variance is $N_s(\frac{I_0}{2})$. By contrast, the likelihood function of the signal being present may be expressed as

$$p_1(Y) = \frac{1}{\sqrt{2\pi N_s I_0}} \cdot \exp\left[-\frac{(Y - \alpha_l N_s \sqrt{E_c})^2}{2N_s I_0}\right], \tag{5.28}$$

where the mean of Equation 5.28 becomes $\alpha_l N_s \sqrt{E_c}$. By using integral manipulations, the probability of false alarm is finally obtained as follows [63]:

$$P_F(\theta) = P(|Y| > Th|H_0) = 2Q\left(\sqrt{\frac{N_s E_c}{I_0}}\right), \tag{5.29}$$

where θ represents a normalised threshold value associated with Th being T_{TA}, where Th is set to $Th = N_s\sqrt{E_c}\theta$, while H_x associated with $x = 0$ represents the hypothesis of the desired signal being absent and $Q(x) \equiv \int_x^\infty (1/\sqrt{2\pi})\exp[-y^2/2]dy$. Similarly, the probability of correct detection is expressed as [63]

$$P_{Dl}(\theta) = P(|Y| > Th|H_1) = Q\left(\sqrt{\frac{N_s E_c}{I_0}}(\theta - \alpha_l)\right) + Q\left(\sqrt{\frac{N_s E_c}{I_0}}(\theta + \alpha_l)\right), \tag{5.30}$$

where H_x using $x = 1$ represents the signal being present. In case of $R = 1$, both Equations. 5.29 and 5.30 will be used for the achievable MAT calculation of both our benchmarker and of the TA stage. On the other hand, when using multiple receive antennas, there is a different way of efficiently detecting, when the desired signal was received. In [10, 155], the authors employed the Coincidence Detection (CD) method [7]. In our $R = 4$ scenario, CD method based scheme is adopted for both our benchmarker and TA stage. Finally, the probability $P_{F_{tot}}$ of false alarm for the CD method is expressed as [155]

$$P_{F_{tot}} = \sum_{m=B}^{A}\left[\frac{A!}{m!(A-m)!}\right] P_F^m (1 - P_F)^{(A-m)}. \tag{5.31}$$

[7] If at least B of a total of A number of samples exceed the predetermined threshold, Th the initial acquisition is deemed to be successfully accomplished. The parameters A and B are considered to be 4 and 2, respectively, because these values were shown to result in a sufficiently good performance [10].

Similarly, the probability $P_{Dl_{tot}}$ of correct detection for the CD method is formulated as [155]

$$P_{Dl_{tot}} = \sum_{m=B}^{A} \left[\frac{A!}{m!(A-m)!} \right] P_{Dl}^{m} (1 - P_{Dl})^{(A-m)}. \tag{5.32}$$

Similarly to the case of $R = 1$, in the $R = 4$ scenario, both Eqs. 5.31 and 5.32 will be employed for the MAT calculation of both our benchmarker and of the TA stage. In case of the CPA stage, the derivation of the correct detection and false alarm probabilities is unfeasible at the current state-of-the-art owing to its iterative behaviour. Hence, they will be evaluated by simulation.

5.6 Mean Acquisition Time

5.6.1 Single-Path Scenario

It may be shown that the generalised expression formulated for calculating the MAT of the serial search based code acquisition scheme is given by [43]:

$$E[T_{ACQ}] = \frac{1}{2P_D}[2 + (2 - P_D)(\nu - 1)(1 + KP_F)] \cdot \tau_D, \tag{5.33}$$

where ν is the total uncertainty region to be searched, K denotes the false locking penalty factor expressed in terms of the number of chip intervals required by an auxiliary device for recognising that the code-tracking loop is still unlocked whilst P_F represents the false alarm probability of the Single Dwell Serial Search (SDSS) scheme employed and τ_D indicates the integral dwell time over which the received samples are accumulated during the correlation operation. For simplicity, we will consider an idealised scenario, where we have $P_D = 1.0$ and $P_F = 0.0$ [43, 70]. Naturally, these idealised conditions may only be satisfied asymptotically, with a certain probability, when we have a sufficiently high E_c/I_0 value, i.e. $E_c/I_0 = -10$ dB. More explicitly, the P_D value of the TA stage recorded for $N_s = 512$ may approach $P_D = 1.0$ for $E_c/I_0 = -10$ dB in Figure 5 of [43]. In this spirit, we may consider that the P_D value of the CPA stage also approaches $P_D = 1.0$ for $E_c/I_0 = -10$ dB, when employing a **135** GP combination and $N_I = 1024$. Accordingly, the MAT formula of Equation 5.33 is further simplified to [43, 70]:

$$E[T_{ACQ}] = \frac{(\nu + 1)}{2} \cdot \tau_D \cong \frac{\nu}{2} \cdot \tau_D. \tag{5.34}$$

Let us now investigate the attainable performance gain of our Two-Stage Iterative Acquisition (TS-IA) arrangement, also referred to as the TA-CPA scheme. We consider four

different schemes, which are as follows: (A) Single-Stage SDSS (SS-SDSS) [6], (B) Two-Stage SDSS (TS-SDSS) [70], (C) Single-Stage Iterative Acquisition (SS-IA) [59] and (D) TS-IA. Owing to the inherently low duty-cycle of the DS-UWB signals seen in Figures 5.10 and 5.13, the uncertainty region ν is increased by a factor of $(\frac{T_f}{T_p})$, because the number of candidate frame timing instants to be searched is proportional to $(\frac{T_f}{T_p})$ [43]. More specifically, for SS-SDSS we have $\nu = (\frac{T_f}{T_p})\cdot(2^S - 1)$. By contrast, in case of the TS-SDSS scheme we have $\nu = 2(\frac{T_f}{T_p}) + (2^S - 1)$ owing to the two-stage approach used [42, 70]. On the other hand, when the iterative acquisition scheme invokes ML decisions based on an N_I-chip segment of the PN sequence received [43], the number of legitimate positions to be searched within the uncertainty region of the CPA stage becomes one. In the SS-IA and TS-IA scenarios we have $\nu = (\frac{T_f}{T_p})$ and $\nu = (2\frac{T_f}{T_p} + 1)$, because the former carries out simultaneous TA and CPA, whereas in the latter a two-stage approach is used [42, 70]. By employing the simplified MAT formula of Equation 5.34 and the above-mentioned ν values considered, the corresponding four different MAT formulas may be expressed as:

$$E[T_{ACQ}]_{(A)} = \frac{1}{2}\cdot(\frac{T_f}{T_p})\cdot(2^S - 1)\cdot N_s\cdot\ [T_f], \tag{5.35}$$

$$E[T_{ACQ}]_{(B)} = \frac{1}{2}\cdot\left[2(\frac{T_f}{T_p}) + (2^S - 1)\right]\cdot 2N_s\ [T_f], \tag{5.36}$$

$$\begin{aligned} E[T_{ACQ}]_{(C)} = \frac{1}{2}\cdot&\left[(\frac{T_f}{T_p} - 1)\cdot(N_I + N_V I_M)\right] \\ &+ (N_I + N_V I_A)\ [T_f], \end{aligned} \tag{5.37}$$

$$E[T_{ACQ}]_{(D)} = \frac{1}{2}\cdot\left[2\frac{T_f}{T_p}2N_s\right] + 2\left[(N_I + N_V I_A)\right]\ [T_f], \tag{5.38}$$

where N_s was defined as the number of chips over which the correlator output is accumulated in the TA stage for the SDSS scheme of scenarios A,B and D. Furthermore N_V is the number of chips used for the verification mode, while I_A represents the average number of iterations and T_f is the basic unit of the MAT.

5.6.2 Multi-Path Scenario

In this section we consider two different schemes, which are (A) Single-Stage Random Search (SS-RS) [5, 6, 45, 63] and (B) our novel proposed Two-Stage Iterative Acquisition (TS-IA). Owing to the inherently low duty-cycle of the transmitted DS-UWB signals seen in Figures 5.10 and 5.13, the uncertainty region ν is increased by a factor of $(\frac{T_f}{T_p})$, because the number of candidate frame timing instants to be searched is proportional to $(\frac{T_f}{T_p})$ [43]. More

specifically, for SS-RS we have $\nu = (\frac{T_f}{T_p})\cdot(2^S - 1)$. On the other hand, the iterative acquisition scheme invokes Maximum Likelihood (ML) decisions based on an N_I-chip segment of the PN sequence received [43], when considering the signal being present. In this scenario, the number of legitimate timing positions to be searched within the uncertainty region of the CPA stage becomes one. Hence only code phase estimation is required. Accordingly, in the TS-IA scenario we have $\nu = \nu|_{TA} + \nu|_{CPA} = (2\frac{T_f}{T_p} + 1)$ [42, 70]. For the sake of simplifying our MAT formulation, a single hypothesis test per chip is assumed.

The analysis of random search based code acquisition stipulates no particular assumptions regarding the arrival times of the multi-path components and hence can be applied to both conventional wideband channel models and the IEEE 802.15.3a models. The H_1 cells of the random search are dispersed randomly among the H_0 cells, hence the overall transfer function may be derived by considering that when the process is located in a H_0 cell, it has a $(1 - L/\nu)$ probability of transitioning to a H_0 cell in the next step and then a $1/\nu$ probability of transitioning to each of the L H_1 cells. Accordingly, the transfer function related to exiting an H_0 cell is expressed as [63]

$$H_0(z) = (P_F z^{K+1} + (1 - P_F)z)\cdot \left[\frac{(\nu - L)}{\nu} H_0(z) + \frac{1}{\nu}\sum_{i=1}^{L} H_i(z)\right], \tag{5.39}$$

where $H_i(z)$ represents the transfer function derived for exiting the i^{th} H_1 cell. On the other hand, when the search is located in the i^{th} H_1 cell, it may move on to the acquisition state having a probability of P_{Di}, to a H_0 cell having a probability of $(1 - P_{Di})(1 - L/\nu)$ and to each of the remaining H_1 cells having a probability of $(1 - P_{Di})(1 - 1/\nu)$. Hence, the transfer function from the i^{th} H_1 cell is obtained as [63]

$$H_i(z) = P_{Di} z + (1 - P_{Di})z\cdot \left[\frac{(\nu - L)}{\nu} H_0(z) + \frac{1}{\nu}\sum_{j=1}^{L} H_i(z)\right], i = 1, 2, ..., L. \tag{5.40}$$

The transfer functions of $H_i(z)$s and $H_0(z)$ may be calculated by solving the $(L + 1)$ equations derived from Equations 5.39 and 5.40, because the search has a $(1 - L/\nu)$ probability of starting in a H_0 cell and a $1/\nu$ probability of commencing in each of the H_1 cells. Hence the effective transfer function leading to the acquisition state may be expressed as [63]

$$H(z) = \frac{(\nu - L)}{\nu} H_0(z) + \frac{1}{\nu}\sum_{i=1}^{L} H_i(z). \tag{5.41}$$

By employing the derivative of Equation 5.41 multiplied by the integral dwell time, τ at $z = 1$, it may be shown that the generalised MAT expression of the random search based

code acquisition scheme is given by [63]:

$$E[T_{ACQ}]|_{(benchmarker)} = \frac{[P_F K(\nu - L) + \nu]}{\sum_{l=1}^{L} P_{Dl}} \cdot \tau, \tag{5.42}$$

where P_F represents the false alarm probability of the SS-RS scheme employed, whilst K denotes the false locking penalty factor expressed in terms of the number of chip intervals required by an auxiliary device for recognising that the code-tracking loop is still unlocked. Still considering Equation 5.42, L indicates the number of the multi-path components considered and τ indicates the integral dwell time over which the received samples are accumulated during the correlation operation. When considering the multi-path components delayed with respect to the LOS component, their E_c/I_0 values are typically at least 3dB lower. However, in order to analyse the attainable performance of the worst-case scenario, it is assumed that all the 15 paths have equal power [91] in our analysis. We considered the initial acquisition scenario, where only the timing of the strongest LOS or NLOS paths must be acquired, but not those of the further delayed ones. Furthermore, the employment of all the paths within 10 dB of the strongest path is feasible, when determining the number of paths. The number of the paths in CM-2 was chosen to be $L = 15$ [62] in our analysis. It is also reasonable to assume that the minimum E_c/I_0 value required for finger-locking in the initial acquisition is set to -12 and -15dB for the $R = 1$ and 4 scenarios, respectively [43, 59].

Let us now investigate the attainable performance gain of our TS-IA arrangement. The main advantage of using our two-stage scheme is to reduce the entire search space. In the TA stage, our objective is to achieve a coarse timing of the received signal within a frame duration. Hence the TA stage does not suffer from having an excessive uncertainty region compared to SS-RS. When considering this reduced uncertainty region, we are capable of selecting both a sufficiently high threshold value T_{TA} and a sufficiently long accumulation period, because even if both conditions may lead to increasing the achievable MAT having a tight threshold value significantly decreases the false alarm probability. Therefore, at a given minimum E_c/I_0 value the value of $P_F K(\nu - L)$ in Equation 5.42 may become negligible. Finally, the MAT formula of Equation 5.42 is simplified as follows:

$$E[T_{ACQ}]|_{(TA)} \cong \frac{\nu}{\sum_{l=1}^{L} P_{Dl}} \cdot \tau. \tag{5.43}$$

When deriving the MAT formula of our proposed scheme, the presence of a false alarm during the TA stage is directly related to the derivation of the MAT formula to be described below during the CPA stage. However, based on the aforementioned conditions, the MAT

formula of the TA stage in Equation 5.43 may be modified for characterising the MAT of the CPA stage, as outlined below. In [59], the P_D value of the verification was assumed to be 1.0,

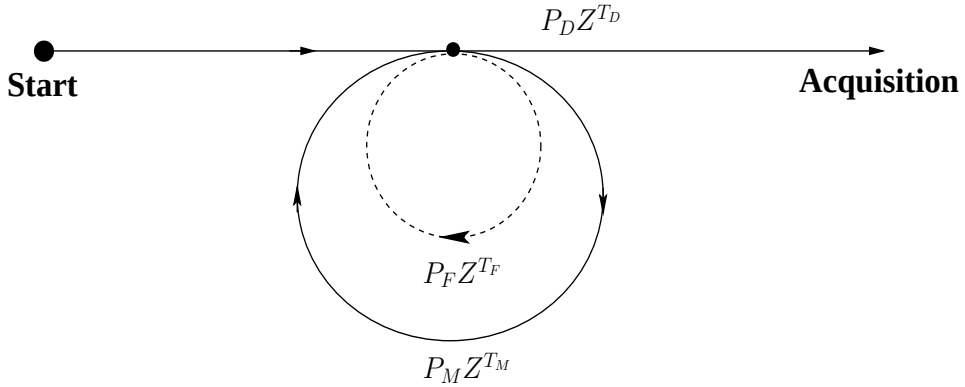

Figure 5.18: State Diagram of CPA stage

but the authors of [59] did not elaborate on how the corresponding stage operates. However, achieving $P_D \approx 1$ plays a pivotal role in deriving the MAT formula of the CPA stage, because unless $P_D = 1$ is ensured during each iteration, the corresponding transfer function exhibits two branches corresponding to the correct detection and missed detection events. Hence, in order to simplify our problem formulation, the value of N_V in the verification is assigned to be 1024 and 896 chips for the $R = 1$ and 4 scenarios, respectively. These values lead to $P_D \approx 1$ for E_c/I_0 values in excess of the minimum required for finger-locking. Then, similarly to the transfer function describing the state diagram of Figure 2 in [21], Figure 5.18 portrays the state diagram of the CPA stage considered. The transfer function of the CPA stage shown in Figure 5.18 is described as

$$U(Z) = \frac{P_D Z^{T_D}}{(1 - (P_M Z^{T_M} + P_F Z^{T_F}))} \tag{5.44}$$

$$= \frac{P_D Z^{T_D}}{(1 - P_D) Z^{T_M}}, \tag{5.45}$$

where T_D represents the processing time of a correct detection event, P_M is the missed detection probability, T_M denotes the processing time of a missed detection event and T_F represents the processing time for a false alarm event, which is also equivalent to the false locking penalty time [8]. There are some differences in our formulation compared to the derivation of the MAT formula in a scenario supported by the transmission of a dedicated

[8]In conventional ML acquisition schemes [21], the false locking penalty time is expressed in terms of the number of chip intervals required by an auxiliary device for recognising that the code-tracking loop is still unlocked. Therefore, both the processing time based on a single hypothesis test and the penalty time assigned are associated with the false alarm event. On the other hand, in our proposed scheme, a value of T_F is sufficiently high and hence after the processing time elapsed, we assumed that this hypothesis test corresponded to a false alarm.

acquisition preamble [21] as follows. First of all, there is no average reset time for a missed detection, because a specific continuous pilot channel pattern is transmitted. Then, T_F also incorporates the false locking penalty factor during the CPA stage. Furthermore, the impact of P_F during the TA stage was eliminated and hence the $P_F Z^{T_F}$ term in the denominator of Equation 5.44 disappears, which was also described by an inner circle denoted by the broken line in Figure 5.18. Then, by exploiting the well-known relationship of $P_D + P_M + P_F = 1$ [21, 43] associated with ML acquisition, the transfer function becomes dependent upon P_D only. The definitions of T_D and T_M are $T_D = (N_I + N_V \cdot I_{AD})(2T_f)$ and $T_M = (N_I + N_V \cdot I_M)(2T_f)$, respectively, where I_{AD} represents the average number of iterations. Setting the derivative of Equation 5.45 leads to the MAT formula of the CPA stage as follows:

$$E[T_{ACQ}]|_{(CPA)} = \frac{dU(Z)}{dZ}|_{Z=1} = T_D + \frac{(1 - P_D)}{P_D} T_M. \tag{5.46}$$

Therefore, the corresponding MAT formulas of the TA and CPA stages in our TS-IA scheme are constituted by Equations 5.43 and 5.46 [9]. The combined MAT formula of our proposed two-stage scheme is expressed as

$$E[T_{ACQ}]|_{(TOT)} = \frac{\nu}{\sum_{l=1}^{L} P_{Dl}} \cdot \tau + \left[T_D + \frac{(1 - P_D)}{P_D} T_M \right]. \tag{5.47}$$

Equation 5.47 will be exploited for the analysis of the achievable MAT performance in the following chapter.

5.7 Chapter Summary and Conclusions

In this chapter, we have provided a detailed study of our proposed code acquisition schemes designed for the SIMO aided DS-UWB DL. Following a brief introduction in Section 5.1, we continued by describing the UWB channel model, which exhibits both large-scale and small-scale fading. We have described the S-V model in Section 5.2. Then the preliminaries of code acquisition designed for the DS-UWB DL were presented in Section 5.3. More specifically, the characteristics of PN codes were highlighted in Section 5.3.1, followed by the detailed calculation of modulo-2 squaring in Section 5.3.2, and by the in-depth illustration of the SPA and offset-based MSA in Sections 5.3.3 and 5.3.4, respectively. In Section 5.3.5 the

[9] We briefly note that in Single-Stage Iterative Acquisition (SS-IA) [59] the exact MAT formula becomes intractable owing to the presence of sparse clumps of multi-path components. However, if it is assumed that the location of the multi-path components is spread uniformly across the entire uncertainty region, where ν is defined as $\nu = (\frac{T_f}{T_p})$, the value of ν is decreased by a factor given by the number of multi-path components considered. Then, the MAT performance of SS-IA and TS-IA schemes can be roughly compared.

decoding procedure of the iterative MP algorithm was elucidated in detail. We also showed in Section 5.3.5 that the iterative acquisition scheme exploiting the characteristics of the higher-order GPs further improved the attainable performance.

Both single-stage and two-stage iterative acquisition schemes were highlighted in Sections 5.4.1 and 5.4.2, respectively. More explicitly, in Section 5.4.1, single-stage iterative acquisition employing both a single- and multiple-component decoder was described. In Section 5.4.2, we proposed a search space reduction aided code acquisition scheme for the sake of reducing the MAT, which employs the iterative MP technique. Then the underlying formulas of both the correct detection and false alarm probabilities were presented in Section 5.5 for the random search based code acquisition scheme, when considering both the SISO and SIMO aided DS-UWB DL. The MAT analysis of our proposed schemes was provided for both the SISO and SIMO aided DS-UWB DL in Sections 5.6.1 and 5.6.2, respectively, when considering both single- and multi-path propagation environments. Finally, in Section 5.7 our summary and conclusions were provided.

Based on the preliminaries of Sections 5.3 and 5.4, as well as on the formulae of Sections 5.5 and 5.6, in Chapter 6 the specific characteristics of our code acquisition schemes will be analysed in both the SISO and SIMO aided DS-UWB DL.

Chapter 6

Performance of Code Acquisition in the Co-located SIMO Aided DS-UWB Downlink

6.1 Introduction

In this chapter, we will provide a quantitative performance analysis of our proposed iterative code acquisition schemes in the co-located SIMO DS-UWB DL. In Section 6.2 we will outline the system parameters used. Based on Sections 5.3, 5.4, 5,5 and 5.6, in Section 6.3 will provide our system performance results. More explicitly, Based on the algorithms outlined in Sections 5.3.4, 5.3.5 and 5.4.1, in Section 6.3.1, we will commence with the correct detection versus SINR per chip performance analysis of the iterative acquisition schemes employing a variety of GPs, different number of the receive antennas and different values of the chip-duration N_I. Then, the correct detection versus SINR per chip performance of multiple component decoders will be characterised in Section 6.3.1. The conceptual description of the message passing used in our proposed scheme will be offered in Section 6.3.1. Finally, the correct detection probability versus false alarm probability behaviour of the random search based scheme will be analysed in Section 6.3.1 based on the formulae provided in Section 5.5. With the aid of Sections 5.4 and 5.6, Section 6.3.2 provides a discussion on the MAT performance of both the initial and post-initial acquisition in the co-located SIMO DS-UWB DL. Our conclusions will be provided in Section 6.4.

6.2 System Parameters

In our analysis, we set $S = 15$, hence the total length of the PN sequence becomes $(2^{15} - 1)$ [43]. Furthermore, $\frac{T_f}{T_p}$ is set to 200 for the single-path scenario [59], where we have $T_p =$ 500 ps and $T_f = 100$ ns, whilst $\frac{T_f}{T_p}$ is set to 160 for the multi-path scenario [69], where $T_p = 500$ ps and $T_f = 80$ ns [69] as defined in the context of Figures 5.10 and 5.14. It is assumed that T_f is longer than the channel's maximum delay spread [62, 69]. The time separation between two successive cells is equal to T_p [69]. In our scenario, in order to analyse the characteristics based on a sufficiently high number of multi-path components, it is reasonable to assume that there are $L = 15$ paths arriving with a relative time delay within T_f, which are assumed to have an equal magnitude [1]. The measurements of DS-UWB channels indicate that their fading amplitude does not obey a Rayleigh fading and that either lognormal or Nakagami-m fading is considered to be a more accurate model [62]. This is because the central limit theorem may become inapplicable for the relatively high number of paths considered, which may result in effectively encountering an AWGN channel. This assumption was considered in [43, 59] along with a specific case of Nakagami-m fading. The maximum affordable number of iterations is considered to be $I_M = 15$ [59]. Furthermore, N_I is assumed to be 135, 512 and 1024, whilst the number of receive antennas is assumed to be $R = 1$,2 and 4. In case of the single-path scenario, N_s and N_V are assumed to be 512. Based on our simulation results of the single-path scenario recorded at $E_c/I_0 = -10$ dB, we set $I_A = 3$, where I_A represents the average number of iterations. During the TA stage of Figure 5.17 it was found to be sufficient to integrate the detector's output over $N_s = 512$ chips for both the $R = 1$ and 4 receive antenna scenarios, while the number of chips over which the accumulator sums the $|\sum(\cdot)|$ envelope detector's output in the SS-RS mode of our benchmarker is assumed to be 256 in both the $R = 1$ and 4 scenarios. The false locking penalty factor of the benchmarker is assumed to be 2560 chip durations. When considering the CPA stage of Figure 5.17, N_I is assumed to be $N_I = 1024$ or 512 chips in the $R = 1$ and 4 scenarios, respectively. Furthermore, we assume $N_V = 1024$ or 896 chips in the $R = 1$ and 4 scenarios, respectively, because we should set N_V to ensure that the correct detection probability P_D approaches 1.0 [59]. Furthermore, the highest GP orders used are 7 and 6 for the $R = 1$ and 4 scenarios, respectively. The Spreading Factor (SF) is set to SF = 128 [43]. The total uncertainty regions of the benchmarker and the TA

[1] The consideration of a specific root mean square delay spread value [62] is not necessary due to the employment of our random search aided scheme, because the random search doe not employ any specific parameters of the channel models except for the number of the multi-path components.

Table 6.1: System Parameters

Impulse duration	500 ps
Frame duration	80 or 100 ns
Length of PN sequence	$2^{15} - 1$
Number of receive antennas	1,2,4
Number of paths (Initial)	single and 15 path(s)
Number of paths (Post-initial)	14 paths
Spreading factor	128
Maximum allowable number of iterations	15
Average number of iterations in single-path scenario at E_c/I_0	3
Highest GP orders	7
Truncated PN sequence-length	135,512 or 1024
Integration interval for the verification mode	512,896 or 1024
Integration interval for the TA stage	512
Integration interval for the our benchmarkers (Single-path scenario)	512
Integration interval for the our benchmarker (Multi-path scenario)	256
Integration interval for the post-initial	256 or 384
Total uncertainty region (Our benchmarker)	$160 * (2^{15} - 1)$ hypotheses
Total uncertainty region (TA stage)	320 hypotheses
Total uncertainty region (Post-initial)	240 hypotheses
False locking penalty factor (Initial)	2560 chip-durations
False locking penalty factor (Post-initial)	2560 or 3840 chip-durations

stage of our proposed scheme are assumed to entail $160 \times (2^{15} - 1)$ and 320 hypotheses, respectively. All the MAT performance curves have been obtained at the threshold value of E_c/I_0 = -12 and -15 dB corresponding to the $R = 1$ and 4 scenarios, respectively. These threshold values are considered as the minimum value required for reliable finger locking. In case of the post-initial acquisition, the total uncertainty region is assumed to entail ± 120, which corresponds to a total of 240 hypotheses and $L = 14$ paths are considered. The false locking penalty factors, K of the post-initial acquisition are assumed to be 2560 and 3840 chip durations corresponding to $N_s = 256$ and 384, respectively. The system parameters employed are also summarised in Table 6.1.

6.3 System Performance Results

6.3.1 Correct Detection Probability

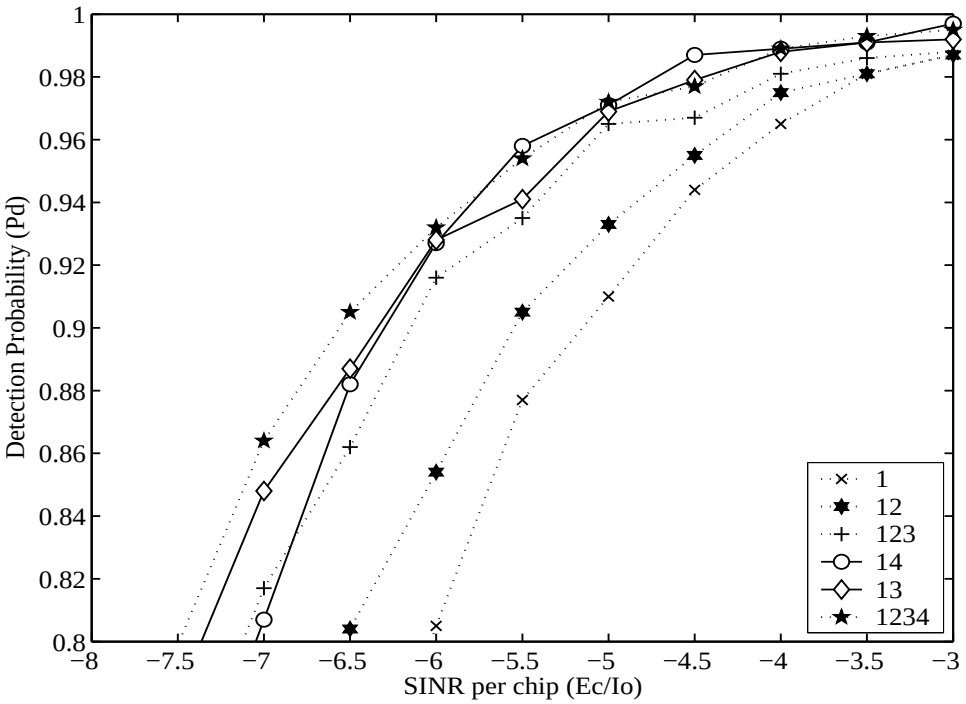

Figure 6.1: Correct detection probability versus SINR per chip of the acquisition schemes employing different GPs and $R = 1$, when considering $N_I = 135$ and using the schematic of Figure 5.11 and Table 6.1.

Figure 6.1 illustrates the P_D versus E_c/I_0 performance of the various combined GPs, when considering $N_I = 135$. Using $N_I = 135$ leads to the employment of 4^{th} order GPs. Observe in Figure 6.1 that the E_c/I_0 gain achieved by the GP combination of **13** and **14** is

slightly higher than that of **123**, where the beneficially combined GPs such as 1^{st} and 3^{rd} order GPs are represented by the **13** GP constellation and the bold numbers indicate the order of the individual component GPs. These findings suggest that using consecutive GP orders - as in the **123** scheme - degrades the efficiency of the MP algorithm. For instance, the joint employment of the GPs $g_1(D) = D^{15} + D + 1$ and $g_2(D) = D^{30} + D^2 + 1$ results in a somewhat correlated pair of PN codes, which is associated with a regularly spaced allocation of the connections between the CNs and VNs. More explicitly, the combination of $g_1(D)$ and $g_2(D)$ may be expected to lead to a relatively localised set of P-C constraints, consequently yielding a less beneficial regular - rather than random - PCM structure. This trend suggests that the degree of correlation among the P-C constraints may be decreased by using appropriately chosen GPs, such as **13** and **14**. Finally, based on Figure 6.1 the acquisition scheme employing the GPs **13** becomes our favourite choice for the $R = 1$ scenario, which is a benefit of the improved P_D performance in comparison to other GP combinations.

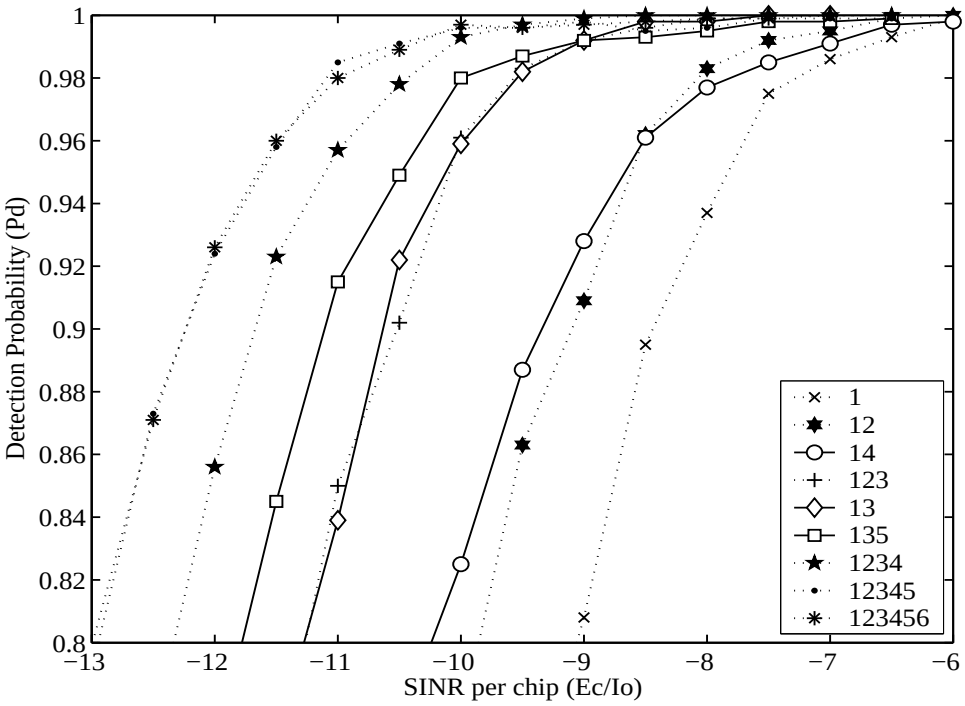

Figure 6.2: Correct detection probability versus SINR per chip of the acquisition schemes employing different GPs and $R = 1$, when considering $N_I = 512$ and using the schematic of Figure 5.11 and Table 6.1.

Figure 6.2 characterises the P_D versus E_c/I_0 performance of the various combined GPs, when considering $N_I = 512$. Observe in Figure 6.2, that the E_c/I_0 gain achieved by the

GP combination of **13** is almost similar to that of **123**. Furthermore, as seen in Figure 6.2, the gain achieved by the GPs **135** is better than that of **123**. Again, these findings suggest that using consecutive GP orders - as in the **123** scheme - degrades the efficiency of MP algorithm. This trend manifests that the degree of correlation among the P-C constraints may be decreased by using appropriately chosen GPs, such as **13**. In contrast, employing $g_1(D) = D^{15} + D + 1$ and $g_4(D) = D^{120} + D^8 + 1$ results in a degraded performance, because the number of P-C connections between the VNs and CNs is decreased by a factor of $(2^{n-1} \cdot S)$, $n = 1,2,...,6$, when the order of the GP is increased. Finally, based on Figure 6.2 the acquisition scheme based on the GPs **13** becomes our favourite choice for the $R = 1$ scenario, which is a benefit of the improved P_D performance in comparison to other GP combinations.

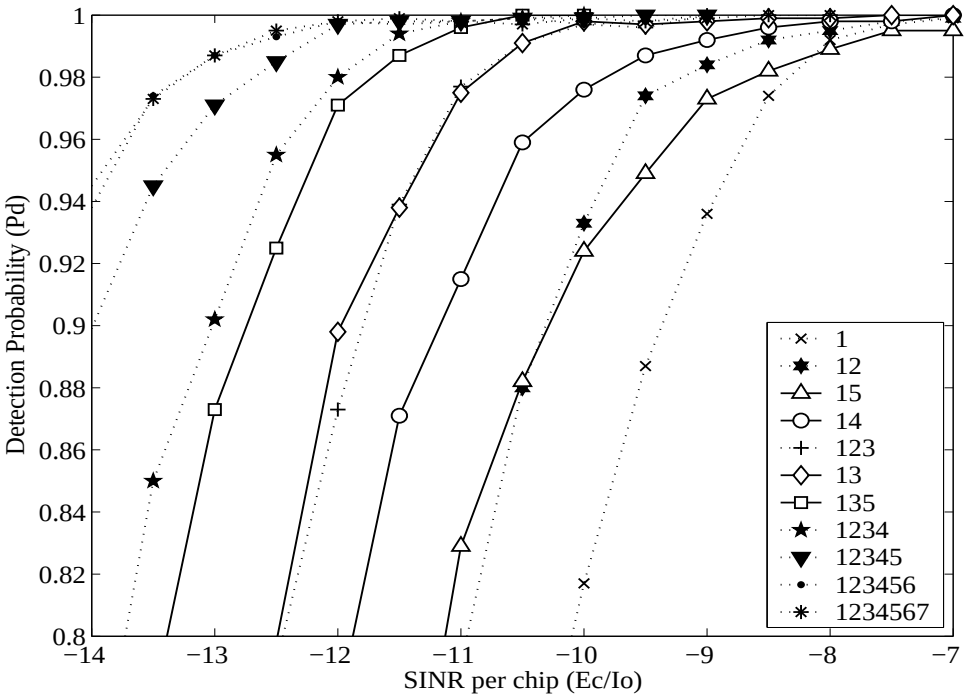

Figure 6.3: Correct detection probability versus SINR per chip of the acquisition schemes employing different GPs and $R = 1$, when considering $N_I = 1024$ and using the schematic of Figure 5.11 and Table 6.1.

Figure 6.3 illustrates the P_D versus E_c/I_0 performance of the various combined GPs, when considering $N_I = 1024$. Observe in Figure 6.3, that the E_c/I_0 gain achieved by the GP combination of **13** is slightly higher than that of **123**. Furthermore, as seen in Figure 6.3, the gain achieved by the GPs **135** is also better than that of **123**. These findings suggest that using consecutive GP orders - as in the **1234** scheme - degrades the

efficiency of MP algorithm. This trend suggests that the degree of correlation among the P-C constraints may be decreased by using appropriately chosen GPs, such as **13** and **135**. In contrast, employing $g_1(D) = D^{15} + D + 1$ and $g_5(D) = D^{240} + D^{16} + 1$ results in a degraded performance, because the number of P-C connections between the VNs and CNs is decreased by a factor of $(2^{n-1} \cdot S)$, n = 1,2,...,7, when the order of the GP is increased. Finally, based on Figure 6.3 the acquisition scheme based on the GPs **135** becomes our favourite choice for the $R = 1$ scenario, which is a benefit of the improved P_D performance in comparison to other GP combinations.

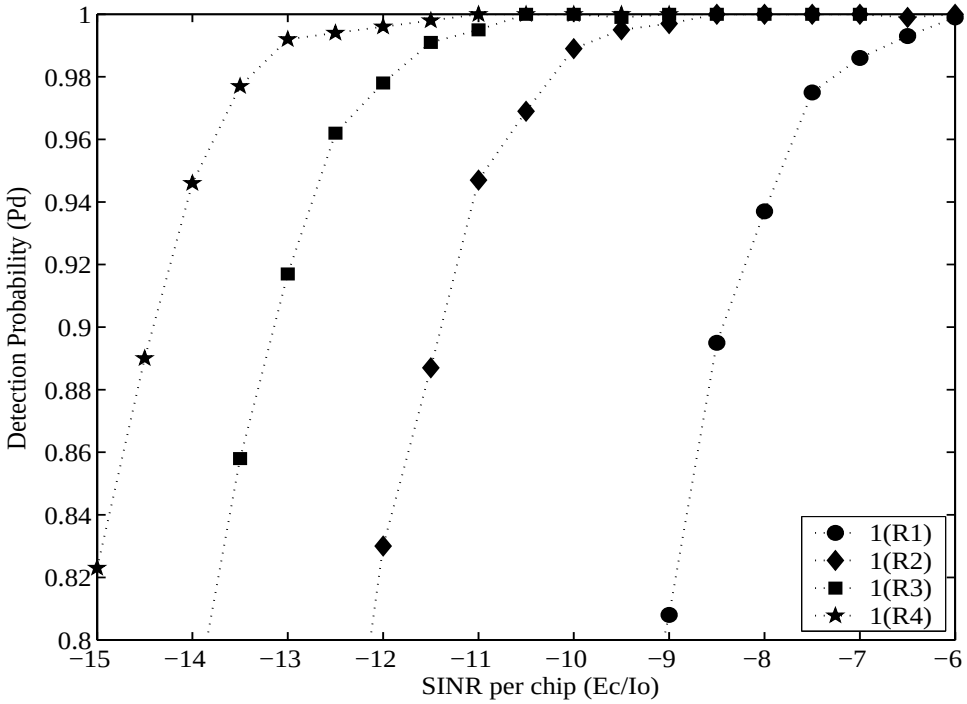

Figure 6.4: Correct detection probability versus SINR per chip of the acquisition schemes employing a PP and R = 1,2,3 and 4, when considering $N_I = 512$ and using the schematic of Figure 5.11 and Table 6.1.

Figure 6.4 characterises the P_D versus E_c/I_0 performance of a PP aided decoder, parameterised with $N_I = 512$ as well as R = 1,2,3 and 4. In comparison to the performance of the GP **1** in Figure 6.3, the P_D performance of the receiver having $R = 1$ antenna is 1dB worse than that of $N_I = 1024$. However, the attainable P_D performance was improved by up to 6 dB for $R = 4$ antennas. Furthermore, based on performance gains recorded for the longer sequence, as described in Figure 6 of [43], further increasing the sequence length no longer achieves further substantial performance gain. Hence the employment of multiple receive antennas is essential for achieving a high performance, when using relatively short

sequences. Figures 6.5 and 6.6 explicitly show the P_D versus E_c/I_0 performance of the

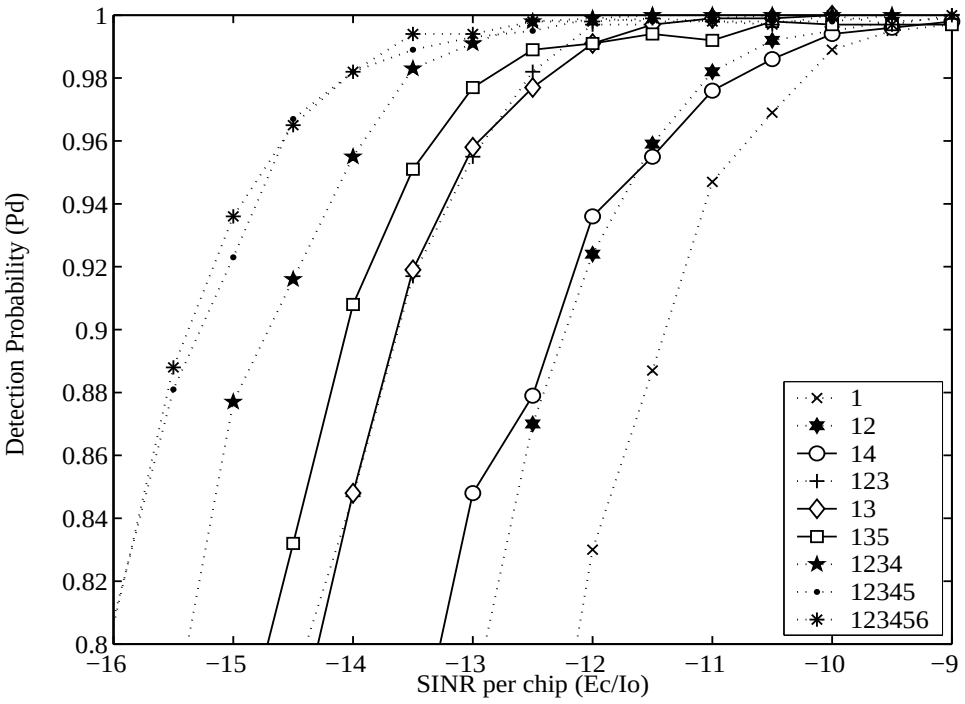

Figure 6.5: Correct detection probability versus SINR per chip of the acquisition schemes employing different GPs and $R = 2$, when considering $N_I = 512$ and using the schematic of Figure 5.11 and Table 6.1.

acquisition schemes using different GPs and $R = 2$ and 4, respectively, when considering $N_I = 512$. When using beneficially chosen GPs such as **13**, an approximately 2.2 dB gain was obtained compared to that of using GP **1**. Accordingly, the employment of both multiple receive antennas and beneficially chosen GPs leads to a combined gain of about 8.2 dB, when employing $R = 4$. During the initial acquisition procedure, the receiver is capable of maintaining a reliable operation, provided that finger-locking was achieved. This suggests the achievable DS-UWB coverage extended by the proposed scheme.

In Figure 6.7, the P_D versus E_c/I_0 performance was recorded for the single-component schemes **13**, **135**, **123** and **1234**, as well as for the multiple-component decoders **13:135** and **1:13:135**, where the value in **( )** represents the maximum affordable number of iterations. Explicitly, **13:135(3:12)** represents a multiple-component decoder, which activates the acquisition schemes using the GPs **13** and **135** for a maximum of three and 12 iterations, respectively. More specifically, the scheme employing the GPs **13** is activated up to three times and, then the decoder exploiting the GPs **135** is enabled for up to 12 iterations. When considering the multi-path components delayed with respect to the LOS components, their

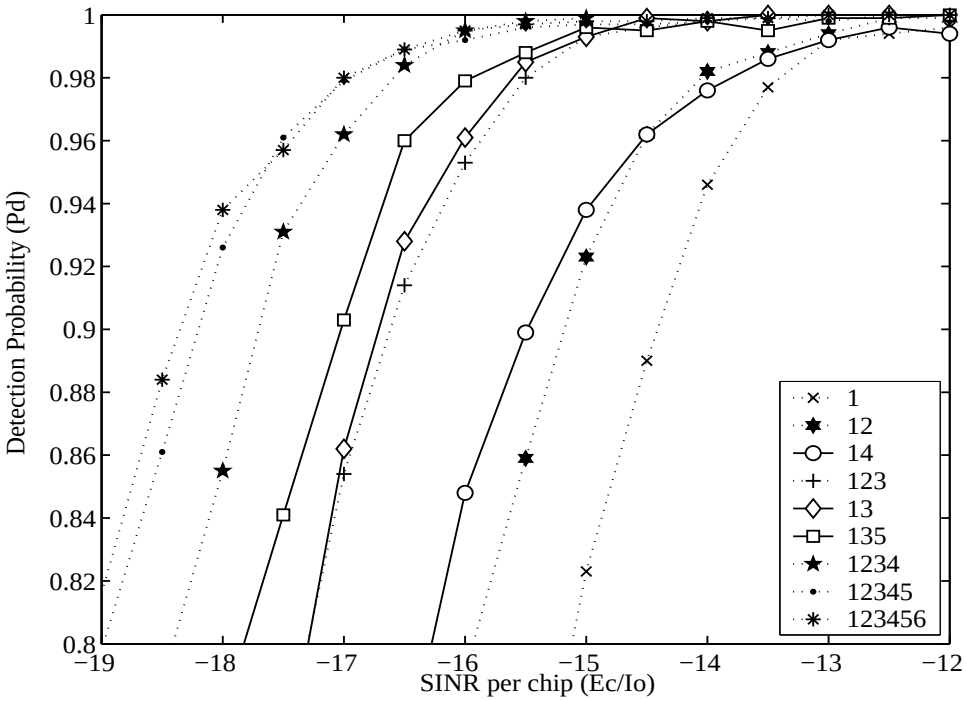

Figure 6.6: Correct detection probability versus SINR per chip of the acquisition schemes employing different GPs and $R = 4$, when considering $N_I = 512$ and using the schematic of Figure 5.11 and Table 6.1.

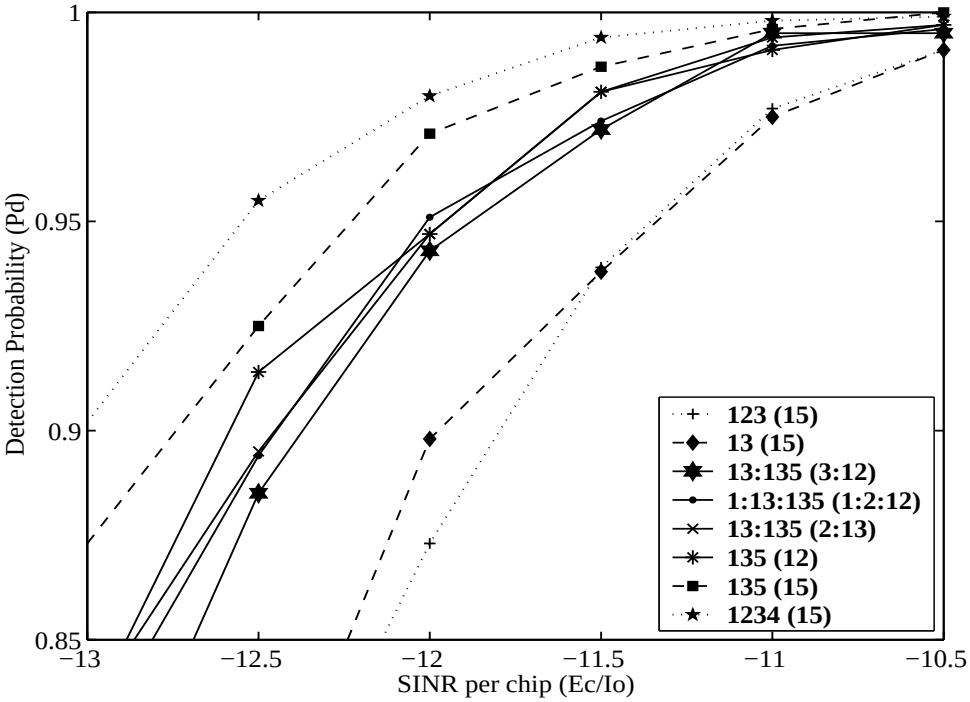

Figure 6.7: Correct detection probability versus SINR per chip of multiple component decoders using the schematic of Figure 5.12 and Table 6.1.

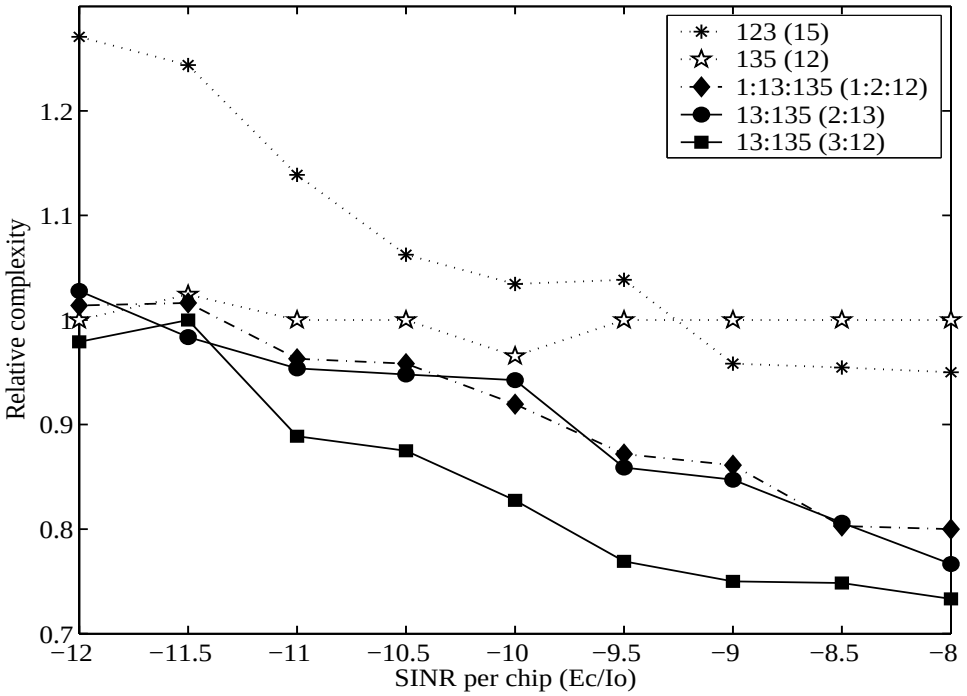

Figure 6.8: Relative complexity versus SINR per chip, when using the schematic of Figure 5.12 and Table 6.1.

E_c/I_0 values are typically at least 3dB lower. Furthermore, some of the strongest LOS or NLOS paths may have a 3 to 6dB higher signal strength than the remaining paths. We considered the initial acquisition scenario, where only the timing of the strongest LOS or NLOS paths must be acquired, but not those of the further delayed ones. Hence, it is reasonable to assume that the minimum E_c/I_0 value required for finger-locking in the initial acquisition is set to -12dB, where we have $P_D \cong 0.94$ [59]. Figure 6.7 suggests that the single-component decoder denoted as **135(12)** and three of the multiple-component decoders have a similar P_D performance. Hence we opted for using that particular decoder, which imposes the lowest complexity. Figure 6.8 portrays the relative complexity versus E_c/I_0 relationship for the two single- and three multiple-component decoders. The complexity was defined as the average number of iterations multiplied by the number of messages exchanged by the MP algorithm. The relative complexity curves of Figure 6.8 were generated by evaluating and plotting the complexity ratio, where the relative complexities of the five different types of decoders were normalised by the complexity of the **135(15)** scheme. Observe in Figure 6.8 that the **135(12)** scheme exhibits a near-constant complexity, regardless of the E_c/I_0 value. Among the three multiple-component decoders the **13:135(3:12)** arrangement imposes the lowest complexity, indicating a complexity reduction of up to 30 % around E_c/I_0 = -6dB.

Accordingly, we can strike an attractive trade-off between the best achievable performance and the affordable complexity.

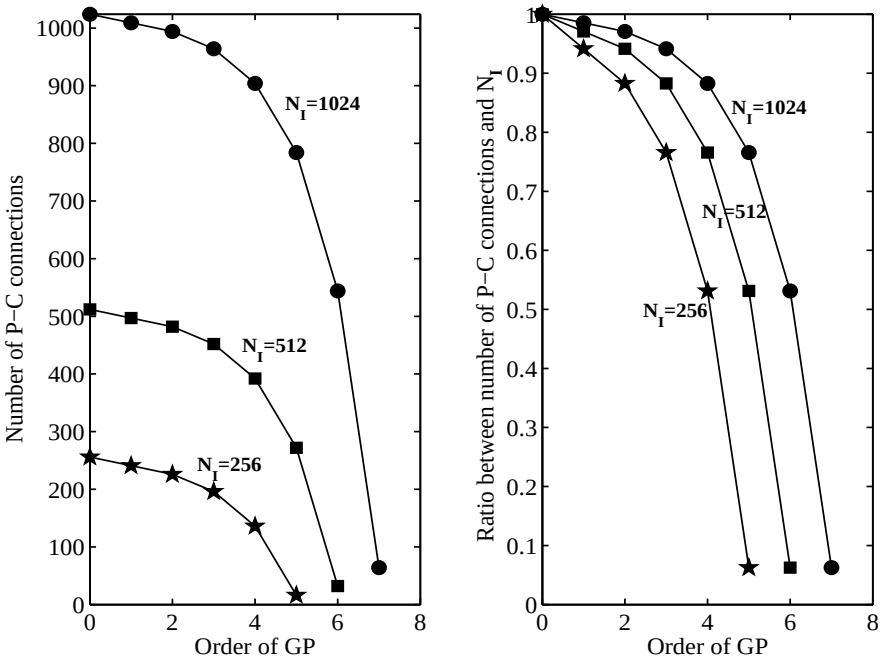

Figure 6.9: Relationship between the number of P-C connections as well as the order of GP relying on $N_I = 256$, 512 and 1024, respectively

The left-hand illustration of Figure 6.9 portrays the relationship between the number of P-C connections in the PCM as well as the order of the GP corresponding to $N_I = 256$, 512 and 1024, respectively. By contrast, the illustration at the right of Figure 6.9 explicitly shows the number of P-C connections normalised by N_I and recorded for the three different lengths of $N_I = 256$, 512 and 1024, respectively. Similarly to Figure 6.9, Table 6.2 also characterises the relationship between the number of P-C connections in the PCM and the order of the GP, where N_1 represents the number of P-C connections in the PCM when considering $N_I = 1024$, whilst N_2 is the number of P-C connections when considering $N_I = 512$. It is clearly shown in Figure 6.9 and Table 6.2 that the number of P-C connections between the VNs and CNs is decreased by a factor of $(2^{n-1} \cdot S)$, $n = 1,2,...$ when the GP order is increased. As an example, in the combined GPs of **135** designed for $N_I = 1024$ the number of P-C connections for 3^{rd} order GP becomes 964, which is 94.14 % of $N_I = 1024$, whereas in case of **13** invoked for $N_I = 512$ this becomes 452, which is 88.22 % of $N_I = 512$. The best possible E_c/I_0 gain can be obtained, when having a sufficiently high number of P-C connections. Furthermore, when combining several GPs, we observed

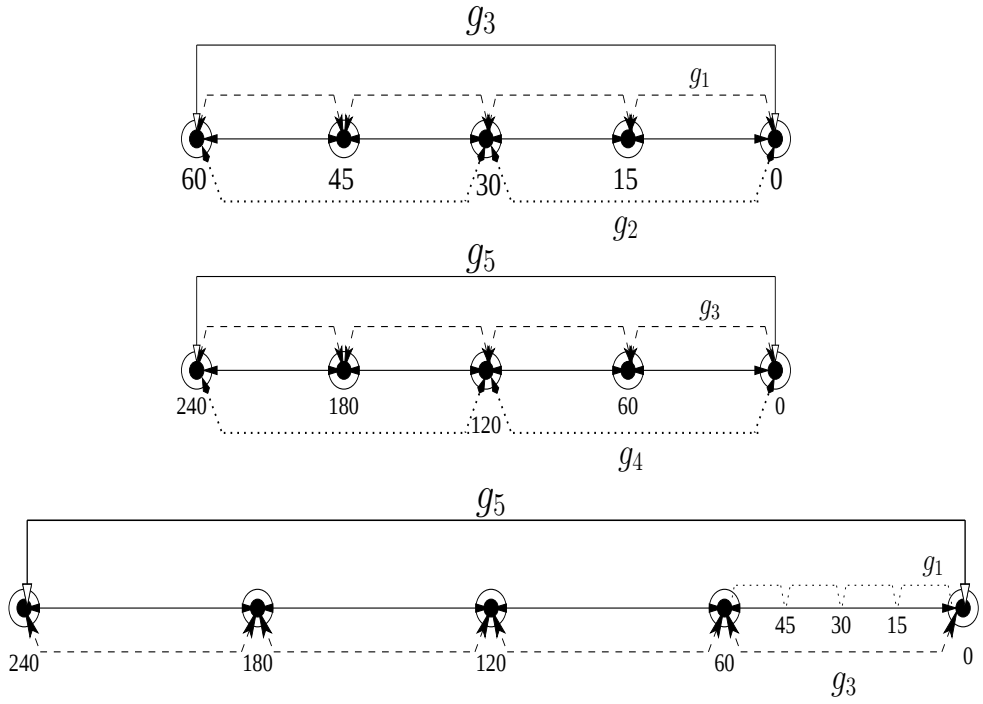

Figure 6.10: Description of a region of massage passing corresponding to each GP

Table 6.2: Relationship between the number of P-C connections and the order of GP corresponding to Figure 6.9

GP Order	**0**	**1**	**2**	**3**
Num. of Co.	N_I	$N_I - S$	$N_I - 2S$	$N_I - 4S$
N_1	1024	1009	994	964
N_1/N_I	1	0.9854	0.9707	0.9414
N_2	512	497	482	452
N_2/N_I	1	0.9707	0.9414	0.8828
GP Order	**4**	**5**	**6**	**7**
Num. of Co.	$N_I - 8S$	$N_I - 16S$	$N_I - 32S$	$N_I - 64S$
N_1	904	784	544	64
N_1/N_I	0.8828	0.7656	0.5313	0.0625
N_2	392	272	32	
N_2/N_I	0.7656	0.5313	0.0625	

another dominant factor affecting the achievable performance. It is worth observing the MP scheme of Figure 6.10 corresponding to each GP, characterising the specific relationships among the GPs employed, where the GPs are $g_1(D) = D^{15}+D+1$, $g_2(D) = D^{30}+D^2+1$, $g_3(D) = D^{60}+D^4+1$, $g_4(D) = D^{120}+D^8+1$ and $g_5(D) = D^{240}+D^{16}+1$. For instance, when replacing $g_1(D)$ by $g_2(D)$ in the top trace of Figure 6.10, the corresponding P-C region in the PCM is increased by a factor of two, but $g_2(D)$ does not contribute independent P-Cs in addition to those of $g_1(D)$ in the specific region of the PCM, where they overlap. In contrast, when employing appropriately selected GPs, such as the GP combination of **13**, there is a twice larger region in the PCM compared to a case of **12**, as described in the bottom trace of Figure 6.10. Hence, it is surmised that the detrimental effects of having correlated P-Cs may be considerably reduced. This trend clearly suggests that the degree of correlation among the P-C constraints is decreased, when exploiting beneficially chosen GPs such as **135**. According to the results of Figures 6.1, 6.2, 6.3, 6.5, 6.6, 6.9 and 6.10 as well as Table 6.2, both the combined GPs of **13** and **135** constitute an attractive tradeoff between the detrimental effect of imposing correlation associated with the P-C regions in the PCM and having a sufficiently high number of P-C connections for attaining the best achievable P_D as well as MAT performance. Hence, for the sake of achieving the best possible P_D performance, the employment of beneficially selected non-consecutive-order GPs is recommended.

Figures 6.11 and 6.12 illustrate the correct detection versus false alarm probability, parameterised by both the number of receive antennas for $R = 1$ as well as 4 and the E_c/I_0 value, when considering $N_S = 512$. The specific value of E_c/I_0 is indicated in the parenthesis next to the number of receive antennas such as $R1$ and $R4$ at the bottom right-hand corner in both Figures 6.11 and 6.12. The three curves in Figure 6.11 were generated by using Equations 5.29 and 5.30, whilst the other three curves seen in Figure 6.12 were generated from Equations 5.31 and 5.32. The reliable operational range of the associated single-dwell based schemes associated with the best possible MAT performance is around a false alarm probability of 10^{-4}, because a false alarm is expected to increase the MAT proportionately to the corresponding false locking penalty factor. In case of E_c/I_0 = -10dB, the $R1$ scenario becomes capable of achieving a reliable performance, whilst the $R4$ requires E_c/I_0 = -15dB. Furthermore, when considering the random search technique of Section 5.6.2 for our benchmarker and for the TA stage of our proposed scheme, a pair of P_D and P_F values generated employing Equations 5.29, 5.30, 5.31 and 5.32 was used for calculating the achievable MAT performance seen in Figures 6.11 and 6.12, since these values allowed us to minimise the

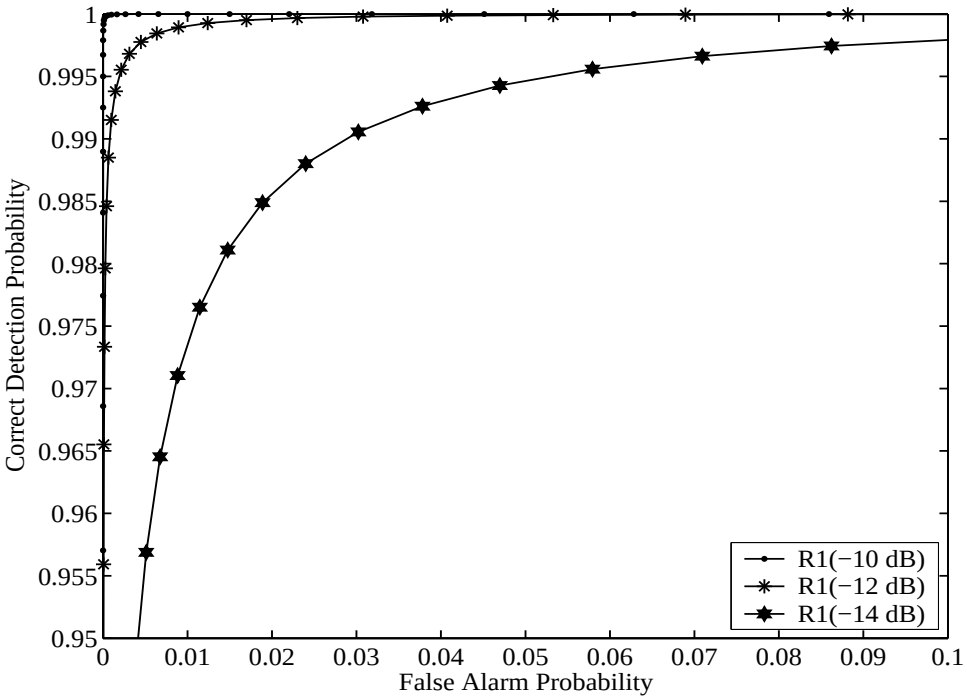

Figure 6.11: Correct detection versus false alarm probability for $R = 1$, when considering $N_S = 512$ and employing Table 6.1.

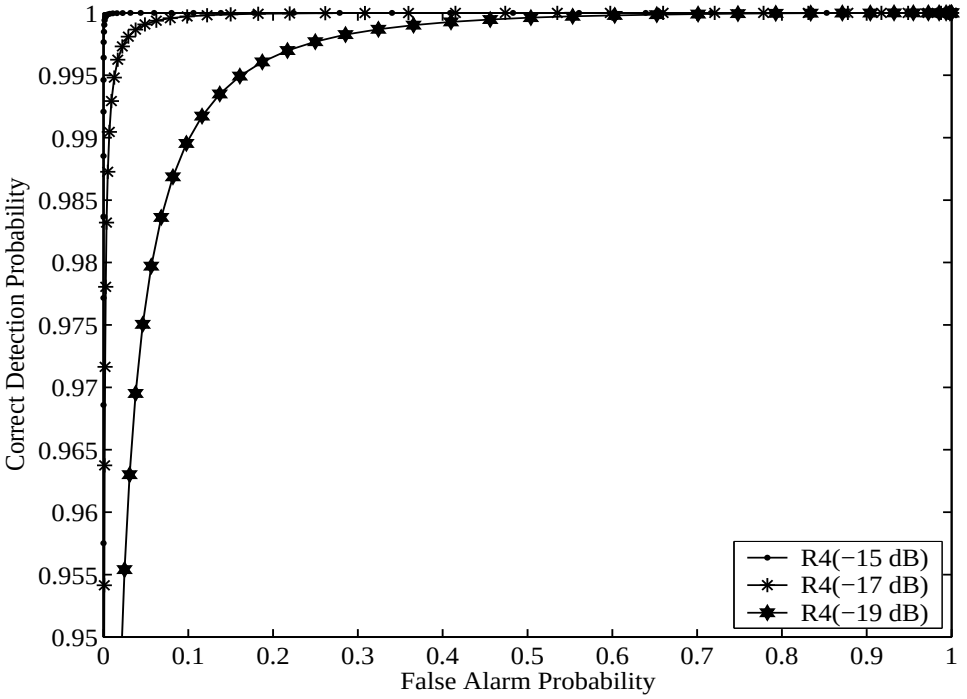

Figure 6.12: Correct detection versus false alarm probability for $R = 4$, when considering $N_S = 512$ and using Table 6.1.

MAT.

6.3.2 Mean Acquisition Time Performance

Table 6.3: MAT performances of four different schemes considered at $E_c/I_0 = -10$ DB

Schemes	(A) SS-SDSS	(B) TS-SDSS	(C) SS-IA	(D) TS-IA
MAT (T_f)	$1.68 * 10^9$	$1.7 * 10^7$	$8.69 * 10^5$	$2.1 * 10^5$

In Table 6.3 the achievable MAT performance of the four different schemes of Section 5.6.1 is characterised at $E_c/I_0 = -10$ dB. Figure 6.13 further illustrates the achievable MAT gain at $E_c/I_0 = -10$ dB, where the MAT values of the four different scenarios attained in a single-path environment were normalised by the MAT of the SS-SDSS scheme in Section 5.6.1. Observe in Figure 6.13 that the MAT performance of TS-SDSS scheme in Section 5.6.1 is about two orders of magnitude better than that of the SS-SDSS scheme. Furthermore, when considering our proposed TS-IA scheme, an almost four order of MAT improvement may be achieved compared to that of the SS-SDSS arrangement. The TS-IA scheme also exhibits an MAT reduction of up to 76 % at $E_c/I_0 = -10$ dB against that of the SS-IA scheme.

Figures 6.14 and 6.15 elucidate the achievable MAT versus SINR per chip performance of the TS-IA scheme employing beneficially chosen GPs for the $R = 1$ and 4 scenarios, respectively. Observe in both Figures 6.14 and 6.15 that the MAT performance of our proposed TS-IA scheme recorded in the multi-path scenario described in Section 5.6.2 is up to 6200 times better than that of the SS-RS scheme. This suggests that more than three orders of magnitude MAT improvements may be achieved compared to the MAT of the SS-RS arrangement. The MAT performance of the CPA stage is up to about four as well as seven times better than that of the TA stage for the $R = 1$ and 4 scenarios, respectively, because a reliable but hence time-consuming verification test was used during the TA stage. By contrast, during the CPA stage only correct code phase estimation was required. The proposed scheme was shown to be capable of achieving an acceptable MAT performance at the minimum E_c/I_0 value required for reliable finger-locking in both the $R = 1$ and 4 scenarios, as evidenced by results of both Figures 6.14 and 6.15 [2].

[2]We also briefly allude to the MAT performance comparison of our TS-IA and SS-IA schemes. Based on Sections 5.6.2 and 6.2, when considering the achievable MAT performance at the minimum E_c/I_0 value required for reliable finger-locking, the approximate MAT formula of the most optimistic scenario based on both $P_D = 1$ and $P_F = 0$, may become $(4.3333T_M + T_D)$, where the uncertainty region $\nu|_{SS-IA}$ becomes (160/15) and the simple derivation of the MAT formula may be based on $\nu|_{SS-IA}/2$ [43]. The TS-IA scheme exhibits an MAT reduction of around 80% at E_c/I_0 = -12 and -15 dB corresponding to the $R = 1$ and 4

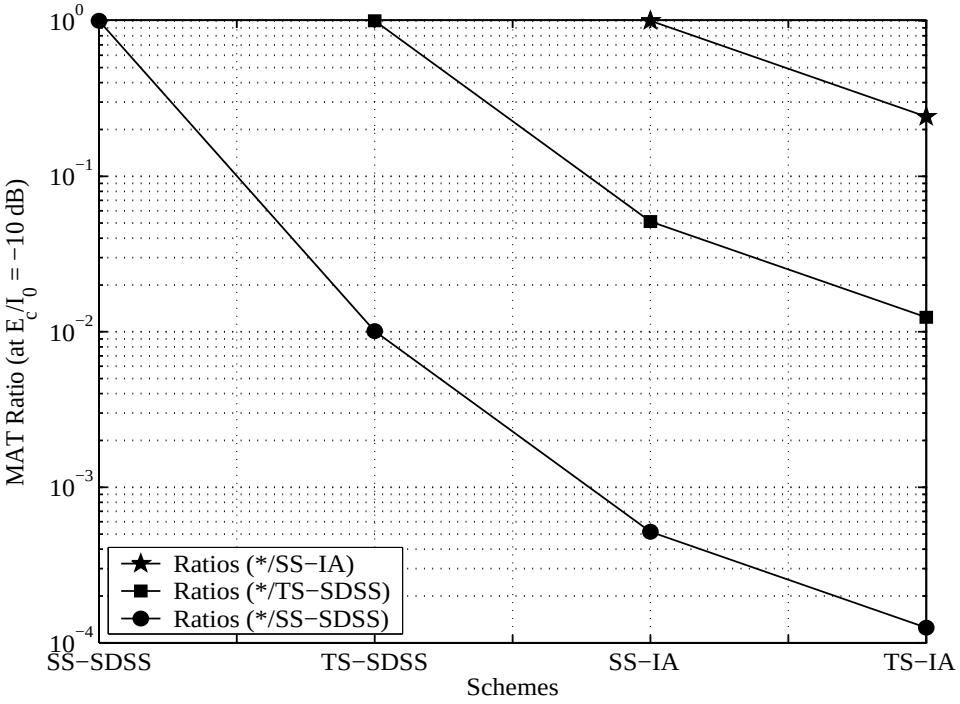

Figure 6.13: MAT ratios of the schemes considered at $E_c/I_0 = -10dB$ using the schematic of Figures 5.11 and 5.17 as well as Table 6.1.

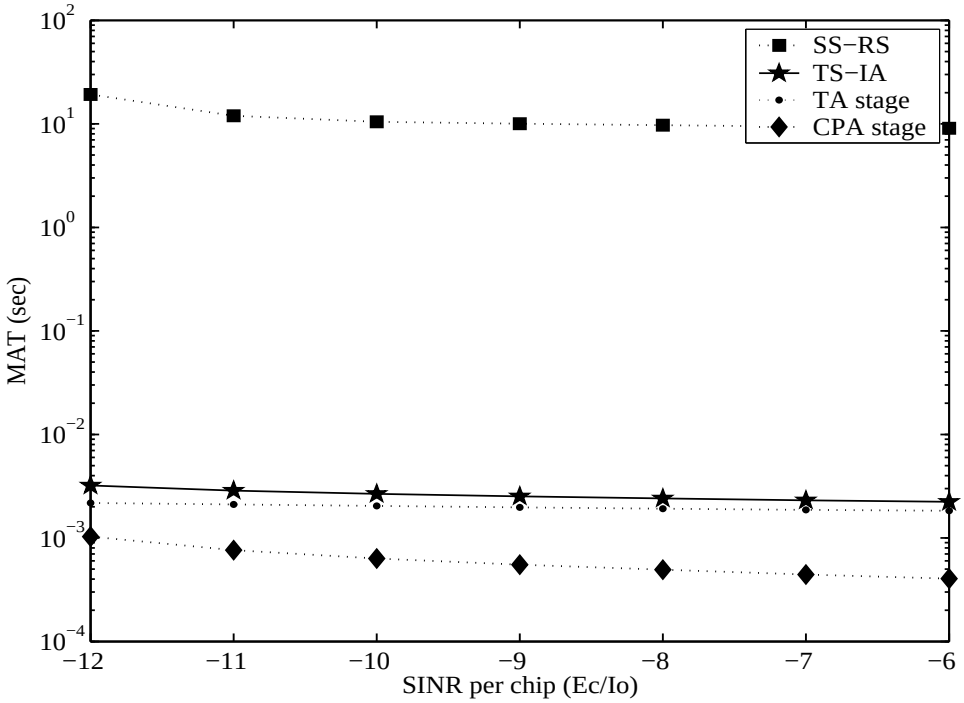

Figure 6.14: MAT versus SINR per chip performance of the two stage scheme employing beneficially chosen GPs and $R = 1$, when considering $N_I = 1024$ and employing the schematic of Figure 5.17 and Table 6.1.

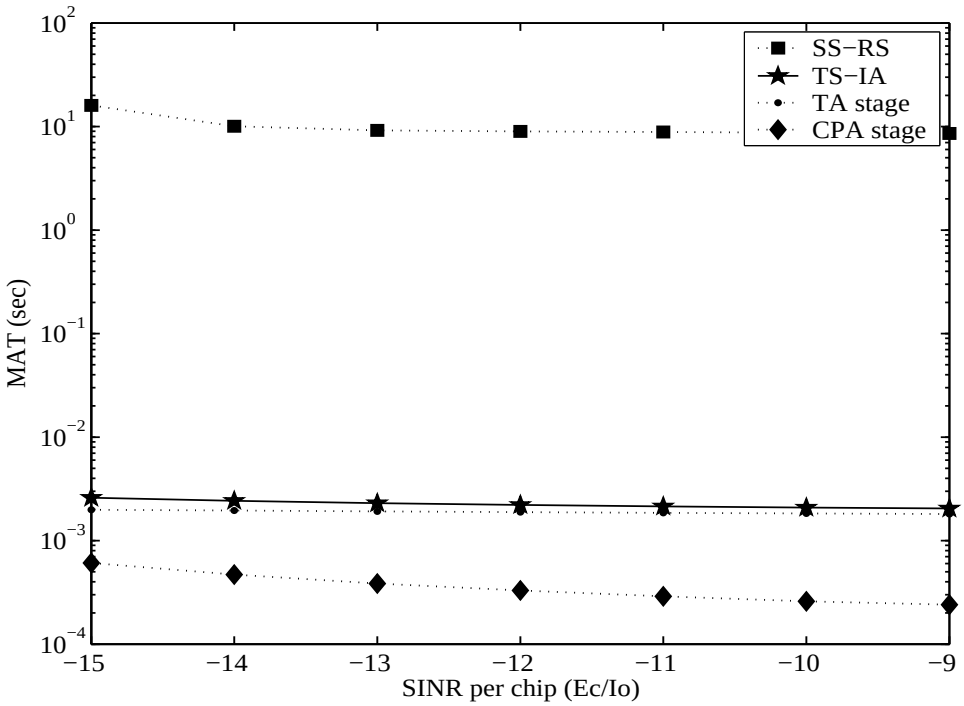

Figure 6.15: MAT versus SINR per chip performance of the two stage scheme employing beneficially chosen GPs and $R = 4$, when considering $N_I = 512$ and employing the schematic of Figure 5.17 and Table 6.1.

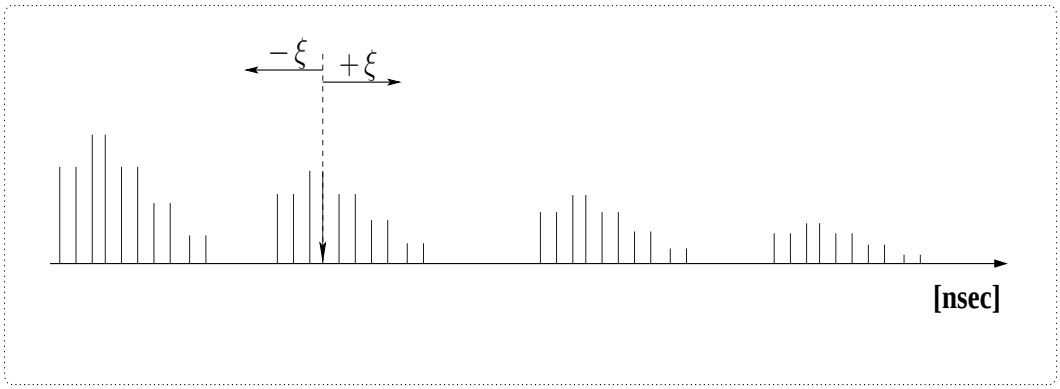

Figure 6.16: An example of the post-initial timing acquisition in DS-UWB downlink

In the DS-UWB DL, the main goal of the initial acquisition is to acquire a coarse timing of any received signal path impinging at the receiver, because the DS-UWB channel exhibits a number of multi-path components. The initial acquisition is required for both coarse timing as well as for code phase alignment, since this timing information is used as that of the reference finger in the Rake receiver. However, achieving accurate timing and code phase alignment constitute a challenging problem owing to the extremely short chip-duration [42, 43].

This leads to a huge search space represented as the product of two factors, namely that of the number of legitimate code phases in the uncertainty region of the PN code and the number of legitimate signalling pulse positions. This renders the problem of initial acquisition critical. By contrast, the post-initial acquisition procedure that extracts the accurate timing positions of the remaining delayed paths and identifies the appropriate paths earmarked for processing by the MRC scheme of the Rake receiver has a major impact on the performance of the Rake receiver [8]. There is a main difference between the initial and post-initial acquisition procedures. Once the first Rake finger is synchronised, the uncertainty region that has to be explored will be shrunk to $\pm\xi$ number of hypotheses surrounding the specific time-instant, where the received path was found. This reduced interval will be referred to as the 'reduced uncertainty region', which will have to be explored after the initial acquisition phase [7]. This search window width is also influenced by the dispersion of the multipath propagation environment encountered. Figure 6.16 portrays the post-initial timing acquisition scenario of the DS-UWB DL, assuming that the timing of the received path was already acquired. The scenario portrayed in Figure 6.16 is based on Figure 5.1, which describes the S-V UWB channel model. To elaborate a little further, Figure 6.16 encompasses four clusters, where each cluster has 10 resolvable multi-path components.

Figures 6.17 and 6.18 characterise the achievable MAT versus SINR per chip performance of the post-initial acquisition scheme for the SS-RS scenario of Section 5.62 having $R = 1$ and 4, respectively. The MAT performances recorded in Figures 6.17 and 6.18 for $R = 1$ and 4 used $N = 256$ and 384. The employment of $N = 256$ is capable of satisfying the reliable operation in the range of finger locking.

scenarios, respectively, in comparison to that of the SS-IA scheme.

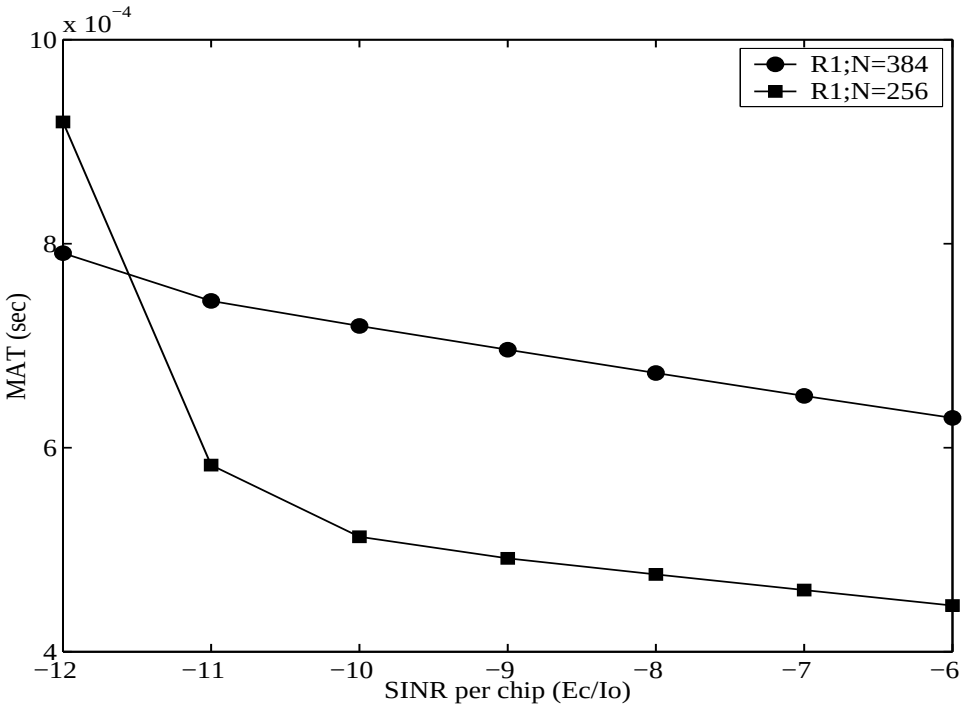

Figure 6.17: MAT versus SINR per chip performance of the post-initial acquisition scheme for SS-RS having $R = 1$ scenario and using Table 6.1.

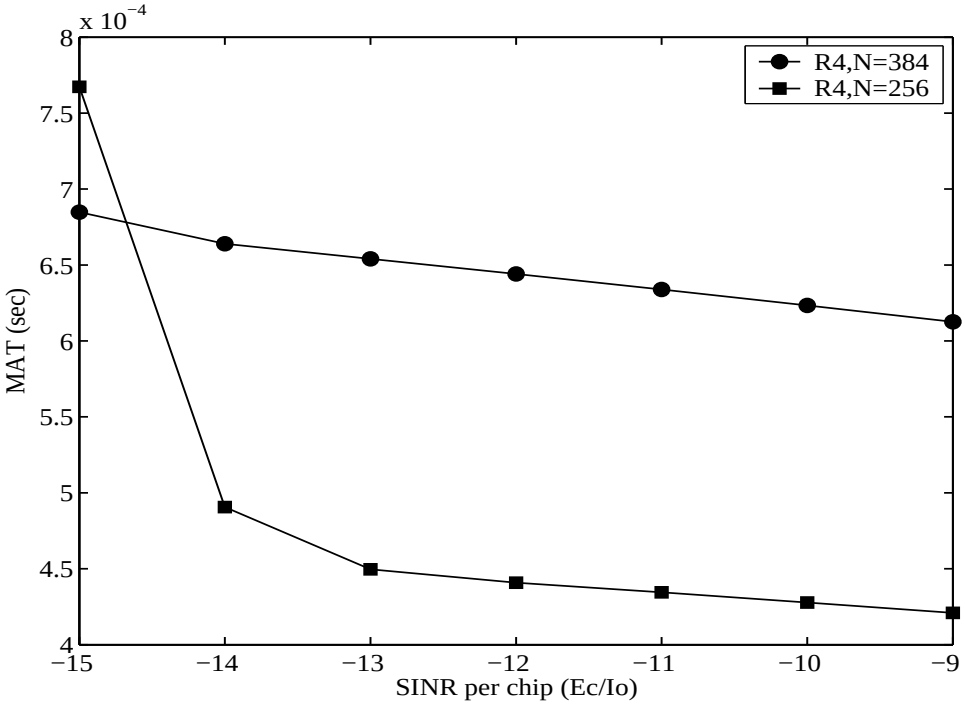

Figure 6.18: MAT versus SINR per chip performance of the post-initial acquisition scheme for SS-RS having $R = 4$ scenario and using Table 6.1.

6.4 Chapter Summary and Conclusions

In this chapter, we have analysed the performance of our proposed iterative acquisition schemes in Figures 5.11, 5.12 and 5.17 of Section 5.4 in the co-located SIMO DS-UWB DL. Our system parameters were provided in Section 6.2, followed by the analysis of the correct detection versus SINR per chip performance of the iterative acquisition schemes employing both single and multiple component decoder(s) in Section 6.3.1. This was followed in Section 6.3.1 by a discussion of the message passing used in our proposed scheme. We also analysed the correct detection probability versus false alarm probability performance of the random search based scheme of Figures 6.11 and 6.12 in Section 6.3.1. Furthermore, we investigated the MAT performance of both the initial and post-initial acquisition schemes in Figures 6.13, 6.14, 6.15, 6.17 and 6.18 in the co-located SIMO DS-UWB DL in Section 6.3.2.

In order to highlight the main benefits of the proposed iterative acquisition schemes, the most salient results are emphasised again in Figures 6.19 and 6.20. More specifically,

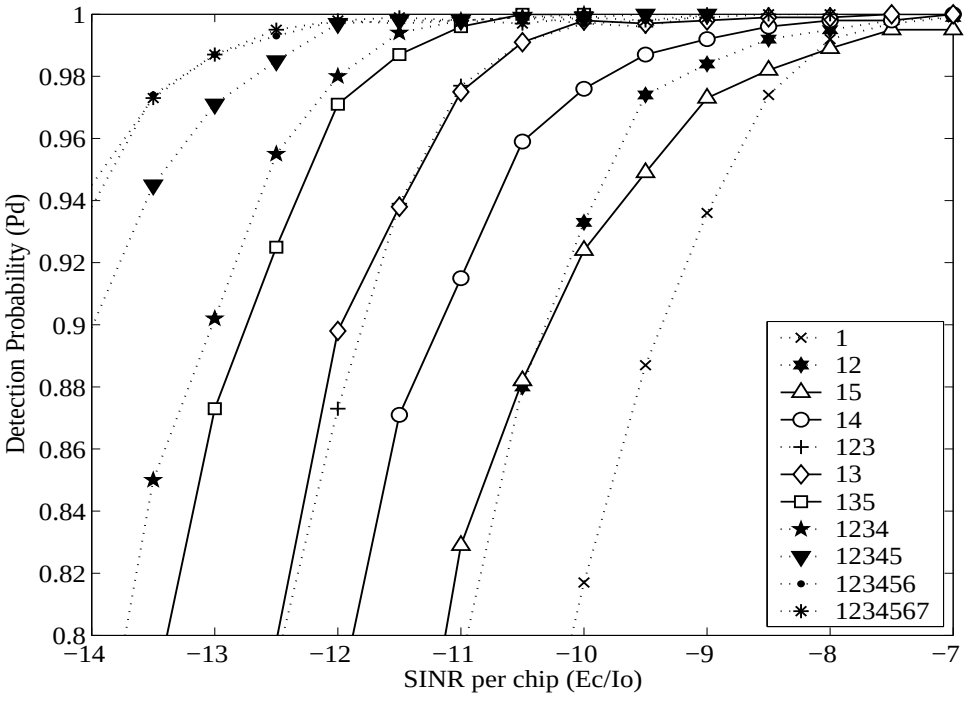

Figure 6.19: Correct detection probability versus SINR per chip of the acquisition schemes employing different GPs and $R = 1$, when considering $N_I = 1024$ and using the schematic of Figure 5.11 and Table 6.1.

Figure 6.19 illustrates the P_D versus E_c/I_0 performance of the various combined GPs, when considering $N_I = 1024$. Observe in Figure 6.19, that the E_c/I_0 gain achieved by

the GP combination of **13** is slightly higher than that of **123**. Furthermore, as seen in Figure 6.19, the gain achieved by the GPs **135** is better than that of **123**. These findings suggest that using consecutive GP orders - as in the **1234** scheme - degrades the efficiency of the MP algorithm. This trend suggests that the degree of correlation among the P-C constraints may be decreased by using appropriately chosen GPs, such as **13** and **135**. In contrast, employing $g_1(D) = D^{15}+D+1$ and $g_5(D) = D^{240}+D^{16}+1$ results in a degraded performance, because the number of P-C connections between the VNs and CNs is decreased by a factor of $(2^{n-1}\cdot S)$, n = 1,2,...,7, when the order of the GP is increased. Finally, based on Figure 6.19 the acquisition scheme using the GPs **135** becomes our favourite choice for the $R = 1$ scenario, which is a benefit of its improved P_D performance in comparison to other GP combinations.

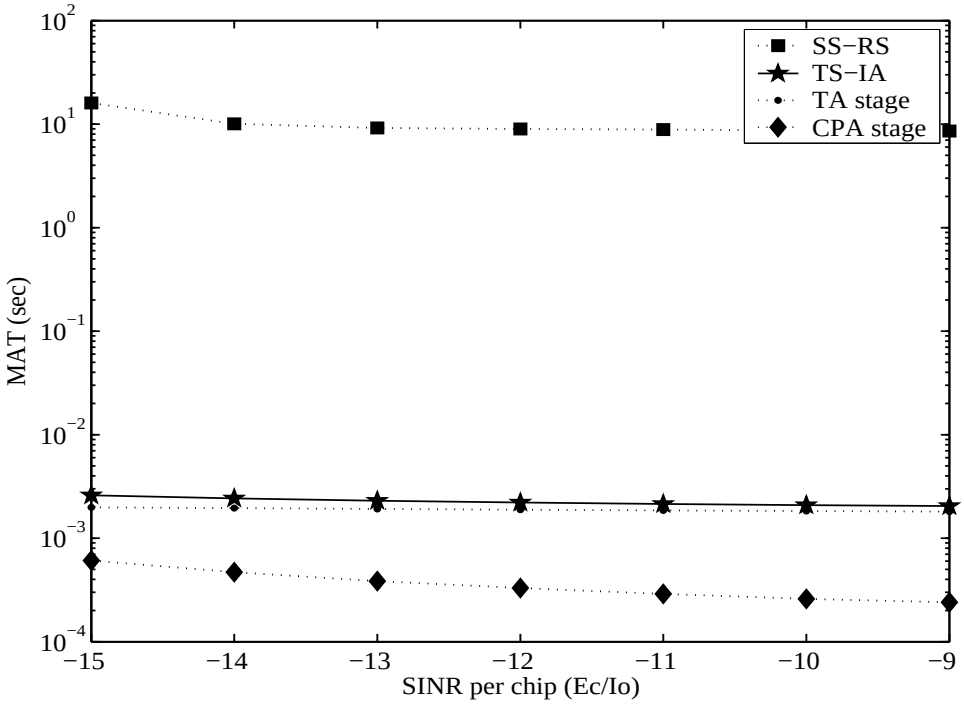

Figure 6.20: MAT versus SINR per chip performance of the two stage scheme employing beneficially chosen GPs and $R = 4$, when considering $N_I = 512$ and employing the schematic of Figure 5.17 and Table 6.1.

Figure 6.20 elucidates the achievable MAT versus SINR per chip performance of the TS-IA scheme employing beneficially chosen GPs for the $R = 4$ scenario. Observe in Figure 6.20 that the MAT performance of our proposed TS-IA scheme is up to about 6200 times better than that of the SS-RS scheme. This suggests that more than three orders of magnitude MAT improvements may be achieved compared to the MAT of the SS-RS arrangement. The MAT performance of the CPA stage is up to about seven times better than that of the

TA stage for the $R = 4$ scenario, because a reliable but hence time-consuming verification test was used during the TA stage. By contrast, during the CPA stage only correct code phase estimation was required. The proposed scheme was shown to be capable of achieving an acceptable MAT performance at the minimum E_c/I_0 value required for reliable finger-locking in the $R = 4$ scenario, as evidenced by results of Figure 6.20.

The benefits of the iterative code acquisition schemes were analysed in terms of their achievable P_D and MAT performances. With the aid of the Tanner graph based structure of MP seen in Figures 5.7 and 5.8 in Section 5.3.5, we found that in order to achieve the best possible P_D performance, the employment of beneficially selected non-consecutive-order GPs is recommended, as evidenced by Figures 6.1, 6.2, 6.3, 6.5 and 6.6. We also found that the employment of multiple receive antennas was essential for achieving a high target performance, when acquiring the correct timing of the entire sequence by using a relatively short segment of the sequence, as evidenced by Figures 6.4, 6.5 and 6.6. Moreover, the employment of appropriately selected multiple-component decoders leads to the lowest possible complexity, as characterised in Figures 6.7 and 6.8. Finally, it was explicitly shown in Figures 6.13, 6.14 and 6.15 that our proposed TS-IA scheme is capable of reducing the MAT by at least three orders of magnitude compared to the benchmark scenario considered. This benefit facilitates its employment in a variety of applications associated with long PN codes.

Chapter 7

Summary and Future Research

7.1 Summary

In the thesis we analysed the performance of serial search based code acquisition in the co-located and cooperative MIMO aided SC- and MC-DS-CDMA DL. We also characterised the performance of iterative code acquisition in the co-located MIMO aided DS-UWB DL. The summary of each chapter is as follows:

Chapter 1

In this chapter, we have provided a brief overview of a range of code acquisition schemes. We commenced the chapter with a brief classification of the family of the code phase acquisition techniques and a generic structure of searcher and Rake receiver on the mobile station in Section 1.1. Then we contrasted the code acquisition procedures of the DL and UL in Section 1.2. This was followed by a discussion on various search strategies in Section 1.3. The underlying serial search based code acquisition was presented in Section 1.3.1, followed by the parallel search (maximum-likelihood) based code acquisition scheme in Section 1.3.2. Then the set of known sequential estimation based code acquisition schemes were classified into four categories in Section 1.3.3, which includes rapid acquisition using sequential estimation, recursion-aided RASE, majority logic decoding based RASE and recursive soft sequential estimation. Finally, in Section 1.3.4, random search based code acquisition was presented.

We introduced a variety of widely used detector structures in Section 1.4. More specifically, NC code acquisition was highlighted in Section 1.4.1. Specifically, both a chip based-DC detection scheme and a Full-Period Correlation (FPC) based DC detection scheme were highlighted in Section 1.4.2. In Section 1.4.3, the concepts of both single-dwell and multiple-dwell based techniques were presented. The widely-used post-detection integration concept of practical code acquisition receivers was highlighted in Section 1.4.4. In Section 1.5, we have briefly summarised the characteristics of various code acquisition schemes designed for Multi-Carrier DS-CDMA systems. Then, code acquisition schemes designed for the DS-UWB DL have been briefly presented in Section 1.6. We summarised the historic evolution of sequential estimation based code acquisition as well as that of DC acquisition schemes in Tables 1.1 and 1.2, respectively. Section 1.7 has briefly summarised Sections 1.1 to 1.6. Then, in Section 1.8 the outline of the thesis was given. Figure 1.14 also classified the outline of the various schemes used in the following chapters. Finally, the novel contributions of the thesis were summarised in Section 1.9.

Chapter 2

In this chapter, we have provided the preliminaries of serial search based code acquisition schemes. Following a brief introduction in Section 2.1, we continued by describing our single- and multi-path channel model, the fading conditions as well as the effects of both spatial and inter-subcarrier fading correlation for our performance analysis provided in Section 2.2. Furthermore, the four most wide-spread MIMO types were briefly summarised in Table 2.1. It was noted that code acquisition schemes specifically designed for scenarios of both SDM and Space-Time Coding MIMOs are considered.

Then the underlying formulae of both the correct detection and false alarm probabilities were derived in Section 2.3 in a co-located MIMO element scenario. The Neyman-Pearson criterion was introduced in Section 2.3.1, followed by the derivation of the decision variable PDFs of a co-located MIMO aided NC code acquisition scheme designed for both the SC-DS-CDMA and MC-DS-CDMA DL, when communicating over a spatially uncorrelated Rayleigh channel in Section 2.3.2 in terms of using both a direct approach and a PDF based one. In Section 2.3.3 the decision variable PDFs of a co-located MIMO aided DC code acquisition scheme used for both the SC-DS-CDMA and MC-DS-CDMA DL, when communicating over a spatially uncorrelated Rayleigh channel were investigated. Finally, the decision variable PDFs of a cooperative MIMO aided NC code acquisition scheme designed for the SC-DS-CDMA DL in Section 2.3.4 in terms of using a PDF based approach were derived. The MAT

analysis of both SDSS and DDSS employed in our code acquisition schemes was provided for both single- and multi-path scenarios in Section 2.4. The specific definition of E_c/I_0 with respect to a DS-CDMA system was introduced and then the in-depth relationship between the E_c/I_0 distribution and the number of users per sector was analysed in Section 2.5. Finally, the chapter's summary and conclusions were provided in Section 2.6.

Chapter 3

In this chapter, we have provided details of the performance analysis of serial search based code acquisition in the co-located MIMO aided SC- and MC-DS-CDMA DL as well as of the cooperative MIMO aided SC-DS-CDMA DL. We commenced the chapter by a brief introduction in Section 3.1, followed by the correct detection versus false alarm probability analysis of serial search based code acquisition employed in the co-located MIMO aided SC-DS-CDMA DL in Section 3.2. This was followed by a discussion of both initial and post-initial acquisition in the serial search based co-located NC MIMO aided SC-DS-CDMA DL in Section 3.3. We analysed the performance of code acquisition in the co-located MIMO aided MC-DS-CDMA DL in Section 3.4. Furthermore, we also investigated the performance of code acquisition in the cooperative NC MIMO assisted SC-DS-CDMA DL in Section 3.5. Finally, the chapter's summary and our conclusions were offered in Section 3.6.

Throughout the above-mentioned sections covering serial search based code acquisition in both the co-located MIMO aided SC- and MC- DS-CDMA DL, ironically, our findings suggest that increasing the number of transmit antennas in a MIMO-aided SC-DS-CDMA system results in combining the low-energy, noise-contaminated signals of the transmit antennas. Furthermore, increasing both the number of transmit antennas and that of the subcarriers in a co-located MIMO-aided MC-DS-CDMA system also results in combining the low-energy, noise-contaminated signals of both the transmit antennas and the subcarriers. This fact ultimately reduces the correct detection probability, and accordingly increases the MAT by an order of magnitude, when the SINR is relatively low. However, it is extremely undesirable to degrade the achievable acquisition performance, when the system is capable of attaining its target bit error rate performance at reduced SINR values. This phenomenon also has a detrimental effect on the performance of Rake receiver based synchronisation, when the perfectly synchronised system is capable of attaining its target bit error rate performance at reduced SINR values, as a benefit of employing multiple transmit antennas and/or frequency diversity. Hence it may be concluded that the achievable cell

coverage determined by the received pilot channel power may be reduced, as the number of transmit antennas is increased, which is a highly undesirable phenomenon, since it has grave repercussions in terms of having to tolerate a high number of handovers per cell. Based on the above-mentioned results justified by information theoretic considerations, our acquisition design guidelines are applicable to diverse co-located NC MIMO aided scenarios.

In contrast to the detrimental effects of sharing the total transmit power across multiple transmit antennas in the co-located and cooperative MIMO based scenarios in Sections 3.2 to 3.4, our findings suggest that employing distributed MIMO elements acting as RSs combined with multiple receive antennas leads to an improved MAT performance. However, these gains are only achievable, if the RSs can afford to contribute toward supplying the extra power used in the 'increased-power-scenario' of Section 3.5. By contrast, when having a high link imbalance, only marginal MAT performance gains may be achieved, regardless whether single-path or multi-path propagation scenarios are considered. Therefore, in order to efficiently exploit the diversity benefits of RS-aided transmissions, the employment of at least two RSs might be recommended. When additionally invoking multiple co-located receive antennas at the MS, further diversity gains may be achieved.

Chapter 4

In this chapter, we have provided a detailed performance analysis of both DC and NC serial search based code acquisition in the co-located MIMO aided both SC- and MC- DS-CDMA DL. We commenced with a brief introduction in Section 4.1. We continued by characterising the achievable performance of the code acquisition scheme in the co-located MIMO aided SC-DS-CDMA DL in Section 4.2. This was followed by a discussion on the performance of the code acquisition in the co-located MIMO aided MC-DS-CDMA DL in Section 4.3. Finally, the chapter's summary and our related conclusions were provided in Section 4.4.

Throughout the above-mentioned two topics discussed in the context of the DC serial search based code acquisition in the co-located MIMO aided SC- and MC- DS-CDMA DL, our findings suggest that increasing both the number of transmit antennas and that of the subcarriers in a co-located MIMO-aided MC-DS-CDMA system results in combining the low-energy, noise-contaminated signals of both the transmit antennas and the subcarriers. Furthermore, the MAT performance degradation imposed by the DC scheme is less severe than that of its NC counterpart. This fact ultimately reduces the correct detection probability, and accordingly increases the MAT by an order of magnitude, when the SINR is

relatively low. It is extremely undesirable to degrade the achievable acquisition performance, when the system is capable of attaining its target bit error rate performance at reduced SINR values. This phenomenon also has a detrimental effect on the performance of Rake receiver based synchronisation, when the perfectly synchronised system is capable of attaining its target bit error rate performance at reduced SINR values, as a benefit of employing multiple transmit antennas and/or frequency diversity. Hence it may be concluded that the achievable cell coverage determined by the received pilot channel power may be reduced, as the number of transmit antennas is increased, which is a highly undesirable phenomenon, since it has grave repercussions in terms of having to tolerate a high number of handovers per cell. Furthermore, based on the above-mentioned results justified by information theoretic considerations, our acquisition design guidelines are applicable to diverse co-located DC MIMO aided scenarios.

Before providing guidelines for designing NC MIMO aided schemes, the characteristics of NC MIMO aided code acquisition schemes are emphasised again in terms of the achievable MAT performance.

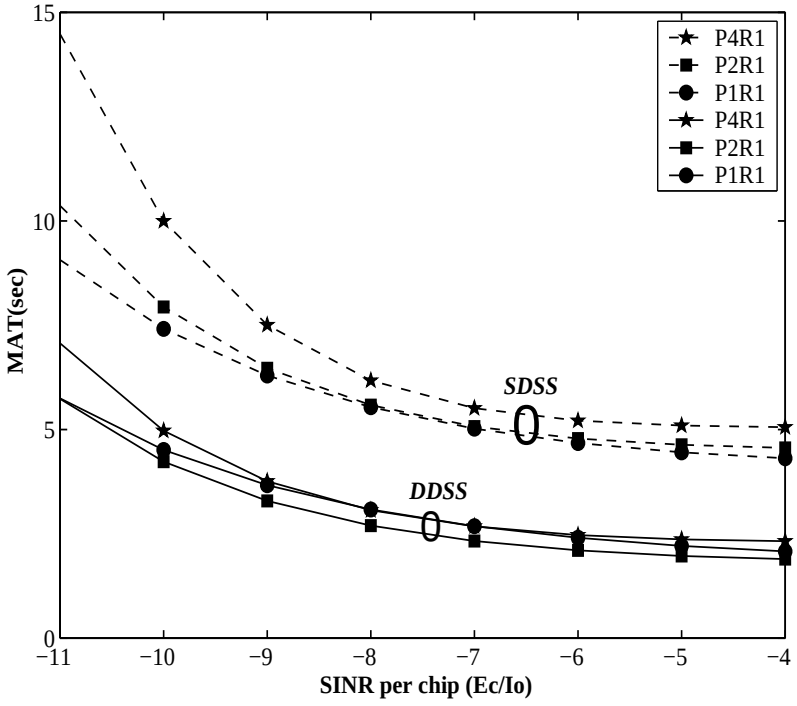

Figure 7.1: MAT versus E_c/I_0 performance comparison between the NC-based DDSS and SDSS code acquisition schemes parameterised with the number of transmit antennas, when using the schematic of Figure 2.5 and Table 3.3.

Figure 7.1 illustrates the attainable MAT versus E_c/I_0 performance of the NC-based DDSS and SDSS code acquisition schemes as a function of the number of transmit antennas for $P = 1$, 2 and 4 as well as that of the number of receive antennas for $R = 1$. In the results of Figure 7.1, the solid lines indicate the performance curves of the DDSS schemes, whereas the dashed lines represent the performance curves of the SDSS schemes. Observe in Figure 7.1 that as the number of transmit antennas is decreased, despite the potentially reduced transmit diversity gain, we experience an improved MAT performance for the single-path scenario of the SDSS scheme. Similarly to the conclusions of the SDSS scenario, as the number of transmit antennas is decreased, all the curves seen in Figure 7.1 for the single-path scenario of the DDSS scheme illustrate an improved MAT performance. However, a useful transmit diversity gain is experienced only for the case of $'P2R1'$, and even this gain was limited to the specific SINR range of -4 and -11 dB. To illustrate the above fact a little further, in the case of $'P2R1'$ the DDSS scheme exhibits a better MAT performance in comparison to the $'P1R1'$ arrangement across the specific SINR range shown in Figure 7.1. It is worth noting that the total uncertainty region of this scenario was assumed to entail 65534 hypotheses for Figure 7.1. On the other hand, the total uncertainty region was assumed to entail 512 hypotheses in both Figures 7.3 and 7.4, as a consequence of the different PN code length. Accordingly, a better correct detection probability was achieved owing to the beneficial transmit diversity gain found in terms of the achievable MAT performance of Figure 7.1 in comparison to the results of both Figures 7.3 and 7.4. This fact clearly implies that DDSS benefits from a significantly higher diversity gain than SDSS. The performance degradation imposed by employing multiple antennas becomes more drastic, as the number of transmit antennas is increased for both the SDSS and DDSS schemes, since the length of coherent summation is highly limited by the clock-drift-induced frequency mismatch. Furthermore, the associated MAT performance discrepancy between the SDSS and DDSS schemes becomes more drastic.

Figure 7.2 illustrates the achievable MAT versus SINR per chip performance of the DDSS code acquisition scheme parameterised with both the grade of link imbalance and with the number of receive antennas for a single RS and a single propagation path, when considering the increased-power scenario. Observe in Figure 7.2 that when the link imbalance is decreased, we experience an improved MAT performance. In the absence of link imbalance, the MAT performance approaches that of having two receive antennas. On the other hand, in case of having a 6 dB imbalance, only a marginal diversity gain is achieved, hence the attainable MAT performance improvement also becomes negligible. The above-mentioned

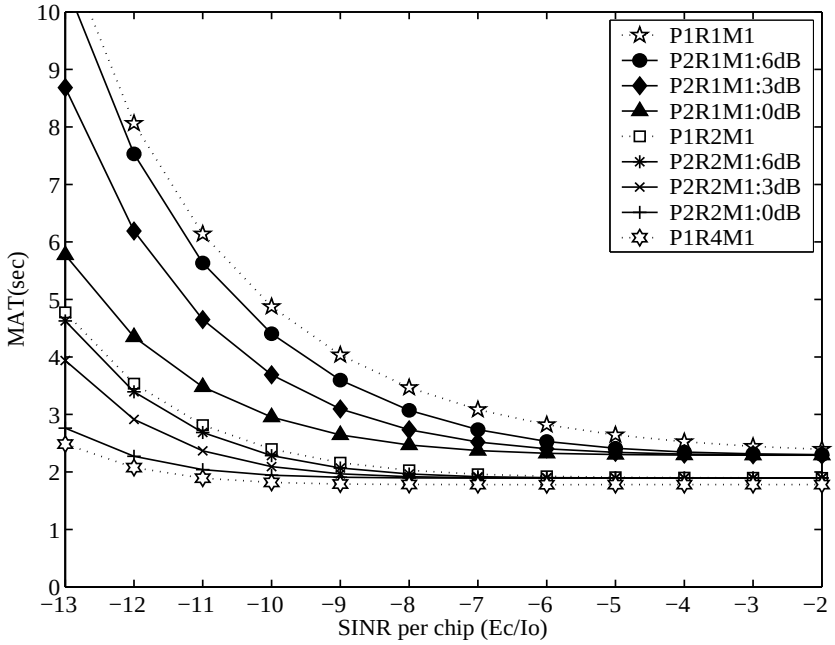

Figure 7.2: MAT versus SINR per chip performance of the code acquisition system for DDSS parameterised with link imbalance and the number of receive antennas for one RS and a single path (increased-power scenario), when employing the schematic of Figure 2.11 and scenarios of Figure 3.19 as well as Table 3.10.

conclusions explicitly demonstrate that employing a single RS is beneficial in terms of the achievable MAT performance, and as expected, the achievable improvements depend on the value of the link imbalance. However, employing a single RS cannot guarantee maintaining a high diversity gain due to the fluctuation of the RS's link quality.

Figure 7.3 illustrates the achievable MAT versus E_c/I_0 performance comparison between the DC- and NC-based SDSS code acquisition schemes parameterised with the number of transmit antennas for $U = 1$ and $U = 4$ subcarriers, respectively. In the results of Figure 7.3, the solid lines indicate the performance curves of the DC-based SDSS scheme for the $U = 1$ scenario, whilst the dashed lines represent the performance curves of the NC-based SDSS scheme for the $U = 4$ scenario. It is worth mentioning that the operating range of both the NC-based SDSS scheme observed for $U = 1$ and that of the DC-based SDSS scheme recorded for $U = 4$ is between that corresponding to both schemes characterised in Figure 7.3. However, for the sake of avoiding obfuscating points in the figure, they were omitted. Similarly to the conclusions of the scenario of Figure 7.1, as the number of transmit antennas is decreased, all the curves explicitly indicate an improved MAT performance, except for the $'P2R1'$ scenario of the DC-based SDSS scheme recorded for $U = 1$. To elaborate on the above observations a little further, a useful transmit diversity gain is only

experienced for the case of $'P2R1'$ for the single-path scenario, and even this was limited to the specific SINR range of -13 to -16 dB. In the case of the MC-DS-CDMA system, the NC SDSS scheme characterised for $U = 4$ in Figure 7.3 benefits from a specific diversity order, which is determined by the number of subcarriers used. It is also assumed that the total transmitted energy per chip is the same in all the scenarios considered. Accordingly, the achievable diversity order is determined by the product of the number of subcarriers and that of the number of transmit antennas. This phenomenon indicates that the employment of MC transmissions leads to exactly the same detrimental effect on the achievable MAT performance, as that imposed by employing multiple transmit antennas owing to the reduced 'per-diversity-branch' power, as further argued below. As the number of transmit antennas is decreased, all the curves of the NC SDSS scheme plotted for $U = 4$ in Figure 7.3 exhibit an improved MAT performance. Furthermore, as a benefit of the inherent performance gain of the DC scheme over the NC one, the overall MAT performance results for the DC scenario of Figure 7.3 are significantly better than those of the NC arrangement. This trend explicitly illustrates that the SDSS-aided MC-DS-CDMA code acquisition scheme considerably degrades the achievable MAT performance of SC-DS-CDMA. This is a consequence of both the low per-antenna power imposed by using multiple transmit antennas for the sake of achieving either a transmit diversity gain or a multiplexing gain as well as that of the low per-subcarrier power imposed by having multiple subcarriers in order to attain a frequency diversity gain. A low level of per-branch and/or per-subcarrier received signal strength is expected to result in a low acquisition performance, despite achieving a high transmit- and frequency-diversity gain.

Figure 7.4 illustrates the achievable MAT versus E_c/I_0 performance of the NCDC and NCNC DDSS code acquisition schemes parameterised with the number of transmit antennas for $U = 1$ and $U = 4$ subcarriers, respectively. In the results of Figure 7.4, the solid lines indicate the performance curves of the NCDC DDSS scheme for the $U = 1$ scenario, while the dashed lines represent the performance curves of the NCNC DDSS scheme for a $U = 4$ scenario. More specifically, the acronym $NCDC$ in Figure 7.4 indicates that both the NC code acquisition aided system used in the search mode and the DC code acquisition assisted scheme employed in the verification mode are characterised for $U = 1$. By contrast, the DDSS system denoted by the acronym $NCNC$ in Figure 7.4 employs the NC code acquisition aided scheme in both its search mode and verification mode for $U = 4$. It is worth mentioning that the operating range of both the NCNC-based DDSS scheme observed for $U = 1$ and that of the NCDC-based DDSS scheme recorded for $U = 4$ are in

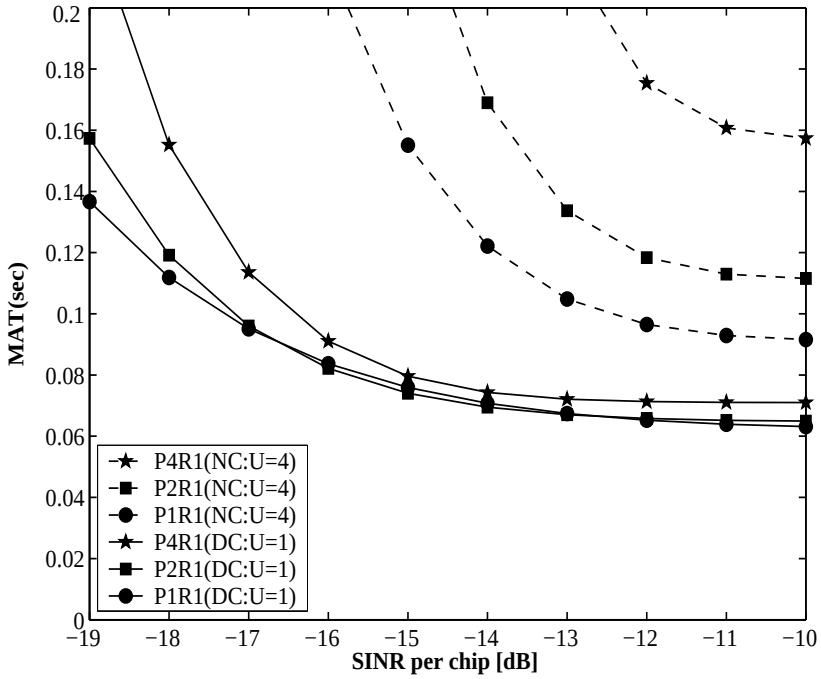

Figure 7.3: MAT versus E_c/I_0 performance comparison between the DC- and NC-based SDSS code acquisition schemes parameterised with the number of transmit antennas for $U = 1$ and $U = 4$ subcarriers, respectively, when employing the schematic of Figure 4.14 and Table 4.4.

between that corresponding to both schemes of Figure 7.4. However, for the sake of avoiding obfuscating points in the figure, they were omitted. Similarly to the conclusions drawn for the scenarios of Figures 7.1 and 7.3, as the number of transmit antennas is decreased, all the curves explicitly indicate an improved MAT performance, except for the $'P2R1'$ scenario of the NCDC-based scheme in the single-path propagation environment, as recorded for the specific SINR range between -13 and -16 dB. To elaborate on the above observation a little further, in the scenario of $'P2R1'$ the DDSS scheme exhibits a slightly better MAT performance in comparison to the $'P1R1'$ scenario right across the specific SINR range considered. The results seen in Figure 7.4 also suggest that the overall performance improvement of the DC scheme in the verification mode is significantly higher than that of the DDSS assisted NC scheme. The DC scheme has a performance gain of just under 3 dB over the NC arrangement, when considering their correct detection probability and false alarm probability. Hence we conclude that the MAT performance curves confirm the expected trends. Moreover, the DC scheme has an advantage over the NC one in the low SINR range [17] in terms of reducing the effects of both the AWGN and interference. Hence, this indicates that the MIMO-aided NCDC scheme experiences a lower MAT performance degradation

owing to the reduced transmit power of the individual transmit antennas than its NCNC counterpart. Furthermore, this result explicitly illustrates that the DDSS-assisted MC-DS-CDMA code acquisition scheme considerably degrades the achievable MAT performance of SC-DS-CDMA. Although the results of the DDSS scenarios characterised in Figure 7.4 exhibit a similar trend to those seen in Figure 7.3, the performance degradation imposed by employing both multiple antennas and multiple subcarriers becomes more drastic in Figure 7.3, when the number of transmit antennas is increased.

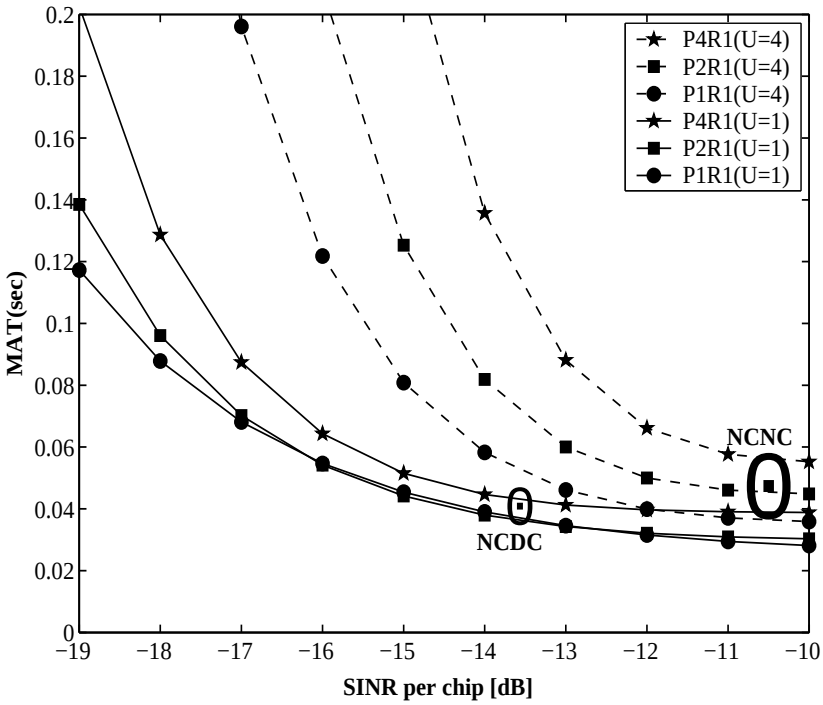

Figure 7.4: MAT versus E_c/I_0 performance comparison between the NCDC- and NCNC-based DDSS code acquisition schemes parameterised with the number of transmit antennas for $'U = 1'$ and $U = 4$ subcarriers, respectively, when using the schematics of Figures 4.14 and 4.15 as well as Table 4.4.

The resultant relationship between the beneficial factors and detrimental factors governing the best attainable MAT performance of the co-located MIMO scenarios is depicted in Figure 7.5. In this figure, the detrimental factors are classified according to the following four categories: 1) Clock-drift-induced frequency mismatch, 2) Number of transmit antennas, 3) Number of subcarriers and 4) Number of resolvable path[1]. On the other hand, the beneficial factors are categorised according to the following three classes: 1) Length of

[1]For example, each of the two delayed paths arrived with a relative time delay of one chip and a 3 dB lower magnitude for the first received path as well as 6 dB lower for both the second and the third received paths, respectively, when compared to the LOS path of a single-path scenario. In other words, the total power assigned to a single-path is exactly the same as that summed over three paths.

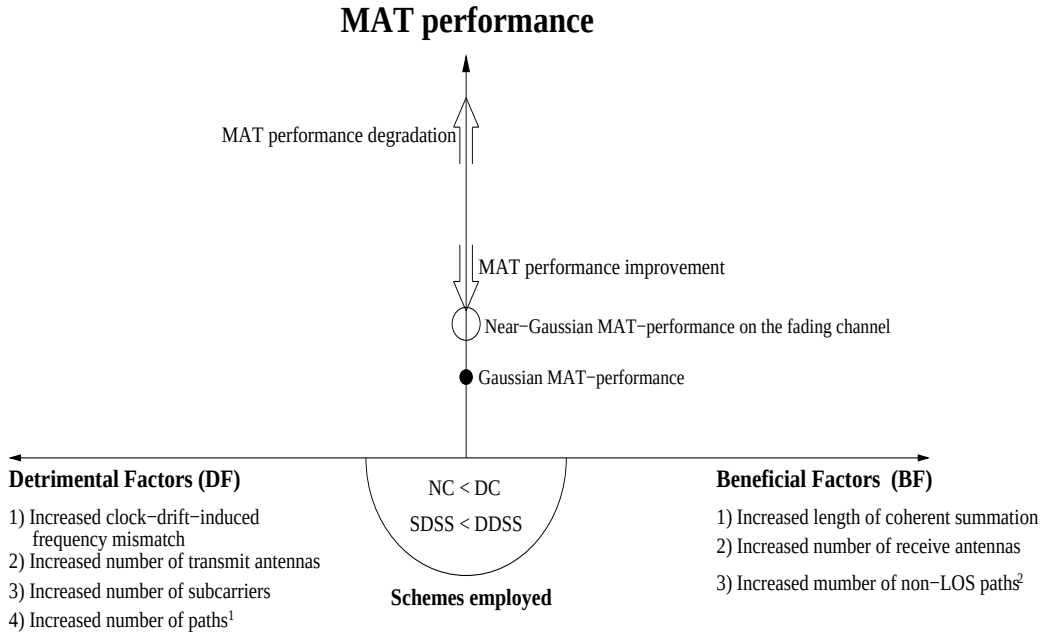

Figure 7.5: Relationship between beneficial factors and detrimental factors in order to achieve the best attainable MAT performance of the co-located MIMO scenarios.

coherent summation, 2) Number of receive antennas and 3) Number of resolvable path[2]. Both NC < DC and SDSS < DDSS seen in the lower half circle situated below the abscissa of Figure 7.5 indicate that the more sophisticated DDSS and/or DC schemes are capable of providing further MAT performance in comparison to using SDSS and/or NC schemes. By optimising the corresponding system parameters a near-Gaussian MAT-performance may be achievable. However, the inherently detrimental factors nonetheless limit the best attainable MAT performance. The term Gaussian MAT-performance is used as the best attainable reference, when communicating over an AWGN channel. The normalised-power scenarios of the cooperative MIMO arrangement also exhibit similar trends to those of the co-located MIMOs.

In contrast to the detrimental effects of sharing the total transmit power across multiple transmit antennas in the co-located and cooperative MIMO based scenarios, the resultant relationship between the beneficial factors and detrimental factors governing the best attainable MAT performance for the increased-power scenario of the cooperative MIMOs is portrayed in Figure 7.6. In this figure, the detrimental factors are classified according to the following three categories: 1) Clock-drift-induced frequency mismatch, 2)The grade of link

[2]For instance, each of the three paths arrives with a relative time delay of one chip with respect to the previous one and has the same magnitude for the first received path as the single-path channel, as well as 3 dB lower for the second and 6 dB lower for the third received paths, respectively. The total power assigned to a single path is less than that accumulated over three paths.

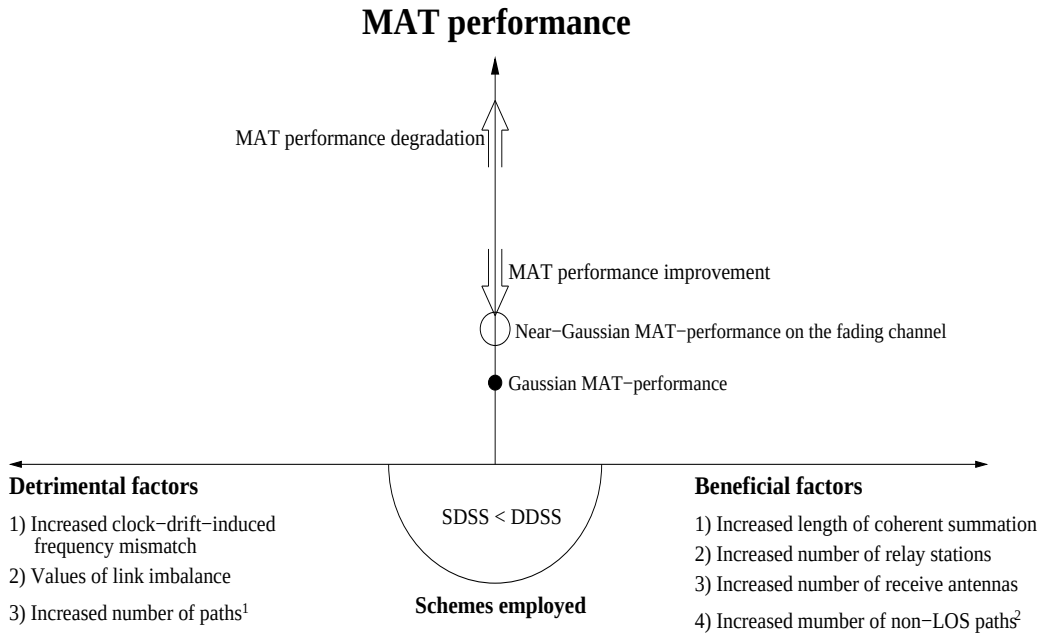

Figure 7.6: Relationship between beneficial factors and detrimental factors in order to achieve the best attainable MAT performance for the increased-power scenario of the cooperative MIMOs.

imbalance and 3) Number of resolvable path[3]. On the other hand, the beneficial factors are categorised according to the following four classes: 1) Length of coherent summation, 2) Number of relay stations, 3) Number of receive antennas and 4) Number of resolvable path[4]. SDSS < DDSS seen in the lower half circle situated below the abscissa of Figure 7.6 indicate that the more sophisticated DDSS scheme is capable of providing further MAT performance improvements in comparison to the SDSS scheme. By optimising the corresponding system parameters a near-Gaussian MAT-performance may be achievable. However, the inherently detrimental factors nonetheless limit the best attainable MAT performance. The terminology of Gaussian MAT-performance is used to indicate the best attainable performance reference, when communicating over an AWGN channel.

Guidelines for Designing NC MIMO Aided Schemes

[3]For example, each of the two delayed paths arrived with a relative time delay of one chip and a 3 dB lower magnitude for the first received path as well as 6 dB lower for both the second and the third received paths, respectively, when compared to the LOS path of a single-path scenario. In other words, the total power assigned to a single-path is exactly the same as that summed over three paths.

[4]For instance, each of the three paths arrives with a relative time delay of one chip with respect to the previous one and has the same magnitude for the first received path as the single-path channel, as well as 3 dB lower for the second and 6 dB lower for the third received paths, respectively. The total power assigned to a single path is less than that accumulated over three paths.

Based on this treatise, the following conclusions for the co-located MIMO scenarios may be inferred:

1) In general, coherently detected space-time transmission schemes benefit from having explicit knowledge of the CIR. However, this is unavailable during the code-acquisition phase.

2) Using multiple transmit antennas typically leads to an MAT performance degradation, owing to the reduced per-antenna power, except for specific scenarios, when encountering a single-path environment, also depending on the allocated bandwidth. In the multi-path scenarios considered all the schemes fail to show a transmit diversity gain. Therefore, during code acquisition activating only a single transmit antenna might be recommended for the sake of maximising the achievable MAT performance of the code acquisition scheme investigated.

3) Using a relatively low number of chips, over which integration or accumulation is carried out imposes further limits on the attainable benefits of MIMO aided schemes [112, 113], as evidenced by all the figures associated with both the MAT performance and the correct detection probability in Chapters 3 and 4.

4) Employing the more sophisticated DDSS and/or DC schemes may provide a rather limited further diversity gain in comparison to using SDSS and/or NC schemes, as suggested by all the figures associated with the MAT performance in Chapters 3 and 4.

5) Exploiting multiple receive antennas increases the achievable receiver diversity gain and has the potential of compensating for the MAT degradation imposed by the low per-branch power of both multiple transmitters and multiple subcarriers, as suggested by all the figures associated with the MAT performance in Chapters 3 and 4.

6) Since no channel coding is used for the pilot signal, no time diversity gain associated with interleaving and channel coding can be achieved [124]. However, the MIMO aided code-acquisition schemes are only capable of achieving a rather limited time diversity, namely, using a sufficiently high number of PDI stages is also available for minimising MAT [3, 45].

7) When the detection threshold θ_2 of Figure. 4.2 is reduced, the resultant code phase estimate often cannot be confirmed by the verification stage of Figure. 4.2 and hence the false alarm probability is increased. At the same time, the correct detection probability is also increased. However, when aiming for the best achievable MAT performance, the

detection threshold optimisation has to strike a balance between increasing the false alarm probability and the correct detection probability, because after a false alarm event the system may require 1000 chip-durations to return to its search mode.

8) The effect of using a pair of fixed thresholds of θ_1 and θ_2 in Figure. 4.2, which are optimised for a specific E_c/I_0 value also limits the attainable MAT performance, since the acquisition threshold should be optimised and controlled as a function of the E_c/I_0 value encountered.

9) For the sake of acquiring the exact timing information of the received paths without any potential performance degradation that might be imposed on the NC MIMO aided scenarios, specifically designed preambles, such as that of the P-SCH of W-CDMA [115] combined with TSTD [116] might be recommended, which is capable of achieving a diversity gain with the aid of a single transmit antenna [113, 114]. In practical scenarios, the received path timing differences of the signals arriving from multiple transmit antennas might be distributed within a fraction of a chip duration [117], although they may vary owing to the time-variant propagation delay, hence using multiple transmit antennas may degrade the performance further. In addition to initial acquisition, the classic pilot channel may also be used for other purposes, such as frequency error correction and channel estimation so as to support coherent MIMO aided scenarios [118].

Furthermore, the following conclusions may be inferred for the cooperative MIMO scenarios:

1) Sharing the total transmit power across multiple transmit antennas in the co-located and cooperative MIMO based scenarios leads to similarly detrimental effects.

2) Employing multiple relay stations increases the achievable transmitter diversity gain, as suggested by all the figures associated with the MAT performance in Chapter 3.

3) The value of link imbalance gravely affects the achievable MAT performance. When having a high link imbalance, only marginal MAT performance gains may be achieved, regardless whether single-path or multi-path propagation scenarios are considered. Therefore, in order to efficiently exploit the diversity benefits of RS-aided transmissions, the employment of at least two RSs might be recommended.

4) When additionally invoking multiple co-located receive antennas at the MS, further diversity gains may be achieved.

Chapter 5

In this chapter, we have provided a detailed study of our proposed code acquisition schemes designed for the SIMO aided DS-UWB DL. Following a brief introduction in Section 5.1, we continued by describing the UWB channel model, which exhibits both large-scale and small-scale fading. We have described the S-V model in Section 5.2. Then the preliminaries of code acquisition designed for the DS-UWB DL were presented in Section 5.3. More specifically, the characteristics of PN codes were highlighted in Section 5.3.1, followed by the detailed calculation of modulo-2 squaring in Section 5.3.2, and by the in-depth illustration of the SPA and offset-based MSA in Sections 5.3.3 and 5.3.4, respectively. In Section 5.3.5 the decoding procedure of the iterative MP algorithm was elucidated in detail. We also showed in Section 5.3.5 that the iterative acquisition scheme exploiting the characteristics of the higher-order GPs further improved the attainable performance.

Both single-stage and two-stage iterative acquisition schemes were highlighted in Sections 5.4.1 and 5.4.2, respectively. More explicitly, in Section 5.4.1, single-stage iterative acquisition employing both a single- and multiple-component decoder was described. In Section 5.4.2, we proposed a search space reduction aided code acquisition scheme for the sake of reducing the MAT, which employs the iterative MP technique. Then the underlying formulas of both the correct detection and false alarm probabilities were presented in Section 5.5 for the random search based code acquisition scheme, when considering both the SISO and SIMO aided DS-UWB DL. The MAT analysis of our proposed schemes was provided for both the SISO and SIMO aided DS-UWB DL in Sections 5.6.1 and 5.6.2, respectively, when considering both single- and multi-path propagation environments. Finally, in Section 5.7 the chapter's summary and our conclusions were provided.

Chapter 6

In this chapter, we have analysed the performance of our proposed iterative acquisition schemes of Section 5.4 in the co-located SIMO DS-UWB DL. Our system parameters were provided in Section 6.2, followed by the analysis of the correct detection versus SINR per chip performance of the iterative acquisition schemes employing both single and multiple component decoder(s) in Section 6.3.1. This was followed in Section 6.3.1 by a discussion of the message passing in our proposed scheme. We also analysed the correct detection probability versus false alarm probability performance of the random search based scheme in Section 6.3.1. Furthermore, we investigated the MAT performance of both the initial

and post-initial acquisition schemes in the co-located SIMO DS-UWB DL in Section 6.3.2. Finally, in Section 6.4 our chapter's summary and conclusions were offered.

In order to highlight the main benefits of the proposed iterative acquisition schemes, the most salient results are emphasised again in Figures 7.7 and 7.8. More specifically, Figure 7.7

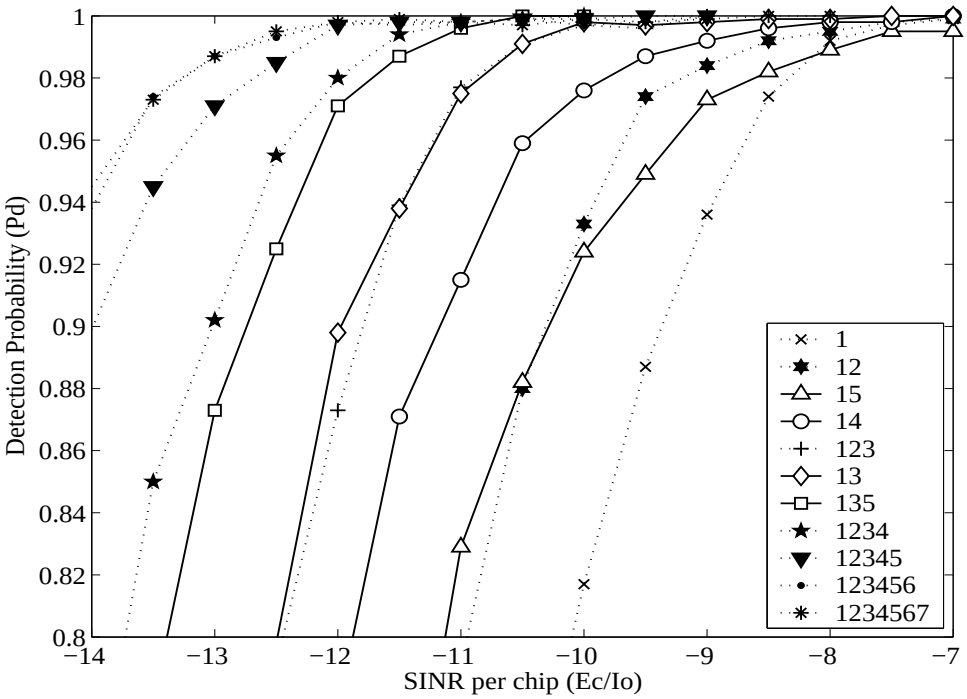

Figure 7.7: Correct detection probability versus SINR per chip of the acquisition schemes employing different GPs and $R = 1$, when considering $N_I = 1024$ and using the schematic of Figure 5.11 and Table 6.1.

illustrates the P_D versus E_c/I_0 performance of the various combined GPs, when considering $N_I = 1024$. Observe in Figure 7.7, that the E_c/I_0 gain achieved by the GP combination of **13** is slightly higher than that of **123**. Furthermore, as seen in Figure 7.7, the gain achieved by the GPs **135** is better than that of **123**. These findings suggest that using consecutive GP orders - as in the **1234** scheme - degrades the efficiency of MP algorithm. This trend suggests that the degree of correlation among the P-C constraints may be decreased by using appropriately chosen GPs, such as **13** and **135**. In contrast, employing $g_1(D) = D^{15}+D+1$ and $g_5(D) = D^{240}+D^{16}+1$ results in a degraded performance, because the number of P-C connections between the VNs and CNs is decreased by a factor of $(2^{n-1}\cdot S)$, n = 1,2,...,7, when the order of the GP is increased. Finally, based on Figure 7.7 the acquisition scheme based on the GPs **135** becomes our favourite choice for the $R = 1$ scenario, which is a benefit of the improved P_D performance in comparison to other GP combinations.

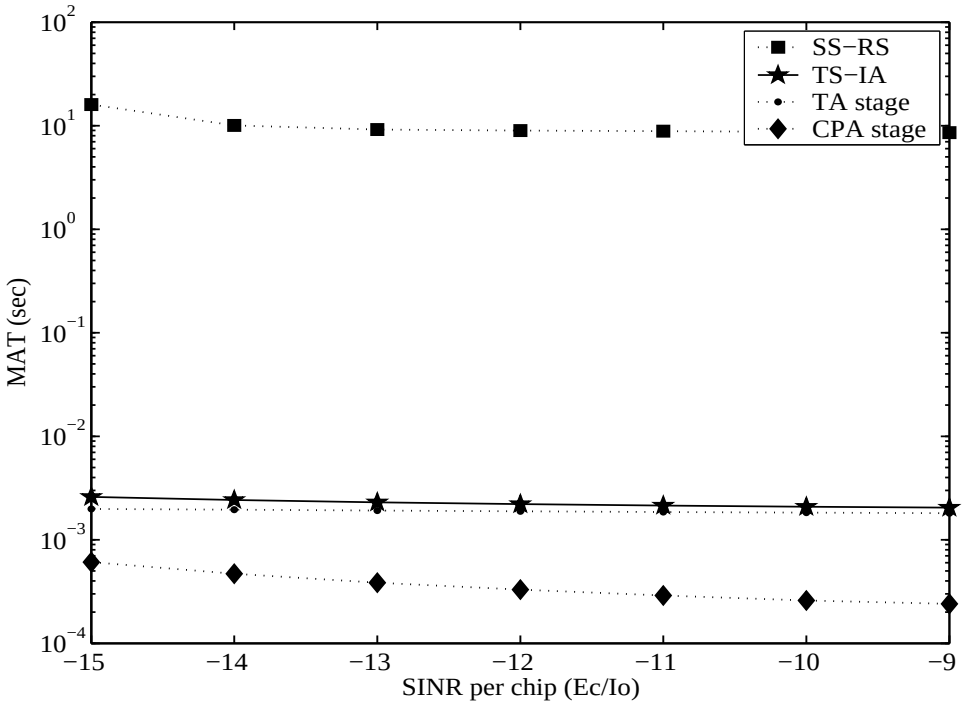

Figure 7.8: MAT versus SINR per chip performance of the two stage scheme employing beneficially chosen GPs and $R = 4$, when considering $N_I = 512$ and employing the schematic of Figure 5.17 and Table 6.1.

Figure 7.8 elucidates the achievable MAT versus SINR per chip performance of the TS-IA scheme employing beneficially chosen GPs for the $R = 4$ scenario. Observe in Figure 7.8 that the MAT performance of our proposed TS-IA scheme is up to about 6200 times better than that of the SS-RS scheme. This suggests that more than three orders of magnitude MAT improvements may be achieved compared to the MAT of the SS-RS arrangement. The MAT performance of the CPA stage is up to about seven times better than that of the TA stage for the $R = 4$ scenario, because a reliable but hence time-consuming verification test was used during the TA stage. By contrast, during the CPA stage only correct code phase estimation was required. The proposed scheme was shown to be capable of achieving an acceptable MAT performance at the minimum E_c/I_0 value required for reliable finger-locking in the $R = 4$ scenario, as evidenced by results of Figure 7.8.

The benefits of the iterative code acquisition schemes were analysed in terms of the achievable P_D and MAT performances. With the aid of the Tanner graph based structure of MP seen in Section 5.3.5, we found that in order to achieve the best possible P_D performance, the employment of beneficially selected non-consecutive-order GPs is recommended. We also found that the employment of multiple receive antennas was essential for achieving a

high target performance, when acquiring the correct timing of the entire sequence by using a relatively short segment of the sequence. Moreover, the employment of appropriately selected multiple-component decoders leads to the lowest possible complexity. Finally, it was explicitly shown that our proposed TS-IA scheme is capable of reducing the MAT by at least three orders of magnitude compared to the benchmark scenario considered. This benefit facilitates its employment in a variety of applications associated with long PN codes.

7.2 Future Research

In future mobile communication systems a variety of multimedia mobile devices will be available. Due to its typically small size, a mobile phone usually has a single receive antenna, but using two $\lambda/2$-spaced receive antennas is feasible. On the other hand, a vehicle is capable of accommodating a high number of co-located MIMO elements in order to achieve more reliable data detection. A co-located eight-by-eight antenna MIMO aided mobile system referred to as the WIreless BROadband (WIBRO) system [156] has been developed and deployed in 2006. Therefore the number of co-located MIMO elements might range from a single antenna to eight antennas. This fact definitely leads to different cell sizes, depending upon the number of the co-located MIMO elements. Furthermore, initial and post-initial acquisition associated with both NC and DC schemes employing co-located multiple transmit antennas suffer from an acquisition performance degradation in the middle to low SINR range, as argued in Chapters 3 and 4. As an example, a scenario of employing four co-located transmit antennas and a single receive antenna results in a considerably reduced cell size, over which reliable serial search based code acquisition can be attained, as evidenced in both Chapters 3 and 4. The size of the cell is limited, because the increased number of the co-located MIMO elements results in a reduced per-antenna power in terms of both the NC and DC schemes, even for the idealised coherent schemes, when using a single receive antenna. As a potential solution, transmitting an unmodulated pilot preamble or uniquely designed pilot preamble is feasible in order to exploit the inherent advantages of NC co-located MIMO systems.

Recently, various cooperative and RS-aided transmission schemes have been proposed. Sharing the total transmit power across multiple transmit antennas in the co-located and cooperative MIMO based scenarios leads to the same detrimental effects. However, employing multiple RSs increases the achievable transmitter diversity gain, as suggested by all the

figures associated with the MAT performance in Chapter 3. Even though the degree of link imbalance is is highly associated with the achievable MAT performance, the employment of at least two RSs might result in the efficient diversity benefits of RS-aided transmissions, regardless whether single-path or multi-path propagation scenarios are considered.

The research of UWB systems has recently attracted a significant interest in both the academic and industrial community. The emerging UWB systems are capable of supporting both wireless personal computers and home entertainment equipment, both requiring high data rates. DS-UWB techniques are characterised by low-duty-cycle pulse trains having a very short impulse duration, because the high bandwidth results in a fine resolution of the timing uncertainty region. In the DS-UWB DL, initial acquisition is required for both coarse timing as well as for code phase alignment and both of these constitute a challenging problem owing to the extremely short chip-duration. This leads to a huge search space size, which is represented as the product of the number of legitimate code phases in the uncertainty region of the PN code and the number of legitimate signalling pulse positions. In order to mitigate the problem regarding the huge search space in the initial acquisition of the DS-UWB DL, the employment of beneficially selected non-consecutive-order GPs is recommended. Furthermore, our proposed TS-IA scheme is capable of reducing the MAT by at least three orders of magnitude compared to the benchmark scenario considered, as evidenced in Chapter 6. This benefit facilitates its employment in a variety of applications associated with long PN codes.

However, there are still idealised assumptions in our investigations of the co-located SIMO aided DS-UWB acquisition scenarios. Our future research will focus on specifically designing iterative LDPC-like acquisition schemes for both the co-located and cooperative MIMO aided DS-UWB acquisition systems [42] for the sake of improving the performance of our proposed iterative acquisition schemes. The following techniques may be taken into account:

(1) The characteristics of iterative acquisition schemes being analysed using EXtrinsic Information Transfer (EXIT) band chart [157, 158];
(2) Iterative acquisition based upon the characteristics of LDPC codes employing the novel concepts of the protograph [159, 160] and factor graph [161];
(3) The analysis of iterative acquisition in cooperative MIMO aided DS-UWB DL scenarios [84];

(4) The performance investigation of the iterative acquisition based on the Nakagami-m distribution using various values of m [62].
(5) Investigations for finding methods showing a better performance than using random search based methods [42];

Bibliography

[1] V. K. Garg, *IS-95 CDMA and cdma 2000: Cellular/PCS Systems Implementation*. Prentice Hall PTR, 1999.

[2] J. S. Blogh and L. Hanzo, *Third Generation Systems and Intelligent Wireless Networking: Smart Antennas and Adaptive Modulation*. John Wiley and Sons, 2002.

[3] A. J. Viterbi, *CDMA: Principles of Spread Spectrum Communication, Chapter 2 and 3*. Addison-Wesley, 1995.

[4] R. L. Peterson, R. E. Ziemer, and D. E. Borth, *Introduction to Spread Spectrum Communications*. Prentice Hall Inc., 1995.

[5] M. K. Simon, J. K. Omura, R. A. Scholtz, and B. K. Levitt, *Spread Spectrum Communications Handbook*. McGraw-Hill Professional, 2001.

[6] L. Hanzo, L. L. Yang, E. Kuan, and K. Yen, *Single- and Multi- Carrier DS-CDMA*. John Wiley & Sons, 2003.

[7] S. Glisic and M. Katz, "Modeling of the Code Acquisition Process for Rake Receivers in CDMA Wireless Networks with Multipath and Transmitter Diversity," *IEEE Journal on Selected Areas in Communications*, vol. 19, no. 1, pp. 21–32, 2001.

[8] S. Won and Y. Kim, "Performance Analysis of Multi-path Searcher for Mobile Station in W-CDMA System Employing Transmit Diversity," *IEE Electronics Letters*, vol. 39, no. 1, pp. 137–139, 2003.

[9] A. Polydoros and S. Glisic, "Code Synchronization: a Review of Principles and Techniques," in *IEEE Proceedings of the International Symposium on Spread Spectrum Techniques and Applications (ISSSTA)*, pp. 115–137, 4-6 July 1994.

[10] E. A. Sourour and S. C. Gupta, "Direct-Sequence Spread-Spectrum Parallel Acquisition in a Fading Mobile Channel," *IEEE Transactions on Communications*, vol. 38, no. 7, pp. 992–998, 1990.

[11] K. K. Chawla and D. V. Sarwate, "Parallel Acquisition of PN Sequences in DS/SS Systems," *IEEE Transactions on Communications*, vol. 42, no. 5, pp. 2155–2164, 1994.

[12] R. B. Ward, "Acquisition of Pseudonoise Signals by Sequential Estimation," *IEEE Transactions on Communications Technology*, vol. 13, no. 4, pp. 475–483, 1965.

[13] L. L. Yang and L. Hanzo, "Acquisition of m-Sequences Using Recursive Soft Sequential Estimation," *IEEE Transactions on Communications*, vol. 52, no. 2, pp. 199–204, 2004.

[14] H. R. Park and B. J. Kang, "On Serial Search Code Acquisition for Direct-Sequence Spread Spectrum System: An Application to IS-95 CDMA system," in *IEEE Vehicular Technology Conference (VTC)*, pp. 291–295, 25-28 July 1995.

[15] H. R. Park, "Performance Analysis of a Double-Dwell Serial Search Technique for Cellular CDMA Networks in the Case of Multiple Pilot Signals," *IEEE Transactions on Vehicular Technology*, vol. 48, no. 6, pp. 1819–1830, 1999.

[16] C. D. Chung, "Differentially Coherent Detection Technique for Direct-Sequence Code Acquisition in a Rayleigh Fading Mobile Channel," *IEEE Transactions on Communications*, vol. 43, no. 234, pp. 1116–1126, 1995.

[17] M. H. Zarrabizadeh and E. S. Sousa, "A Differentially Coherent PN Code Acquisition Receiver for CDMA Systems," *IEEE Transactions on Communications*, vol. 45, no. 11, pp. 1456–1465, 1997.

[18] J. C. Lin, "Differentially Coherent PN Code Acquisition with Full-Period Correlation in Chip-Synchronous DS/SS Receivers," *IEEE Transactions on Communications*, vol. 50, no. 5, pp. 698–702, 2002.

[19] E. A. Sourour and S. C. Gupta, "Direct-Sequence Spread-Spectrum Parallel Acquisition in Nonselective and Frequency-Selective Rician Fading Channels," *IEEE Journal on Selected Areas in Communications*, vol. 10, no. 3, pp. 535–544, 1992.

[20] R. R. Rick and L. B. Milstein, "Optimal Decision Strategies for Acquisition of Spread-Spectrum Signals in Frequency-Selective Rician Fading Channels," *IEEE Transactions on Communications*, vol. 46, no. 5, pp. 686–694, 1998.

[21] H. R. Park and B. J. Kang, "On the Performance of a Maximum-Likelihood Code-Acquisition Technique for Preamble Search in a CDMA Reverse Link," *IEEE Transactions on Vehicular Technology*, vol. 47, no. 1, pp. 65–74, 1998.

[22] L. L. Yang and L. Hanzo, "Serial Acquisition of DS-CDMA Signals in Multipath Fading Mobile Channels," *IEEE Transactions on Vehicular Technology*, vol. 50, no. 2, pp. 617–628, 2001.

[23] L. L. Yang and L. Hanzo, "Serial Acquisition Performance of Single-Carrier and Multi-carrier DS-CDMA over Nakagami-m Fading Channels," *IEEE Transactions on Wireless Communications*, vol. 1, no. 4, pp. 692–702, 2002.

[24] R. Steele and L. Hanzo, *Mobile Radio Communications 2nd ed.* Wiley, 1999.

[25] L. L. Yang and L. Hanzo, "Multicarrier DS-CDMA: A Multiple Access Scheme for Ubiquitous Broadband Wireless Communications," *IEEE Communications Magazine*, vol. 41, no. 10, pp. 116–124, 2003.

[26] L. L. Yang and L. Hanzo, "Performance of Generalized Multicarrier DS-CDMA over Nakagami-m Fading Channels," *IEEE Transactions on Communications*, vol. 50, no. 6, pp. 956–966, 2002.

[27] L. Hanzo, M.Münster, B. Choi, and T.Keller, *OFDM and MC-CDMA for Broadcasting Multi-User Communications, WLANs and Broadcasting.* John Wiley & Sons, 2003.

[28] V. M. DaSilva and E. S. Sousa, "Performance of Orthogonal CDMA Codes for Quasi-Synchronous Communication Systems," in *Proceeding of ICUPC*, pp. 995–999, 12-15 October 1993.

[29] S. Kondo and B. Milstein, "Performance of Multicarrier DS CDMA Systems," *IEEE Transactions on Communications*, vol. 44, no. 2, pp. 238–246, 1996.

[30] E. A. Sourour and M. Nakagawa, "Performance of Orthogonal Multicarrier CDMA in a Multipath Fading Channel," *IEEE Transactions on Communications*, vol. 44, no. 3, pp. 356–367, 1996.

[31] S. Hara and R. Prasad, "Overview of Multicarrier CDMA," *IEEE Communications Magazine*, vol. 35, no. 12, pp. 126–133, 1997.

[32] D. Lee and L. B. Milstein, "Analysis of a Multicarrier DS-CDMA Code Acquisition System," vol. 47, no. 8, pp. 1233–1244, 1999.

[33] D. Gesbert, M. Shafi, D. S. Shiu, P. J. Smith, and A. Naguib, "From Theory to Practice: An overview of MIMO Space-Time Coded Wireless Systems," *IEEE Journal on Selected Areas in Communications*, vol. 21, no. 3, pp. 281–302, 2003.

[34] R. A. Soni and R. M. Buehrer, "On the Performance of Open-Loop Transmit Diversity Techniques for IS-2000 Systems: A Comparative Study," *IEEE Transactions on Wireless Communications*, vol. 3, no. 5, pp. 1602–1615, 2004.

[35] S. Ng and L. Hanzo, "On the MIMO Channel Capacity of Multidimensional Signal Sets," *IEEE Transactions on Vehicular Technology*, vol. 55, no. 2, pp. 528–536, 2006.

[36] R. R. Rick and L. B. Milstein, "Parallel Acquisition Schemes Using Antenna Arrays for Antenna Diversity," *IEEE Transaction on Communications*, vol. 45, no. 8, pp. 903–905, 1997.

[37] W. H. Ryu, M. K. Park, and S. K. Oh, "Code Acquisition Schemes Using Antenna Arrays for DS-SS Systems and Their Performance in Spatially Correlated Fading Channels," *IEEE Transaction on Communications*, vol. 50, no. 8, pp. 1337–1347, 2002.

[38] S. Kim, "Acquisition Performance of CDMA Systems with Multiple Antennas," *IEEE Transactions on Vehicular Technology*, vol. 53, no. 5, pp. 1341–1353, 2004.

[39] S. Roy, J. Foerster, V. Somayazulu, and D. Leeper, "Ultrawideband Radio Design: The Promise of High-Speed, Short-Range Wireless Connectivity," *Proceedings of The IEEE*, vol. 92, no. 2, pp. 295–311, 2004.

[40] L. Yang and G. Giannakis, "Ultra-wideband Communications: An Idea Whose Time Has Come," *IEEE Signal Processing Magazine*, vol. 21, no. 6, pp. 26–54, 2004.

[41] R. Qiu, H. Liu, and X. Shen, "Ultra-wideband for Multiple Access Communications," *IEEE Communications Magazine*, vol. 43, no. 2, pp. 80–87, 2005.

[42] S. Aedudodla, S. Vijayakumaran, and T. Wong, "Timing Acquisition in Ultra-wideband Communication Systems," *IEEE Transactions on Vehicular Technology*, vol. 54, no. 5, pp. 1570–1583, 2005.

[43] K. Chugg and M. Zhu, "A New Approach to Rapid PN Code Acquisition Using Iterative Message Passing Techniques," *IEEE Journal on Selected Areas in Communications*, vol. 23, no. 5, pp. 884–897, 2005.

[44] G. Corazza, C. Caini, A. Vanelli-Coralli, and A. Polydoros, "DS-CDMA Code Acquisition in the Presence of Correlated Fading-Part I: Theoretical Aspects," *IEEE Transaction on Communications*, vol. 52, no. 7, pp. 1160–1168, 2004.

[45] B. G. Lee and B. H. Kim, *Scrambling Techniques For CDMA Communications, Chapter 2 and 3.* Kluwer Academic Publishers, 2001.

[46] R. Ward and K. Yiu, "Acquisition of Pseudonoise Signals by Recursion-Aided Sequential Estimation," *IEEE Transaction on Communications*, vol. 25, no. 8, pp. 784–794, 1977.

[47] C. Kilgus, "Pseudonoise Code Acquisition Using Majority Logic Decoding," *IEEE Transaction on Communications*, vol. 21, no. 6, pp. 772–774, 1973.

[48] C. Berrou, A. Glavieux, and P. Thitimajshima, "Near-Shannon Limit Error-Correcting Coding and Ddecoding: Turbo-Codes. 1," in *Proceedings of the IEEE International Conference on Communications (ICC)*, pp. 1064–1070, 23-26 May 1993.

[49] C. Berrou and A. Glavieux, "Near Optimum Error-Correcting Coding and Ddecoding: Turbo-Codes," *IEEE Transaction on Communications*, vol. 44, no. 10, pp. 1261–1271, 1996.

[50] B. Sklar, "A Primer on Turbo Code Concepts," *IEEE Communications Magazine*, vol. 35, no. 12, pp. 94–102, 1997.

[51] J. Woodard and L. Hanzo, "Comparative Study of Turbo Decoding Techniques: An Overview," *IEEE Transaction on Vehicular Technology*, vol. 49, no. 6, pp. 2208–2233, 2000.

[52] L. L. Yang and L. Hanzo, "Iterative Soft Sequential Estimation Assisted Acquisition of m-Sequences," *IEE Electronics Letters*, vol. 38, no. 24, pp. 1550–1551, 2002.

[53] L. L. Yang and L. Hanzo, "Differentially Acquisition of m-Sequences Using Recursive Soft Sequential Estimation," *IEEE Transactions on Wireless Communications*, vol. 4, no. 1, pp. 128–136, 2005.

[54] S. Lin and D. J. Costello, *Error Control Coding, 2nd ed.* Prentice Hall, 2004.

[55] J. H. Lee, I. H. Song, S. R. Park, and J. M. Lee, "Rapid Acquisition of PN Sequences with a New Decision Logic," *IEEE Transactions on Vehicular Technology*, vol. 53, no. 1, pp. 49–60, 2004.

[56] S. Benedetto, D. Divsalar, G. Montorsi, and F. Pollara, "A Soft-Input Soft-Output APP Module for Iterative Decoding of Concatenated Codes," *IEEE Communications Letters*, vol. 1, no. 1, pp. 772–774, 1997.

[57] H. Tanaka, K. Furusawa, and S. Kaneku, "A Novel Approach to Soft Decision Decoding of Threshold Decodable Codes," *IEEE Transactions on Information Theory*, vol. 26, no. 2, pp. 244–246, 1980.

[58] J. Hagenauer, E. Offer, and L. Papke, "Iterative Decoding of Binary Block and Convolutional Codes," *IEEE Transactions on Information Theory*, vol. 42, no. 2, pp. 429–445, 1996.

[59] O. W. Yeung and K. Chugg, "An Iterative Algorithm and Low Complexity Hardware Architecture for Fast Acquisition of Long PN Codes in UWB Systems," *SPRINGER Journal on VLSI and Signal Processing (SPECIAL ISSUE ON UWB)*, vol. 43, no. 1, 2006.

[60] L. S. Lee and J. H. Chiu, "An Improved Sequential Estimation Scheme for PN Acquisition," *IEEE Transaction on Communications*, vol. 36, no. 10, pp. 1182–1184, 1988.

[61] R. T. Barghouthi and G. L. Stüber, "Rapid Sequence Acquisition for DS/CDMA Systems Employing Kasami Sequences," *IEEE Transaction on Communications*, vol. 42, no. 234, pp. 1957–1968, 1994.

[62] A. Molisch, J. Foerster, and M. Pendergrass, "Channel Models for Ultrawideband Personal Area Networks," *IEEE Wireless Communications*, vol. 10, no. 6, pp. 14–21, 2003.

[63] I. Ramachandran and S. Roy, "On Acquisition of Wideband Direct-sequence Spread Spectrum Signals," *IEEE Transactions on Wireless Communications*, vol. 5, no. 6, pp. 1537–1546, 2006.

[64] H. S. Liaw and C. D. Chung, "Differentially Coherent Correlation Technique for DS-SS Code Acquisition in a Fast Rayleigh Fading Channel," *IEE Electronics Letters*, vol. 30, no. 21, pp. 1738–1740, 1994.

[65] T. Ristaniemi and J. Joutsensalo, "Code Timing Acquisition for DS-CDMA in Fading Channels by Differential Correlations," *IEEE Transaction on Communications*, vol. 49, no. 5, pp. 899–910, 2001.

[66] Y. K. Jeong, O. S. Shin, and K. B. Lee, "Fast Slot Synchronization for Intercell Asynchronous DS/CDMA Systems," *IEEE Transactions on Wireless Communications*, vol. 1, no. 2, pp. 353–360, 2002.

[67] J. C. Lin, "Differentially Coherent PN Code Acquisition with Full-period Correlation in Chip-Asynchronous DS/SS Receivers," *IEEE Transactions on Vehicular Technology*, vol. 51, no. 6, pp. 1596–1599, 2002.

[68] O. S. Shin and K. B. Lee, "Differentially Coherent Combining for Double-Dwell Code Acquisition in DS-CDMA Systems," *IEEE Transactions on Communications*, vol. 51, no. 7, pp. 1046–1050, 2003.

[69] J. Ibrahim and R. M. Buehrer, "Two-Stage Acquisition for UWB in Dense Multipath," *IEEE Journal on Selected Areas in Communications*, vol. 24, no. 4, pp. 801–807, 2006.

[70] J. Furukawa, Y. Sanada, and T. Kuroda, "Novel Initial Acquisition Scheme for Impulse-based UWB Systems," in *Proceeding 2004 Intl. Workshop Ultra Wideband Systems*, pp. 278–282, 18-21 May 2004.

[71] S. Aedudodla, S. Vijayakumaran, and T. Wong, "Ultra-wideband Signal Acquisition with Hybrid DS-TH Spreading," *IEEE Transactions on Wireless Communications*, vol. 5, no. 9, pp. 2504–2515, 2006.

[72] J. S. Lee and L. E. Miller, *CDMA Systems Engineering Handbook, Chapter 11, CDMA Optimization Issues*. Artech House Publishers, 1998.

[73] S. Won and L. Hanzo, "Analysis of Serial Search Based Code Acquisition in the Multiple Transmit Antenna Aided DS-CDMA Downlink," in *Proceeding of IEEE VTC'05 Fall*, pp. 98–102, 25-28 September 2005.

[74] S. Won and L. Hanzo, "Analysis of Serial Search Based Code Acquisition in the Multiple Transmit/Multiple Receive Antenna Aided DS-CDMA Downlink," *IEEE Transactions on Vehicular Technology*, vol. 57, no. 2, pp. 1032–1039, 2008.

[75] S. Won and L. Hanzo, "Initial and Post-Initial Acquisition in the Serial Search Based Noncoherent Multiple Transmit/Receive Antenna Aided DS-CDMA Downlink," in *Proceeding of IEEE VTC'06 Spring*, pp. 2246–2250, 7-10 May 2006.

[76] S. Won and L. Hanzo, "Initial and Post-Initial Code Acquisition in the Non-Coherent Multiple Input/Multiple Output Aided DS-CDMA Downlink," *To appear in the IEEE Transactions on Vehicular Technology*, 2008.

[77] S. Won and L. Hanzo, "Serial Search Based Initial Code Acquisition in the Multiple Transmit/Receive Antenna Aided Multi-Carrier DS-CDMA Downlink," in *IEEE Proceedings of the International Symposium on Spread Spectrum Techniques and Applications (ISSSTA)*, pp. 64–68, 28-31 August 2006.

[78] S. Won and L. Hanzo, "Non-Coherent Code Acquisition in the Multiple Transmit/Multiple Receive Antenna Aided Single- and Multi-Carrier DS-CDMA Downlink," *IEEE Transactions on Wireless Communications*, vol. 6, no. 11, pp. 3864–3869, 2007.

[79] S. Won and L. Hanzo, "Differentially Coherent Code Acquisition in the Multiple Transmit/Receive Antenna Aided DS-CDMA Downlink," in *Proceeding of WCNC2006*, pp. 1009–1014, 3-6 April 2006.

[80] S. Won and L. Hanzo, "Non-coherent and Differentially Coherent Code Acquisition in MIMO Assisted DS-CDMA Multi-path Downlink Scenarios," *IEEE Transactions on Wireless Communications*, vol. 7, no. 5, pp. 1585–1593, 2008.

[81] S. Won and L. Hanzo, "Differentially Coherent Code Acquisition in the Multiple Transmit/Receive Antenna Assisted Multi-Carrier DS-CDMA Downlink," in *Proceeding of IEEE VTC'07 Spring*, pp. 1831–1835, 23-25 April 2007.

[82] S. Won and L. Hanzo, "Differentially Coherent Code Acquisition in the MIMO-Aided Multi-Carrier DS-CDMA Downlink," *IET Proceedings Communications*, vol. 1, no. 4, pp. 662–670, 2007.

[83] S. Won, K. Lee, and L. Hanzo, "Serial Search Based Code Acquisition in the Cooperative MIMO Aided DS-CDMA Downlink," in *the Proceeding of ICC 2008.*

[84] S. Won, K. Lee, and L. Hanzo, "Initial Code Acquisition in the Cooperative Noncoherent MIMO DS-CDMA Downlink," *Revised for the IEEE Transactions on Vehicular Technology, April*, 2008.

[85] S. Won and L. Hanzo, "Iterative Code Acquisition for the DS-UWB Downlink Using Multiple-Component Decoders," *IET Electronics Letters*, vol. 44, no. 2, pp. 162–163, 2008.

[86] S. Won and L. Hanzo, "Two-Stage Code Acquisition Employing Search Space Reduction and Iterative Detection in the DS-UWB Downlink," in *the Proceeding of WCNC 2008.*

[87] S. Won and L. Hanzo, "Initial Acquisition Performance of the Multiple Receive Antenna Assisted DS-UWB Downlink Using Search Space Reduction and Iterative Code Phase Estimation," *Revised for the IEEE Transactions on Wireless Communications, June 2008.*, 2008.

[88] S. Won and L. Hanzo, "Iterative Spreading-Sequence Acquisition in the Multiple Receive Antenna Aided DS-UWB Downlink," in *the Proceeding of IEEE VTC'08 Fall (Accepted).*

[89] J. Iinatti and S. Kerhuel, "Code Sysnchronisation in Two-Path Channel:Effect of Interpath Interference on Acquisition," *IEE Electronics Letters*, vol. 35, no. 12, pp. 960–962, 1999.

[90] J. Iinatti, "On the Threshold Setting Principles in Code Acquisition of DS-SS Signals," *IEEE Journal on Selected Areas in Communications*, vol. 18, no. 1, pp. 62–72, 2000.

[91] J. Iinatti, "Performance of DS Code Acquisition in Static and Fading Multipath Channels," *IEE Proceedings-Communications*, vol. 147, no. 6, pp. 355–360, 2000.

[92] O. S. Shin and K. B. Lee, "Utilization of Multipaths for Spread-Spectrum Code Acquisition in Frequency-Selective Rayleigh Fading Channels," *IEEE Transaction on Communications*, vol. 49, no. 4, pp. 734–743, 2001.

[93] J. Proakis, *Digital Communications, 4th ed. Chapter 2.* McGraw-Hill, 2001.

[94] C. Caini, G. Corazza, and A. Vanelli-Coralli, "DS-CDMA Code Acquisition in the Presence of Correlated Fading-Part II: Application to Cellular Networks," *IEEE Transaction on Communications*, vol. 52, no. 8, pp. 1160–1168, 2004.

[95] G. J. Foschini, "Layered Space-Time Architecture for Wireless Communication in a Fading Environment When Using Multi-Element Antennas," *Bell Labs. Technical Journal*, vol. 1, no. 2, pp. 41–59, 1996.

[96] S. M. Alamouti, "A Simple Transmit Diversity Technique for Wireless Communications," *IEEE Journal on Selected Areas in Communications*, vol. 16, no. 8, pp. 1451–1458, 1998.

[97] V. Tarokh, A. Naguib, N. Seshadri, and A. Calderbank, "Space-Time Codes for High Data Rate Wireless Communication: Performance Criteria in the Presence of Channel Estimation Errors, Mobility, and Multile Paths," *IEEE Transactions on Communications*, vol. 47, no. 2, pp. 199–207, 1999.

[98] L. Hanzo, T. H. Liew, and B. L. Yeap, *Turbo Coding, Turbo Equalisation and Space-Time Coding for Transmission Over Fading Channels.* John Wiley & Sons Ltd., 2002.

[99] J. Blogh and L. Hanzo, *Third-Generation Systems and Intelligent Networking.* John Wiley and IEEE Press, 2002.

[100] S. Kim, "Effect of Spatial Fading Correlation on CDMA Code-Acquisition Performance," *IEE Proceedings - Communication*, vol. 152, no. 1, pp. 103–112, 2005.

[101] W. C. Lee, *Mobile Communications Engineering.* McGraw-Hill, 2nd Ed., 1998.

[102] R. N. McDonough and A. D. Whalen, *Detection of Signals in Noise, Chapter 5.* Academic Press, 1995.

[103] A. Leon-Garcia, *Probability and Random Processes for Electrical Engineering: 2^{nd} edition, Chapter 4, Multiple Random Variables.* Addison-Wesley, 1994.

[104] H. Holm and M.-S. Alouini, "Sum and Difference of Two Squared Correlated Nakagami Variates in Connection with the McKay Distribution," *IEEE Transaction on Communications*, vol. 52, no. 8, pp. 1367–1376, 2004.

[105] J. Laiho, A. Wacker, and T. Novosad, *Radio Network Planning and Optimisation for UMTS: 2nd edition*. Wiley, 2006.

[106] 3GPP2, *3GPP2 WG5 Evaluation AHG, 1xEV-DV Evaluation Methodology - Addendum (V6)*. 3GPP2, 2001.

[107] 3GPP, *3GPP TR 25.896 V1.3.1, Feasibility Study for Enhanced Uplink for UTRA FDD (Release 6)*. 3GPP, 2004.

[108] A. C. Soong and F. Zhou, *3GPP2 TSG-C, Wrap Around System Simulation Description for 1xEV-DV Reverse Link*. 3GPP2, 2001.

[109] S. Das, W. M. MacDonald, and H. Viswanathan, "Sensitivity Analysis of Handoff Algorithms on CDMA Forward Link," *IEEE Transactions on Vehicular Technology*, vol. 54, no. 1, pp. 272–285, 2005.

[110] C. Noblet, M. Fadridis, and R. Owen, "Downlink Transmit Power Issues in a WCDMA Cellular System," in *3G Mobile Communication Technologies*, pp. 244–249, 8-10 May 2002.

[111] 3GPP, *3GPP TS 25.101 V4.11.0, User Equipment (UE) Radio Transmission and Reception (FDD)*. 3GPP, 2004.

[112] T. Marzetta and B. Hochwald, "Capacity of a Mobile Multiple-Antenna Communication Link in Rayleigh Flat Fading," *IEEE Transactions on Information Theory*, vol. 45, no. 1, pp. 139–157, 1999.

[113] L. Zheng and D. N. C. Tse, "Communication on the Grassman Manifold: A Geometric Approach to the Noncoherent Multiple-Antenna Channel," *IEEE Transactions on Information Theory*, vol. 48, no. 2, pp. 359–383, 2002.

[114] C. Rao and B. Hassibi, "Analysis of Multiple-Antenna Wireless Links at Low SNR," *IEEE Transactions on Information Theory*, vol. 50, no. 9, pp. 2123–2130, 2004.

[115] Y.-P. Wang and T. Ottosson, "Cell Search in W-CDMA," *IEEE Journal on Selected Areas in Communications*, vol. 18, no. 8, pp. 1470–1482, 2000.

[116] J. M. Wang and Y. Lee, "Rapid Slot Synchronization in the Presence of Large Frequency Offset and Doppler Spread in WCDMA Systems," *IEEE Journal on Wireless Communications*, vol. 4, no. 4, pp. 1325–1330, 2005.

[117] M. S. S. Fukumoto, K. Higuchi and F. Adachi, "Experiments on Space Time Block Coding Transmit Diversity (STTD) in W-CDMA Forward Link," *IEICE Transactions on Fundamentals*, vol. E84-A, no. 12, pp. 3045–3057, 2001.

[118] 3GPP, *3GPP TS 25.211 V7.0.0, Physical Channels and Mapping of Transport Channels onto Physical Channels (FDD)*. 3GPP, 2006.

[119] S. Ray, M. Medard, and L. Zheng, "On MIMO Capacity in the Ultra-Wideband Regime," in *Signals, Systems and Computers,2004. Conference Record of the Thirty-Eighth Asilomar Conference on*, pp. 1516–1520, 7-10 November 2004.

[120] A. Sendonaris, E. Erkip, and B. Aazhang, "User Cooperation Diversity-Part I: System Description," *IEEE Transactions on Communications*, vol. 51, no. 11, pp. 1927–1938, 2003.

[121] J. N. Laneman, D. N. C. Tse, and G. W. Wornell, "Cooperative Diversity in Wireless Networks: Efficient Protocols and Outage Behavior," *IEEE Transactions on Information Theory*, vol. 50, no. 12, pp. 3062–3080, 2004.

[122] R. Pabst, B. H. Walke, D. C. Schultz, P. Herhold, H. Yanikomeroglu, S. Mukherjee, H. Viswanathan, M. Lott, W. Zirwas, M. Dohler, H. Aghvami, D. D. Falconer, and G. P. Fettweis, "Relay-based Deployment Concepts for Wireless and Mobile Broadband Radio," *IEEE Communications Magazine*, vol. 42, no. 9, pp. 80–89, 2004.

[123] W.-H. Sheen, J.-K. Tzeng, and C.-K. Tzou, "Effects of Cell Correlations in A Matched-Filter PN Code Acquisition for Direct-Sequence Spread-Spectrum Systems," *IEEE Transactions on Vehicular Technology*, vol. 48, no. 3, pp. 724–732, 1999.

[124] H.-F. Lu and P. Kumar, "Rate-Diversity Tradeoff of Space-Time Codes With Fixed Alphabet and Optimal Constructions for PSK Modulation," *IEEE Transactions on Information Theory*, vol. 49, no. 10, pp. 2747–2751, 2003.

[125] S. Ghassemzadeh, R. Jana, C. Rice, W. Turin, and V. Tarokh, "Measurement and Modeling of an Ultra-wide Bandwidth Indoor Channel," *IEEE Transactions on Communications*, vol. 52, no. 10, pp. 1786–1796, 2004.

[126] M. Win and R. Scholtz, "On the Robustness of Ultra-wide Bandwidth Signals in Dense Multipath Environments," *IEEE Communications Letters*, vol. 2, no. 2, pp. 51–53, 1998.

[127] M. Win and R. Scholtz, "On the Energy Capture of Ultrawide Bandwidth Signals in Dense Multipath Environments," *IEEE Communications Letters*, vol. 2, no. 9, pp. 245–247, 1998.

[128] Z. Irahhauten, H. Nikookar, and G. Janssen, "An Overview of Ultra Wide Band Indoor Channel measurements and Modeling," *Microwave and Wireless Components Letters*, vol. 14, no. 8, pp. 386–388, 2004.

[129] T. Rappaport, *Wireless Communications Principles and Practice*. Prentice Hall, 1999.

[130] Q. Z. Ahmed, *Ultrawide Bandwidth (UWB) DS-CDMA Wireless Communications (Minithesis)*. University of Southampton, 2006.

[131] A. Durantini, W. Ciccognani, and D. Cassioli, "UWB Propagation Measurements by PN-sequence Channel Sounding," in *IEEE International Conference on Communications*, pp. 3414–3418, 20-24 June 2004.

[132] J. Reed, *An Introduction to Ultra Wideband Communication Systems*. Prentice Hall, 2005.

[133] A. Molisch, "Ultrawideband Propagation Channels-Theory, Measurement and Model," *IEEE Transactions on Vehicular Technology*, vol. 54, no. 5, pp. 1528–1545, 2005.

[134] A. Saleh and R. Valenzuela, "A Statistical Model for Indoor Multipath Propagation," *IEEE Journal on Selected Areas in Communications*, vol. 5, no. 2, pp. 128–137, 1987.

[135] D. Cassioli, M. Win, and A. Molisch, "The Ultra-wide bandwidth Indoor Channel: from Statistical Model to Simulations," *IEEE Journal on Selected Areas in Communications*, vol. 20, no. 6, pp. 1247–1257, 2002.

[136] J. Proakis, *Digital Communications, 4th ed.* McGraw-Hill, 2001.

[137] R. McEliece, D. MacKay, and J.-F. Cheng, "Turbo Decoding as an Instance of Pearl's 'Belief Propagation' Algorithm," *IEEE Journal on Selected Areas in Communications*, vol. 16, no. 2, pp. 140–152, 1998.

[138] F. Kschischang and B. Frey, "Iterative Decoding of Compound Codes by Probability Propagation in Graphical Models," *IEEE Journal on Selected Areas in Communications*, vol. 16, no. 2, pp. 219–230, 1998.

[139] F. Kschischang, B. Frey, and H.-A. Loeliger, "Factor Graphs and the Sum-Product Algorithm," *IEEE Transactions on Information Theory*, vol. 47, no. 2, pp. 498–519, 2001.

[140] F. Kschischang, "Codes Defined on Graphs," *IEEE Communications Magazine*, vol. 41, no. 8, pp. 118–125, 2003.

[141] J. Chen and M. Fossorier, "Density Evolution for Two Improved BP-based Decoding Algorithms of LDPC Codes," *IEEE Communications Letters*, vol. 6, no. 5, pp. 208–210, 2002.

[142] N. Bonello, *Channel Coding Using Turbo, LDPC and LT Codes (MSc Thesis).* University of Southampton, 2006.

[143] D. MacKay, *Information Theory, Inference and Learning Algorithms.* Cambridge University Press, 2003.

[144] A. Anastasopoulos, "A Comparison Between the Sum-product and the Min-sum Iterative Detection Algorithms Based on Density Evolution," in *IEEE Global Telecommunications Conference*, pp. 1021–1025, 25-29 November 2001.

[145] E. Eleftheriou, T. Mittelholzer, and A. Dholakia, "Reduced-complexity Decoding Algorithm for Low-density Parity-check Codes," *IEE Electronics Letters*, vol. 37, no. 2, pp. 102–104, 2001.

[146] X.-Y. Hu, E. Eleftheriou, D.-M. Arnold, and A. Dholakia, "Efficient Implementations of the Sum-product Algorithm for Decoding LDPC Codes," in *IEEE Global Telecommunications Conference*, pp. 1036–1036E, 25-29 November 2001.

[147] J. Chen, A. Dholakia, E. Eleftheriou, M. Fossorier, and X.-Y. Hu, "Near-optimum Reduced-complexity Decoding Algorithms of LDPC Codes," in *Proceeding IEEE Int. Symp. Information Theory, pp.455, 2002.*

[148] J. Chen and M. Fossorier, "Near Optimum Universal Belief Propagation Based Decoding of Low-density Parity Check Codes," *IEEE Transactions on Communications*, vol. 50, no. 3, pp. 406–414, 2002.

[149] J. Chen and M. Fossorier, "Density Evolution for BP-based Decoding Algorithms of LDPC Codes and Their Quantized Versions," in *IEEE Global Telecommunications Conference*, pp. 1378–1382, 17-21 November 2002.

[150] J. Zhao, F. Zarkeshvari, and A. Banihashemi, "On Implementation of Min-sum Algorithm and Its Modifications for Decoding Low-density Parity-check (LDPC) Codes," *IEEE Transactions on Communications*, vol. 53, no. 4, pp. 549–554, 2005.

[151] M. Yazdani, S. Hemati, and A. Banihashemi, "Improving Belief Propagation on Graphs with Cycles," *IEEE Communications Letters*, vol. 8, no. 1, pp. 57–59, 2004.

[152] S. Gounai, T. Ohtsuki, and T. Kaneko, "Modified Belief Propagation Decoding Algorithm for Low-density Parity Check Code Based on Oscillation," in *IEEE 63rd Vehicular Technology Conference-Spring*, pp. 1467–1471, 7-10 May 2006.

[153] R. Tanner, "A Recursive Approach to Low Complexity Codes," *IEEE Transactions on Information Theory*, vol. 27, no. 5, pp. 533–547, 1981.

[154] M. Schwartz and A. Vardy, "On the Stopping Distance and the Stopping Redundancy of Codes," *IEEE Transactions on Information Theory*, vol. 52, no. 3, pp. 922–932, 2006.

[155] S. Lee and J. Kim, "Optimum Threshold for Double-Dwell DS-SS Code Acquisition System in PCS Channel Mode," *IEE Electronics Letters*, vol. 34, no. 7, pp. 634–635, 1998.

[156] S. Lee, N. Park, C. Cho, H. Lee, and S. Ryu, "The Wireless Broadband (WIBRO) System for Broadband Wireless Internet Services," *IEEE Communications Magazine*, vol. 44, no. 7, pp. 106–112, 2006.

[157] J. Lee and R. Blahut, "Generalized EXIT Chart and BER Analysis of Finite-length Turbo Codes," in *Global Telecommunications Conference*, pp. 2067–2072, 1-5 December 2003.

[158] G. Yue, B. Lu, and X. Wang, "Analysis and Design of Finite-Length LDPC Codes," *IEEE Transactions on Vehicular Technology*, vol. 56, no. 3, pp. 1321–1332, 2007.

[159] J. Thorpe, "Low Density Parity Check (LDPC) Codes Constructed from Protographs," *JPL INP Progress Report*, 2003.

[160] D. Divsalar, S. Dolinar, and C. Jones, "Low-rate LDPC Codes with Simple Protograph Structure," in *International Symposium on Information Theory*, pp. 1622–1626, 4-9 September 2005.

[161] H.-A. Loeliger, "An Introduction to Factor Graphs," *IEEE Signal Processing Magazine*, vol. 21, no. 1, pp. 28–41, 2004.

Index

Author Index

M

N

O

P

Q

R

S

T

V

W

Y

Z